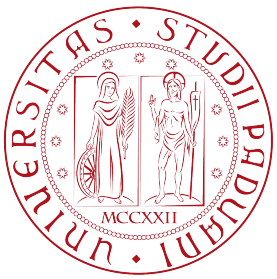

Università degli Studi di Padova
Centro Ricerche Fusione

Ghent University

JOINT RESEARCH DOCTORATE IN FUSION SCIENCE AND ENGINEERING
Cycle XXXIV

Alfvén waves excitation in toroidal fusion plasmas

Coordinator: Prof. Fabio Villone

Supervisor at Università degli Studi di Padova (Home University):
Dr. Daniele Bonfiglio

Supervisor at Università degli Studi di Padova (Home University):
Prof. Leonardo Giudicotti

Supervisor at Ghent University (Host University): Prof. Kristel Crombé

Ph.D. student: Artur Kryzhanovskyy

Padova, March 2022

Thanks to my family's support

Abstract

Nuclear fusion reactions are among the most important processes in the Universe, representing the phenomenon that allows the stars to shine and a source of energy potentially inexhaustible for humanity. The primary aim of the research on nuclear fusion is to obtain a new energy source to help satisfying a growing and sustainable consumption. The attempt to harvest the energy obtained from fusion reactions has led to the study of the confining technique of plasmas called magnetic confinement, which exploits the tendency of charged particles to follow the lines of the magnetic field. A large part of technological and scientific efforts are focused on obtaining controlled nuclear fusion plasmas in toroidal configurations such as tokamak, stellarator and reversed-field pinch (RFP), with the plasmas consisting of deuterium and tritium ions.

In order to make a fusion reaction in an experimental device, the reactants must be magnetically confined in a high-density high-temperature regime for a sufficiently long time, in order to overcome the Coulomb barrier between them. The magnetic confinement can however be deteriorated by magnetic fluctuations within the plasma, called Alfvén waves [Cramer, 2001]. They can provide an additional heat transport mechanism resulting in the degradation of the confinement properties of fusion plasmas. Energetic particles, such as alpha particles, can also resonantly destabilise the Alfvén waves [Dippolito et al., 1980; Holst et al., 2000; Chen et al., 2016], with two negative effects: energy transfer from alpha particles to the Alfvén waves and a loss of alpha particles before thermalization due to the resulting Alfvénic fluctuations [Donne et al., 2012]. All of these detrimental effects can compromise the stability of the plasma and its performance, with consequent increases of the requirements for operations in self-sustained ignited plasmas. On the other hand, the fact that Alfvén modes are frequently observed in tokamak, stellarator and RFP plasmas suggests that they could be used as a diagnostic of plasma equilibrium parameters. This MHD spetroscopy has shown how measurements of Alfvén waves mode structures can provide information on plasma parameters at particular points in the plasma [Holties et al., 1997]. In principle, Alfvén eigenmodes could also provide the basis for a plasma heating scheme as supplementary heating of fusion plasmas [Vaclavik et al., 1991; Poedts et al., 1992; Villard et al., 1995]. The scientific challenge in this context is to find the proper balance between desired and detrimental effects of the various magnetohydrodynamics (MHD) modes, to develop methods and tools for active feedback control of Alfvén modes [Garcia-Munoz et al., 2019] and identify new issues that may arise in approaching the ignition margin.

The importance of Alfvén waves is not limited to fusion plasmas, indeed they have been theoretically predicted and studied for the first time in the context of space and solar plasmas. In particular, Alfvén waves are thought to play a fundamental role in the heating of the solar corona [Parnell et al., 2012; Escande et al., 2019; Stefani et al., 2021], a physical process which is still not fully understood.

The research activity of my PhD focuses on the study of the 3D nonlinear magnetohydrodynamics model applied to the numerical study of the Alfvén waves in Tokamak and RFP configurations.

The main aim of my research is the characterization and interpretation of Alfvén waves spectra and their excitation mechanism based on periodic magnetic reconnection events in Tokamak and RFP configurations. This is achieved after a thorough analysis of simpler cases, which provide renewed occasion for numerical code benchmarking.

The main results obtained during my PhD are the prediction by nonlinear MHD simulations of excitation of Alfvén eigenmodes related to the magnetic reconnection events, together with a possible explanation of the physical origin of the experimentally observed Alfvén waves during Ohmic discharges in a number of present day RFP and Tokamak experiments. A possible theoretical identification as Alfvén eigenmodes of the coherent peaks experimentally observed in the power spectrum of the magnetic fluctuations at the plasma edge of RFX-mod, the biggest RFP experiment in the world, located in Padova, was achieved as well.

My PhD research activity and results can be divided into four main areas. A preliminary analytical calculation of dispersion relations of Alfvén waves in cylindrical geometry employing the ideal MHD model, both in uniform and non-uniform plasmas, were computed. All the theoretical formulas thus obtained were used in the following research activity to compute the theoretically expected frequency spectra for the different mean-field configurations and compare them with the numerical spectra from nonlinear MHD simulations. The first area of research consisted in the study of the dynamics of cyclic relaxation events in a set of Tokamak and RFP configuration cases, through numerical solution of the 3D nonlinear visco-resistive MHD model. The second area dealt with classification of Alfvén waves spectra for different single Fourier mode (single wave) simulations. The third area of research focused on the study of Alfvén waves excitation resulting from quasi-periodic sawtooth relaxation events in Tokamak plasmas. The fourth area covered the study of Alfvén waves excitation by periodic relaxations events in between Quasi-Single Helicity (QSH) states, and the comparison of results obtained with experimental observation in RFX-mod.

The *first area of research* deals with the study of the dynamics of relaxation events in RFP and Tokamak configurations. In particular in Tokamak configuration the dynamics of quasi-periodic sawtooth cycles were analised, starting from a helically-symmetric case with resistivity characterized by an internal m/n=1/1 (poloidal and toroidal mode numbers respectively) kink instability. Then a case with lower resistivity was considered for which the first appearance of secondary tearing instabilities, called plasmoids, was observed by using proper resolution (number of harmonics) of the main internal kink mode. These are thought to play an important role in the fast magnetic reconnection processes. By further lowering the resistivity a complete evolution of plasmoids is observed: formation, coalescence into a single larger secondary island and subsequent complete reconnection with the primary island of the internal kink instability. Subsequently, plasmoids are studied in fully 3D Tokamak configurations, with aspects such as magnetic and kinetic energy cascades and the magnetic topology of the configurations being investigated. Lastly a summary of a published study of fully 3D RFP simulations characterized by a systematic repetition of QSH states in between magnetic reconnection events was reported, as analogous simulations with different parameters were performed in this Thesis for the study of self-consistent dynamics of the plasma in fully 3D RFP configuration.

The *second area of research* is centered around numerical analysis and theoretical interpretation of frequency spectra in different magnetic and density configurations, to be used in subsequent analyses

for the identification of Alfvén modes in cylindrical geometry. The first analysed configuration (the simplest one) was an equilibrium configuration with uniform axial magnetic field with a uniform density profile. This case was used as a verification testbed, since it is the only one for which an exact analytical solution for different Alfvénic modes (namely the shear Alfvén wave, SAW, and compressional Alfvén eigenmodes, CAEs) can be obtained from the theoretical models. Next the analysis of a tokamak configuration considered first with a uniform density profile, then with a variable one, was performed. Identification of Alfvén waves in the frequency spectrum was achieved by employing techniques such as the Wentzel–Kramers–Brillouin (WKB) approximation. Compared to the previous case a new mode, the global Alfvén eigenmode (GAE) and new phenomena, like the phase mixing phenomenon, a damping mechanism for the continuous Alfvén waves, and a coupling between different Alfvén modes, were observed as theoretically predicted. The last configuration considered was an RFP-like equilibrium configuration with two different density profiles. Compared with the previous case, the frequencies of CAEs are lower and in particular the frequency of the first CAE crosses the SAW continuum. As a consequence the resonance absorption phenomena was observed, which is another damping mechanism for Alfvén waves, specifically for the compressional modes (CAEs) under certain conditions.
The *third area of research* dealt with analysing the frequency spectra of the Tokamak cases discussed above, in order to detect whenever the sawtooth dynamic could excite Alvénic modes and characterize under which condition this occurs. An initial weak excitation of Alfvénic modes is observed in the marginal case for the formation of plasmoids: the 1^{st} and 2^{nd} CAEs can be detected and are damped rapidly over time. A much stronger excitation is observed in simulations with lower resistivity: the SAW and the first three CAEs are clearly excited by the magnetic reconnection event. In the fully 3D configurations excitation of Alfvén waves with 1/0 periodicity are investigated, as experimentally the n=0 was found to be the dominant toroidal mode in several tokamak devices operating in Ohmic regime. Two methods for nonlinear coupling between 1/1 and 1/0 modes (in order to self consistenly excite the latter) are considered and compared.
The *fourth area of research* focuses on the analysis of the frequency spectra of the fully 3D RFP case discussed above, to detect the Alfvénic activity following the relaxation events in between QSH states. Investigation of a wide range of Fourier modes determined the 1/0 mode to be the most excited one, which is consistent with experimental observations in RFP devices in Ohmic regime. Finally a comparison between the numerical results and experimental observations was carried out, providing a possible interpretation of the coherent peaks experimentally observed in the power spectrum of the magnetic fluctuations at the plasma edge of RFX-mod device.

This Thesis contains several elements of originality, as it focuses on non-linear macroscopic effects that allowed to achieve novel results. The nonlinear approach of the performed numerical analysis (that allows to follow the temporal evolution of Alfvén waves) is rather original since most of the relevant literature uses the linear approach that can only provide the spectrum but not the dynamics of Alfvén waves (notable exceptions being several fully kinetic and gyrokinetic codes, together with hybrid kinetic-MHD codes such as HYMAGIC and MEGA [Vlad et al., 2021]). Regarding the results, excitation and detection of Alfvén waves in Ohmic plasmas is generally not much studied and understood as currently the research on this subject is mostly centered around the excitation of Alfvén waves by fast particles with velocities of the order of Alfvén speed, produced by neutral-beam injection (NBI), ion cyclotron resonance heating (ICRH), or even fusion born alpha particles. In this Thesis we showed the correlation between magnetic reconnection events and the excitation of Alfvén eigenmodes in Ohmic plasmas,

both in Tokamak and RFP configurations, a further confirmation of the common physics basis between the two confinement techniques. Moreover, the qualitative comparison with respect to experimental measurements in RFX-mod provided a first theoretical interpretation of the experimentally observed coherent modes.

The Thesis is organized in four parts.
The first part is an introduction to nuclear fusion in magnetically confined plasmas, and provides the definition of Alfvén waves and experimental highlights of RFX-mod device. The second part gives a basic analytical description of the Alfvén waves in plain and cylindrical configurations, presents the numerical tools employed and the numerical modeling of Tokamak and RFP configurations dynamics used later for Alfvén waves study. The third part includes the characterization of Alfvén waves first in single wave benchmark cases, followed by the study of the self-consistent dynamics in 2D and 3D tokamak and RFP configurations. In this part the main results are presented. In the fourth part final discussion and general conclusions are drawn. Technical aspects not covered in the main body of the Thesis are included in the appendices.

Part I: Introduction

In *Chapter 1* a definition of magnetized plasmas is given. Then we give a short and intuitive description of Alfvén waves, namely the shear Alfvén wave (SAW) and the compressional Alfvén wave (CAW), and their main features in the context of the ideal MHD model.

In *Chapter 2* the concept of thermonuclear fusion is introduced. The need to confine the fusion reactants, which are in the plasma state due to the high fusion temperature, leads to the study of the magnetic plasma confinement. After a summary about the general properties of the magnetically confined plasmas, we discuss two of the main devices for magnetic confinement employed in this Thesis, the tokamak configuration, which is the most exploited worldwide, and in deeper details the reversed-field pinch (RFP) configuration, which is another promising configuration and whose experimental observations are investigated in this Thesis.

In *Chapter 3* the main features of the RFX-mod device are introduced. RFX-mod was the first experimental device to show and investigate improved confinement RFP states, the so-called QSH states, for which a brief overview is given. Then experimental observations of Alfvén waves in the RFX-mod discharges, characterized by periodic magnetic reconnection events, are presented.

Part II: MHD model and Alfvén waves, SpeCyl code and reference simulations

In *Chapter 4* the MagnetoHydroDynamics (MHD) model is described. The MHD model is then used to describe plasma equilibrium state and the main types of plasma instabilities: ideal instabilities and resistive instabilities. Then a brief theoretical description of magnetic reconnection is given. In the end we give a rigorous analytical description of Alfvén waves in cartesian geometry, SAW and CAE modes, employing the MHD model in the ideal approximation.

In *Chapter 5* we will compute the equations of Alfvén waves in cylindrical geometry employing the ideal MHD model. In particular we will consider waves in a straight periodic cylinder with both uniform and non-uniform plasma (with non uniform density and/or magnetic field). The non-uniform case, compared to the uniform one (characterized only by the shear and the compressional modes), will be characterized by a new Alfvén mode, the Global Alfvén Eigenmode (GAE), and new phenomena like phase mixing and Alfvén resonance absorption. All the theoretical

formulas derived in this Chapter will be then used in the following chapters to compute the theoretically expected frequency spectra, to be compared with numerical spectra from nonlinear MHD simulations.

In *Chapter 6* the numerical tool used for solving the MHD model equations will be presented. This numerical tool, called SpeCyl, provided the numerical simulations employed for the analysis of Alfvén waves in different magnetic and density configurations, for both single wave cases and helically-symmetric 2D/ fully 3D cases. In particular we will present a systematic study of the dynamics of sawtooth relaxation events in a Tokamak configuration, moving from a classical dynamic with higher resistivity characterized by the presence of an internal kink instability to a dynamics with smaller resistivity containing also secondary tearing instabilities called plasmoids. These modeling simulations will be used in Chapter 8 to study Alfvén waves excitation by magnetic reconnection events. Similarly, we will present the results of a modeling study, based on RFP simulations performed with the SpeCyl code, which shows a systematic repetition of QSH states in between the reconnection events. The same simulations from this study will be used in the Chapter 9 to characterize the Alfvén waves in the most realistic RFP conditions presently achievable with the SpeCyl code.

Part III: Alfvén waves excitation in nonlinear MHD simulations

In *Chapter 7* we analyse single wave simulations (containing a single Fourier mode) for different density profiles and magnetic configurations: from a purely axial uniform magnetic field, to a non-uniform tokamak magnetic field and lastly an RFP-like magnetic field. For each simulation case, the spectrum of Alfvén waves is computed by performing the Fourier analysis. Then, the features of the computed numerical spectrum are discussed, including its temporal evolution, and a physical interpretation based on the expected theoretical model is provided.

In *Chapter 8* we analyse the excitation of Alvén waves in the Tokamak configuration characterized by the quasi periodic sawtooth instability. In other words, in this and the next chapter Alfvén modes are excited by the self-consistent MHD dynamics instead of by initial velocity perturbations as in the previous chapter. In particular we analyse different cases discussed in Chapter 6, going from helically-symmetric 2D to fully 3D configurations.

In *Chapter 9* we analyse the excitation of Alfvén waves in the fully 3D RFP configuration characterized by QSH states in between the magnetic reconnection events discussed in Chapter 6. In the end we make a qualitative comparison of numerical results for the RFP configuration with the experimental observations on the RFX-mod device.

Part IV: Summary and conclusions

In this Part, the results described in the Thesis are summarized and the final conclusions are drawn together with the future perspectives that can be traced.

Appendices

Here appendices, which clarify important details and give useful informations not included in the body of the Thesis, can be found. A relevant bibliography is also provided at the end.

Prefazione

Le reazioni di fusione nucleare sono tra i processi più importanti dell'Universo, rappresentano il fenomeno che permette alle stelle di brillare e una fonte di energia potenzialmente inesauribile per l'umanità. L'obiettivo primario della ricerca sulla fusione nucleare è ottenere una nuova fonte di energia per contribuire a soddisfare un consumo crescente e sostenibile. Il tentativo di raccogliere l'energia ottenuta dalle reazioni di fusione ha portato allo studio della tecnica di confinamento dei plasmi chiamata confinamento magnetico, che sfrutta la tendenza delle particelle cariche a seguire le linee del campo magnetico. Gran parte degli sforzi tecnologici e scientifici sono concentrati sull'ottenimento di plasmi di fusione nucleare controllata in configurazioni toroidali come tokamak, stellarator e reversed-field pinch (RFP), con plasmi costituiti da ioni deuterio e trizio.

Per realizzare una reazione di fusione in un dispositivo sperimentale, i reagenti devono essere confinati magneticamente in un regime ad alta densità e ad alta temperatura per un tempo sufficientemente lungo, in modo da superare la barriera coulombiana tra di loro. Il confinamento magnetico può tuttavia essere deteriorato dalle fluttuazioni magnetiche all'interno del plasma, chiamate onde di Alfvén [Cramer, 2001]. Esse possono fornire un ulteriore meccanismo di trasporto del calore, con conseguente degradazione delle proprietà di confinamento dei plasmi da fusione. Anche le particelle energetiche, come le particelle alfa, possono destabilizzare in modo risonante le onde di Alfvén [Dippolito et al., 1980; Holst et al., 2000; Chen et al., 2016], con due effetti negativi: il trasferimento di energia dalle particelle alfa alle onde di Alfvén e la perdita di particelle alfa prima della termalizzazione, a causa delle fluttuazioni alfveniche risultanti [Donne et al., 2012]. Tutti questi effetti negativi possono compromettere la stabilità del plasma e le sue prestazioni, con conseguente aumento dei requisiti per le operazioni in plasmi da fusione autosostenuti. D'altra parte, il fatto che i modi di Alfvén siano frequentemente osservati nei plasmi dei tokamak, degli stellarator e degli RFP suggerisce che potrebbero essere utilizzati come diagnostica dei parametri di equilibrio del plasma. Questa spetroscopia MHD ha mostrato come le misure delle strutture dei modi di Alfvén possano fornire informazioni sui parametri del plasma in particolari punti del plasma [Holties et al., 1997]. In linea di principio, gli autovalori di Alfvén potrebbero anche fornire la base per uno schema di riscaldamento del plasma come riscaldamento supplementare dei plasmi da fusione [Vaclavik et al., 1991; Poedts et al., 1992; Villard et al., 1995]. La sfida scientifica in questo contesto è trovare il giusto equilibrio tra gli effetti desiderati e quelli dannosi dei vari modi magnetoidrodinamici (MHD), sviluppare metodi e strumenti per il controllo attivo dei modi Alfvén [Garcia-Munoz et al., 2019] e identificare nuovi problemi che possono sorgere nell'avvicinarsi al margine di ignizione.

L'importanza delle onde di Alfvén non è limitata ai plasmi di fusione, infatti sono state previste e studiate teoricamente per la prima volta nel contesto dei plasmi spaziali e solari. In particolare, si ritiene che le onde di Alfvén svolgano un ruolo fondamentale nel riscaldamento della corona solare [Parnell

et al., 2012; Escande et al., 2019; Stefani et al., 2021], un processo fisico ancora non del tutto compreso.

L'attività di ricerca del mio dottorato si concentra sullo studio del modello magnetoidrodinamico 3D non lineare applicato allo studio numerico delle onde di Alfvén in configurazioni Tokamak e RFP.

L'obiettivo principale della mia ricerca è la caratterizzazione e l'interpretazione degli spettri delle onde Alfvén e del loro meccanismo di eccitazione basato su eventi di riconnessione magnetica periodica in configurazioni Tokamak e RFP. Questo obiettivo viene raggiunto dopo un'analisi approfondita di casi più semplici, che forniscono una nuova occasione per il benchmark dei codici numerici.

I principali risultati ottenuti durante il mio dottorato sono la previsione, tramite simulazioni MHD non lineari, dell'eccitazione degli autovalori di Alvén legati agli eventi di riconnessione magnetica, insieme a una possibile spiegazione dell'origine fisica delle onde di Alfvén osservate sperimentalmente durante le scariche ohmiche in alcuni esperimenti RFP e Tokamak attuali. È stata anche raggiunta una possibile identificazione teorica come autovalori di Alfvén dei picchi coerenti osservati sperimentalmente nello spettro di potenza delle fluttuazioni magnetiche al bordo del plasma di RFX-mod, il più grande esperimento RFP del mondo, situato a Padova.

L'attività di ricerca e i risultati del mio dottorato possono essere suddivisi in quattro aree principali. È stato effettuato un calcolo analitico preliminare delle relazioni di dispersione delle onde di Alfvén in geometria cilindrica utilizzando il modello MHD ideale, sia in plasmi uniformi che non uniformi. Tutte le formule teoriche così ottenute sono state utilizzate nella successiva attività di ricerca per calcolare gli spettri di frequenza teoricamente attesi per le diverse configurazioni di campo medio e confrontarli con gli spettri numerici ottenuti da simulazioni MHD non lineari. La prima area di ricerca è consistita nella simulazione dinamica di un plasma confinato magneticamente nelle configurazioni RFP e Tokamak attraverso la soluzione numerica del modello MHD non lineare visco-resistivo 3D. La seconda area ha riguardato la classificazione degli spettri delle onde di Alfvén per diverse simulazioni a singolo modo di Fourier (onda singola). La terza area di ricerca si è concentrata sullo studio dell'eccitazione delle onde di Alfvén derivanti da eventi di rilassamento quasi-periodici a dente di sega nei plasmi Tokamak. La quarta area ha riguardato lo studio dell'eccitazione delle onde di Alfvén da parte di eventi di rilassamento periodico in stati di quasi-singola elicità (QSH) e il confronto dei risultati ottenuti con l'osservazione sperimentale in RFX-mod.

La *prima area di ricerca* riguarda lo studio della dinamica degli eventi di rilassamento nelle configurazioni RFP e Tokamak. In particolare, nella configurazione Tokamak è stata analizzata la dinamica dei cicli quasi-periodici a dente di sega, partendo da un caso classico a simmetria elicoidale con resistività relativamente alta, caratterizzato da un'instabilità interna di tipo kink m/n=1/1 (numeri di modo poloidale e toroidale rispettivamente). È stato poi considerato un caso marginale con resistività di soglia per il quale è stata osservata la prima comparsa di instabilità secondarie tearing, chiamate plasmoidi, se si considera un numero sufficientemente elevato di armoniche del modo kink interno principale. Si ritiene che queste giochino un ruolo importante nei processi di riconnessione magnetica veloce. Abbassando ulteriormente la resistività si osserva un'evoluzione completa dei plasmoidi: formazione, coalescenza in un'unica isola secondaria più grande e successiva riconnessione completa con l'isola primaria dell'instabilità kink interna. Successivamente, i plasmoidi sono stati studiati in configurazioni Tokamak completamente 3D, con aspetti quali le cascate di energia magnetica e cinetica e la topologia magnetica delle configurazioni. Infine, è stata riportata una sintesi di uno studio pubblicato di simulazioni RFP completamente 3D caratterizzate da una ripetizione sistematica degli stati QSH tra gli eventi di riconnessione magnetica, in quanto simulazioni analoghe con parametri diversi sono state eseguite in questa Tesi per lo studio della

dinamica autoconsistente del plasma in configurazione RFP completamente 3D.
La *seconda area di ricerca* è incentrata sull'analisi numerica e sull'interpretazione teorica degli spettri di frequenza in diverse configurazioni magnetiche e di densità, da utilizzare nelle successive analisi per l'identificazione dei modi di Alfvén in geometria cilindrica. La prima configurazione analizzata (la più semplice) è stata una configurazione di equilibrio con campo magnetico assiale uniforme e profilo di densità uniforme. Questo caso è stato utilizzato come banco di prova, poiché è l'unico per il quale è possibile ottenere dai modelli teorici una soluzione analitica esatta per i diversi modi di Alfvén (in particolare l'onda shear di Alfvén, SAW, e gli compressional Alfvén eigenmodes, CAE). Successivamente è stata eseguita l'analisi di una configurazione di tokamak considerata prima con un profilo di densità uniforme, poi con uno variabile. L'identificazione delle onde di Alfvén nello spettro di frequenza è stata ottenuta utilizzando l'approssimazione di Wentzel-Kramers-Brillouin (WKB). Rispetto al caso precedente, è stato osservato un nuovo modo, il global Alfvén eigenmode (GAE) e nuovi fenomeni, come il fenomeno del phase mixing, un meccanismo di smorzamento per il continuum SAW e un accoppiamento tra diversi modi di Alfvén, come previsto teoricamente. L'ultima configurazione considerata è stat una configurazione di equilibrio di tipo RFP con due diversi profili di densità. Rispetto al caso precedente, le frequenze delle CAE sono più basse e in particolare la frequenza della prima CAE attraversa il continuum SAW. Di conseguenza, è stato osservato il fenomeno del resonance absorption, che rappresenta un altro meccanismo di smorzamento per le onde di Alfvén, in particolare per i modi compressionali (CAE) in determinate condizioni.
La *terza area di ricerca* si occupa di analizzare gli spettri di frequenza dei casi Tokamak discussi in precedenza, al fine di individuare quando la dinamica a dente di sega può eccitare i modi di Alfvén e caratterizzare in quali condizioni ciò si verifica. Una debole eccitazione iniziale dei modi di Alfvén si osserva nel caso marginale della formazione di plasmoidi: la 1^a e 2^a CAE possono essere rilevate e vengono smorzate rapidamente nel tempo. Nelle simulazioni con resistività inferiore si osserva un'eccitazione molto più forte: la SAW e le prime tre CAE sono chiaramente eccitate dall'evento di riconnessione magnetica. Nelle configurazioni completamente tridimensionali si studia l'eccitazione delle onde di Alfvén con periodicità 1/0, poiché sperimentalmente si è riscontrato che n=0 è il modo toroidale dominante in diversi dispositivi tokamak operanti in regime ohmico. Vengono considerati e confrontati due metodi per l'accoppiamento non lineare tra i modi 1/1 e 1/0 (al fine di eccitare in modo autoconsistente quest'ultimo).
La *quarta area di ricerca* si concentra sull'analisi degli spettri di frequenza del caso RFP completamente 3D discusso in precedenza, per individuare l'attività alfvenica che segue gli eventi di rilassamento tra gli stati QSH. L'analisi di un'ampia gamma di modi di Fourier ha determinato che il modo 1/0 è quello più eccitato, il che è coerente con le osservazioni sperimentali nei dispositivi RFP in regime ohmico. Infine, è stato effettuato un confronto tra i risultati numerici e le osservazioni sperimentali, fornendo una possibile interpretazione dei picchi coerenti osservati sperimentalmente nello spettro di potenza delle fluttuazioni magnetiche al bordo del plasma del dispositivo RFX-mod.

Questa tesi contiene diversi elementi di originalità, in quanto si concentra sullo studio di effetti non lineari macroscopici che hanno permesso di ottenere risultati inediti. L'approccio non lineare dell'analisi numerica effettuata (che permette di seguire l'evoluzione temporale delle onde di Alfvén) è piuttosto originale, poiché la maggior parte della letteratura in materia utilizza un approccio lineare che può fornire solo lo spettro ma non la dinamica delle onde di Alfvén (eccezioni degne di nota sono diversi codici completamente cinetici e girocinetici, insieme a codici ibridi cinetici-MHD come HYMAGIC e MEGA

[Vlad et al., 2021]). Per quanto riguarda i risultati, l'eccitazione e la rivelazione delle onde di Alfvén nei plasmi ohmici non è generalmente molto studiata e compresa, poiché attualmente la ricerca su questo argomento è per lo più incentrata sull'eccitazione delle onde di Alfvén da parte di particelle veloci con velocità dell'ordine di quella di Alfvén, prodotte dall'iniezione di fasci neutri (NBI), dal riscaldamento a risonanza ciclotronico ionico (ICRH) o anche da particelle alfa nate dalla fusione. In questa Tesi abbiamo dimostrato la correlazione tra eventi di riconnessione magnetica e l'eccitazione di autovalori di Alfvén in plasmi ohmici, sia in configurazione Tokamak che RFP, un'ulteriore conferma della base fisica comune tra le due tecniche di confinamento. Inoltre, il confronto qualitativo con le misure sperimentali in RFX-mod ha fornito una prima interpretazione teorica dei modi coerenti osservati sperimentalmente.

La Tesi è organizzata in quattro parti.
La prima parte è un'introduzione alla fusione nucleare in plasmi confinati magneticamente e fornisce la definizione di onde di Alfvén e le caratteristiche sperimentali del dispositivo RFX-mod. La seconda parte fornisce una descrizione analitica di base delle onde di Alfvén in configurazioni cartesiane e cilindriche, presenta gli strumenti numerici impiegati e la modellazione numerica delle dinamiche delle configurazioni Tokamak e RFP utilizzate successivamente per lo studio delle onde di Alfvén. La terza parte comprende la caratterizzazione delle onde di Alfvén prima in casi di riferimento a onda singola, seguita dallo studio della dinamica autoconsistente in configurazioni tokamak e RFP 2D e 3D. In questa parte vengono presentati i principali risultati. Nella quarta parte si discutono i risultati finali e si traggono le conclusioni generali. Gli aspetti tecnici non trattati nel corpo principale della Tesi sono inclusi nelle appendici.

Parte I: Introduzione

Nel *Capitolo 1* viene data una definizione di plasmi magnetizzati. Viene poi fornita una breve e intuitiva descrizione delle onde di Alfvén, ovvero l'onda shear di Alfvén (SAW) e l'onda compressionale di Alfvén (CAW), e delle loro caratteristiche principali nel contesto del modello MHD ideale.

Nel *Capitolo 2* viene introdotto il concetto di fusione termonucleare. La necessità di confinare i reagenti della fusione, che si trovano allo stato di plasma a causa dell'elevata temperatura di fusione, porta allo studio del confinamento magnetico del plasma. Dopo un riepilogo sulle proprietà generali dei plasmi confinati magneticamente, discutiamo due dei principali dispositivi per il confinamento magnetico utilizzati in questa Tesi, la configurazione tokamak, che è la più utilizzata a livello mondiale, e in modo più approfondito la configurazione reversed-field pinch (RFP), che è un'altra configurazione promettente e le cui osservazioni sperimentali sono studiate in questa Tesi.

Nel *Capitolo 3* vengono introdotte le caratteristiche principali del dispositivo RFX-mod. RFX-mod è stato il primo dispositivo sperimentale a mostrare e studiare stati RFP a confinamento migliorato, i cosiddetti stati QSH, di cui viene fornita una breve panoramica. Vengono poi presentate le osservazioni sperimentali delle onde di Alfvén nelle scariche di RFX-mod, caratterizzate da eventi periodici di riconnessione magnetica.

Parte II: Modello MHD e onde di Alfvén, codice SpeCyl e simulazioni di riferimento

Nel *Capitolo 4* viene descritto il modello magnetoidrodinamico (MHD). Il modello MHD viene poi utilizzato per descrivere lo stato di equilibrio del plasma e i principali tipi di instabilità del plasma: instabilità ideali e instabilità resistive. Viene poi fornita una breve descrizione

teorica della riconnessione magnetica. Infine, viene fornita una descrizione analitica rigorosa delle onde di Alfvén in geometria cartesiana, dei modi SAW e CAE, impiegando il modello MHD nell'approssimazione ideale.

Nel *Capitolo 5* calcoleremo le equazioni delle onde di Alfvén in geometria cilindrica impiegando il modello MHD ideale. In particolare, considereremo le onde in un cilindro rettilineo periodico con plasma sia uniforme sia non uniforme (con densità e/o campo magnetico non uniformi). Il caso non uniforme, rispetto a quello uniforme (caratterizzato solo dai modi shear e compressional), sarà caratterizzato da un nuovo modo di Alfvén, il Global Alfvén Eigenmode (GAE), e da nuovi fenomeni come il phase mixing e il resonance absorption. Tutte le formule teoriche ricavate in questo capitolo saranno poi utilizzate nei capitoli successivi per calcolare gli spettri di frequenza teoricamente attesi, da confrontare con gli spettri numerici ottenuti da simulazioni MHD non lineari.

Nel *Capitolo 6* verrà presentato lo strumento numerico utilizzato per risolvere le equazioni del modello MHD. Questo strumento numerico, chiamato SpeCyl, ha fornito le simulazioni numeriche impiegate per l'analisi delle onde di Alfvén in diverse configurazioni magnetiche e di densità, sia per i casi di onda singola che per i casi elicoidali simmetrici 2D e completamente 3D. In particolare, presenteremo uno studio sistematico della dinamica degli eventi di rilassamento a dente di sega in configurazione Tokamak, passando da una dinamica classica con resistività più elevata, caratterizzata dalla presenza di un'instabilità interna di tipo kink, a una dinamica con resistività più ridotta che contiene anche instabilità secondarie tearing chiamate plasmoidi. Queste simulazioni di modellizzazione saranno utilizzate nel Capitolo 8 per studiare l'eccitazione delle onde di Alfvén da parte di eventi di riconnessione magnetica. Allo stesso modo, presenteremo i risultati di uno studio modellistico, basato su simulazioni RFP eseguite con il codice SpeCyl, che mostra una ripetizione sistematica degli stati QSH tra gli eventi di riconnessione. Le stesse simulazioni di questo studio saranno utilizzate nel Capitolo 9 per caratterizzare le onde di Alfvén nelle condizioni RFP più realistiche attualmente ottenibili con il codice SpeCyl.

Parte III: Eccitazione delle onde di Alfvén nelle simulazioni MHD non lineari

Nel *Capitolo 7* analizziamo simulazioni di onda singola (contenenti un singolo modo di Fourier) per diversi profili di densità e configurazioni magnetiche: da un campo magnetico uniforme puramente assiale, a un campo magnetico non uniforme di tokamak e infine a un campo magnetico di tipo RFP. Per ogni caso di simulazione, lo spettro delle onde di Alfvén viene calcolato eseguendo l'analisi di Fourier. Vengono poi discusse le caratteristiche dello spettro numerico calcolato, compresa la sua evoluzione temporale, e viene fornita un'interpretazione fisica basata sul modello teorico previsto.

Nel *Capitolo 8* analizziamo l'eccitazione delle onde di Alvén nella configurazione tokamak caratterizzata dall'instabilità quasi periodica a dente di sega. In altre parole, in questo e nel prossimo capitolo i modi di Alfvén sono eccitati dalla dinamica MHD autoconsistente invece che da perturbazioni della velocità iniziale come nel capitolo precedente. In particolare, analizziamo diversi casi discussi nel Capitolo 6, passando da configurazioni elico-simmetriche 2D a configurazioni completamente 3D.

Nel *Capitolo 9* analizziamo l'eccitazione delle onde di Alfvén nella configurazione RFP completamente 3D caratterizzata da stati QSH tra gli eventi di riconnessione magnetica discussi nel Capitolo 6. Alla fine viene effettuato un confronto qualitativo dei risultati numerici per la config-

urazione RFP con le osservazioni sperimentali sul dispositivo RFX-mod.

Parte IV: Riepilogo e conclusioni

In questa parte si riassumono i risultati descritti nella Tesi e si traggono le conclusioni finali insieme alle prospettive future che si possono tracciare.

Appendici

Qui si trovano le appendici, che chiariscono dettagli importanti e forniscono informazioni utili non incluse nel corpo della Tesi. Alla fine è riportata la bibliografia.

Abstract

Kernfusiereacties behoren tot de belangrijkste processen in het heelal en vormen het verschijnsel dat de sterren laat schijnen en een energiebron die potentieel onuitputtelijk is voor de mensheid. Het onderzoek op het gebied van kernfusie is in de eerste plaats gericht op het verkrijgen van een nieuwe energiebron waarmee kan worden voldaan aan een toenemend en duurzaam verbruik. De poging om de uit fusiereacties verkregen energie te oogsten heeft geleid tot de bestudering van de opsluitingstechniek van plasma's, magnetische opsluiting genaamd, die gebruik maakt van de neiging van geladen deeltjes om de lijnen van het magnetisch veld te volgen. Een groot deel van de technologische en wetenschappelijke inspanningen is gericht op het verkrijgen van gecontroleerde kernfusieplasma's in toroïdale configuraties, zoals tokamak, stellarator en reversed-field pinch (RFP), waarbij de plasma's bestaan uit deuterium- en tritium-ionen.

Om een fusiereactie tot stand te brengen in een experimenteel apparaat, moeten de reactanten voldoende lang magnetisch opgesloten zijn in een regime met hoge dichtheid en hoge temperatuur, om de Coulomb-barrière tussen hen te overwinnen. De magnetische opsluiting kan echter worden verslechterd door magnetische fluctuaties binnen het plasma, de zogenaamde Alfvén-golven [Cramer, 2001]. Deze kunnen zorgen voor een extra warmtetransportmechanisme waardoor de opsluitingseigenschappen van fusieplasma's worden aangetast. Energetische deeltjes, zoals alfadeeltjes, kunnen ook resonant de Alfvén golven destabiliseren [Dippolito et al., 1980; Holst et al., 2000; Chen et al., 2016], met twee negatieve effecten: energieoverdracht van alfadeeltjes naar de Alfvén golven en een verlies van alfadeeltjes vóór de thermalisatie als gevolg van de resulterende Alfvénische fluctuaties [Donne et al., 2012]. Al deze schadelijke effecten kunnen de stabiliteit van het plasma en zijn prestaties in het gedrang brengen, met als gevolg dat de vereisten voor operaties in zelfonderhoudende ontstoken plasma's hoger worden. Anderzijds suggereert het feit dat Alfvén modes frequent worden waargenomen in tokamak, stellarator en RFP plasma's dat ze zouden kunnen gebruikt worden als een diagnosticum voor plasma-evenwichtsparameters. Deze MHD spetroscopie heeft aangetoond hoe metingen van Alfvén eigenmodes structuren informatie kunnen verschaffen over plasma parameters op bepaalde punten in het plasma [Holties et al., 1997]. In principe zouden Alfvén eigenmodes ook de basis kunnen vormen voor een plasmaverwarmingsschema als aanvullende verwarming van fusieplasma's [Vaclavik et al., 1991; Poedts et al., 1992; Villard et al., 1995]. De wetenschappelijke uitdaging in deze context is om de juiste balans te vinden tussen gewenste en nadelige effecten van de verschillende magnetohydrodynamische (MHD) modi, om methoden en instrumenten te ontwikkelen voor actieve terugkoppelingscontrole van Alfvén modi [Garcia-Munoz et al., 2019] en om nieuwe problemen te identificeren die zich kunnen voordoen bij het benaderen van de ontstekingsmarge.

Het belang van Alfvén-golven is niet beperkt tot fusieplasma's, ze zijn zelfs voor het eerst theoretisch

voorspeld en bestudeerd in de context van ruimte- en zonneplasma's. In het bijzonder wordt gedacht dat Alfvén-golven een fundamentele rol spelen in de verhitting van de zonnecorona [Parnell et al., 2012; Escande et al., 2019; Stefani et al., 2021], een fysisch proces dat nog steeds niet volledig begrepen is.

De onderzoeksactiviteit van mijn doctoraat spitst zich toe op de studie van het 3D niet-lineaire magnetohydrodynamica-model toegepast op de numerieke studie van de Alfvén-golven in Tokamak- en RFP-configuraties.

Het hoofddoel van mijn onderzoek is de karakterisering en interpretatie van Alfvén-golfspectra en hun excitatiemechanisme gebaseerd op periodieke magnetische herverbindingsgebeurtenissen in Tokamak- en RFP-configuraties. Dit wordt bereikt na een grondige analyse van eenvoudiger gevallen, die een nieuwe gelegenheid bieden voor het benchmarken van numerieke code.

De belangrijkste resultaten verkregen tijdens mijn doctoraat zijn de voorspelling door niet-lineaire MHD simulaties van excitatie van Alvén eigenmodes gerelateerd aan de magnetische herconnectie gebeurtenissen, samen met een mogelijke verklaring van de fysische oorsprong van de experimenteel waargenomen Alfvén golven tijdens Ohmse ontladingen in een aantal hedendaagse RFP en Tokamak experimenten. Een mogelijke theoretische identificatie als Alfvén eigenmodes van de coherente pieken die experimenteel zijn waargenomen in het vermogensspectrum van de magnetische fluctuaties aan de plasma-rand van RFX-mod, het grootste RFP-experiment ter wereld, dat in Padua is gevestigd, werd ook bereikt.

Mijn PhD-onderzoeksactiviteiten en -resultaten kunnen worden onderverdeeld in vier hoofdgebieden. Een eerste analytische berekening van dispersierelaties van Alfvén-golven in cilindrische geometrie met behulp van het ideale MHD-model, zowel in uniforme als niet-uniforme plasma's, werd berekend. Alle aldus verkregen theoretische formules werden gebruikt in de volgende onderzoeksactiviteit om de theoretisch verwachte frequentiespectra te berekenen voor de verschillende gemiddelde-veld configuraties en deze te vergelijken met de numerieke spectra uit niet-lineaire MHD simulaties. Het eerste onderzoeksgebied bestond uit de dynamische simulatie van een magnetisch opgesloten plasma in RFP- en Tokamak-configuraties door numerieke oplossing van het 3D niet-lineaire visco-resistieve MHD-model. Het tweede gebied betrof de classificatie van Alfvén-golfspectra voor verschillende simulaties met enkele Fourier-modus (enkele golf). Het derde onderzoeksgebied richtte zich op de studie van de excitatie van Alfvén-golven als gevolg van quasi-periodieke zaagtandrelaxatiegebeurtenissen in Tokamakplasma's. Het vierde gebied betrof de studie van de excitatie van Alfvén-golven door periodieke relaxatiegebeurtenissen tussen Quasi-Single Helicity (QSH)-toestanden, en de vergelijking van de verkregen resultaten met experimentele waarnemingen in RFX-mod.
Het eerste gebied van onderzoek heeft betrekking op de studie van de dynamica van relaxatiegebeurtenissen in RFP- en Tokamak-configuraties. In het bijzonder in Tokamak-configuraties werd de dynamica van quasi-periodieke zaagtandcycli geanalyseerd, uitgaande van een helically-symmetrisch klassiek geval met relatief hoge weerstand, gekenmerkt door een interne m/n=1/1 (poloidal en toroidal mode numbers respectievelijk) knikinstabiliteit. Vervolgens werd een marginaal geval met drempelweerstand in ogenschouw genomen waarbij het eerste optreden van secundaire scheurinstabiliteiten, plasmoïden genaamd, werd waargenomen indien een voldoende groot aantal harmonischen van de belangrijkste interne knikmode in ogenschouw werd genomen. Deze worden verondersteld een belangrijke rol te spelen in de snelle magnetische herverbindingsprocessen. Door de weerstand verder te verlagen wordt een volledige evolutie van plasmoïden waargenomen: vorming, coalescentie tot een enkel groter secundair eiland en vervolgens volledige reconnectie met het primaire eiland van de interne knikinstabiliteit. Ver-

volgens worden plasmoïden bestudeerd in volledig 3D Tokamak-configuraties, waarbij aspecten zoals magnetische en kinetische energiecascades en de magnetische topologie van de configuraties worden onderzocht. Tenslotte werd een samenvatting gerapporteerd van een gepubliceerde studie van volledig 3D RFP simulaties gekenmerkt door een systematische herhaling van QSH toestanden tussen magnetische herverbindingsgebeurtenissen, zoals analoge simulaties met verschillende parameters werden uitgevoerd in dit proefschrift voor de studie van zelfconsistente dynamica van het plasma in volledig 3D RFP configuratie.
Het tweede onderzoeksgebied is geconcentreerd rond numerieke analyse en theoretische interpretatie van frequentiespectra in verschillende magnetische en dichtheidsconfiguraties, om te worden gebruikt in latere analyses voor de identificatie van Alfvénmodes in cilindrische geometrie. De eerste geanalyseerde configuratie (de eenvoudigste) was een evenwichtsconfiguratie met een uniform axiaal magnetisch veld met een uniform dichtheidsprofiel. Dit geval werd gebruikt als verificatietestbed, omdat het de enige is waarvoor een exacte analytische oplossing voor verschillende Alfvénische toestanden (namelijk de afschuiving van de Alfvén-golf, SAW, en de samendrukking van de Alfvén- eigenmodes, CAE's) uit de theoretische modellen kan worden verkregen. Vervolgens werd de analyse uitgevoerd van een tokamakconfiguratie die eerst met een uniform dichtheidsprofiel en vervolgens met een variabel dichtheidsprofiel werd beschouwd. Identificatie van Alfvén-golven in het frequentiespectrum werd bereikt door gebruik te maken van technieken zoals de Wentzel-Kramers-Brillouin (WKB) benadering. In vergelijking met het vorige geval werden een nieuwe modus, de globale Alfvén eigenmode (GAE) en nieuwe fenomenen, zoals het fenomeen van de fasemixing, een dempingsmechanisme voor de continue Alfvén golven, en een koppeling tussen verschillende Alfvén modi, waargenomen zoals theoretisch voorspeld. De laatste beschouwde configuratie was een RFP-achtige evenwichtsconfiguratie met twee verschillende dichtheidsprofielen. Vergeleken met het vorige geval zijn de frequenties van de CAE's lager en in het bijzonder kruist de frequentie van de eerste CAE het SAW-continuüm. Dientengevolge werd het resonantie-absorptieverschijnsel waargenomen, dat een ander dempingsmechanisme is voor Alfvéngolven, specifiek voor de compressiemodi (CAE's) onder bepaalde omstandigheden.
Het derde onderzoeksgebied betrof de analyse van de frequentiespectra van de hierboven besproken Tokamakgevallen, om te detecteren wanneer de zaagtanddynamiek Alvénische toestanden zou kunnen exciteren en te karakteriseren onder welke voorwaarde dit gebeurt. Een aanvankelijk zwakke excitatie van Alfvénische modi wordt waargenomen in het marginale geval voor de vorming van plasmoïden: de eerste en tweede CAE's kunnen worden gedetecteerd en worden in de loop van de tijd snel gedempt. Een veel sterkere excitatie wordt waargenomen in simulaties met lagere weerstand: de SAW en de eerste drie CAEs worden duidelijk geëxciteerd door de magnetische reconnectie gebeurtenis. In de volledig 3D configuraties wordt de excitatie van Alfvén golven met 1/0 periodiciteit onderzocht, aangezien experimenteel werd vastgesteld dat n=0 de dominante toroïdale modus is in verschillende tokamak apparaten die in het Ohmse regime werken. Twee methoden voor niet-lineaire koppeling tussen 1/1 en 1/0 modi (om deze laatste op een zelfconsistente manier te exciteren) worden overwogen en vergeleken.
Het vierde onderzoeksgebied richt zich op de analyse van de frequentiespectra van het volledig 3D RFP geval dat hierboven besproken is, om de Alfvénische activiteit te detecteren die volgt op de relaxatiegebeurtenissen tussen QSH toestanden in. Onderzoek van een breed scala van Fourier modes bepaalde dat de 1/0 mode de meest geëxciteerde is, hetgeen consistent is met experimentele waarnemingen in RFP apparaten in het Ohmse regime. Tenslotte werd een vergelijking uitgevoerd tussen de numerieke resultaten en experimentele waarnemingen, wat een mogelijke interpretatie geeft van de coherente pieken

die experimenteel werden waargenomen in het vermogensspectrum van de magnetische fluctuaties aan de plasma-rand van RFX-mod apparaten.

Dit proefschrift bevat verschillende elementen van originaliteit, aangezien het zich concentreert op niet-lineaire macroscopische effecten die toelieten om nieuwe resultaten te bereiken. De niet-lineaire benadering van de uitgevoerde numerieke analyse (die toelaat om de temporele evolutie van Alfvén golven te volgen) is eerder origineel aangezien de meeste relevante literatuur de lineaire benadering gebruikt die enkel het spectrum maar niet de dynamica van Alfvén golven kan weergeven (opmerkelijke uitzonderingen zijn verschillende volledig kinetische en gyrokinetische codes, samen met hybride kinetische-MHD codes zoals HYMAGIC en MEGA [Vlad et al., 2021]). Wat de resultaten betreft, is de excitatie en detectie van Alfvén golven in Ohmse plasma's over het algemeen niet veel bestudeerd en begrepen, omdat momenteel het onderzoek over dit onderwerp vooral gericht is op de excitatie van Alfvén golven door snelle deeltjes met snelheden in de orde van Alfvén snelheid, geproduceerd door neutrale bundel injectie (NBI), ion cyclotron resonantie verwarming (ICRH), of zelfs door fusie geboren alfa deeltjes. In dit proefschrift hebben we de correlatie aangetoond tussen magnetische herverbindings-gebeurtenissen en de excitatie van Alfvén eigenmodes in Ohmse plasma's, zowel in Tokamak- als RFP-configuraties, een verdere bevestiging van de gemeenschappelijke fysische basis tussen de twee opsluitingstechnieken. Bovendien leverde de kwalitatieve vergelijking met experimentele metingen in RFX-mod een eerste theoretische interpretatie op van de experimenteel waargenomen coherente modi.

Het proefschrift bestaat uit vier delen.
Het eerste deel is een inleiding tot kernfusie in magnetisch opgesloten plasma's, en geeft de definitie van Alfvén-golven en experimentele hoogtepunten van RFX-mod apparatuur. Het tweede deel geeft een analytische basisbeschrijving van de Alfvén-golven in gewone en cilindrische configuraties, presenteert de gebruikte numerieke hulpmiddelen en de numerieke modellering van de dynamica van Tokamak- en RFP-configuraties die later voor de studie van Alfvén-golven worden gebruikt. Het derde deel omvat de karakterisering van Alfvén golven eerst in enkele golf benchmark gevallen, gevolgd door de studie van de zelfconsistente dynamica in 2D en 3D tokamak en RFP configuraties. In dit deel worden de belangrijkste resultaten gepresenteerd. In het vierde deel worden eindbesprekingen gevoerd en algemene conclusies getrokken. Technische aspecten die niet in het hoofdgedeelte van het proefschrift aan de orde komen, zijn opgenomen in de bijlagen.

Deel I: Inleiding

In *Hoofdstuk 1* wordt een definitie gegeven van gemagnetiseerde plasma's. Vervolgens geven we een korte en intuïtieve beschrijving van Alfvén-golven, namelijk de shear Alfvén-golf (SAW) en de compressional Alfvén-golf (CAW), en hun belangrijkste kenmerken in de context van het ideale MHD-model.

In *Hoofdstuk 2* wordt het concept van thermonucleaire fusie geïntroduceerd. De noodzaak om de fusiereactanten, die zich door de hoge fusietemperatuur in de plasmatoestand bevinden, op te sluiten, leidt tot de studie van de magnetische plasmaopsluiting. Na een samenvatting van de algemene eigenschappen van magnetisch opgesloten plasma's, bespreken we twee van de belangrijkste apparaten voor magnetische opsluiting die in dit proefschrift worden gebruikt, de tokamak-configuratie, die wereldwijd het meest wordt gebruikt, en in meer detail de omgekeerde-veld-knijp (RFP)-configuratie, die een andere veelbelovende configuratie is en waarvan de experimentele waarnemingen in dit proefschrift worden onderzocht.

In *Hoofdstuk 3* worden de belangrijkste kenmerken van de RFX-mod apparatuur geïntroduceerd. RFX-mod was het eerste experimentele apparaat dat verbeterde opsluiting van RFP toestanden, de zogenaamde QSH toestanden, toonde en onderzocht, waarvoor een kort overzicht wordt gegeven. Vervolgens worden experimentele waarnemingen van Alfvén golven in de RFX-mod ontladingen, gekarakteriseerd door periodieke magnetische reconnectie gebeurtenissen, gepresenteerd.

Deel II: MHD model en Alfvén golven, SpeCyl code en referentie simulaties

In *Hoofdstuk 4* wordt het magnetohydrodynamica-model (MHD) beschreven. Het MHD-model wordt vervolgens gebruikt om de plasma-evenwichtstoestand te beschrijven en de belangrijkste typen plasma-instabiliteiten: ideale instabiliteiten en resistieve instabiliteiten. Vervolgens wordt een korte theoretische beschrijving van magnetische reconnectie gegeven. Tenslotte geven we een rigoureuze analytische beschrijving van Alfvén golven in cartesische geometrie, SAW en CAE modes, gebruik makend van het MHD model in de ideale benadering.

In *Hoofdstuk 5* zullen wij de vergelijkingen van Alfvén-golven in cilindrische geometrie berekenen met behulp van het ideale MHD-model. In het bijzonder zullen wij golven in een rechte periodieke cilinder met zowel uniform als niet-uniform plasma (met niet-uniforme dichtheid en/of magnetisch veld) beschouwen. Het niet-uniforme geval, vergeleken met het uniforme (enkel gekarakteriseerd door de afschuif- en compressiemodi), zal gekarakteriseerd worden door een nieuwe Alfvén modus, de Globale Alfvén Eigenmode (GAE), en nieuwe fenomenen zoals fasemixing en Alfvén resonantie-absorptie. Alle theoretische formules die in dit hoofdstuk worden afgeleid, zullen vervolgens in de volgende hoofdstukken worden gebruikt om de theoretisch verwachte frequentiespectra te berekenen, die vervolgens zullen worden vergeleken met numerieke spectra uit niet-lineaire MHD-simulaties.

In *Hoofdstuk 6* wordt het numerieke instrument gepresenteerd dat gebruikt is voor het oplossen van de MHD model vergelijkingen. Dit numerieke gereedschap, SpeCyl genaamd, leverde de numerieke simulaties die gebruikt werden voor de analyse van Alfvén golven in verschillende magnetische en dichtheidsconfiguraties, voor zowel enkele golf gevallen als spiraalvormig-symmetrische 2D/ volledig 3D gevallen. In het bijzonder zullen wij een systematische studie presenteren van de dynamica van zaagtandrelaxaties in een Tokamak-configuratie, overgaand van een klassieke dynamica met hogere weerstand, gekenmerkt door de aanwezigheid van een interne knikinstabiliteit, naar een dynamica met kleinere weerstand die ook secundaire scheurinstabiliteiten bevat, plasmoïden genaamd. Deze simulaties zullen in Hoofdstuk 8 gebruikt worden om de excitatie van Alfvén golven door magnetische herconnectie te bestuderen. Ook zullen we de resultaten presenteren van een modelstudie, gebaseerd op RFP simulaties uitgevoerd met de SpeCyl code, die een systematische herhaling laat zien van QSH toestanden tussen de reconnectiegebeurtenissen in. Dezelfde simulaties uit deze studie zullen worden gebruikt in Hoofdstuk 9 om de Alfvén golven te karakteriseren in de meest realistische RFP omstandigheden die momenteel haalbaar zijn met de SpeCyl code.

Deel III: Alfvén golven excitatie in niet-lineaire MHD simulaties

In *Hoofdstuk 7* analyseren we simulaties van enkele golven (die een enkele Fourier mode bevatten) voor verschillende dichtheidsprofielen en magnetische configuraties: van een zuiver axiaal uniform magnetisch veld, tot een niet-uniform tokamak magnetisch veld en tenslotte een

RFP-achtig magnetisch veld. Voor elk simulatiegeval wordt het spectrum van Alfvén-golven berekend door de Fourier-analyse uit te voeren. Vervolgens worden de kenmerken van het berekende numerieke spectrum besproken, met inbegrip van de temporele evolutie, en wordt een fysische interpretatie gegeven op basis van het verwachte theoretische model.

In *Hoofdstuk 8* analyseren we de excitatie van Alvén golven in de Tokamak configuratie die gekenmerkt wordt door de quasi periodieke zaagtand instabiliteit. Met andere woorden, in dit en het volgende hoofdstuk worden Alfvén golven geëxciteerd door de zelfconsistente MHD dynamica in plaats van door initiële snelheidsverstoringen zoals in het vorige hoofdstuk. In het bijzonder analyseren we verschillende gevallen die in Hoofdstuk 6 zijn besproken, gaande van spiraalvormig-symmetrische 2D tot volledig 3D configuraties.

In *Hoofdstuk 9* analyseren we de excitatie van Alfvén golven in de volledig 3D RFP configuratie, gekenmerkt door QSH toestanden tussen de magnetische herverbindingsgebeurtenissen die in Hoofdstuk 6 zijn besproken. Tenslotte maken we een kwalitatieve vergelijking van de numerieke resultaten voor de RFP configuratie met de experimentele waarnemingen aan het RFX-mod apparaat.

Deel IV: Samenvatting en conclusies

In dit Deel worden de in het proefschrift beschreven resultaten samengevat en worden de eindconclusies getrokken, samen met de toekomstperspectieven die kunnen worden nagestreefd.

Bijlagen

Hier zijn bijlagen te vinden, die belangrijke details verduidelijken en nuttige informatie geven die niet in de hoofdtekst van het proefschrift is opgenomen. Aan het eind is ook een relevante bibliografie opgenomen.

Contents

Part I

Introduction

Chapter 1

Magnetized plasmas and Alfvén waves

At the beginning of the 20th century it was discovered that low-frequency electromagnetic waves are able to propagate in conducting fluids, such as plasmas, even though they cannot propagate in rigid conductors. Hannes Alfvén, in 1942, investigated the properties of plasmas, assuming the plasma medium to be a highly conducting, magnetized and incompressible fluid. He found that a distinctive wave mode arises in the fluid, propagating along the magnetic field direction. This wave is now called the shear or torsional Alfvén wave. The existence of this wave, in the conducting fluid mercury, was experimentally verified by Lundquist in 1949. The importance of the waves discovered by Alfvén for space and astrophysical plasmas was soon realized, and the compressible plasma case, which leads to the fast and slow magnetoacoustic waves in addition to the shear Alfvén wave, was treated by Herlofsen in 1950.

The shear Alfvén and magnetoacoustic waves, which are the basic low-frequency wave modes of magnetized plasmas, have been the subject of intense study in the last decades. The main reason for the great interest in these waves is that they play important roles in the heating and energy transport in laboratory, space and astrophysical plasmas. The "Alfvén wave heating" scheme has been investigated theoretically and experimentally as a supplementary heating mechanism of the solar and stellar coronae. Alfvén waves are believed to underlie the transport of magnetic energy in the solar and stellar winds, transfer angular momentum in interstellar molecular clouds during star formation, play roles in magnetic pulsations in the Earth's magnetosphere, and provide scattering mechanisms for the acceleration of cosmic rays in astrophysical shock waves. These and many other applications of these waves may be found in the laboratory, space physics and astrophysics literature.

In realistic physical problems in all plasma environments, shear Alfvén and magnetoacoustic waves propagate in nonuniform plasmas. As a result, the waves may be reflected, transmitted or absorbed. It is also believed that Alfvén's waves provide a means of transport for the internal heat of magnetically confined plasmas. This phenomenon of transport covers an important role in the propagation of heat from the center of the fusion plasmas to their edges resulting in the degradation of their confinement, and therefore in a loss of fusion alpha particles which are needed to provide the required energy input to keep the plasma in steady state (known as *ignition* condition, see Section 2.2). Energetic particles, such as alpha particles, can also resonantly destabilise the Alfvén waves, with two negative effects: energy transfer from alpha particles to the Alfvén waves and a loss of alpha particles due to the resulting Alfvénic fluctuations. The practical question of the heating to high temperatures of laboratory fusion plasmas that

are contained in a vessel, and are therefore necessarily nonuniform, involves such processes. Hence the study of those waves is extremely important for the research field of thermonuclear controlled fusion as it involves a toroidally confined plasma by a powerful magnetic field. This field of research is of strong interest as it is one of the most promising energy sources for the future, since it is intrinsically safe and the reactants are practically unlimited.

In this chapter we give a definition of magnetized plasmas and a very short and intuitive description of Alfvén waves and their main features.

1.1 The concept of plasma

At the temperature values required to trigger fusion reactions, the matter is in the plasma state. A plasma can be defined as an *almost neutral ionized gas that exhibits collective behaviour*.

Plasmas make up 99% of the observable universe, and can vary in a wide spectrum of density, temperature and size. In plasma physics, density is generally indicated in terms of particles per unit volume (m^{-3}) and temperature, T, in elettronvolt (eV). In particular, in this Thesis, we are interested in magnetized thermonuclear plasma, characterized by density of particles of the order of $n \approx 10^{19} \div 10^{20}$ m^{-3} and temperatures of the order of $T \approx 0.1 \div 10$ keV.

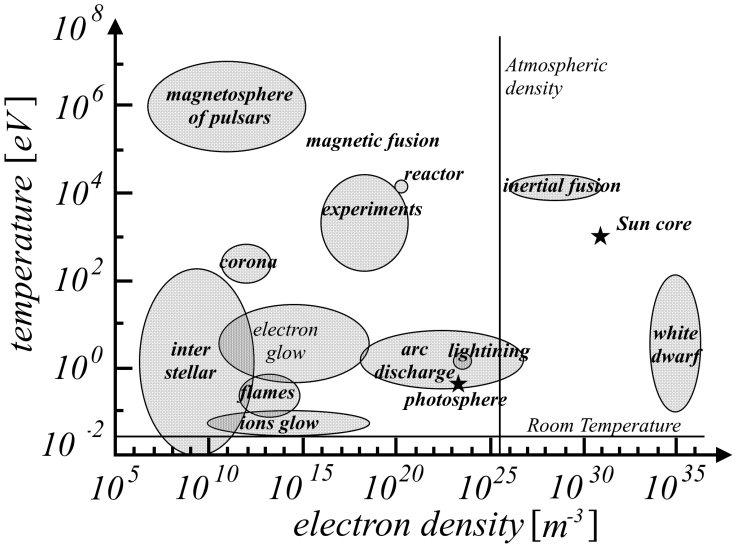

Figure 1.1: Position of various types of plasmas in the temperature-density graph. The conditions necessary for an ionized gas to behave like a plasma are fulfilled in a wide range of parameters.

Plasma dynamics is dominated by a collective behavior, which means that the dynamics of a single charged particle of the plasma depends on long-range interactions with other charged particles, interactions that tend to balance any spatial charge dishomogeneity, resulting in the screening of electrostatic potential. The approximate thickness of such screening effect is represented by the so-called *Debye length* λ_D, which measures the maximum distance where the charge inhomogeneities can take place and

is defined as

$$\lambda_D = \sqrt{\frac{\epsilon_0 K T_e}{n_e e^2}}, \tag{1.1}$$

where T_e is the electron temperature and n_e the electron (number) density. On spatial scales larger than Debye's length, plasma is globally neutral, that is, neutral enough so that one can take, over length-scales much larger than λ_D,

$$n_i \simeq n_e \simeq n, \tag{1.2}$$

where n_i is the ion (number) density and n is a common density called the *plasma density*. Anyway, the plasma is not so neutral that all interesting electrostatic effects vanish. Equation 1.2 is the *quasi-neutrality condition*. In addition, any concentrations of positive or negative charges are neutralized in a time scale given by the inverse of plasma frequency:

$$\omega_p = \sqrt{\frac{n_e e^2}{m_e \epsilon_0}}. \tag{1.3}$$

The typical size of Debye length λ_D for plasmas used to study the fusion phenomenon varies from micrometer to millimeter, while plasma frequency ω_p ranges from gigahertz to terahertz. The study of phenomena occurring on longer time scales than the inverse of plasma frequency and spatial scales larger than Debye length, which is the case for typical fusion plasmas, therefore allows to treat the plasma as a neutral fluid, as for example in the ideal magnetohydrodynamic model (MHD) that will be described in the next chapters.

1.2 Alfvén waves

Any wave in nature is driven by some restoring force which opposes displacements in the system. In the context of the MHD model (whose equations will be discussed in Chapter 4), two types of restoring forces are possible: one arising out of magnetic stresses; and the other arising out of pressure gradients. The ideal MHD theory can therefore support two basic types of magnetohydrodynamic waves, the Alfvén waves, called *Torsional Alfvén Wave* or *Shear Alfvén Wave* (SAW) and *Compressional Alfvén Wave* (CAW), also called *magnetoacoustic* or *magnetosonic* waves. The magnetoacoustic mode can be further split up into two distinct modes, the *fast* and *slow* magnetoacoustic waves. Below we give a short and intuitive description of Alfvén's shear and compressional waves features.

1.2.1 Shear Alfvén Wave

The MHD fluid undergoes a magnetic tension B^2/μ_0 along the field lines and an isotropic pressure $B^2/2\mu_0$. The magnetic field lines therefore act as strings under tension connected to masses (plasma particles are constrained to the field lines in ideal MHD, as we discuss in Appendix A). Whenever the magnetic field lines are distorted by a transverse perturbation, the magnetic tension tries to oppose the distortion. Just as a transverse wave can be started in a string by plucking it, similarly we have the transverse Alfvén wave moving along the field lines. The velocity of the transverse oscillations moving

along a stretched string can be shown to be

$$v_A = \left(\frac{tension}{density}\right)^{1/2} = \left(\frac{B^2}{\mu_0 \rho}\right)^{1/2}. \tag{1.4}$$

This is the *Alfvén's velocity*. Figure 1.2(a) illustrates the transverse nature of fluid motion and the frozen magnetic field lines. There aren't density or pressure fluctuations associated with this wave, the magnetic tension being the only restoring force for it. Because of this characteristics this wave is called "torsional" or "shear" Alfvén's wave.

1.2.2 Compressional Alfvén Wave

By extending the analogy, we expect to observe longitudinal oscillations due to pressure fluctuations. Those are called "magnetoacoustic", or "magnetosonic" or more simply "compressional" waves involving compressions and rarefactions of the plasma and magnetic field lines. Such a wave propagates with a speed v_M so to satisfy the relation

$$\nabla\left(p + \frac{B^2}{2\mu_0}\right) = v_M^2 \nabla\rho, \tag{1.5}$$

which implies

$$v_M^2 = \frac{\mathrm{d}}{\mathrm{d}\rho}\left(p + \frac{B^2}{2\mu_0}\right)_{\rho_0} = c_S^2 + \frac{\mathrm{d}}{\mathrm{d}\rho}\left(\frac{B^2}{2\mu_0}\right)_{\rho_0}, \tag{1.6}$$

where $c_S^2 = \gamma p_0/\rho_0$ is the sound speed and p_0, ρ_0 are respectively the pressure and density of the unperturbed plasma. Note that we have included the magnetic pressure in the restoring force. Because the particles are constrained to the field lines, we have $B/\rho = B_0/\rho_0$ and therefore

$$v_M^2 = c_S^2 + \frac{\mathrm{d}}{\mathrm{d}\rho}\left(\frac{B_0^2\rho^2}{2\mu_0\rho_0^2}\right)_{\rho_0} = c_S^2 + v_A^2, \tag{1.7}$$

where v_A is Alfvén's speed defined above and B_0 is a uniform magnetic field. The nature of a magnetoacoustic wave is illustrated in Figure 1.2(b). This wave is a mixture of acoustic and magnetic waves, where both types of restoring forces are present. Furthermore it can be split up into two distinct modes, the fast and slow magnetoacoustic waves. For the first one of these modes, the pressure and magnetic restoring forces are roughly in phase, making the mode propagate fast, so it was called the fast mode. The other mode, for which these restoring forces are roughly out of phase, is known as the slow mode. Any arbitrary disturbance in our system, described by ideal MHD theory, can be represented as a superposition of the Alfvén, fast and slow modes.

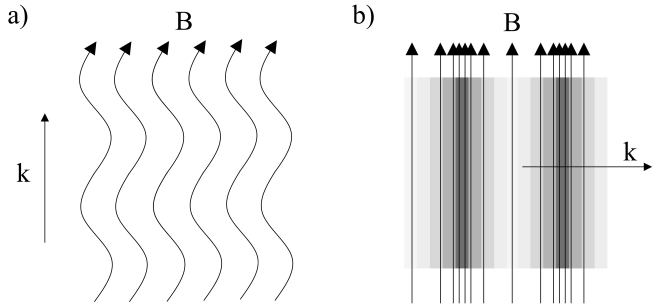

Figure 1.2: a) Shear Alfvén Wave. b) Compressional Alfvén Wave.

Chapter 2

Thermonuclear controlled fusion

Thermonuclear controlled fusion is one of the most promising energy source for the future, since it is intrinsically safe and the reactants are practically unlimited. In order to make a fusion reaction, the reactants (ionized hydrogen isotopes) must be confined in a high-density high-temperature regime for a sufficiently long time, in order to overcome the Coulomb barrier between them. In these conditions the burning gas, which is fully ionized due to the high fusion temperature, is found in the plasma state. The plasma can be confined by embedding it in a confining magnetic field. The most advanced device for magnetic plasma confinement is the tokamak, an axis-symmetric toroidal configuration. Other promising configurations are the stellarator and the reversed-field-pinch (RFP).

In this chapter we give a short introduction about thermonuclear controlled fusion, magnetic confinement and toroidal devices such as the tokamak and the RFP.

2.1 The fusion reaction

Nuclear fusion plays an important role in the Universe as it represents the process which powers the stars. The nuclear fusion reaction in the stars consists of a chain of reactions (called *pp-chain*) that from four protons creates an alpha particle, transforming the energy, resulting from mass defect between final products and initials reactants, in photons and kinetic energy of reaction products.

Other chain reactions are used in laboratory situations as the fusion of two protons to form deuterium, the first step of the *pp-chain*, is a process that involves weak interaction, hence characterized by a low cross section and therefore only possible in the stars, where the large amount of hydrogen allows to compensate for the low probability of reaction and to obtain anyway the deuterium needed to allow the faster successive steps.

In choosing alternative reactions to *pp-chain*, the use of light nuclei is mandatory, as well as their easier availability, for two additional reasons: the first is that the Coulombian repulsion, which we must overcome in order to bring the reactant nuclei within the range of the nuclear force, is proportional to the charge product of the nuclei involved, while the latter is due to the fact that when the particles involved have a smaller mass than that of ^{56}Fe (this isotope has the highest binding energy per nucleon, as shown in Figure 2.1), the sum of the masses of the starting nuclei is higher than the final nuclei, and the mass defect, according to Einstein's equation $E = mc^2$, released as kinetic energy in the reaction products.

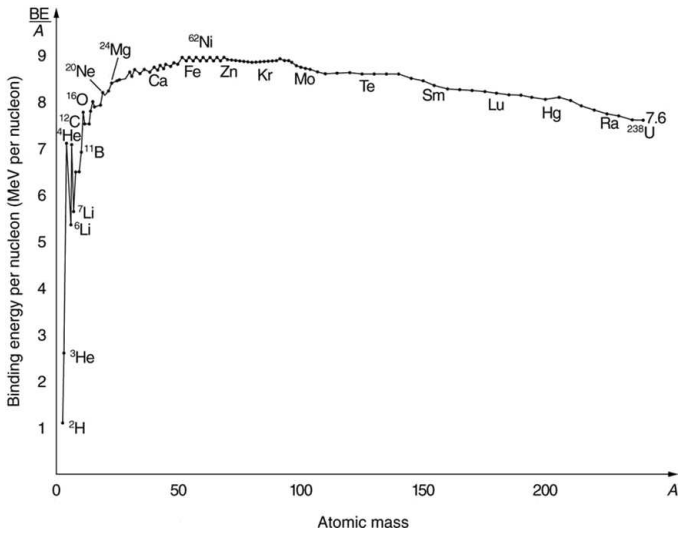

Figure 2.1: Average binding energy per nucleon as a function of atomic mass A.

In choosing the fusion reaction that best suits a laboratory plasma , it is also necessary to consider the trend of cross section with the energy of the reagents and the reaction rates, which impose strict limits on the choice of the energy range in which the reaction will occur.

Combining all these aspects the best candidate for the reaction is that between deuterium and tritium:

$$ {}^{2}_{1}\mathrm{D} + {}^{3}_{1}\mathrm{T} \rightarrow {}^{4}_{2}\mathrm{He}\ (3.5\ \mathrm{Mev}) + {}^{1}_{0}\mathrm{n}\ (14.1\ \mathrm{Mev}) \tag{2.1} $$

characterized by a cross section that at temperatures between 20 and 100 keV, the range in which a hypothetical thermonuclear fusion reactor must operate, is two orders of magnitude greater than that of other possible reactions, as can be seen in Figure 2.2.

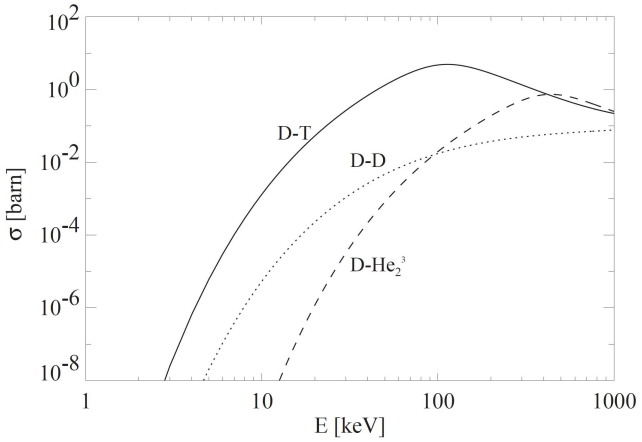

Figure 2.2: Cross section for typical fusion reactions: deuterium-tritium (D-T), deuterium-deuterium (D-D) and deuterium-helium (D-He_2^3). 1 barn = 10^{-24} cm^2.

Nevertheless, the optimal temperature of fusing nuclei is of ~ 10 keV, because the required reactions occur in the high energy tail of the Maxwellian distribution of the heated particles.

Considering the availability of reagents, it should be noted that since tritium is a radioactive element with an average life of about 12 years, it is not present in nature. It can however be obtained from the following lithium-engaging reaction:

$$ {}^{6}_{3}\mathrm{Li} + {}^{1}_{0}\mathrm{n} \rightarrow {}^{4}_{2}\mathrm{He}\ (2.1\ \mathrm{Mev}) + {}^{3}_{1}\mathrm{T}\ (2.7\ \mathrm{Mev}) \tag{2.2} $$

The natural resources needed to obtain energy from the nuclei are potentially inexhaustible since the deuterium can be obtained from ordinary water (about 33g from 1 ton), while current estimates of lithium reserves indicate that they are sufficient to meet the world's energy demand for a time of millions of years.

2.2 Thermonuclear ignition criteria

The aim of nuclear fusion research is to get more energy from the fusion processes than the energy required to trigger one and confine the plasma, having electron and ion density n and temperature T. Confinement of the plasma can never be absolute, as there are various causes of energy loss. The two main ones are given by bremsstrahlung, that is, the emission of radiation by accelerated charged particles and transport losses leading to plasma and energy confinement loss in a characteristic time τ_E.
It is therefore necessary to reinvest, to offset these losses, some of the energy provided by the fusion reactions. In a device that magnetically confines plasma, the alpha particles produced by the reaction (2.1), being charged, may be confined and thus represent the means to transfer part of the fusion energy to the plasma, the remaining part being stored in the neutrons, which cannot be confined and coming out of the confinement chamber are going to feed some system that converts heat into electricity. We can summarize this with the relation:

$$ \frac{\partial W}{\partial t} = P_{heat} + P_{\alpha} - P_{loss}, \tag{2.3} $$

where W is the plasma energy density, P_{heat} is the external heating power, P_{loss} the power losses and P_{α} the power given by the alpha particles.

The ignition criteria formalizes the energy balance in the situation where the reactor is self-sustaining thanks to the sole power supplied by alpha particles, providing a condition that links density n, confinement time τ_E of the energy of plasma and plasma temperature T [Wesson, 2004]. The trend of the $n\tau_E$ product, required for ignition, as a function of temperature T is shown in Figure 2.3. The curve has a minimum around $T = 25 - 30$keV, which is therefore the temperature at which it is easiest to obtain a positive energy balance. At this temperature the ignition condition is given by:

$$ n\tau_E > 1.5 \cdot 10^{20}\,\mathrm{m}^{-3}\mathrm{s}. \tag{2.4} $$

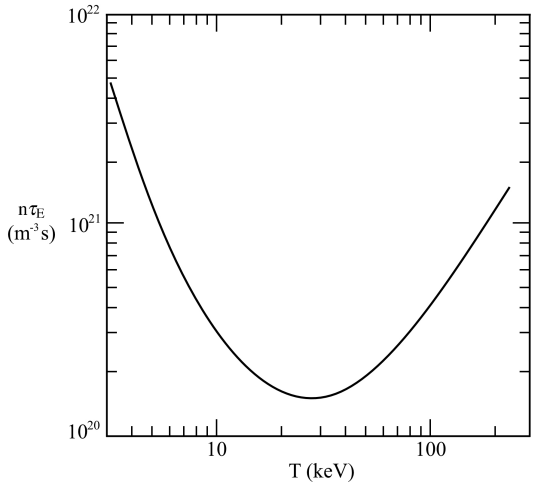

Figure 2.3: The minimum value of $n\tau_E$ required to obtain ignition, as a function of temperature.

A different more compact expression to define fusion conditions is the use of the so-called *fusion triple product*:

$$nT\tau_E > 3 \cdot 10^{21}\,\mathrm{m}^{-3}\mathrm{keVs}. \tag{2.5}$$

The previous condition does not allow complete freedom in the choice of parameter values. In particular, the presence of a material wall that cannot withstand too high power densities places a limit on the density of plasma, with $n \sim 10^{20}\,\mathrm{m}^{-3}$. The typical plasma temperature in a experiment, as seen in Figure 2.3 , need to have a value $T \sim 20\,\mathrm{keV}$, leading to confinement time of energy, the most critical parameter, to be $\tau \sim 1\,\mathrm{s}$.

We have seen that, in order to obtain thermonuclear fusion, the plasma must be kept in a regime of high temperature and high density for a sufficiently long time. This process is called *plasma confinement*. Two schemes of plasma confinement are presently studied:

Inertial Confinement. In this case spherical targets of deuterium and tritium are uniformly irradiated by sharp electromagnetic impulses in order to compress them and obtain conditions of temperature and density leading to a complete burn before thermal equilibrium.

Magnetic Confinement. Plasma is confined through magnetic fields, and heated with ohmic dissipation, radio frequency waves and neutral beams. In the following Sections we give a general introduction of this scheme.

2.3 Magnetic confinement: the toroidal configuration

One of the main confinement techniques is the magnetic one, which originates from the knowledge of the motion characteristics of a charged particle in a magnetic field.
In the presence of a uniform and static magnetic field B, the motion of a particle with mass m and charge q can be decomposed in a uniform straight motion in the direction parallel to the field and in a uniform

circular motion in a perpendicular direction, the latter characterized by a frequency said *cyclotronic frequency* and a radius said *Larmor's radius*, defined as:

$$\omega_c \equiv \frac{q|B|}{m} \qquad\qquad r_L \equiv \frac{v_\perp}{\omega_c} = \frac{mv_\perp}{q|B|}, \tag{2.6}$$

where $v_\perp$ is the velocity of the particle in the direction perpendicular to the magnetic field. For a thermonuclear fusion plasma the value of r_L range from fractions of millimeter for ions to microns for electrons, small compared to the size of the confinement chamber.
The fact that in the direction of the field the motion is straight and uniform, has led to the exclusion of configurations in which the magnetic field lines are not closed and to consider a toroidal type system.
The presence of drift motions due to the curvature and possible disomogeneities of the magnetic field lines in a toroidal configuration makes it more problematic to prevent the plasma from touching the wall of the vacuum chamber; the solution is to create a magnetic field characterized by a helical structure that appropriately compensates for such drift motions.
A torus can be more easily described considering the following frame of reference:

minor radius r which spans the region from the center of the plasma ($r = 0$) to the boundary ($r = a$);

poloidal angle θ which measures the angle on the shorter loop;

toroidal angle ϕ which measures the angle with respect to the toroidal axis, i.e. the longer loop.

The ratio between the major radius R_0 and the minor one a is called aspect ratio. This frame of reference is sketched in Figure 2.4, along with another possible choice, namely the (R, ϕ, Z) frame of reference, involving the radial coordinate R which measures the distance with respect to the toroidal axis and the coordinate Z along the axis itself.

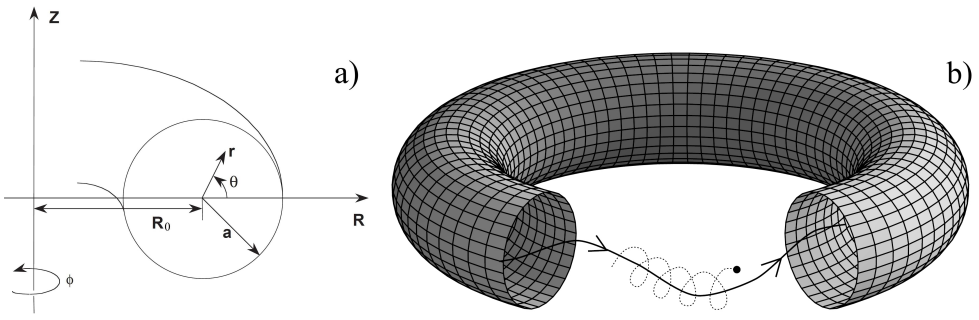

Figure 2.4: a) The toroidal system of reference (r, θ, ϕ) and the cylindrical coordinates (R, ϕ, Z). b) Motion of gyration of a charged particle around a force line of the magnetic field.

In toroidal geometry, a field can be expressed in normal modes as a Fourier expansion over the poloidal and toroidal angles. For instance, the magnetic field B can be written as

$$\mathrm{B}(r,\theta,\phi) = \sum_{m,n} \mathrm{B}_{mn}(r) e^{i(m\theta + n\phi)}, \tag{2.7}$$

where (m,n) is a pair of integer numbers and $B_{mn}(r)$ is the Fourier component of the normal mode (m,n), whose (geometric) helicity h is hence defined as

$$h \equiv -\frac{n}{m}. \tag{2.8}$$

In particular, the $(0,0)$ Fourier component corresponds to the axis-symmetric part of the field $\mathbf{B}_0$, which does not depend on θ and ϕ:

$$\mathbf{B}_0 \equiv \mathbf{B}^{(0,0)}(r), \tag{2.9}$$

whereas the perturbation to $\mathbf{B}_0$ is referred as $\mathbf{B}_1$.

2.4 The main toroidal devices for magnetic confinement

The main toroidal devices for magnetic confinement of plasma are distinguished by their geometry and by different role of the magnetic field components. There are three different configurations: the stellarator, the tokamak and the reversed field pinch (RFP).

The stellarator belongs to the category of non-axisymmetric toroidal devices. The magnetic field is entirely produced by a complex helical arrangement of the coils around the plasma, designed to obtain a helical magnetic field in equilibrium. This implies that a stellarator configuration does not have a plasma current that would create additional magnetic fields than that generated by the coils.

Tokamak and RFP belong to the category of axisymmetric toroidal devices. The formation of plasma from the gas contained in the toroidal confinement chamber of a device such as tokamak or RFP occurs by inducing a toroidal electric field through the use of a transformer whose primary circuit consists of an iron or an air core and whose secondary is the plasma itself. The electric field thus produced ionizes the atoms of the gas thus becoming capable of supporting a plasma current I_p in the toroidal direction which, by the Ampère's law, produces a poloidal magnetic field. The toroidal component of the magnetic field is generated by an external coil system, in which the current flows in a poloidal direction, forming a solenoid-like device.
The sum of the two magnetic field components thus obtained leads to the formation of a magnetic field with lines helically wrapped on coaxial toroidal surfaces. Figure 2.5 shows a representation of all the external structures needed to create and maintain the plasma.

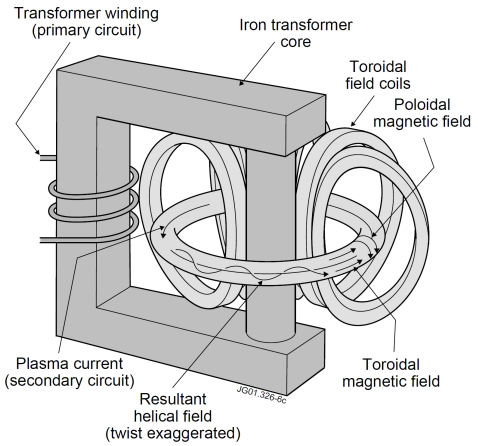

Figure 2.5: Main components of the plasma-forming circuit (transformer) and its confinement (external coils).

2.4.1 Tokamak configuration

In the tokamak the main component of the magnetic field is the toroidal, B_ϕ, generated by a series of external coils. The magnetic field component in the poloidal direction B_θ, created by the plasma current circulating in the torus, is typically one order of magnitude smaller.
An important parameter that regulates plasma dynamics in a tokamak device that magnetically confines plasma is the *safety factor*:

$$q(r) \equiv \frac{r}{R_0} \frac{B_\phi(r)}{B_\theta(r)}. \tag{2.10}$$

It can be interpreted as the number of toroidal turns for a single poloidal turn of field line, and in a tokamak, for stability reason, it is always greater than one. This results in a greater intensity of the field toroidal component than the poloidal component, as seen in Figure 2.6, which also schematizes the components of the magnetic field in the RFP configuration, which we discuss in the following section.

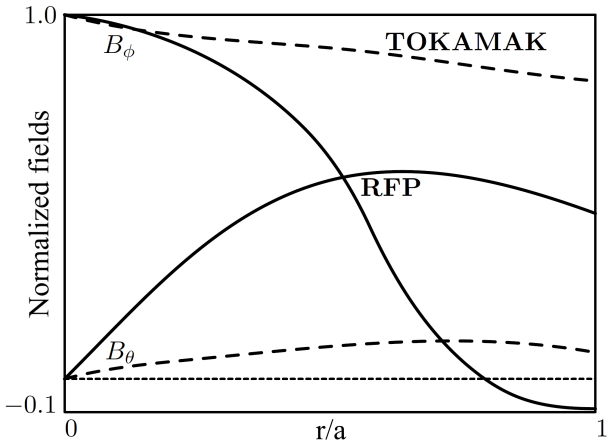

Figure 2.6: Radial profiles of the poloidal and toroidal components of the magnetic field in typical tokamak and RFP configurations. a represents the minor radius of the torus.

The safety factor in a tokamak can be also expressed as function of the current density, in particular, in axis its given by:

$$q(r=0) = q_0 = \frac{2B_\phi}{\mu_0 j_{\phi 0} R_0}. \tag{2.11}$$

2.4.2 RFP configuration

The RFP configuration shares with the tokamak the main features, in particular the axial symmetrical toroidal structure and the fact that the circulating current in the plasma produces a component of the magnetic field further to that generated by the outer coils, which is crucial for plasma confinement.
The features that distinguish the RFP from tokamak are primarily the intensity of the magnetic field generated by the coils external to the plasma, which in a tokamak experiment typically results in an order of magnitude greater than that in a RFP experiment, which also translates into a different energy cost for field creation (the energy associated with a magnetic field is proportional to the square of its intensity).
The two configurations are distinguished by the different ratio between the intensity of the toroidal and poloidal components of the magnetic field: these have on average the same order of magnitude in the RFP, as can be seen in Figure 2.7, unlike the tokamak in which the toroidal component dominates.
The peculiar feature of the RFP is then the reversal of the toroidal magnetic field that in the edge area of the confining chamber assumes a negative value, lesser in absolute value than that present in the axis of the torus. This is a technological advantage with respect to the tokamak, because the outer coils have to produce only the small and reversed magnetic field at the edge, while the field in the central region is mainly generated by currents circulating in the plasma itself. The poloidal component, which compresses and confines the plasma (squeezing "pinch" effect), has a higher value in RFP than tokamak, and is also created by the plasma current I_p circulating in the plasma: the fact that I_p is very high makes it possible to heat the plasma up to high temperatures with only ohmic heating, without the use of additional methods (radiofrequency heating and injection of neutral particles beam) that are required in a tokamak reactor.
From a technological point of view the fact of having to produce with external conductors a much smaller magnetic field intensity in the RFP promises to overcome problems such as excessive strain on outer coils and the need of superconductor technology and related expensive cooling systems (a tokamak thermonuclear reactor will require magnetic fields greater than 10 T).

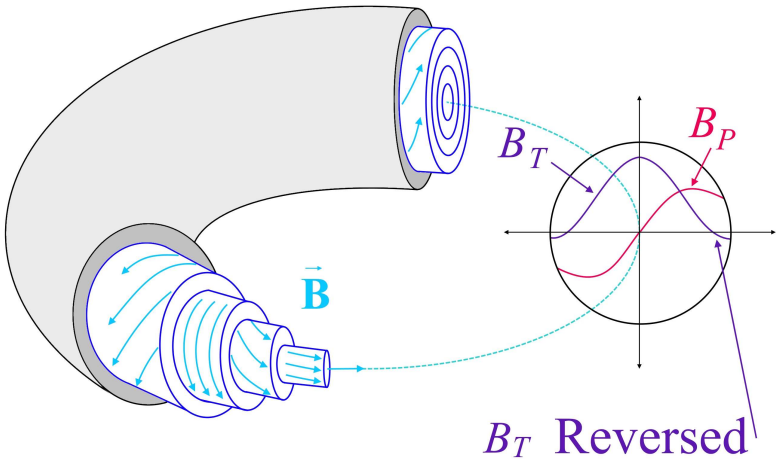

Figure 2.7: Radial profile of the poloidal and toroidal components of the magnetic field in RFP.

Another effect of reversal the toroidal field at the edge of the RFP is on the profile of the safety-factor q, defined in equation (2.10), which is quite different between the two configurations, as can be seen in Figure 2.8.

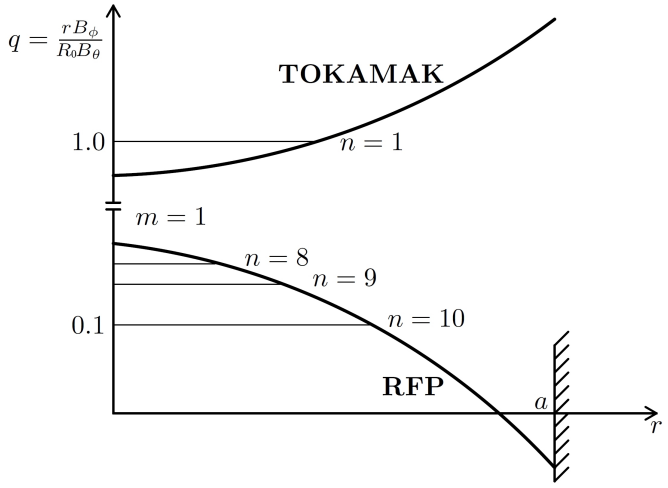

Figure 2.8: Typical radial profiles of the safety factor q for tokamak and the Reversed Field Pinch.

The reversal of the magnetic field is observed beyond a certain value of the *pinch parameter* defined as:

$$\Theta = \frac{B_\theta(a)}{< B_\phi >} = \frac{\mu_0 a I_P}{2\Phi}, \tag{2.12}$$

wherein a, I_P, Φ represent the radius of the plasma column, the plasma current and the toroidal flux of the magnetic field, B_θ and B_ϕ the poloidal and toroidal components of the magnetic field, $< \cdot >$ an average on a section at a fixed toroidal position. The parameter Θ represents substantially the relationship between the plasma current and toroidal flux of the magnetic field, and its typical value in the RFP configuration

is greater than one, whereas in the tokamak case, in which the toroidal field is much more intense than the poloidal one, Θ assumes values lower then one.

Another useful parameter to describe how deep the reversal of the field at the edge is in the RFP configuration is given by:

$$F = \frac{B_\phi(a)}{< B_\phi >}, \tag{2.13}$$

said *reversal parameter*, which represents the normalized toroidal field at the edge.

Chapter 3

The RFX-mod device and experimental highlights

RFX-mod (Reversed Field eXperiment-modified) is the largest experiment in the world to investigate the magnetic confinement of hot plasmas in the RFP configuration, and is located in Padua, Italy. For the RFP part of this Thesis, we took RFX-mod and its experimental results as a reference to compare with the results of our MHD numerical simulations in RFP configuration.
RFX-mod was the first experimental device to show and investigate improved confinement RFP states, previously theoretically predicted using the MHD model. Such improved confinement RFP states are characterized by a dominant mode in the MHD spectrum, which impresses its helical symmetry to the plasma column, and are hence called quasi-single helicity (QSH) states. The RFX-mod experiment is also equipped with a system of saddle coils for the feedback control of MHD instabilities, and with a full set of diagnostics. In particular in-vessel magnetic probes make possible to measure and characterize Alfvénic oscillations, whose theoretical interpretation is provided in this Thesis.
Experimentally high-frequency magnetic activity has been detected at the edge region of the RFX-mod device. In particular a presence of five coherent peaks, in the form of Alfvén Waves (AW) in the power spectrum of the magnetic fluctuation, were measured at the edge of the plasma. While the first three peaks at lower frequency ($\leq$ 1MHz) are present only during the SHAx (Single Helicity Axis) state, the two highest frequency peaks (around 1 MHz) are found during almost the full discharge duration. The Alfvénic nature of all the peaks were deduced by a linear relation between their frequency and the Alfvén velocity.

In this Chapter we will introduce the main features of the RFX-mod device, and we will briefly discuss the discovery of improved confinement QSH states and experimental observation of Alfvén Waves.

3.1 The RFX-mod device

The main geometrical and physical features of the RFX-mod experiments are shown in table 3.1.

R_0	2.00 m
a	0.459 m
I_P	$\leq$ 2.0 MA
B	$\leq$ 0.7 T
p_{vacuum}	$\sim 10^{-10}$ Pa
p_{plasma}	10^3 Pa
n_{plasma}	$5 \cdot 10^{19}$ m^{-3}
$T_{e,max}$	1.5 keV
t_{max}	0.5 s

Table 3.1: Main features of the RFX-mod experiment. R_0 and a represent the major radius and the minor radius of the torus, I_P represents the maximum achievable plasma current, B the maximum magnetic field strength that can be created by the coils and p_{vacuum} the pressure inside the confinement chamber before the gas is inserted, usually hydrogen or helium, whose ionization will form the plasma. p_{plasma} represents the typical pressure of the plasma, n_{plasma} the density of ions and electrons, $T_{e,max}$ the maximum electronic temperature obtained and t_{max} the maximum duration of a discharge.

The main components of the system for confinement and the creation of the magnetic field are described below (for further details see [Sonato et al., 2003]):

- The confinement chamber in toroidal geometry, with a major radius R_0 and a minor radius a, is characterized by an aspect ratio of 4.
- The inner surface of the confinement chamber is composed of 18 mm thick graphite plates, a material chosen because of the low Z value which reduces the effective value of the atomic number of ions present as impurities in the plasma.
- Outside the confinement chamber there is a copper toroidal structure (3 mm thick stabilizing shell) that contains it, its role is important in the control of the characteristics of balance and stability of the plasma contained in the vacuum chamber.
- The 48 poloidal coils that generate a toroidal magnetic field of maximum intensity equal to about 0.7 T.
- The magnetizing winding provides for the oscillation of the poloidal flux which causes the plasma current to grow up to 2 MA. It is composed of 200 windings that form 40 coils, each carrying a maximum current of 50 kA.
- The field shaping windings are formed by 16 coils that provide a vertical magnetic field that guarantees the correct positioning of the plasma in the vacuum chamber.
- A set of 192 coils for a feedback control of the magnetic field, they allow a good control of the external surface of the plasma avoiding excessive interactions between plasma and wall.

The main components of the machine are shown in Figure 3.1:

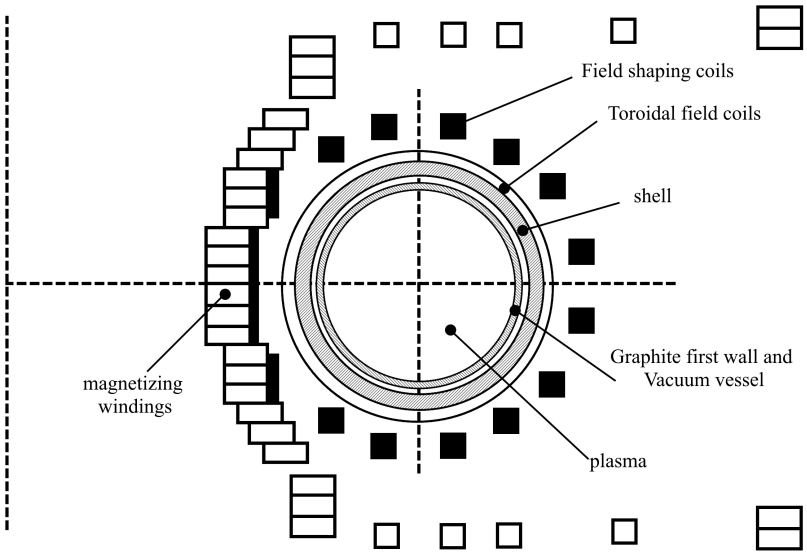

Figure 3.1: Schematic poloidal section of the RFX-mod machine.

3.2 Quasi Single Helicity RFP states

For several decades the RFP magnetized plasma has been observed in the so-called Multiple Helicity (MH) state, characterized by high levels of magnetic fluctuations that led to reduced confinement levels. MH are states in which the non axis-symmetric perturbations are spectrally characterized by a wide range of the wave numbers m, n, in particular $m = 0$ and $m = 1$. The interaction of a broad spectrum of perturbed modes, that can be modelled using the magnetohydrodynamic model, leads to a turbulent behavior of the plasma. In particular, the magnetic field lines become chaotic and are free to move from the central region of the plasma to the edge one, which establishes a very fast transport mechanism of particles and energy, a mechanism that clearly degrades the confinement properties of the RFP plasma.

A strategy for the reduction of chaos in the RFP configuration was based on the theoretical prediction of the possible existence of the RFP in the so-called single helicity (SH) configuration, in which only one helical mode and its harmonics are present [Cappello et al., 1992; Escande et al., 2000b].
Starting from the 2000s, first on the RFX experiment (previous to RFX-mod) and then on other RFP experiments around the world, quasi-helical states with a spectrum called QSH (Quasi-Single-Helicity) have been observed, which approach the ideal SH states theoretically predicted, and which possess improved confinement thanks to the reduced level of magnetic chaos compared to the MH states [Martin et al., 2003]. The experimental results of the last few years on RFX-mod and on other operational RFPs showed, in particular through high current operations, a tendency of the RFP plasma to move to the QSH regime. From the most recent experiments on RFX-mod it is observed that as the plasma current I_P increases, the system tends to spend a longer and longer time in the QSH state, moreover, always with increasing current, the QSH tends towards a state of SH equilibrium, in the sense that the amplitude of secondary modes decreases [Piovesan et al., 2009a].

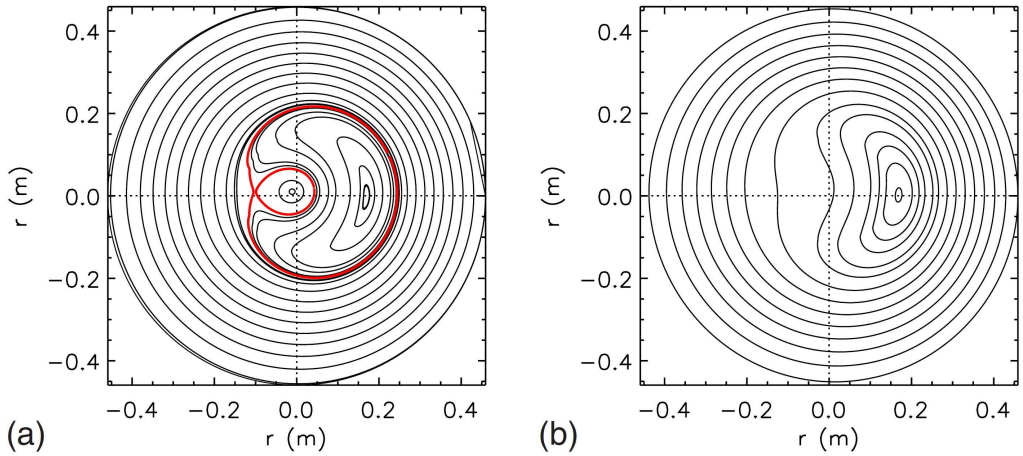

Figure 3.2: Magnetic topology reconstructed using only the axisymmetric fields and the eigenfunction of the dominant mode: (a) QSH with a magnetic island, (b) SHAx state. (from [Lorenzini et al., 2009a]).

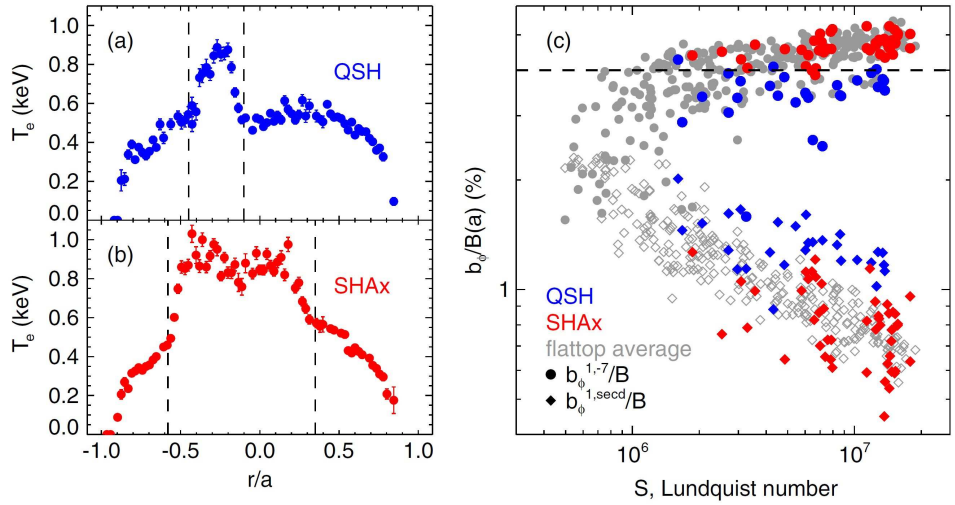

Figure 3.3: Electron temperature profiles measured by Thomson scattering during (a) a QSH state and (b) a SHAx state. (c) Relative amplitudes of the $n = -7$ mode (circles) and of the secondary modes (diamonds): flattop average (grey) and instantaneous values, when Thomson scattering data are available, during QSH (blue) and SHAx (red) (from [Piovesan et al., 2009a]).

It is also observed that if the dominant perturbed mode reaches a width equal to about 4% of the poloidal field at the edge, a topological change takes place in the configuration of the magnetic field, as shown in Figure 3.2, that brings the plasma to achieve an almost stationary equilibrium with helical symmetry with a single magnetic axis (Single-Helical-Axis, SHAx, to distinguish it from the previous case with two different magnetic axis, double-helical-axis, DHAx) [Piovesan et al., 2009a; Lorenzini

et al., 2009a; Lorenzini et al., 2009b]. Improvement of RFP confinement properties ("chaos healing") following the expulsion of the magnetic separatrix of the dominant mode, DHAx-SHAx transition, was theoretically predicted in [Escande et al., 2000a]. This new state exhibits the presence of strong transport barriers, characterized by the presence of high temperature gradients of the electrons associated with the presence of regions of good confinement, as shown in Figure 3.3.

3.3 Experimental observation of Alfvén Waves in RFX-mod plasmas

High-frequency magnetic activity has been detected at the edge region of the RFX-mod reversed-field pinch (RFP) device [Spagnolo et al., 2011]. In particular, in this section, we will focus on the observation of coherent peaks in the power spectrum of the magnetic fluctuation measured at the plasma edge. These peaks are interpreted as Alfvén waves because their frequencies scale linearly with the Alfvén velocity of the plasma.

In Figure 3.4, taken from Ref. [Spagnolo et al., 2011], the color-coded spectrogram of a signal coming from a probe measuring the time derivative of the poloidal magnetic field ($\dot{b}_\theta$) fluctuation at $r/a = 1$ (where a is the minor radius of the torus) is shown, along with the time trace of the plasma current. Superimposed to the spectrogram, in red, is the time behavior of amplitude of the $(m,n) = (1,-7)$ mode (actually what is shown is the toroidal magnetic field component at the edge) to highlight the spontaneous transitions to the SHAx (Single Helical Axis) state. The vertical bright lines occurring during the crashes of the dominant mode are a sign of a global (i.e. at all frequencies) enhancement of the fluctuation level.

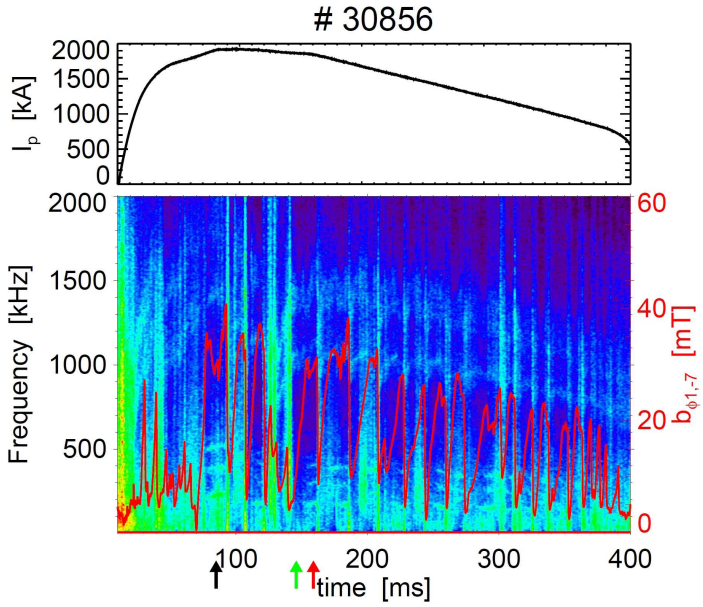

Figure 3.4: Top: plasma current I_p time trace; bottom: spectrogram of a $\dot{b}_\theta$ signal and (red line) amplitude of the dominant (m,n)=(1,-7) mode (y-axis on the right-hand side). The three arrows refer to the three time instants for the analysis in Figure 3.6 (from [Spagnolo et al., 2011]).

During the phases associated to large values of the dominant mode amplitude, a number of coherent

modes (where coherent means in this case localized in frequency) are instead (hardly) visible, at values in the range $130 \div 500$ kHz. Indeed five distinct peaks, as more evident in Figure 3.5, where a frequency power spectrum evaluated during a single helical plasma is shown, are recognizable.

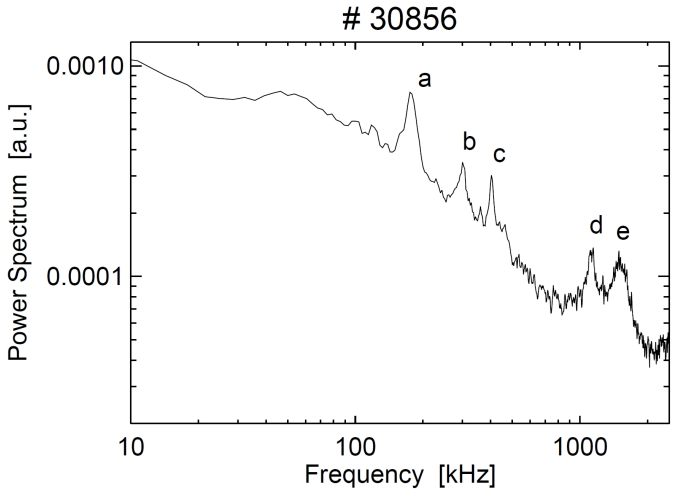

Figure 3.5: Power spectrum of a $\dot{b}_\theta$ signal evaluated during a SHAx state.

These peaks have been named a, b and c, d and e following the increase of their frequency (the amplitude associated to such coherent fluctuation is of the order of few tens of μT). While the first three peaks (a, b, c) are present only during the SHAx state, the two highest frequency peaks, d and e, (around 1 MHz) are found to exhibit different characteristics: they do not seem to be associated to any particular behavior of the dominant mode, being present during almost the full discharge duration.

To clarify this point, in Figure 3.6 three power spectra, evaluated in different time instants are plotted together. The time instants chosen for this analysis are those indicated by the three arrows in Figure 3.4. Two of the spectra shown (black and red ones) are associated to single helical axis states (it is worth to note the frequency shift associated to different plasma conditions), while the third one (green) is evaluated in an axis-symmetric RFP plasma. The three low frequency peaks are not present in the green spectrum, while the d and e ones seem not to be affected by the magnetic topology of the discharge.

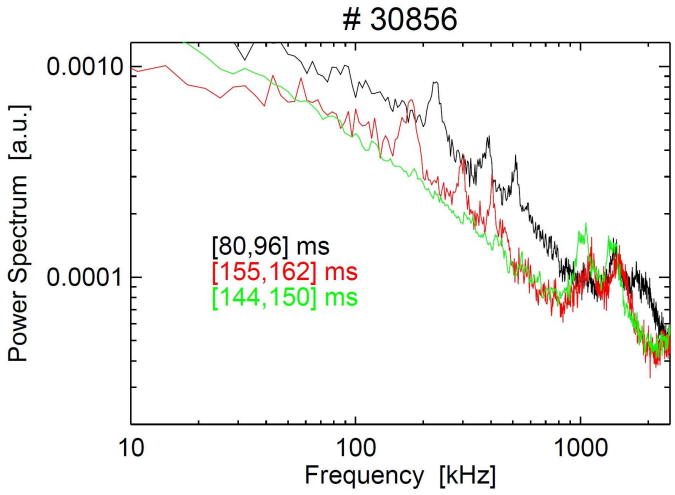

Figure 3.6: Power spectrum of a $\dot{b}_\theta$ signal evaluated during the three time instants indicated by the arrows of Figure 3.4: black and red lines refer to SHAx states, the green one to an axis-symmetric state.

The Alfvénic nature of all the peaks observed has been deduced by the linear relation between their frequency and the Alfvén velocity (evaluated by considering the poloidal magnetic field at the edge, and the electron density deduced by a central chord of the interferometer, and assuming $Z_{eff} = 1.5$ as a reasonable value for H discharges) in a number of discharges, as shown in Figure 3.7. In particular, in the shots analyzed the plasma current I_p was varied in the range 300 kA - 2 MA. The usual working gas is Hydrogen, but also Helium discharges have been considered. It is worth to note that, while the highest frequency modes (d and e) have been observed at almost all plasma current values, modes a, b and c, being associated to SHAx states, are present in the spectra only at the highest plasma currents, $I_p > 1.5$ MA.

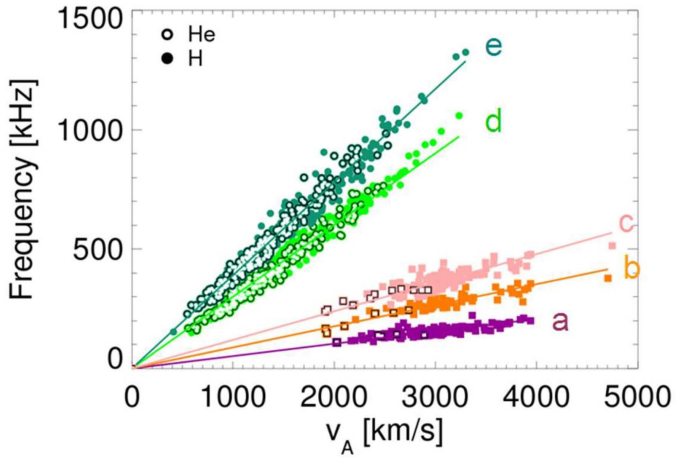

Figure 3.7: Relation between modes frequency and Alfvén velocity for a large database of H and He plasmas.

In the next chapters we will try to explain the above experimental observations from a theoretical point of view, through the analysis of frequency spectra from nonlinear MHD simulations with the SpeCyl code and the comparison with related analytical results deduced from ideal MHD model.

We want to stress out that these observations were made in RFX-mod Ohmic discharges without additional heating, which is not much studied and understood as currently the research on AEs destabilization is mostly centered around their excitation by fast particles with velocities of the order of Alfvén speed, produced by neutral-beam injection (NBI), ion cyclotron resonance heating (ICRH), or even fusion born alpha particles, through the inverse Landau damping mechanism. Moreover Alfvénic eigenmodes have also been observed in other RFP devices, including Extrap-T2R [Regnoli et al., 2005] and MST [Koliner et al., 2012; Lin et al., 2014; Bonofiglo et al., 2019]. AEs observed in MST are mainly found to be induced by NBI. Therefore, several recent papers addressed the MST observations by modeling and analytical study of energetic particle driven AEs in RFPs [Koliner et al., 2012; Cai et al., 2014; Li et al., 2014]. On the other hand, AEs in Extrap-T2R have been observed in Ohmic discharges, similarly to the observations in RFX-mod.

Part II

MHD model and Alfvén waves, SpeCyl code and reference simulations

Chapter 4

The magnetohydrodynamic model and Alfvén Waves

There are many physical models for the description of astrophysical and laboratory plasmas that differ in the level of complexity and the resulting physical phenomena they can describe.

There are two fundamental approaches: the microscopic-kinetic and the macroscopic-fluid one [Chen, 1984; Goldston et al., 1995; White, 2013]. The first , i.e., the microscopic approach, deals with the description of a plasma as a system of many interacting bodies through long-range electromagnetic forces and works through the knowledge of the system configuration in phase space; this is done by determining the equations that describe the time evolution of the distribution function $f(r,v,t)$, which represents the density of particles in the phase space. The second approach leads to describe the characteristics of plasma by macroscopic quantities that are a function of the three-dimensional position in space and of time, and through the relationships that determine the temporal evolution and the mutual relations. Modeling in terms of macroscopic quantities such as density, temperature, velocity and pressure is called the fluid approach.

The relationship between the two approaches is hierarchical because one can obtain the equations of the fluid model by starting from those that describe the distribution function, assuming that the frequency of the collisions between the components of the plasma is such as to bring the plasma close to thermodynamic equilibrium. In the process of derivation of a fluid model from a kinetic one some information is lost, which limits the field of application of the fluid model with respect to the kinetic one even if, within the limits of the approximations made, the macroscopic model describes a wide variety of phenomena in a much simpler way than its microscopic counterpart.

Macroscopic fluid models, in turn, can provide basically two levels of description: the description of a plasma as composed by two or more fluids of charged particles coupled together by the collisions and the Maxwell equations (for example, an electron fluid and an ion fluid), or the single-fluid MHD description, which is obtained through further approximations and will be analyzed and used in the following.

As we already stated previously, the MHD theory can support two basic types of magnetohydrodynamic waves, the Shear Alfvén Wave (SAW), also called torsional Alfvén wave, and the Compressional Alfvén Wave (CAW), also called magnetoacoustic or magnetosonic wave. The magnetoacoustic mode

can be further divided into two distinct modes, the fast and slow magnetoacoustic waves. In this Chapter we will obtain the exact analytical solution for those waves, considering small amplitude linear waves in a spatially uniform plasma and in cartesian coordinates. This will provide a reference for the discussion in the following chapters of the waves in the nonuniform plasmas and cylindrical geometry. The waves will be assumed to have frequencies below the ion cyclotron frequency.

In this chapter we will introduce the magnetohydrodynamic model and its application limits. Then we will describe the waves in the MHD model: the Alfvén waves and their characteristics. The material discussed in this chapter is a synthesis of several textbooks and scientific articles [Cramer, 2001; Choudhuri, 1998; Wesson, 2004; Chapman, 2011].

4.1 The single-fluid MHD model

The *single-fluid magnetohydrodynamics model*, also simply called MHD model, provides a description of a plasma as a conductive fluid in an electromagnetic field, with its own mass density ρ, velocity $\mathbf{v}$, and pressure p through a system of differential equations.
Appropriate algebraic manipulations of the two fluid model equations described in [Goldston et al., 1995] make possible to derive a system of single fluid differential equations in which unknown quantities such as ρ, $\mathbf{v}$ and p are defined as appropriate linear combinations of relative quantities for ions and electrons. The use of specific approximations, which will be described below, then allows to obtain the equations of the single-fluid magnetohydrodynamic model, which we will call MHD model for brevity, which are given by:

$$\nabla \cdot \mathbf{B} = 0 \qquad \text{No magnetic monopoles} \tag{4.1a}$$

$$\nabla \times \mathbf{E} = -\frac{\partial \mathbf{B}}{\partial t} \qquad \text{Faraday's law} \tag{4.1b}$$

$$\nabla \times \mathbf{B} = \mu_0 \mathbf{J} \qquad \text{Ampére's law} \tag{4.1c}$$

$$\mathbf{E} = \eta \mathbf{J} - \mathbf{v} \times \mathbf{B} \qquad \text{Ohm's law} \tag{4.1d}$$

$$\frac{\partial \rho}{\partial t} + \nabla \cdot (\rho \mathbf{v}) = 0 \qquad \text{Continuity equation} \tag{4.1e}$$

$$\rho \left[\frac{\partial \mathbf{v}}{\partial t} + (\mathbf{v} \cdot \nabla)\mathbf{v} \right] = \mathbf{J} \times \mathbf{B} - \nabla p + \rho \nu \nabla^2 \mathbf{v} \qquad \text{Equation of fluid motion} \tag{4.1f}$$

$$\frac{\mathrm{d}}{\mathrm{d}t}\left(\frac{p}{\rho^\gamma}\right) = 0 \qquad \text{Adiabatic equation of state} \tag{4.1g}$$

where $\mathbf{E}$ and $\mathbf{B}$ represent the electrical and magnetic field, $\mathbf{J}$ current density, γ represents the ratio between the specific heat at constant pressure and constant volume, and η and ν represent the electrical resistivity and the viscosity of the fluid.
This model can describe the equilibrium, stability and dynamical properties of a plasma in a wide range of physical parameters, which encompass astrophysical, laboratory and fusion plasmas. From now on, our discussion will mainly focus to the field of thermonuclear fusion plasma, which is the subject of this Thesis.

Scope of validity and approximations

The scope of validity of the MHD model is determined by the approximations made to obtain equations (4.1), which essentially consist in limiting to the study of phenomena characterized by times scales longer than the inverse of plasma frequency ω_p and spatial scales greater than the Debye length λ_D, both of which are defined in section 1.1. This allows the study of the macroscopic dynamics of a fusion plasma in a magnetic confinement device, as the two constraints described above are widely respected.
Considering this spatial and temporal constraints is equivalent to imposing the quasi-neutrality of the plasma, $n_i \sim n_e$, which allows to neglect the density of electric charge $\rho_c = n_i - n_e$. It should be noted however that the quasi-neutral condition does not imply that the electric field is divergence-free, as can be seen by integrating the Poisson equation $\epsilon_0 \nabla \cdot \mathbf{E} = \rho_c$ once the equations (4.1) are solved.
A further approximation is to neglect the mass of electrons compared to that of the ions, while the isotropic viscosity term in (4.1f) is a simplification of the general case in which the viscosity is a tensor quantity. The MHD model suffers from an additional limitation: it neglects kinetic effects, that is, those related to the shape of the distribution function in phase space. Thus it loses the ability of describing phenomena related to wave-particle resonances. This is perfectly fine, for the RFP, as long as it stays very far from the ignition conditions.
If the electrical resistance η and the viscosity ν of the plasma are neglected, the equations (4.1) are called *the ideal MHD model*.

4.1.1 Ideal MHD equilibrium of toroidal plasmas

The use of the MHD model allows the study of the properties that a magnetic field has to possess in order to produce the forces necessary to maintain a plasma in a state of equilibrium. The configuration of the magnetic field in such a situation must be such as to compensate, with the forces it exerts, the tendency of the plasma to expand outwardly.
The simplifications to be used to study equilibrium situations using the MHD model consist of assuming a stationary state, where no physical quantity depends on time, and a static plasma, so $\mathbf{v} = 0$. A further simplification is to consider the ideal MHD model, which therefore imposes $\mathbf{E} = 0$ for (4.1d).

Under this simplifications, an equilibrium of the toroidal configuration is regulated by the ideal MHD equilibrium equation, the so-called *force-balance equation*

$$\nabla p = \mathbf{J} \times \mathbf{B}. \tag{4.2}$$

If we substitute for $\mathbf{J}$ from Ampère's law into the force-balance equation (4.2), we obtain the *pressure balance condition*

$$\nabla \left(p + \frac{B^2}{2\mu_0} \right) = \frac{1}{\mu_0} (\mathbf{B} \cdot \nabla) \mathbf{B}. \tag{4.3}$$

The terms on the right-hand side of equation (4.3) comes from the *bending* and *parallel compression* of the field lines, whereas the terms on the left-hand side indicate that the magnetic field may be considered to have a *magnetic pressure* given by $B^2/2\mu_0$. The ratio of the plasma pressure to the magnetic pressure is defined as

$$\beta = \frac{2\mu_0 p}{B^2}. \tag{4.4}$$

The quantity β is a measure of the efficiency of a given magnetic field to sustain a given plasma equilibrium. Laboratory plasmas tends to have β values in the range of a ten per cent at most, so that the magnetic field plays a major role in the dynamics of the plasma.

Equation (4.2) obviously tells us that **J** and **B** are each perpendicular to ∇p. As a result, they must lie on the surfaces of constant p, which are called *magnetic surfaces*. In the axis-symmetric case, the magnetic field profiles of the equilibrium configuration can be obtained by solving the Grad-Shafranov equation. In this approach, the magnetic field is computed by solving an equation for the poloidal magnetic flux function Ψ, and the magnetic surfaces correspond to surfaces of constant Ψ [Grad et al., 1958]. In a first approximation, one can assume $\beta = 0$, thus neglecting toroidal effects. In this case, the magnetic field admits a component B_ϕ in the toroidal direction and a component B_θ in the poloidal one, but no radial component; the same is true for every other field. Moreover, there is a smooth radial density gradient ∇p so that the surfaces of constant p are nested, concentric tori. The magnetic axis (defined as the zero radius magnetic surface) corresponds to the geometric axis of the torus. This configuration is sketched in Figure 4.1.

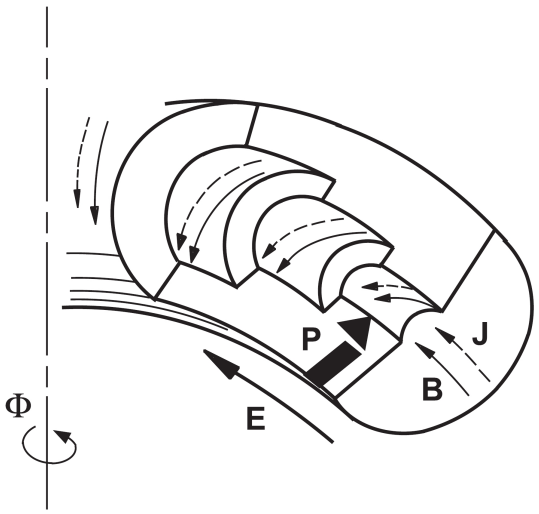

Figure 4.1: Schematic view of magnetic and current density field lines, pressure gradient and magnetic surfaces for a typical magnetic confinement configuration. The toroidal system of reference and the cylindrical coordinates are shown in Figure 2.4.

Since the resulting equilibrium configuration is axis-symmetric, the torus can be approximated as a straight periodical cylinder. The toroidal coordinate ϕ is thus substituted by the axial coordinate

$$z \equiv R_0 \phi, \tag{4.5}$$

and all of the equilibrium variables are taken to be periodical in this coordinate.

4.1.2 Ideal instabilities

Once an equilibrium configuration has been obtained, the stability properties of such a configuration must be studied. In general, an equilibrium is stable if any perturbation applied to it does not grow in

time. We expect that unstable displacements cause the magnetic field lines to bend: since this, in general, results in an increase of the magnetic energy, the instability is further stabilized by the elastic reaction of the field line, which behaves like a rubber band.

The stabilizing effect vanishes in special surfaces where the wavefront $\mathbf{k}$ of the perturbation is parallel to the magnetic field:

$$0 = \mathbf{k} \cdot \mathbf{B} = k_\phi B_\phi + k_\theta B_\theta = \frac{n}{R_0} B_\phi + \frac{m}{r} B_\theta, \tag{4.6}$$

where

$$\mathbf{k} \equiv \frac{n}{R_0} \hat{\mathbf{e}}_\phi + \frac{m}{r} \hat{\mathbf{e}}_\theta \tag{4.7}$$

is the wave vector of the perturbation, described by an helical normal mode in the plasma. Indeed, it can be proved that unstable perturbations are localized near these surfaces.

The stability of the equilibrium configuration can be characterized using the safety factor $q(r)$ defined in (2.10). The resonance condition (4.6) then becomes

$$q(r) = -\frac{m}{n}. \tag{4.8}$$

Magnetic modes (i.e. m,n pairs) for which equation (4.8) is satisfied are called *resonant modes*, and surfaces where a magnetic mode is resonant are called *resonant surfaces*. Clearly, on such surfaces the field lines close upon themselves after a finite number of toroidal transits. In principle, unstable perturbations with mode numbers (m,n) can be avoided by constructing the magnetic geometry such that the corresponding resonant surface does not appear in the plasma. One of the most common modes in toroidal confinement devices is a *kink mode* with poloidal mode number $m = 1$, whose dynamics is characterized by a helical displacement of the toroidal plasma, as shown in Figure 4.2.

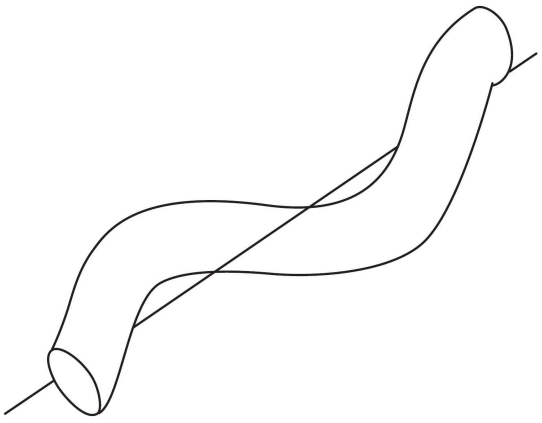

Figure 4.2: Plasma perturbation corresponding to a long wavelength $m = 1$ kink instability (from [Freidberg, 2014, p. 374]).

The previous discussion applies to perfectly conducting (i.e. zero resistivity) plasmas, whose instabilities are thus called *ideal instabilities*. The characteristic time scale associated with those modes

comes from a possible solution for incompressible waves propagating along the field lines, which travels with Alfvén velocity:

$$v_A = \frac{|B|}{\sqrt{\rho\mu_0}}. \tag{4.9}$$

The characteristic time spent for travelling a distance equal to the system size is called the *Alfvén time*:

$$\tau_A = \frac{a}{v_A}, \tag{4.10}$$

which represents the shortest time scale supported by the MHD model.

4.1.3 Resistive instabilities

The introduction of resistivity can completely alter the stability properties of the plasma described by the MHD model. Indeed, in the ideal case the plasma is tied to the magnetic field lines, and the topology of the magnetic field cannot change. On the contrary, the addition of even the smallest amount of resistivity relaxes this constraint and allows the magnetic field lines to *reconnect* across the resonant surface, with a change in magnetic topology, and the formation of a *magnetic island*.

Modes of this type are called *resistive instabilities*, and the most common of these is the *tearing mode*, so named because the magnetic flux surface "tears" at the resonant surface. The tearing modes evolve on a time scale which is between τ_A and τ_R, where

$$\tau_R \equiv \frac{\mu_0 a^2}{\eta} \tag{4.11}$$

is the so-called *resistive diffusion time* which in hot plasmas is the longest of the time scales described by resistive MHD equations. The ratio between these two time scale is given by the so-called *Lundquist number*

$$S = \frac{\tau_R}{\tau_A}. \tag{4.12}$$

In most cases of interest $S \gg 1$ ($S \sim 10^6$ for thermonuclear plasmas, $S \sim 10^{12}$ for solar corona). Thus tearing modes evolve on a time scale that can be many order of magnitude slower that that of ideal instabilities or Alfvén waves.

Of course, though the addition of resistivity introduces a new class of instabilities, ideal instabilities can be present in resistive plasmas too. In other words each ideal instability has a resistive counterpart. For instance, with a finite resistivity the kink mode is called resistive kink.

4.1.4 Magnetic reconnection

As mentioned in the previous section, the introduction of a finite resistivity allows the magnetic field lines to reconnect across the resonant surfaces, with a change in magnetic topology. In fact the magnetic topology is perfectly preserved only in a magnetofluid with zero electrical resistivity, as the *Alfvén's theorem of flux-freezing* states (see Appendix A). Since electrical resistivity appears in the *induction equation* (for derivation see Appendix A)

$$\frac{\partial \mathbf{B}}{\partial t} = \nabla \times (\mathbf{v} \times \mathbf{B}) + \frac{\eta}{\mu_0} \nabla^2 \mathbf{B}, \tag{4.13}$$

as a coefficient in front of the second derivative $\nabla^2\mathbf{B}$, even if it's small, its effect can become important in a layer where the magnetic field gradient is large. Since large gradients of magnetic field are associated with large current densities, such regions are often called *current sheets*. In a low-resistivity plasma, cutting and pasting of field lines can take place within current sheets, while everywhere else the magnetic topology may be taken to be preserved.

To explain this phenomenon lets consider a typical current sheet with oppositely directed magnetic fields above and below, as shown in Figure 4.3. The large value of $\nabla^2\mathbf{B}$ in the central region would make the electrical resistivity term important there and hence the magnetic field would decay away in the central region. Since the magnetic fields have the pressure $B^2/2\mu_0$ associated with them, a decrease in the magnetic field would cause a pressure decrease in the central region. If the plasma-β defined in Eq. (4.4) is of the order of 1 or smaller, then the magnetic pressure constitutes an important fraction of the total pressure and the decay of the magnetic field in the central region would cause an appreciable depletion of the total pressure there. Therefore we expect that the plasma from above and below with fresh magnetic fields would be sucked into the central region. This fresh magnetic field would then decay and more plasma from above and below would be sucked in to compensate for the pressure decrease due to this decay. Thus the cutting and pasting of field lines takes place in the central region. This process, known as *magnetic reconnection* or *neutral-point reconnection*, may go on as long as fresh magnetic fields are brought to the central region. Since plasmas from the top and the bottom in Figure 4.3 push against the central region, the plasma in the central region is eventually squeezed out sideways with an outward velocity v_0. This process therefore converts the magnetic energy of the plasma into the kinetic energy.

The solar flares are a striking example of magnetic reconnection events that takes place on the Sun's surfaces and cause the coronal mass ejection. An analogous phenomenon in the fusion plasmas (in particular tokamak) are the so-called *sawtooth oscillations*, in which due to the resistive internal kink instability there is a periodic collapse of the core temperature as a result of periodic reconnection phenomena [Wesson, 2004, p. 365].

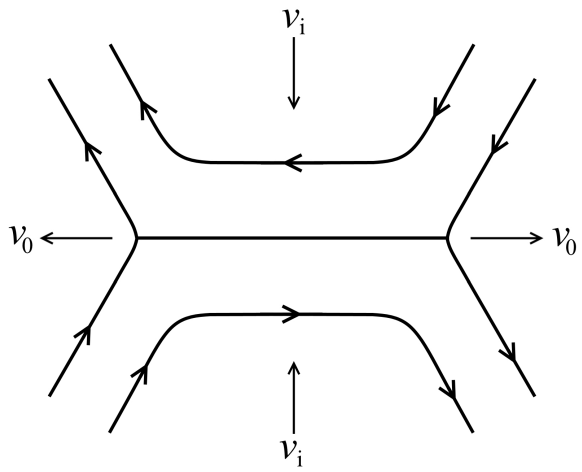

Figure 4.3: Magnetic reconnection in a current sheet with oppositely directed magnetic field lines above and below (from [Choudhuri, 1998, p. 322]).

4.1.5 Sawtooth oscillations

We will briefly give a basic description of the *sawthoot instability*, which is an example of a *resistive instability* that can trigger *magnetic reconnection events* and will be used later in this Thesis to study Alfvén waves excitation in self-consistent Tokamak configurations (Chapters 6 and 8).

Sawtooth oscillations are periodic relaxations of the core plasma density and temperature [Wesson, 2004; White, 2013]. These periodic redistributions of the core plasma surrounding the magnetic axis were first observed in 1974 [Goeler et al., 1974] and have subsequently been seen on most tokamaks. In particular, the future ITER experimental fusion device will have a baseline scenario characterized by $q_0 < 1$ and thus will have sawtooth oscillations [Perkins et al., 1995]. They are usually accompanied by an m/n=1/1 internal kink displacement [Wesson, 2004; White, 2013; Hastie et al., 1987]. Typical sawtooth cycles are depicted in Figure 4.4, where temporal traces of electron density are plotted, and each cycle shows the three phases: (i) the sawtooth ramp phase during which the plasma density and temperature increase approximately linearly with respect to time; (ii) the precursor phase, during which a helical magnetic perturbation grows until (iii) the fast collapse phase, when the density and temperature drop rapidly. In terms of safety factor q, the basic picture of the sawtooth cycle states that under central heating, the temperature profile peaks and the current profile follows due to $\sigma \propto T^{3/2}$. The increase in central current density leads to a decrease in $q_0 = q(r = 0)$ (see Eq. 2.11). Once $q_0 < 1$, the 1/1 mode becomes unstable and leads to the crash, mixing the plasma inside q=1 and at the same time redistributing poloidal flux such that $q_0 \geq 1$. After a relaxation, the flattened current density and safety factor profiles, become peaked again as the core reheats on the energy confinement time scale, and the central safety factor drops below unity again as the current density resistively diffuses back into the core. In this way, the sawtooth relaxation occurs repeatedly in time with average period τ_{st}.

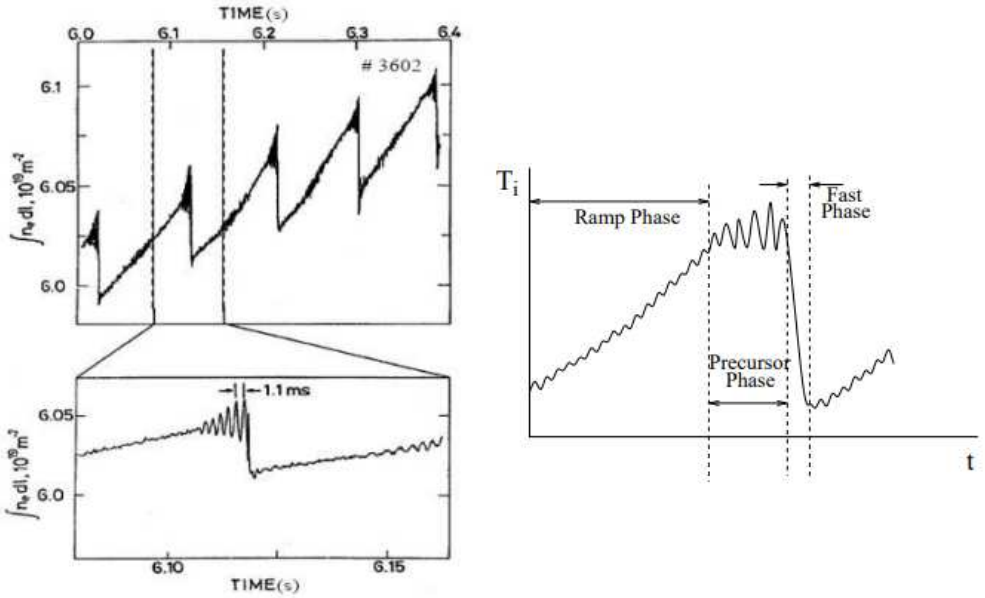

Figure 4.4: The line-integrated electron density of an early JET sawtoothing plasma. The sawtooth oscillation typically consists of a ramp phase, then a precursor oscillation followed by the fast collapse phase. (from [Chapman, 2011]).

4.2 Waves in the MHD model: Alfvén waves

In this section we consider the properties of small amplitude waves in a spatially uniform plasma, using the ideal MHD or hydromagnetic model described in section 4.1. The properties of small amplitude waves in the uniform plasma provide a reference for the discussion in the following chapters of the waves in the nonuniform plasmas. The waves will be assumed to have frequencies below of the ion cyclotron frequency $\Omega_i \equiv Be/m_i$.

Let us assume the equilibrium with the plasma at rest and with no zero-order electric field. We neglect the inertial term $(\mathbf{v}\cdot\nabla)\mathbf{v} \simeq 0$ in Eq. (4.1f) and we assume that the plasma has zero resistivity and viscosity (the ideal MHD model condition). If subscript 0 denote the equilibrium state, and subscript 1 denote the first-order perturbations associated with the wave motion, the equilibrium satisfies the force balance equation obtained from Eq. (4.1f),

$$\nabla p_0 = \mathbf{J}_0 \times \mathbf{B}_0. \tag{4.14}$$

From Eq. (4.1e) and Eq. (4.1g), the perturbed density and pressure satisfy

$$\frac{\partial \rho_1}{\partial t} + \nabla \cdot (\rho_0 \mathbf{v}_1) = 0 \tag{4.15}$$

and

$$p_1 = \frac{\gamma p_0}{\rho_0}\rho_1. \tag{4.16}$$

From the equation of fluid motion (4.1f), the perturbed fluid velocity satisfies

$$\rho_0 \frac{\partial \mathbf{v}_1}{\partial t} = -\nabla p_1 + \mathbf{J}_0 \times \mathbf{B}_1 + \mathbf{J}_1 \times \mathbf{B}_0. \tag{4.17}$$

The perturbed electric and magnetic fields satisfy the equations

$$\frac{\partial \mathbf{B}_1}{\partial t} = -\nabla \times \mathbf{E}_1 \tag{4.18}$$

and, from Eq. (4.1d) with $\eta = 0$,

$$\mathbf{E}_1 = -\mathbf{v}_1 \times \mathbf{B}_0. \tag{4.19}$$

If the wavelengths are much shorter than the scale lengths over which the equilibrium quantities ρ_0, p_0 and B_0 change, these quantities can be assumed to be constant, and the plasma is effectively uniform. The equilibrium current density $\mathbf{J}_0$ can therefore be neglected in Eq. (4.17). We have from Eq. (4.1c)

$$\mu_0 \mathbf{J}_1 = \nabla \times \mathbf{B}_1. \tag{4.20}$$

The uniform equilibrium magnetic field is chosen to lie along the z-axis. Let us also define the fluid vorticity in the magnetic field direction as

$$\zeta_{1z} = (\nabla \times \mathbf{v}_1)_z. \tag{4.21}$$

Equations (4.15)-(4.20) can then be manipulated to yield the following set of six differential equations:

$$\rho_0 \frac{\partial \zeta_{1z}}{\partial t} - B_0 \frac{\partial J_{1z}}{\partial z} = 0 \tag{4.22}$$

$$\mu_0 \frac{\partial J_{1z}}{\partial t} - B_0 \frac{\partial \zeta_{1z}}{\partial z} = 0 \tag{4.23}$$

$$\rho_0 \frac{\partial}{\partial t} \nabla \cdot \mathbf{v}_1 + \frac{B_0}{\mu_0} \nabla^2 B_{1z} + c_s^2 \nabla^2 \rho_1 = 0 \tag{4.24}$$

$$\frac{\partial B_{1z}}{\partial t} + B_0 \left(\nabla \cdot \mathbf{v}_1 - \frac{\partial v_{1z}}{\partial z} \right) = 0 \tag{4.25}$$

$$\rho_0 \frac{\partial v_{1z}}{\partial t} + c_s^2 \frac{\partial \rho_1}{\partial z} = 0 \tag{4.26}$$

$$\frac{\partial \rho_1}{\partial t} + \rho_0 \nabla \cdot \mathbf{v}_1 = 0. \tag{4.27}$$

where $c_s = (\gamma p/\rho)^{1/2}$ is the sound speed.

It is seen that the two differential equations (4.22) and (4.23) for ζ_{1z} and J_{1z} are uncoupled from the four differential equations (4.24)-(4.27) for $\nabla \cdot \mathbf{v}_1$, B_{1z}, v_{1z} and ρ_1. We should also note that in the equations for ζ_{1z} and J_{1z}, the spatial derivatives are only in the direction of the equilibrium magnetic field. Taking the Fourier transforms (see Appendix B) of Eq. (4.22) and Eq. (4.23) (or simply substituting the plane wave solution Eq. (B.3) into the differential equations), we obtain a consistency equation for a nontrivial solution which relates the frequency to the wavenumber. This is the dispersion equation for waves described by the variables ζ_{1z} and J_{1z}:

$$\omega^2 - v_A^2 k_z^2 = 0, \tag{4.28}$$

where the Alfvén speed v_A in the equilibrium plasma is given by

$$v_A = \frac{B_0}{(\mu_0 \rho_0)^{1/2}}. \tag{4.29}$$

The dispersion equation (4.28) is independent of the components of the wavevector perpendicular to the equilibrium magnetic field, and is also independent of the sound speed c_s.

Taking the Fourier transforms of Eqs. (4.24)-(4.27) yields a separate dispersion equation for waves described by the variables $\nabla \cdot \mathbf{v}_1$, B_{1z}, v_{1z} and ρ_1:

$$\omega^4 - \omega^2 (v_a^2 + c_s^2) k^2 + v_a^2 c_s^2 k^2 k_z^2 = 0, \tag{4.30}$$

where $k = |\mathbf{k}|$. This dispersion equation does involve the perpendicular components of the wavevector, and the sound speed, in contrast to Eq. (4.28).

It is evident that the two dispersion equations (4.28) and (4.30), together with their corresponding sets of characteristic wave field variables, correspond to two distinct types of wave modes. The waves described by Eq. (4.28) are called *shear Alfvén waves*, and the waves described by Eq. (4.30) are called *magnetoacoustic* (or *magnetosonic*) waves (see Table 4.1). The magnetoacoustic mode may be further split into two distinct modes, the fast and slow magnetoacoustic waves. An arbitrary low-frequency disturbance can be represented as a superposition of the Alfvén wave and the fast and slow magnetoacoustic waves.

	Dispersion equation	Characteristic variables
Shear Alfvén wave	$\omega^2 - v_A^2 k_z^2 = 0$	J_{1z}, ζ_{1z}
Magnetoacoustic waves	$\omega^4 - \omega^2(v_A^2 + c_s^2)k_z^2$ $+v_A^2 c_s^2 k^2 k_z^2 = 0$	$\nabla \cdot \mathbf{v}_1$, v_{1z}, B_{1z}, ρ_1

Table 4.1: The dispersion equations and characteristic variables for the Alfvén and magnetoacoustic modes in the ideal MHD model.

Let us define the angle θ between the wavevector and the magnetic field $\mathbf{B}_0$, so that $k_z = k\cos\theta$. The first dispersion equation (4.28) then gives the positive frequency solution

$$\omega_A = v_a|k_z| = v_A k|\cos\theta| \tag{4.31}$$

of the shear Alfvén mode. The second dispersion equation (4.30) gives two positive frequency solutions: the fast magnetoacoustic mode, with

$$\omega_F^2 = \frac{k^2}{2}\left(v_A^2 + c_s^2 + ((v_A^2 + c_s^2)^2 - 4v_A^2 c_s^2\cos^2\theta)^{(1/2)}\right) \tag{4.32}$$

and the slow magnetoacoustic mode, with

$$\omega_S^2 = \frac{k^2}{2}\left(v_A^2 + c_s^2 - ((v_A^2 + c_s^2)^2 - 4v_A^2 c_s^2\cos^2\theta)^{(1/2)}\right). \tag{4.33}$$

We note that the phase velocity $v_{ph} = \omega/k$ is independent of k for all three modes, so all the modes are nondispersive, although they are anisotropic because v_{ph} depends on the angle of propagation θ. The characteristic phase velocity surfaces, that is, polar plots of the phase velocities of three modes against the angle θ, are plotted in Fig. 4.5

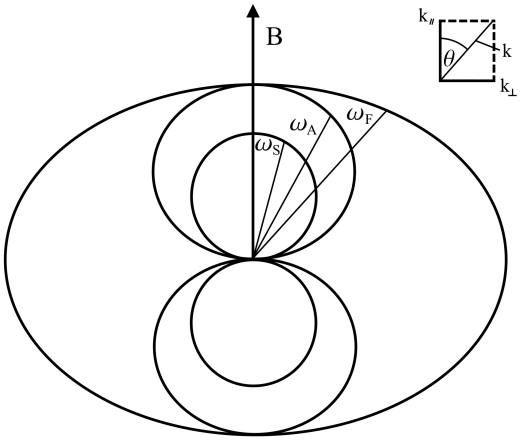

Figure 4.5: Dispersion curves $\omega_{A,F,S}(\theta)$, Eqs. (4.31), (4.32), (4.33), for $v_A^2/c_s^2 = 2$.

4.2.1 The Shear Alfvén Wave

If the wave is purely in the shear Alfvén mode, we can assume the characteristic variables listed in Table 4.1 for the magnetoacoustic mode to be zero. Also without loss of generality, for a uniform plasma we can choose the **k** vector to lie in the x-z plane

$$\mathbf{k} = (\sin\theta, 0, \cos\theta). \tag{4.34}$$

Thus we have (with $k_y = 0$),

$$v_{1z} = 0 \qquad \text{and} \qquad \nabla \cdot \mathbf{v}_1 = ik_x v_{1x} = 0. \tag{4.35}$$

Provided that $k_x \neq 0$ (i.e. $\sin\theta \neq 0$), we conclude that $v_{1x} = 0$ (the case of $k_x = 0$, i.e. propagation parallel or antiparallel to the magnetic field, is discussed in the next section). Thus the velocity perturbation $\mathbf{v}_1 = \mathbf{v}_A$ of the Alfvén mode is in the y-direction only, perpendicular to both the equilibrium magnetic field $\mathbf{B}_0$ and the wavevector **k**. Therefore the field lines are bent, giving the rise to a magnetic tension. Also because $\nabla \cdot \mathbf{v}_1 = 0$, there is no density or particle pressure perturbation for this mode.

Since $B_{1z} = 0$ and $\nabla \cdot \mathbf{B}_1 = 0$, it follows that $B_{1x} = 0$, so that this mode only has a magnetic field perturbation in the y-direction, as exemplified in Figure 4.6. The absence of a magnetic field perturbation in the equilibrium magnetic field direction implies, since we have $\mathbf{B}_1 \cdot \mathbf{B}_0 = 0$ and $B^2 \simeq B_0^2 + 2\mathbf{B}_1 \cdot \mathbf{B}_0$ (to first order), that the magnetic field strength is constant to first order. The strengths of the magnetic and particle pressures in the plasma are thus each conserved; there is no compressive stress due to this wave, which therefore is said to be a noncompressional *shear* wave. The phase speed of the wave lies between the speeds of the slow and fast magnetoacoustic waves (see Figure 4.5), so the shear Alfvén wave is also sometimes referred to as the *intermediate* wave.

Plasma flow across the magnetic field can increase the bending of the field; the shear wave acts to reduce the additional curvature of the field line. The currents that are set up to reduce the bending are closed partly along the field, so the shear wave introduces the field-aligned current J_{1z}. In a cylindrical geometry, the shear Alfvén wave is referred to as a *torsional* wave, with adjacent magnetic surfaces able to shear past each other without coupling to each other. Since ω is independent of $k_\perp$, the mode may be strongly localized to some field lines. This property is the origin of the singular Alfvén modes in and inhomogeneous sheared configuration which form the Alfvén *continuum* (as we will discuss in Section 5.2.1).

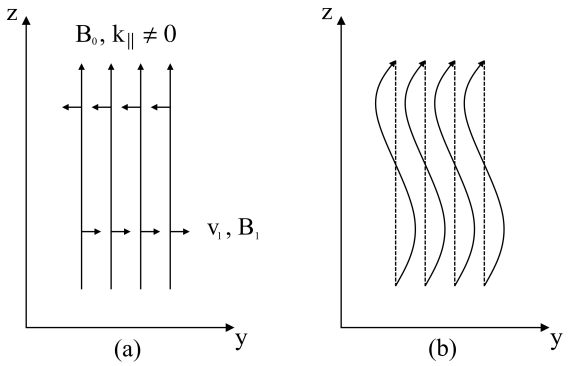

Figure 4.6: Magnetic field and velocity perturbations for the shear Alfvén wave shown in (a) vector component form and (b) combined form (from [Freidberg, 2014, p. 332]).

An important point to note is that the shear Alfvén wave dispersion relation is independent of the wavevector component perpendicular to the equilibrium magnetic field, and the wave cannot propagate perpendicular to the field (i.e. the phase velocity drops to zero). The group velocity

$$\mathbf{v}_g = \frac{\partial \omega_A}{\partial k} = v_A \cos\theta\, \hat{\mathbf{z}} \tag{4.36}$$

is aligned with the background magnetic field, that is, the wave energy is always carried along the direction of the background field, regardless of the direction of the wavevector.

4.2.2 The Fast and Slow Magnetoacoustic Modes

For a wave in the fast and slow magnetosonic mode, the characteristic variables for the shear Alfvén mode are zero. Thus, with the choice (Eq. 4.34) for the direction of $\mathbf{k}$, we have

$$\zeta_{1z} = i\mathbf{k} \times \mathbf{v}_1|_z = ik_x v_{1y} = 0, \tag{4.37}$$

so $v_{1y} = 0$. Also since $J_{1z} = 0$ and $\mu_0 \mathbf{J}_1 = \nabla \times \mathbf{B}_1$, it follows that $B_{1y} = 0$.

There are density perturbation in the wave (since $\nabla \cdot \mathbf{v}_1 \neq 0$), and perturbations of the magnetic field parallel to $\mathbf{B}_0$ (and thus of the field strength). Thus these modes are compressive in nature, even if the sound speed is zero. In contrast to the shear Alfvén wave, the fast and slow magnetoacoustic waves act to reduce magnetic or particle pressure gradients in the plasma.

The fast wave is sometimes called a *compressional Alfvén* wave. In the case of a low-β plasma, that is with $v_A^2 \gg c_s^2$, the fast wave dispersion relation is

$$\omega_F = v_A k \tag{4.38}$$

and the $\mathbf{v}_1$ is perpendicular to $\mathbf{B}_0$. See Figure 4.7. The fast wave can propagate and transport energy in any direction. The particle pressure and magnetic pressure in the fast wave increase and decrease in phase. In the slow wave, the particle and magnetic pressure vary out of phase.

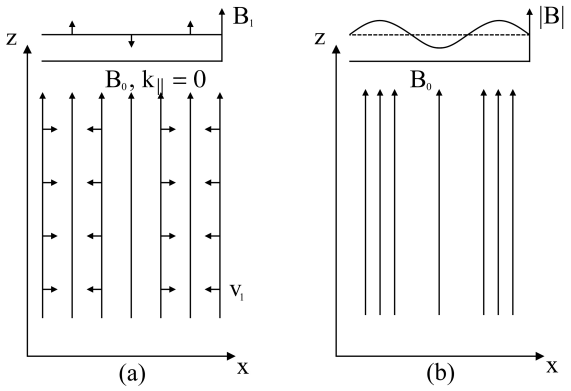

Figure 4.7: Magnetic field and velocity perturbations for the compressional Alfvén wave shown in (a) vector component form and (b) combined form (from [Freidberg, 2014, p. 333]).

For parallel or antiparallel propagation ($\sin\theta = 0$), the fast mode loses its compressive character and becomes degenerate with the Alfvén mode, in that both modes have a phase speed v_A, with a perturbation magnetic field perpendicular to the equilibrium field. The slow mode in this case is a pure sound mode with phase speed c_s.

Equations (4.31), (4.32) and (4.33) indicate that $\omega^2 \geq 0$. Hence frequencies are real. Adding dissipation will only introduce wave damping, $\omega \rightarrow \omega + i\gamma$, $\gamma < 0$. There are no unstable MHD modes in a homogeneous plasma, which represents global thermodynamic equilibrium, the lowest energy state a system may reach. Instability arises only for sufficiently strong spatial inhomogeneity. The overall above analysis of waves solutions in the MHD model will be considered again in Chapter 5 for cylindrical plasmas, both uniform and with space inhomogeneities.

Chapter 5

Alfvén waves in cylindrical plasmas

In the ideal MHD approximation, the behaviour of the shear Alfvén wave is not sensitive to the plasma geometry since this wave propagates only along $\mathbf{B}_0$ lines and does not reflect off the plasma boundaries. However, the compressional wave does reflect off the plasma boundary or off metal wall boundaries, which can act like a waveguide or resonant cavity. Thus eigenmodes of the waves may exist, with spectra of discrete eigenfrequencies called Compressional Alfvén Eigenmode (CAE). The geometry is therefore very significant in determining the modes of propagation of the compressional wave. Nevertheless, wave propagation in a toroidal plasma is often modelled in cylindrical geometry, first because the mathematics is much simpler and second because a torus behaves, in most respects, like a bend cylinder.

In this Chapter we will compute the equations of Alfvén waves in cylindrical geometry and with ideal boundary condition (perfectly conducting wall that contains the plasma). This analytical study is an original synthesis of several textbooks and scientific articles [Cramer, 2001; Villard et al., 1997; Musielak et al., 1989]. The resulting equations will be compared to those for free Alfvén waves in cartesian coordinates, as derived in Chapter 4. In particular we will consider waves in periodic straight cylindrical column of both uniform and non-uniform plasma (with non uniform density $\rho_0(r)$ and /or magnetic field $\mathbf{B}_0(r)$). The non-uniform case, compared to the uniform one, will be characterised by a new Alfvén mode, the Global Alfvén Eigenmode (GAE), and new phenomena like phase mixing and Alfvén resonance absorption. As we will see, while in the uniform case we are still able to obtain an analytical solution for shear and compressional modes, in the non-uniform case this is not always possible. Therefore we will employ the *local* or *Wentzel-Kramers-Brillouin* (WKB) approximation and numerical calculations to obtain the frequencies we are interested in for the analysis of SpeCyl simulations in Chapter 8.

It has to be noted that the SpeCyl code, as discussed in Section 6.1.1, is a visco-resistive numerical code, with viscosity and resistivity given by Eqs. (6.2), and so one could argue that the ideal MHD model is not suited for the analysis of SpeCyl simulations. But as we will see in the following chapters these dissipative terms only introduce a damping effect and cause the fields to decay in time, without actually significantly affecting the frequency spectra themselves. A more detailed discussion of the effects of dissipative terms on MHD waves can be found in [Cramer, 2001, p. 29].

5.1 Uniform plasma case

In this Section we will consider a uniform plasma in cylindrical geometry with ideal boundary conditions. As in Chapter 4 we will use the ideal MHD model in the cold plasma approximation ($p = 0$). Therefore, as before, we assume the equilibrium with the plasma at rest and with no zero-order electric field. We neglect the inertial term $(\mathbf{v}\cdot\nabla)\mathbf{v} \simeq 0$ in Eq. (4.1f) and we assume that the plasma has zero resistivity and viscosity (the ideal MHD model condition). The subscript 0 will denote the equilibrium state, and subscript 1 will denote the first-order perturbations associated with the wave motion. In particular we will compute the dispersion relations for shear Alfvén and compressional modes to see if and how they change from the free case discussed in Chapter 4.

5.1.1 Shear Alfvén Wave

We now will compute the dispersion relation for the Shear Alfvén Wave in a uniform axial magnetic field $\mathbf{B}_0$, uniform density ρ_0 and $\mathbf{v}_0 \equiv 0$ (plasma at rest), in the cold plasma approximation $p_0 = 0$. For the shear Alfvén mode we can assume the characteristic variables listed in Table 4.1 for the magnetoacoustic mode to be zero. Therefore $\rho_1 = 0$ and for Eq. 4.16 $p_1 = 0$. If the equilibrium quantities ρ_0 and B_0 are constant, the equilibrium current density $\mathbf{J}_0$ can be neglected in Eq. (4.17).

From Eq. (4.17) and Eq. (4.20), the perturbed velocity then satisfy

$$\rho_0 \frac{\partial \mathbf{v}_1}{\partial t} = \frac{1}{\mu_0}(\nabla\times\mathbf{B}_1)\times\mathbf{B}_0. \tag{5.1}$$

From Eq. (4.18) and Eq. (4.19), and the following identity

$$\nabla\times(\mathbf{A}\times\mathbf{B}) = \mathbf{A}(\nabla\cdot\mathbf{B}) - \mathbf{B}(\nabla\cdot\mathbf{A}) + (\mathbf{B}\cdot\nabla)\mathbf{A} - (\mathbf{A}\cdot\nabla)\mathbf{B}, \tag{5.2}$$

we can see that the perturbed magnetic field satisfies

$$\frac{\partial \mathbf{B}_1}{\partial t} = \nabla\times(\mathbf{v}_1\times\mathbf{B}_0) = (\mathbf{B}_0\cdot\nabla)\mathbf{v}_1 = B_0\frac{\partial \mathbf{v}_1}{\partial z}, \tag{5.3}$$

where in the last two steps we used fact that $\mathbf{B}_0$ is uniform and $\nabla\cdot\mathbf{v}_1 = 0$ (condition (4.35)).

Taking the time derivative of Eq. (5.1) and putting it together with the previous equation we obtain

$$\rho_0\frac{\partial^2\mathbf{v}_1}{\partial t^2} = \frac{1}{\mu_0}\left(\nabla\times\frac{\partial\mathbf{B}_1}{\partial t}\right)\times\mathbf{B}_0 = \frac{B_0}{\mu_0}\left(\nabla\times\frac{\partial\mathbf{B}_1}{\partial t}\right)\times\hat{\mathbf{z}} = \frac{B_0^2}{\mu_0}\left(\nabla\times\frac{\partial\mathbf{v}_1}{\partial z}\right)\times\hat{\mathbf{z}}.$$

Using the two identities:

$$\nabla(\mathbf{A}\cdot\mathbf{B}) = \mathbf{A}\times(\nabla\times\mathbf{B}) + \mathbf{B}\times(\nabla\times\mathbf{A}) + (\mathbf{A}\cdot\nabla)\mathbf{B} + (\mathbf{B}\cdot\nabla)\mathbf{A} \tag{5.4}$$

and

$$\mathbf{A}\times(\mathbf{B}\times\mathbf{C}) = (\mathbf{A}\cdot\mathbf{C})\mathbf{B} - (\mathbf{A}\cdot\mathbf{B})\mathbf{C}, \tag{5.5}$$

and the condition $v_{1z} = 0$ (4.35) it follows that

$$\begin{aligned}\frac{B_0^2}{\mu_0}\left(\nabla\times\frac{\partial\mathbf{v}_1}{\partial z}\right)\times\hat{\mathbf{z}} &= \frac{B_0^2}{\mu_0}\left[-\nabla\left(\hat{\mathbf{z}}\cdot\frac{\partial\mathbf{v}_1}{\partial z}\right)+\frac{\partial\mathbf{v}_1}{\partial z}\times(\nabla\times\hat{\mathbf{z}})+(\hat{\mathbf{z}}\cdot\nabla)\frac{\partial\mathbf{v}_1}{\partial z}+\left(\frac{\partial\mathbf{v}_1}{\partial z}\cdot\nabla\right)\hat{\mathbf{z}}\right]\\ &= \frac{B_0^2}{\mu_0}\left[-\nabla\frac{\partial v_{1z}}{\partial z}+\frac{\partial^2\mathbf{v}_1}{\partial z^2}\right]\\ &= \frac{B_0^2}{\mu_0}\frac{\partial^2\mathbf{v}_1}{\partial z^2}.\end{aligned}$$

Finally we get

$$\frac{\partial^2\mathbf{v}_1}{\partial t^2}-v_A^2\frac{\partial^2\mathbf{v}_1}{\partial z^2}=0, \tag{5.6}$$

where $v_A^2 = B_0^2/(\mu_0\rho_0)$ is the Alfvén velocity.

Let us compute this equation in cylindrical coordinate. We seek solutions of perturbed velocity in the form

$$\mathbf{v}_1(t,r,\theta,z) = \mathbf{v}_1^{m,n}(r)\exp^{i\left(m\theta+\frac{n}{R}z-\omega t\right)}. \tag{5.7}$$

Putting it in Eq. (5.6) we obtain

$$\left(\omega^2-v_A^2\frac{n^2}{R^2}\right)\mathbf{v}_1^{m,n}(r)=0,$$

and finally the dispersion relation is

$$\omega^2-v_A^2k_z^2=0, \tag{5.8}$$

where $k_z^2 = n^2/R^2$. This expression is identical to the one obtained in cartesian coordinates (Eq. 4.28). This is due the fact that, as said before, the shear Alfvén wave is not sensitive to the plasma geometry since it propagates only along $\mathbf{B}_0$ lines and does not reflect off the plasma boundaries, which we indeed did not had to impose in this discussion. In Figure 5.1 the normalized frequency dependence on k_z wavevector component is shown, in the case of $m = 0$, for the shear Alfvén wave.

5.1.2 Compressional Alfvén Eigenmode

To compute the compressional mode dispersion relation let us rewrite Eqs. (4.24)-(4.26) in the cold plasma approximation ($p_0 = 0 \Rightarrow c_s^2 = \gamma p_0/\rho_0 = 0$)

$$\rho_0\frac{\partial}{\partial t}\nabla\cdot\mathbf{v}_1+\frac{B_0}{\mu_0}\nabla^2B_{1z}=0 \tag{5.9}$$

$$\frac{\partial B_{1z}}{\partial t}+B_0\left(\nabla\cdot\mathbf{v}_1-\frac{\partial v_{1z}}{\partial z}\right)=0 \tag{5.10}$$

$$\rho_0\frac{\partial v_{1z}}{\partial t}=0. \tag{5.11}$$

Taking the time derivative of Eq. (5.10)

$$\frac{\partial^2B_{1z}}{\partial t^2}+B_0\left[\frac{\partial}{\partial t}(\nabla\cdot\mathbf{v}_1)-\frac{\partial}{\partial z}\frac{\partial v_{1z}}{\partial t}\right]=0$$

and using the Eqs. (5.11) and (5.9) we get

$$\frac{\partial^2 B_{1z}}{\partial t^2} - v_A^2 \nabla^2 B_{1z} = 0, \tag{5.12}$$

where $v_A^2 = B_0^2/(\mu_0 \rho_0)$ is the Alfvén velocity.

Let's compute this equation in cylindrical coordinates

$$B_{1z}(t, r, \theta, z) = B_{1z}^{m,n}(r) \exp^{i\left(m\theta + \frac{n}{R} z - \omega t\right)}. \tag{5.13}$$

We seek solutions of Eq. (5.12), with ideal boundary conditions

$$0 = E_\theta\big|_{r=a} = \eta J_\theta\big|_{r=a} = \frac{\eta}{\mu_0} \frac{\mathrm{d}}{\mathrm{d}r} B_z\bigg|_{r=a}. \tag{5.14}$$

Replacing Eq. (5.13) in Eq. (5.12) we obtain

$$\frac{\partial^2 B_{1z}}{\partial t^2} - v_A^2 \left[\frac{1}{r} \frac{\partial}{\partial r} \left(r \frac{\partial B_{1z}}{\partial r} \right) + \frac{1}{r^2} \frac{\partial^2}{\partial \theta^2} B_{1z} + \frac{\partial^2}{\partial z^2} B_{1z} \right] = 0.$$

Deriving B_{1z}

$$\left\{ -\omega^2 - v_A^2 \left[\frac{\mathrm{d}^2}{\mathrm{d}r^2} + \frac{1}{r} \frac{\mathrm{d}}{\mathrm{d}r} - \frac{m^2}{r^2} - \frac{n^2}{R^2} \right] \right\} B_{1z}^{mn}(r) = 0,$$

and multiplying both members with $-r^2/v_A^2$ we obtain

$$\left[r^2 \frac{\mathrm{d}^2}{\mathrm{d}r^2} + r \frac{\mathrm{d}}{\mathrm{d}r} + \left(\frac{\omega^2}{v_A^2} - \frac{n^2}{R^2} \right) r^2 - m^2 \right] B_{1z}^{mn}(r) = 0. \tag{5.15}$$

Defining the quantity

$$\xi^2 \equiv \left(\frac{\omega^2}{v_A^2} - \frac{n^2}{R^2} \right), \tag{5.16}$$

and performing the following substitution

$$r' = \xi r \tag{5.17}$$

we obtain the *Bessel's differential equation*

$$\left[r'^2 \frac{\mathrm{d}^2}{\mathrm{d}r'^2} + r' \frac{\mathrm{d}}{\mathrm{d}r'} + r'^2 - m^2 \right] B_{1z}^{mn}(r') = 0, \tag{5.18}$$

where m is the order of the Bessel function.

The solution is given by a Bessel function of order m, which expression is, resubstituting r,

$$B_{1z}^{mn}(r) = B_{1z}^{mn}(0) J_m(\xi r). \tag{5.19}$$

Let's now impose the ideal boundary condition (5.14)

$$\frac{\mathrm{d}}{\mathrm{d}r}B_{1z}^{mn}(r=a)=0 \quad \Longrightarrow \quad B_{1z}^{mn}(0)\frac{\mathrm{d}}{\mathrm{d}r}J_m(\xi a)=0. \tag{5.20}$$

The solutions are the roots of the first derivative of the Bessel function of order m (this values can be derived and are well know), which we name χ_{mj}, where j is the j-th root,

$$\xi a = \chi_{mj} \qquad \text{with} \quad j=1,2,3\ldots. \tag{5.21}$$

Therefore, taking the square of Eq. (5.21), we find the following dispersion relation

$$\xi^2 = \frac{\omega_{mj}^2}{v_A^2} - \frac{n^2}{R^2} = \frac{{\chi_{mj}}^2}{a^2}$$

$$\omega_{mj}^2 = v_A^2\left(k_z^2 + \frac{{\chi_{mj}}^2}{a^2}\right) \qquad \text{with} \quad j=1,2,3\ldots, \tag{5.22}$$

where $k_z^2 = n^2/R^2$.

The first thing to note is that in this case we are considering only the fast magnetoacoustic mode, indeed assuming $c_s^2 = 0$ the slow magnetoacoustic mode's frequency is null, as can be seen from Eq. (4.33). Furthermore the expression of the compressional mode itself is different from the one in cartesian coordinates (Eq. (4.32)). In fact the effect of moving to cylindrical geometry and imposing the ideal boundary conditions (5.14) brings a set of Compressional Alfvén Eigenmodes (CAEs), whose frequency depends on j-th root of the derivative of Bessel function of order m. In Figure 5.1 the normalized frequency dependence on k_z wavevector component is shown, in the case of $m = 0$, for the first five CAEs.

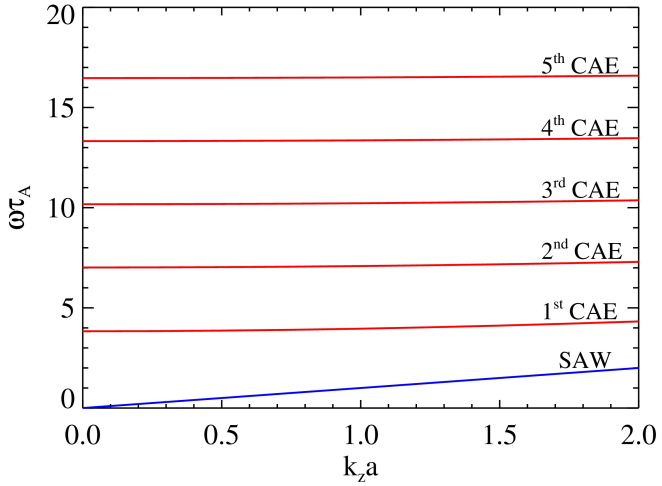

Figure 5.1: Case $m = 0$. Normalized frequency dependence on k_z wavevector component for SAW and the first five CAEs in cylindrical geometry.

5.2 Non-uniform plasma case

In this Section we will consider the case of a non-uniform plasma in cylindrical geometry with ideal boundary conditions. Compared to the previous uniform case, now the magnetic field $\mathbf{B}_0$ and/or plasma density ρ_0 are allowed to vary with radial coordinate r. Apart from that, we will use the same model and conditions used in the previous Section. In particular we will compute the dispersion relations for shear Alfvén and compressional modes as well as for the new Alfvén mode, the Global Alfvén Eigenmode. Also we will briefly discuss the new phenomena that arise from the non-uniformity of the plasma: phase mixing and Alfvén resonance absorption.

5.2.1 Continuous Shear Alfvén Wave and phase mixing

The magnetic field is assumed to have θ and z components and is allowed to vary with r in magnitude and direction:

$$\mathbf{B}_0(r) = B_{0\theta}(r)\hat{\boldsymbol{\theta}} + B_{0z}(r)\hat{\boldsymbol{z}}. \tag{5.23}$$

The plasma density ρ_0 is also allowed to vary with r.

To derive the shear Alfvén dispersion relation we start from the general case with finite pressure ($p_0 \neq 0$). Let us consider the linearized MHD equation of motion (4.1f) expressed in terms of perturbed fluid velocity $\mathbf{v}_1$, magnetic field $\mathbf{B}_1$ and (particle plus magnetic) pressure p_T:

$$\rho_0 \frac{\partial \mathbf{v}_1}{\partial t} = -\nabla p_T + \frac{1}{\mu_0}(\mathbf{B}_1 \cdot \nabla)\mathbf{B}_0 + \frac{1}{\mu_0}(\mathbf{B}_0 \cdot \nabla)\mathbf{B}_1. \tag{5.24}$$

We also employ Faraday's equation (4.1b), combined with Ohm's law (4.1d) with zero resistivity $\eta = 0$:

$$\frac{\partial \mathbf{B}_1}{\partial t} = \nabla \times (\mathbf{v}_1 \times \mathbf{B}_0) \tag{5.25}$$

and the linearized version of the adiabatic equation of state (4.1g). For a wave of given frequency ω, we can derive from Eqs. (5.24)-(5.25), in cylindrical geometry, two coupled differential equations in p_T and velocity component v_{1r} (the analogous calculus but in cartesian coordinates was done by Musielak et al., 1989):

$$\frac{\mathrm{d}p_T}{\mathrm{d}r} - \tau v_{1r} = 0 \tag{5.26}$$

$$\frac{1}{r}\frac{\mathrm{d}}{\mathrm{d}r}(r v_{1r}) - \frac{q^2}{\tau} p_T = 0 \tag{5.27}$$

where

$$\tau = i\frac{\rho_0}{\omega}\left(\omega^2 - (\mathbf{k}\cdot\mathbf{v}_A)^2\right) \tag{5.28}$$

and

$$q^2 = k^2 - \frac{\omega^4}{\omega^2(c_s^2 + v_A^2) - c_s^2(\mathbf{k}\cdot\mathbf{v}_A)^2}, \tag{5.29}$$

where $\mathbf{k} = (0, k_\theta, k_z) = (0, m/r, n/R)$ is the wavevector, $k = |\mathbf{k}|$ and $\mathbf{v}_A = \mathbf{B}_0/\sqrt{\mu_0\rho_0}$ is the vector Alfvén velocity which now depends on r. The Alfvén wave and fast and slow magnetoacoustic waves described by ideal MHD model in Section 4.2 can be recovered, using cartesian geometry, from Eqs. (5.26) and

(5.27) in the limit of a uniform plasma density and magnetic field (in the z-direction). This shows us that in the non-uniform case the two waves are coupled. In general when the wavevector $\mathbf{k}$ of the perturbation is not parallel or perpendicular to the equilibrium magnetic field $\mathbf{B}_0$ but oblique to it, we expect such perturbation to excite both types of the waves.

The second-order differential equation for v_{1r} is then

$$\frac{\mathrm{d}}{\mathrm{d}r}\left[\frac{\tau}{q^2 r}\frac{\mathrm{d}}{\mathrm{d}r}(rv_{1r})\right] - \tau v_{1r} = 0 \tag{5.30}$$

and that for p_T is

$$\frac{\tau}{r}\frac{\mathrm{d}}{\mathrm{d}r}\left(\frac{r}{\tau}\frac{\mathrm{d}p_T}{\mathrm{d}r}\right) - q^2 p_T = 0. \tag{5.31}$$

There are two possible singularities of Eqs. (5.30) and (5.31). One singularity occurs where $\tau = 0$, that is, at a point where

$$\omega(r) = |\mathbf{k}\cdot\mathbf{v}_A| = |k_\parallel(r)\cdot v_A(r)| = \frac{|k_\theta B_{0\theta} + k_z B_{0z}|}{\sqrt{\mu_0\rho_0}} = \frac{|\frac{m}{r}B_{0\theta} + \frac{n}{R}B_{0z}|}{\sqrt{\mu_0\rho_0}}, \tag{5.32}$$

where $k_\parallel = \mathbf{k}\cdot\mathbf{B}_0/|\mathbf{B}_0|$ and $v_A = |\mathbf{B}_0|/\sqrt{\mu_0\rho_0}$. This is the *Alfvén resonance condition*.

The condition (5.32) is also said to define the *continuous shear Alfvén wave spectrum*, or the *Alfvén continuum*, in a nonuniform plasma. For a given frequency and $\mathbf{k}$, the condition (5.32) is possibly satisfied only at isolated points in the density and magnetic field profiles. However, if just $\mathbf{k}$ is specified, every point in the plasma profile is associated with different frequency, given by Eq. (5.32). In a smoothly varying plasma profile we therefore have a continuous spectrum of frequencies, which formally corresponds to localized shear Alfvén waves with the same wavevector. It is noteworthy that the analogous calculation in cartesian coordinates bring the same result ($\omega = |\mathbf{k}\cdot\mathbf{v}_A|$). The existence of the continuous spectrum is also related to a *phase mixing* in time, leading to the decay of wave fields. We will discuss this phenomenon shortly below.

A second singularity occurs where $1/q^2 = 0$, that is, at a position in the density and magnetic field profile where the following condition holds:

$$\omega^2 = \frac{c_s^2(\mathbf{k}\cdot\mathbf{v}_A)^2}{v_A^2 + c_s^2}. \tag{5.33}$$

This condition is called the *cusp* or *compressive resonance condition*. However, in our case of cold plasma approximation, this singularity does not occur as $c_s^2 = 0$. Therefore in the following sections we will introduce a consequence of Alfvén resonance condition, that is the *Alfvén resonance absorption* process.

To illustrate the phase mixing phenomena let us consider a simpler case: an equilibrium uniform magnetic field $\mathbf{B}_0 = B_0\hat{\mathbf{z}}$ and non-uniform plasma density profile $\rho_0(r)$, with corresponding local Alfvén speed $v_A(r)$. For a wave with given frequency ω, we can derive from Eqs. (5.24)-(5.25), in cylindrical geometry, two coupled differential equation in p_T and the fields components $v_{1\theta}$ and $B_{1\theta}$:

$$\rho_0\frac{\partial v_{1\theta}}{\partial t} = -ik_\theta p_T + \frac{B_0}{\mu_0}\frac{\partial B_{1\theta}}{\partial z} \tag{5.34}$$

$$\frac{\partial B_{1\theta}}{\partial t} = B_0 \frac{\partial v_{1\theta}}{\partial z}. \tag{5.35}$$

Taking $k_\theta = m/r = 0$, the perturbed velocity component $v_{1\theta}$ than satisfies the equation

$$\frac{\partial^2 v_{1\theta}}{\partial t^2} = v_A^2(r) \frac{\partial^2 v_{1\theta}}{\partial z^2}, \tag{5.36}$$

with the local dispersion relation $\omega(r) = k_z v_A(r)$ for each magnetic surface oscillating with its own frequency. For the initial condition of standing wave of fixed k_z, as time proceeds the phase of the wave on each field line changes, that is, we have phase mixing. In fact, each field line oscillates at the local Alfvén frequency, losing coherence with the motion of adjacent lines. This fact qualitatively explains the reason of the name "phase mixing". This effect effectively leads to the damping of any initial Alfvén perturbation in an inhomogeneous plasma at the rate:

$$\gamma_d \sim \left| \frac{\mathrm{d}}{\mathrm{d}r} \left(k_z v_A(r) \right) \right|. \tag{5.37}$$

Of course this considerations are also valid for any mode numbers (m, n) and in case of non-uniform magnetic field $\mathbf{B}_0$ and uniform plasma density ρ_0 or both $\mathbf{B}_0$ and ρ_0 non-uniform, as long as the shear dispersion relation is given by Eq. (5.32).

5.2.2 Compressional Alfvén Eigenmode and resonance absorption

Compared to the uniform case, with nonuniform magnetic field and/or plasma density there are no exact solutions for the compressional mode. In fact we can still solve the MHD equations in cylindrical geometry and ideal boundary conditions, Equations from (5.14) to (5.15). In this case, however, ξ will depend on the radial coordinate r

$$\xi^2 = \left(\frac{\omega^2}{v_A^2(r)} - \frac{n^2}{R^2} \right), \tag{5.38}$$

where, in the general case

$$v_A^2(r) = \frac{B_0^2(r)}{\mu_0 \rho_0(r)}. \tag{5.39}$$

Therefore the differential equation (5.18) with $\xi(r)$ cannot be cast anymore in the form of a Bessel equation and does not possess an analytic solution.

We can still solve the CAE equation (5.15) using a *local* or *WKB approximation* (similarly to what was done in Cramer, 2001, p. 183). That is we assume that each point in the plasma locally satisfies the homogeneous plasma dispersion relation. It's a good approximation when the density or magnetic field varies by only a small amount in a distance equal to one wavelength in the radial direction. Nevertheless, the WKB approximation is very useful for qualitative discussion even in cases with relatively high variable density and/or magnetic field in radial coordinate.

When this approximation is applied, the solution of the differential equation for B_{1z}^{mn} is found in the form

$$B_{1z}^{mn}(r) \propto J_m \left(\int_0^r \xi(r') \mathrm{d}r' \right). \tag{5.40}$$

Of course if ξ doesn't depend on r this expression becomes the same as in the homogeneous case (5.19).

Imposing the ideal boundary condition (5.14) we get

$$\frac{\mathrm{d}}{\mathrm{d}r} B_{1z}^{mn}(r=a) = 0 \quad \Longrightarrow \quad \frac{\mathrm{d}}{\mathrm{d}r} J_m \left(\int_0^a \xi(r')\mathrm{d}r' \right) = 0. \tag{5.41}$$

In this case the solution, from which we can derive the frequencies of the CAEs, is given by the condition

$$\int_0^a \xi(r')\mathrm{d}r' = \chi_{mj} \qquad \text{with} \quad j = 1, 2, 3 \ldots, \tag{5.42}$$

where, as before, χ_{mj} is the j-th root of derivative of Bessel function of order m.

We can rewrite the previous condition as

$$\int_0^a \left(\frac{\omega_{mj}^2}{v_A^2(r')} - \frac{n^2}{R^2} \right)^{1/2} \mathrm{d}r' = \chi_{mj} \qquad \text{with} \quad j = 1, 2, 3 \ldots, \tag{5.43}$$

with the following constrain on ω_{mj}^2 values

$$\omega_{mj}^2 \geq \frac{n^2}{R^2} v_A^2(r') \quad \forall r' \in [0, a]. \tag{5.44}$$

The values of the frequencies ω_{mj} can be derived then via numerical calculation, searching for ω_{mj} values for which the conditions (5.43) and (5.44) are satisfied.

A smooth plasma nonuniformity has an important effect for the propagation of the fast magnetoacoustic wave. This process, called Alfvén resonant absorbtion, has been proposed as a mean of providing supplementary heating of fusion plasmas, and as a possible explanation of the heating of the corona of the Sun and other stars.

When a magnetoacoustic wave propagates in a plasma of varying density and/or magnetic field, it can be absorbed under certain conditions, leading to a local heating of the plasma. The damping of the magnetoacoustic wave occurs because of the coupling with the continuous spectrum of the shear Alfvén wave. In particular it occurs when, in a specific location of the plasma, the frequency of the compressional wave is equal to that of the Alfvén resonance condition (5.32).

The ideal MHD model confirms the existence of this process and can describe some of its characteristics, but it doesn't provide an explicit damping mechanism and so gives no indication of how the energy in the wave is finally dissipated. When more realistic models, including kinetic effects, are employed, it is shown that the energy of the compressional mode may be absorbed via mode conversion into a short-wavelength mode, such as Kinetic Alfvén Wave (KAW) or Inertial Alfvén Wave (IAW), with subsequent collisionless and collisional damping of those waves.

Because of the difficulty in dealing analytically with this process, in this Thesis we will limit ourselfs into discussing the phenomenological features of this process when encountered in the analysed numerical simulations. For more information on this phenomenon see [Cramer, 2001; Vlad et al., 2008; Chen et al., 1974].

5.2.3 Global Alfvén Eigenmode

In case the Alfvén continuum, given by the Eq. (5.32), has a minimum in its spectrum (for instance due to a non-uniform density $\rho_0(r)$), a new type of mode appears just below the Alfvén continuum minimum, the so-called Global Alfvén Eigenmode (GAE). To analytically describe the Global Alfvén Eigenmode we present here the analysis made by Villard et al., 1997, which perfectly suits the plasma model (ideal MHD model) and configuration (cylindrical geometry) we are interested in this Thesis.

Let's start considering a toroidal axis-symmetric plasma that we assume to be in an ideal magneto-hydrodynamic (MHD) equilibrium configuration with nested flux surfaces labelled with the variable ψ. Let us define $\mathbf{e}_\parallel = \mathbf{B}_0/B_0$, $\mathbf{e}_n = \nabla\psi/|\nabla\psi|$, $\mathbf{e}_b = \mathbf{e}_\parallel \times \mathbf{e}_n$. The electromagnetic oscillations are described by the variational form

$$\int_{V_p} \left\{ \left|\nabla\times\mathbf{E} - \mathbf{J}E_b\right|^2 - 2\mathbf{J}\cdot\nabla_\parallel\mathbf{e}_n|E_b|^2 - \frac{\omega^2}{c^2}\mathbf{E}^*\cdot\begin{pmatrix}\epsilon_{nn} & \epsilon_{nb}\\ \epsilon_{bn} & \epsilon_{bb}\end{pmatrix}\cdot\mathbf{E}\right\}\mathrm{d}^3x + \\ + \int_{V_v}\left|\nabla\times\mathbf{E}\right|^2\mathrm{d}^3x = 0, \tag{5.45}$$

where $\mathbf{J} = (\mu_0\mathbf{j}_0\times\mathbf{e}_n)/B_0$, $\mathbf{j}_0$ is the equilibrium current, V_p and V_v are the plasma and vacuum volumes respectively, and

$$\epsilon_{nn} = \epsilon_{bb} = \frac{c^2}{v_A^2}\sum_i \frac{f_i}{1-(\omega/\omega_{ci})^2} \tag{5.46a}$$

$$\epsilon_{nb} = \epsilon_{bn}^* = i\frac{c^2}{v_A^2}\sum_i \frac{f_i(\omega/\omega_{ci})}{1-(\omega/\omega_{ci})^2} \tag{5.46b}$$

$$f_i = \frac{n_i m_i}{\sum_j n_j m_j}. \tag{5.46c}$$

The plasma is surrounded by a vacuum region V_v, enclosed by a perfectly conducting wall. This model includes finite ω/ω_{ci}, and, in the limit $\omega/\omega_{ci}\to 0$, is equivalent to linearized full ideal MHD in the approximation of $\gamma p \to 0$, where γ is the adiabaticity index and p is the plasma pressure. There are no limiting assumptions on the ratio of the poloidal to the toroidal components of the magnetic field. There are no geometrical expansions or simplifications.

In order to obtain approximate dispersion relations with analytical means we model the toroidal axis-symmetric plasma of major radius R by a cylindrical, circular, current carrying plasma column of periodicity $2\pi R$. In general both $B_{0\theta}$ and B_{0z} are functions of the radial coordinate r. The equations for the low frequency oscillations in the ideal MHD model limit ($\omega/\omega_{ci}\to 0$) can be written as

$$\frac{\mathrm{d}}{\mathrm{d}r}\left(\frac{AB_0^2}{A-k_b^2}\frac{1}{r}\frac{\mathrm{d}}{\mathrm{d}r}(r\xi_r)\right) + \\ + \left[AB_0^2 - \frac{r}{R^2}\frac{\mathrm{d}}{\mathrm{d}r}\left(\frac{B_{0z}^2}{q^2}\right) - \frac{4n^2B_{0z}^2}{R^4q^2(A-k_b^2)} + r\frac{\mathrm{d}}{\mathrm{d}r}\left(\frac{2nk_bB_0B_{0z}}{R^2qr(A-k_b^2)}\right)\right]\xi_r = 0, \tag{5.47}$$

with

$$q = \frac{rB_{0z}}{RB_{0\theta}} \tag{5.48}$$

the safety factor (defined in (2.10)), and

$$k_{\parallel} = \frac{B_{0z}}{B_0 R}\left(n + \frac{m}{q}\right) \tag{5.49}$$

$$k_b = \frac{B_{0z}}{B_0}\left(\frac{m}{r} - \frac{nr}{qR^2}\right) \tag{5.50}$$

$$A = \frac{\omega^2 - \omega_A^2}{v_A^2} \tag{5.51a}$$

$$\omega_A^2 = v_A^2 k_{\parallel}^2 \tag{5.51b}$$

$$v_A^2 = \frac{B_0^2}{\mu_0 \rho_0}, \tag{5.51c}$$

where n and m are as usual the toroidal and poloidal mode numbers, ξ_r is the plasma radial displacement and $\rho_0 = \rho_0(r)$ is the mass density. Equation (5.47) is equivalent to Eq. (5.45) in the limit of large aspect ratio and small ω/ω_{ci}. It is important to point out that no approximation on the smallness of $B_{0\theta}/B_{0z}$ has been made in the derivation of Eqs. (5.45) and (5.47).

Equation (5.47) describes two types of wave: a continuum, which we have already discussed, and a discrete set of eigenmodes called the GAEs. The existence of GAEs can be demonstrated by carrying out a Wentzel-Kramers-Brillouin (WKB) analysis of Eq. (5.47). We obtain

$$\omega^2 = \omega_A^2 - \frac{1}{\mu_0 \rho_0 k_r^2}\left[\left(\frac{2B_{0z}n}{qR^2}\right)^2 - k_b^2 \frac{r}{R^2}\frac{\mathrm{d}}{\mathrm{d}r}\left(\frac{B_{0z}^2}{q^2}\right)\right]. \tag{5.52}$$

For $n = 0$, we have then

$$k_r^2 = \frac{(-1/\mu_0\rho_0)}{\omega_A^2 - \omega^2}\frac{B_{0z}^2}{B_0^2}\frac{m^2}{r}\frac{1}{R^2}\frac{\mathrm{d}}{\mathrm{d}r}\left(\frac{B_{0z}^2}{q^2}\right). \tag{5.53}$$

For a plasma of finite size (radius a) the quantization condition

$$\int_0^a k_r \mathrm{d}r = j\pi \qquad \text{with} \quad j = 1, 2, 3\ldots \tag{5.54}$$

gives a discrete spectrum of eigenfrequencies of the Alfvén wave.

We can rewrite the Eq. (5.53) as

$$k_r^2 = -\frac{B_{0z}^2}{B_0^2}\frac{1}{r}\frac{1}{\triangle}\left(\frac{\mathrm{d}}{\mathrm{d}r}\ln(\omega_A^2) + \frac{\mathrm{d}}{\mathrm{d}r}\ln\rho_0\right), \tag{5.55}$$

where

$$\triangle \equiv \frac{\omega_A^2 - \omega^2}{\omega_A^2} \tag{5.56}$$

is the frequency separation between the GAEs and the continuum.

Putting together Eqs. (5.55) and (5.54) and after a few steps we obtain the following condition:

$$\int_0^a \left[-\frac{\omega_A^2(r)}{\omega_A^2(r)-\omega_j^2} \frac{B_{0z}^2}{B_0^2} \frac{1}{r} \left(\frac{\mathrm{d}}{\mathrm{d}r} \ln(\omega_A^2(r)) + \frac{\mathrm{d}}{\mathrm{d}r} \ln \rho_0(r) \right) \right]^{1/2} \mathrm{d}r = j\pi \qquad \text{with} \quad j = 1, 2, 3 \ldots \tag{5.57}$$

with the following constrain on ω_j^2 values

$$\omega_j^2 < \omega_A^2(r) \quad \forall r \in [0, a]. \tag{5.58}$$

The values of the frequencies ω_j can be derived then via numerical calculation, in analogous way as for the CAEs in nonuniform plasmas we discussed before. That is searching for the values of ω_j for which the conditions (5.57) and (5.58) are satisfied.

Keeping in mind the Eq. (5.49), for n=0 we can write the continuum frequency as

$$\omega_A^2(r) = \frac{B_{0z}^2(r) m^2}{\mu_0 \rho_0(r) q^2(r) R^2}. \tag{5.59}$$

Let's analyze the case we are interested in, that is when $\omega_A^2(r)$ has a local extremum at $r = r_c \neq 0$. This means that

$$\frac{\mathrm{d}}{\mathrm{d}r} \left(\frac{B_{0z}^2}{q^2 \rho_0} \right) \Bigg|_{r=r_c} = 0. \tag{5.60}$$

Defining $x \equiv r - r_c$ and looking for solutions of the type $\xi_r = x^\alpha$, the characteristic equation can be written as

$$\alpha^2 + \alpha - g = 0 \tag{5.61a}$$

$$g = -\frac{2}{r} \frac{B_{0z}^2}{B_0^2} \frac{\mathrm{d}(\ln \rho_0)/\mathrm{d}r}{\mathrm{d}^2(\ln \omega_A^2)/\mathrm{d}r^2}. \tag{5.61b}$$

If the discriminant of Eqs. (5.61) is negative then there exists an oscillatory solution in the vicinity of $r = r_c$ and the extremum of the continuum is an accumulation point of a discrete spectrum, whose frequencies ω_j are given by the condition (5.57). The sufficient condition for this is $g > 1/4$.

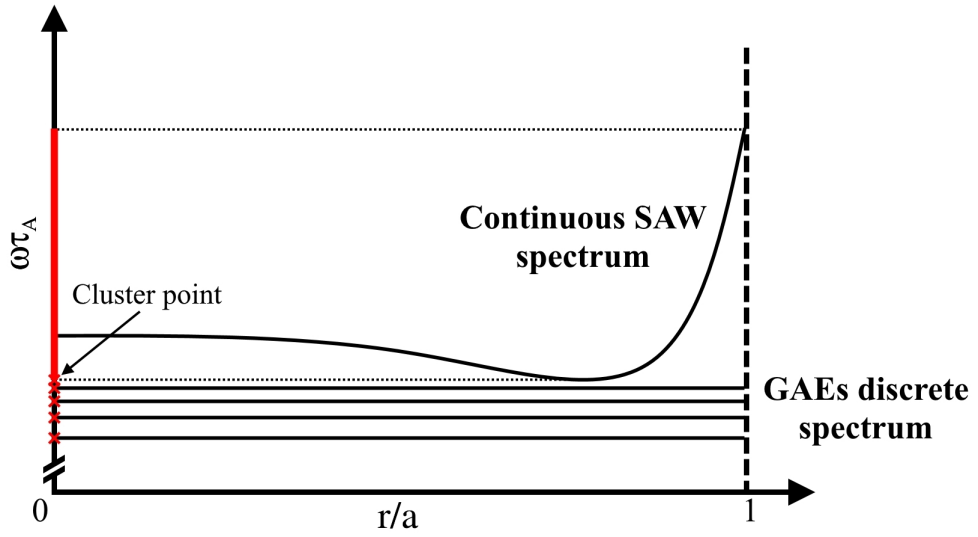

Figure 5.2: Schematic diagram of GAEs discrete spectrum and continuous SAW spectrum in the cylindrical plasma. The *red line* represents the continuous spectrum and *red crosses* show the discrete spectrum.

Standing wave structure

It has to be noted that because of the condition (6.6), in all SpeCyl simulations analyzed in the following chapters, all of the Alfvén modes previously computed have a standing wave structure as the perturbed velocity field **v** (for simplicity we omit the subscript 1) and magnetic field **B** are a superposition of two couples of mode numbers (m,n) with opposite signs that satisfies such condition. We can easily show this by considering the perturbed velocity field as a superposition of two such modes: for example one with $(m,n) = (0,1)$ Fourier component and the other with $(m,n) = (0,-1)$. Choosing $\mathbf{v} = \mathbf{v}_{01} + \mathbf{v}_{0-1}$ and using the expression (5.7) we have

$$\begin{aligned}\mathbf{v}(r) &= \mathbf{v}_{01}(0)\left[e^{i\left(\frac{1}{R}z-\omega_1 t\right)} + e^{i\left(\frac{1}{R}z+\omega_1 t\right)}\right] \\ &= \mathbf{v}_{01}(0)e^{i\frac{z}{R}}\left[e^{-i\omega_1 t} + e^{i\omega_1 t}\right] \\ &= \mathbf{v}_{01}(0)e^{i\frac{z}{R}}\cos(\omega_1 t),\end{aligned} \tag{5.62}$$

where ω_1 is the frequency of shear Alfvén or compressional mode with the toroidal and poloidal mode numbers $n = 1$ and $m = 0$. Thus we obtained a standing wave solution. An analogous consideration applies to **B**.

For GAE case we can see that Eq. (5.47) is invariant under the couples of mode numbers (m,n) that satisfies the condition (6.6). This means that for any given eigenfrequency the eigensolution is a superposition of two such modes and the GAE will also have a standing wave structure.

Chapter 6

The nonlinear 3D MHD code SpeCyl and Tokamak/RFP configurations modeling

The SpeCyl code is a non-linear visco-resistive 3D MHD code, that is used since the early 90ties in the theoretical physics group of Consorzio RFX as the main modeling tool for numerical simulations of RFP and tokamak plasmas. The SpeCyl code was used to provide nonlinear MHD simulations of Alfvén waves analyzed in this Thesis. In this Chapter we will first introduce its physical model and numerical formulation. Next, we will present a series of modeling cases of sawtooth relaxation events in a Tokamak configuration using the SpeCyl code. In particular we will present cases with Lundquist and viscous Lundquist numbers going from $S = 10^6$, $M = 10^3$ to $S = 10^8$, $M = 10^6$, and charactherize their MHD dynamics. These cases will be used in Chapter 8 to study the Alfvén waves excitation by magnetic reconnection events in Tokamak configuration. Afterwards, in a similar fashion, we will present the results of a modeling study, based on RFP simulations performed with the SpeCyl code, which shows a systematic repetition of quasi-single helicity states (QSH) in between the reconnection events, in agreement with experimental observations from the RFX-mod device. The numerical simulations studied in that work will be used in Chapter 9 to characterize the Alfvén waves in the most realistic RFP conditions achievable with the SpeCyl code.

6.1 Numerical simulations of fusion plasma: the SpeCyl code

The SpeCyl code [Cappello et al., 1996] is a numerical code that integrates numerically, in cylindrical geometry, the equations of a simplified version of the visco-resistive MHD model. This model derives from the equations of the visco-resistive MHD model under two fundamental hypotheses: the first is that the density of the plasma remains constant during the temporal evolution of the plasma, while the second consists in neglecting the role of pressure, a hypothesis justified by the value assumed in the RFP configuration by the beta parameter $\beta < 0.1$. As we will see in the next chapters, even with these approximations the code is able to provide a qualitative agreement with the frequency spectrum of Alfvén waves observed experimentally. The importance of the SpeCyl code in the work carried out in this Thesis is given by the fact that the frequency spectrum, used to study and characterize the Alfvén waves, is derived from the simulation data by tacking their Fast Fourier Transform and Continuous Wavelet Transform.

6.1.1 Physical model

SpeCyl solves the equations of the MHD model written in dimensionless form. The derivation of MHD equations using dimensionless quantities is carried out in Appendix C, and leads to the following set of equations:

$$\rho\left[\frac{\partial \mathbf{v}}{\partial t}+(\mathbf{v}\cdot\nabla)\mathbf{v}\right]=\mathbf{J}\times\mathbf{B}+\rho\nu\nabla^2\mathbf{v} \tag{6.1a}$$

$$\frac{\partial \mathbf{B}}{\partial t}=\nabla\times(\mathbf{v}\times\mathbf{B}-\eta\mathbf{J}) \tag{6.1b}$$

$$\nabla\times\mathbf{B}=\mathbf{J} \tag{6.1c}$$

$$\nabla\cdot\mathbf{B}=0. \tag{6.1d}$$

Here, the radial coordinate r is normalized to a, time and velocity are normalized to the Alfvén time τ_A and velocity v_A respectively, ρ is normalized to the initial value ρ_0 on axis and $\mathbf{B}$ is normalized to the initial value B_0 of the toroidal magnetic field on axis. Moreover, η is the inverse Lundquist number, $\eta=\tau_A/\tau_R\equiv S^{-1}$, and ν corresponds to the inverse viscous Lundquist number, $\nu=\tau_A/\tau_V\equiv M^{-1}$.

In the SpeCyl code, the resistivity and viscosity profiles are not calculated in a self-consistent manner but are given a priori and kept constant throughout the duration of the simulation. In particular, the functional form for these profiles is:

$$\nu(r)=\nu_0\left(1+ar^b\right) \tag{6.2a}$$

$$\eta(r)=\eta_0\left(1+cr^d\right) \tag{6.2b}$$

with the values of the parameters a, b, c, and d chosen to have profiles similar to those estimated experimentally.

The choice of the η_0 value allows to define the number of Lundquist S that characterizes the system, while the choice of the central value of the viscosity profile ν_0 allows to fix the value of another important dimensionless quantity called *magnetic Prandtl number*:

$$P\equiv\frac{\nu_0}{\eta_0}. \tag{6.3}$$

Another important parameter that controls the dynamics of the system, in particular in situations in which the term of inertia in the equations is negligible, is the *Hartmann number*:

$$H\equiv(\eta_0\nu_0)^{-\frac{1}{2}}. \tag{6.4}$$

An important feature of the code is the geometry in which the equations are solved. This is the cylindrical geometry, with periodic conditions on the cylinder bases. This choice allows to simulate the plasma of a toroidal device for magnetic confinement (such as a tokamak or an RFP) in the approximation of large aspect ratio R_0/a, where the toroidal effects are negligible. This approximation is particularly suitable for treatment of plasmas of the RFP type for which the effects due to the toroidal geometry are less important.

Up to recent years the plasma boundary conditions were chosen to be an ideal, i.e. perfectly conducting shell. The magnetic field was tangent to the shell, while the electric field was perpendicular

to it. Plasma flow was taken to be vanishing at $r = 1$. In [Bonfiglio et al., 2013] (a brief review is given in Section 6.3) the boundary conditions were generalized to also admit an imposed radial component of the magnetic field.

The parameters which must be set for each simulation are the applied axial electric field and the profiles of resistivity and viscosity. From these parameters, the initial magnetic field profiles are derived, which also define the plasma current, toroidal flux and pinch parameter. The model equations are hence solved by finite differencing in the radial coordinate r and a Fourier decomposition along the periodic θ and z coordinates. The discretization in time is performed using the so-called semi-implicit algorithm, which allows for a relatively large time step Δt and prevents numerical instabilities [Cappello et al., 1996].
The nonlinear verification benchmark between SpeCyl and another MHD code, called PIXIE3D, demonstrated an excellent agreement between the two codes in their common limit of application, showing that both code solve the nonlinear MHD equations with high accuracy and reliability [Bonfiglio et al., 2010].

6.1.2 Spectral formulation of the code

The equation system (6.1) is solved in cylindrical coordinates (r, θ, z) with $r \in [0:1]$, $\theta \in [0:2\pi]$, $z \in [0:2\pi R_0]$ where R_0 is given by the aspect ratio of the torus. Typically we use $R_0 = 4$ to have the same aspect ratio as the RFX-mod experimental device.

The spatial discretization of the physical quantities is carried out in a radial direction through the finite difference method on a mesh formed by a number N_r of points, while the periodicity conditions in the directions θ and z allow a spectral decomposition formed by N_θ harmonics in the poloidal direction and by N_z harmonics in axial direction.

It follows that the generic quantity $f(r, \theta, z, t)$ can be written in the following form:

$$f(r,\theta,z,t) = \sum_{m=-N_\theta}^{N_\theta} \sum_{n=-N_z}^{N_z} f_{m,n}(r,t) \exp\left[i \left(m\theta + \frac{n}{R_0} z \right) \right], \tag{6.5}$$

in which the Fourier components $f_{m,n}(r,t)$ are constrained by the condition on the reality of the quantity $f(r,\theta,z,t)$, which can be written as:

$$f_{-m,-n} = f^*_{m,n}. \tag{6.6}$$

Using the Fourier decomposition (6.5) to rewrite equations (6.1) provides the following system of equations:

$$\rho \frac{\mathrm{d}\mathbf{v}_{m,n}}{\mathrm{d}t} + \rho \left[(\mathbf{v}\cdot\nabla)\,\mathbf{v} \right]_{m,n} = \left[\mathbf{J}\times\mathbf{B} \right]_{m,n} + \rho \left[\nu \nabla^2 \mathbf{v} \right]_{m,n} \tag{6.7a}$$

$$\frac{\partial \mathbf{B}_{m,n}}{\partial t} = \left[\nabla \times (\mathbf{v}\times\mathbf{B}) \right]_{m,n} - \left[\nabla (\eta \mathbf{J}) \right]_{m,n} \tag{6.7b}$$

$$\left[\nabla \times \mathbf{B} \right]_{m,n} = \mathbf{J}_{m,n} \tag{6.7c}$$

$$\left[\nabla \cdot \mathbf{B} \right]_{m,n} = 0 \tag{6.7d}$$

where $[\quad]_{m,n}$ denotes the Fourier component (m,n) of the term in brackets. Notice that, in SpeCyl, the desnity ρ is function of the radial coordinate r only (it does not change with time). Nonlinear terms such

as $[\mathbf{J}\times\mathbf{B}]_{m,n}$ are computed through convolution sums like:

$$a_{m,n} = \sum_{p,q} J_{p,q} B^*_{p-m,q-n}. \tag{6.8}$$

The advantage of the spectral formulation consists in being able to select the Fourier modes to be included in the calculation, based on their importance in the dynamics of the system. This allows a quite significant reduction in the calculation time compared to other numerical approaches. In the practical use of the code, one can choose a single mode (and possibly its helical harmonics) that allows to make 2D simulations with a given helical symmetry, or a range of modes with different helicity, which allows to do "fully-3D" simulations.

6.2 Sawtooth relaxation events in Tokamak modeling

In this section we will present a series of modeling cases of sawthooth relaxation events in a Tokamak configuration using the SpeCyl code. Since sawtooth relaxation events are usually accompanied by an (m,-n)=(1,1) kink displacement [White, 2013; Wesson, 2004; Hastie et al., 1987], much of the work will center around the MHD dynamics of the 1/1 internal kink mode (with its harmonics). The 1/1 mode and its harmonics will evolve non-linearly in time in a 2D/3D Fourier spectrum depending on whether we consider helically-symmetric 2D or fully 3D tokamak configurations with multiple helicities. These cases will be used in Chapter 8 to study the Alfvén waves excitation by magnetic reconnection events in Tokamak configuration. The progressive choice of parameters and configurations for different cases analized in the following were influenced by the need of accomplishing this goal.

The following setup was used for the Tokamak simulations. We used ideal boundary conditions, aspect ratio $R/a = 4$ and a radial resolution of 256 points. The dissipation parameters were spatially uniform with ranging values $S \in [10^6 - 10^8]$ and $M \in [10^3 - 10^6]$. The simulations time step is $10^{-3}/10^{-4}\tau_A$, and fields were saved every $0.1\tau_A$. Both helically-symmetric and fully 3D simulations start from an axisymmetric unstable Ohmic equilibrium with pinch parameter Θ (defined in Equation 2.12). This configuration is a numerical solution of the 1D zero-β paramagnetic pinch equilibrium equations, discussed for instance in [Bonfiglio et al., 2010]. In Figure 6.1 are displayed this equilibrium main features. The safety factor q, plotted in the fourth panel, is computed from Equation 2.10 using the time-evolving axisymmetric part of the magnetic fields components. A uniform induction electric field $\mathbf{E} = E_0\widehat{\mathbf{z}}$ is imposed to sustain the plasma current. Moreover, an initial radial magnetic field perturbation of variable amplitude $\ll 1$ starts the MHD dynamics, typically driven by modes of resistive-kink/tearing nature. In the begining we will consider perfectly up-down symmetric initial perturbations, while for simulations with lower resitivity η, i.e. large S, we will use asymmetric perturbations, as high-S dynamics changes depending on whether the simulation is up-down symmetric or not. In the following the temporal behaviour of the magnetic E_m and kinetic E_k energy will be discussed: they are defined as $E_m = 1/2\int_{vol} \mathrm{d}V\ \mathbf{B^2}$ and $E_k = 1/2\int_{vol} \mathrm{d}V\ \rho\mathbf{v^2}$.

6.2.1 Helically-symmetric Tokamak configurations

In this section we will analyse non-linear MHD simulations in helically-symmetric tokamak configuration. That is 2D simulations for which the magnetic field varies only along two coordinates, the radial

and a helical one. In particular we will consider the (m,-n)=(1,1) internal kink mode dynamics with up to 32 of its harmonics (modes with same geometric helicity $h = 1$ defined in Equation 2.8). The reason for employing helical simulations in cylindrical geometry is that, since there is no toroidal coupling, modes with different helicity do not couple except by non-linear three-wave coupling. Thus, if only the 1/1 mode is initially perturbed, this mode and its harmonics will be the only modes present in the simulation (even if a more complete spectrum of modes with multiple helicities is enabled).

6.2.1.1 Standard simulations without plasmoids

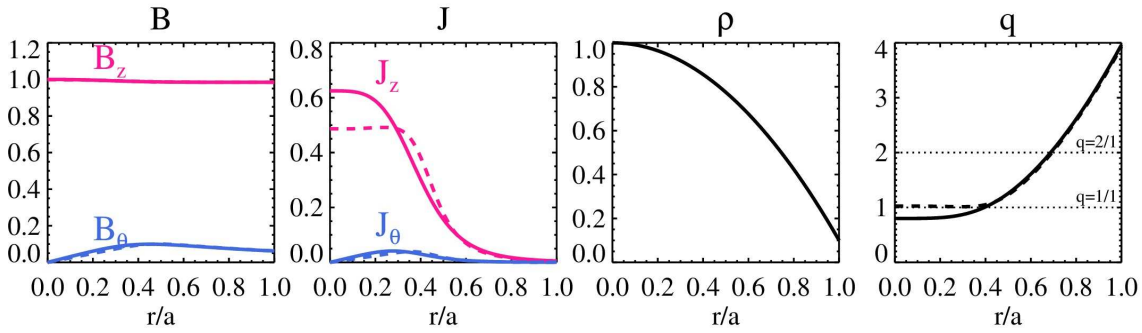

Figure 6.1: Equilibrium profiles for the tokamak configuration. From left to right: tokamak equilibrium radial profiles, the corresponding current density profiles, bell shaped density profile and q value profile. Magnetic field is normalized to its on-axis initial value. Solid lines refer to the initial 1D equilibrium solution. Dotted lines represent the same quantities after ($t = 11000\tau_A$ in Fig.(6.3)) the relaxation event following a slight perturbation of the initial equilibrium, resulting in the beginning of the 3D MHD dynamics.

We start by describing a simulation in tokamak configuration and bell-shaped density profile characterised by typical sawthooth relaxation events. Here we are considering a Fourier spectrum with 4 harmonics of (m,-n)=(1,1). This dynamics is shown in Figure 6.2 where temporal traces of the on-axis safety factor q_0 (for different values of viscosity ν) display characteristic cyclic instability whose time traces resemble the shape of sawteeth. Unlike in the basic physical picture of the sawtooth cycles described in Section 4.1.5, in SpeCyl the resistivity does not depend on the temperature, nor we have a temperature profile. In our simulations this dynamics is reproduces by the fast growth phase of q_0, given by the MHD dynamics of 1/1 mode, followed by a slow decrease phase, given by the use of fixed in time resistivity profile consistent with a 1D equilibrium with $q_0 < 1$. This numerical dynamics can also reproduce the flattening of the current density and the safety factor profiles after the relaxation event, displayed with dashed curves in Figure 6.1, which is tipically observed in tokamak sawtooth oscilations as described in Section 4.1.5. On the other hand, with this approach it is not possible to obtain a self-consistent and possibly realistic dynamics in particular regarding the time scales of both the growth and relaxation phases. But this is not a critical issue for this Thesis, because we are not interested in the sawtooth dynamics itself, but on its effect on the triggering of Alfvénic modes.

Four time traces corresponding to a scan in viscosity ν (M^{-1}) of sawtooth period τ_{st} and its intensity (i.e. degree of variation of q_0) are shown in Figure 6.2. By varying the viscosity we go from a small

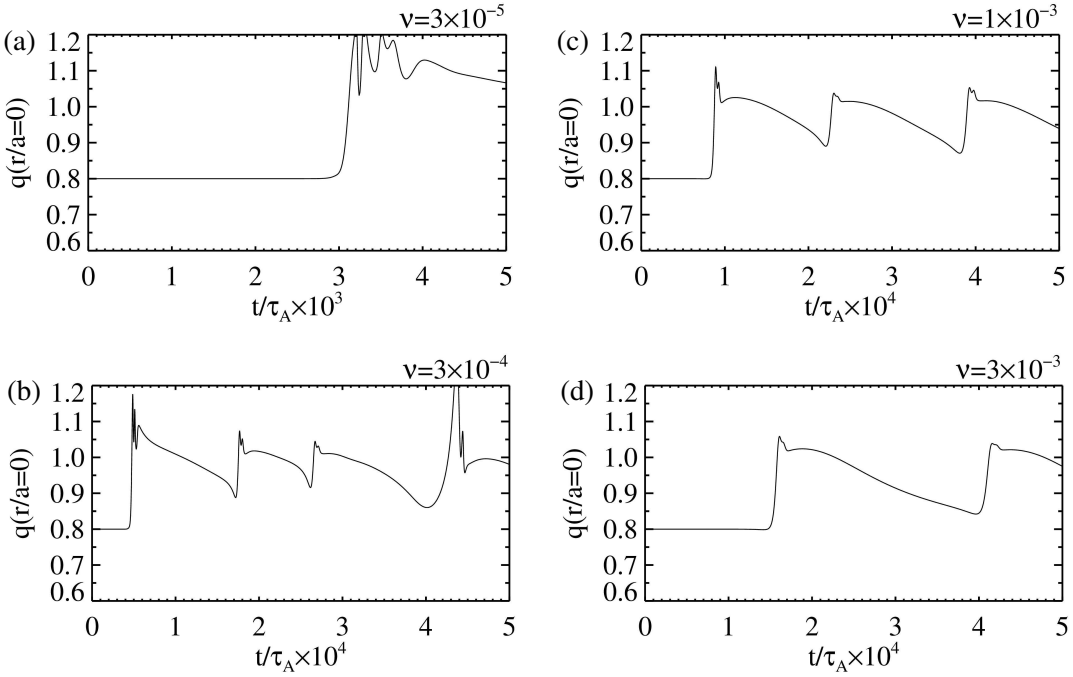

Figure 6.2: Temporal evolution of q value profiles in axis for different viscosities (same Lundquist $S = 10^6$), from lowest (a) to highest (d), charactherised by quasi periodic sawtooth relaxation events.

viscosity regime where after the first crash the dynamics is not very regular and there are no subsequent crashes (panel a), to a more regular sawtooth dynamics at intermediate viscosity (panels b,c,d), up to a dynamics (which is reported for instance in [Bonfiglio et al., 2010]) that ends up with a stationary helical state at large viscosity. The sawtooth dynamics most suitable to our needs was given by the simulation with $M = \nu^{-1} = 1 \times 10^3$ (Fig. 6.2c). This case was chosen both to keep sawtooth periods shorter (easier to simulate) and more importantly to have lower viscosity that dampens less the Alfvén oscillations. So in the following we used this parameter of viscosity to obtain a tokamak simulation characterised by a well-defined dynamics of sawtooth cycles accompanied by magnetic reconnection events. This sawtooth dynamic is depicted in Figure 6.3 which shows via time traces of radial magnetic field component on axis, for every cycle, typical sawtooth dynamics, characterized by a ramp phase ($t = 0 - 8800\tau_A$) during which the resistive-kink/tearing modes amplitude grows exponentialy in time until they saturate and enter the non-linear phase of the evolution during which the harmonics of the 1/1 mode become comparable in amplitude, until the collapse phase ($t = 8800 - 9400\tau_A$), which flatens the current density and the q value profiles (displayed with dashed curves in Figure 6.1).

A signature of reconnection events is a spike in the intensity of the kinetic energy, as part of the magnetic energy contained in the plasma is converted into it. In the Figure 6.3 the temporal evolution of the absolute value of the total magnetic and kinetic energy is plotted: one observes that quasi-periodically the total magnetic energy suddenly decreases (like at $t \sim 9200, 24000, 40000\tau_A$), and part of it is converted into kinetic energy, the rest is transported outside by the Poynting vector and dissipated by viscosity and resistivity. After the reconnection event, the value of magnetic energy remains almost

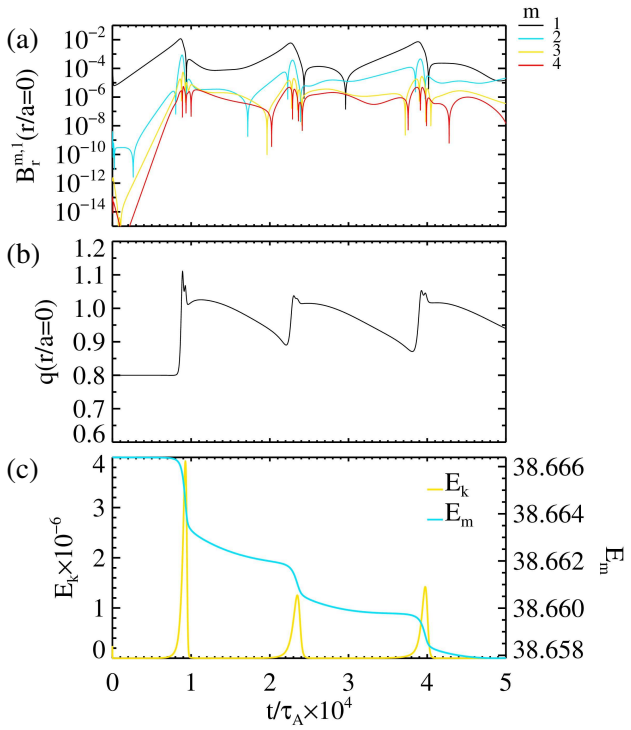

Figure 6.3: a) Temporal evolution of the radial magnetic field component in axis ($S = 10^6$, $M = 10^3$) associated with different harmonics of the internal kink mode (m,-n)=(1,1). b) The corresponding temporal evolution of q value profile in axis (same profile as in Fig.(6.2c)). c) The corresponding evolution of the total magnetic and kinetic energies. When the magnetic energy (blue curve) starts decreasing kinetic energy (yellow curve) starts to increase (note the different vertical axes). In the following of the work we will focus on the times around the magnetic reconnection events: here a dissipation of magnetic energy and a partial conversion into kinetic energy can be observed.

constant until the next crash and the sawthooth cycles repeat.

As mentioned above the sawtooth relaxation event is usually accompanied by an 1/1 kink displacement charaterized by a magnetic reconnection event. Reconnection in plasmas happens in situations in which magnetic field lines of opposite direction come close to each other. The schematic model of magnetic reconnection considers a 2D slab where magnetic field lines in opposite directions are present (see for example [Biskamp, 1993; White, 2013; Zohm, 2014]). In pinches this happens locally when the safety factor has a rational value. Consider the equilibrium field described in Figure 6.1, in particular the safety factor profile in the fourth panel, and a rational value $q_r = 1/1$. Because of the shear of the magnetic field, if we follow the field lines on both sides of the resonant surface with $q = q_r$ they will either lag behind or advance the field line on the resonant surface, creating a component of the magnetic field relative to the $q = q_r$ surface which changes sign across it. A transversal magnetic field, manifesting itself as a current-driven "tearing" instability results in the opening of a magnetic island. This sequence of events can be observed looking at Figure 6.4, where the contour levels of the helical flux function χ (defined in Eq. D.4 in Appendix D) are plotted. The initial radial magnetic field perturbation that

triggers the internal kink instability is up-down symmetric. The magnetic island associated with the 1/1 internal kink mode grows on the right-hand side of the plots, while a current sheet develops on the left-hand side around X-point (panel a). This creates a topology with two axes, one corresponding to the unperturbed axis-symmetric one and the other related to the O-point of the magnetic island (clearly visible in panel b). In the nonlinear evolution, the plasma core inside the $q = 1$ surface is driven into the resistive reconnection layer (panels c and d). The island replaces the core when the core has completely reconnected so that the final state has closed nested flux surfaces (panel e), and the center of the island is the new magnetic axis. In the final state, the safety factor is greater than unity everywhere inside $q = 1$ (see fourth panel in Figure 6.1). The sawthooth evolution process just described is consistent with Kadomtsev nonlinear complete reconnection model [Kadomtsev, 1975]. For higher S values, however, the dynamics is found to be qualitatively different from the well-known Kadomtsev's model, as we wil see in the following.

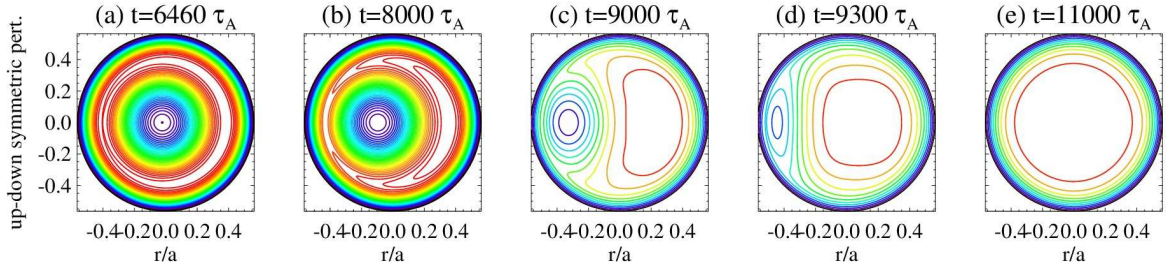

Figure 6.4: Time evolution of the internal kink mode in the cylindrical tokamak ($S = 10^6$, $M = 10^3$) around the first sawtooth relaxation event in Fig. (6.3). Magnetic reconnection event is observed at the current sheet on the $q = 1$ surface. Contour levels of the helical flux function with 1/1 helicity are shown for different time snapshots. Simulation with perfectly up–down symmetric initial perturbation.

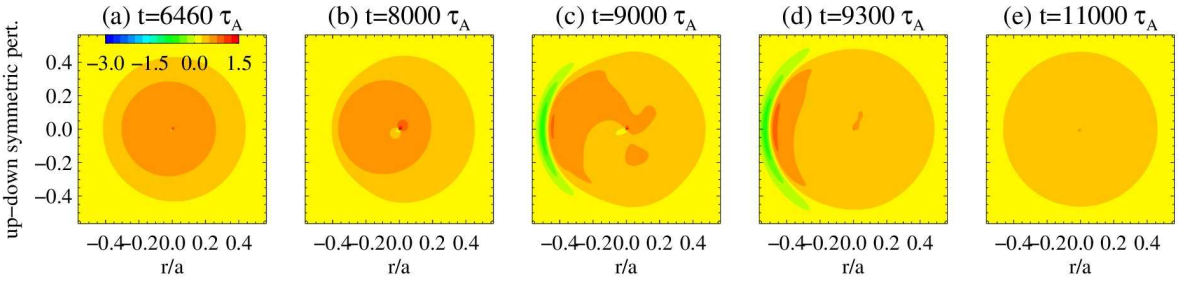

Figure 6.5: Time evolution of the axial component of the plasma current density ($S = 10^6$, $M = 10^3$), whose contour levels are shown for the same time snapshots of Fig. (6.4). Simulation with perfectly up-down symmetric initial perturbation.

In Figure 6.5 the contour plots of the axial component of the plasma current density are plotted, corresponding to the main part of the parallel current density, showing a correspondence between the structures observed in Figure 6.4. A thin current layer forms at the resonant surface on the X-point

side (panels c and d). Such current spike at the X-point is foreseen during the process of magnetic reconnection (see for example [White, 2013]). The strong negative current sheet at the X-point, and the positive current in the island O-point are both intuitively understandable as inductive response of the plasma to this shift of current profile. Namely, the negative current sheet at the X-point and the positive current flowing down the island O-point both partially cancel the leftward shift of the original current column, and oppose the island growth. Of course all these structures have helical 1/1 symmetry.

6.2.1.2 Lundquist treshold condition: plasmoids appearance

4 harmonics of 1/1 mode

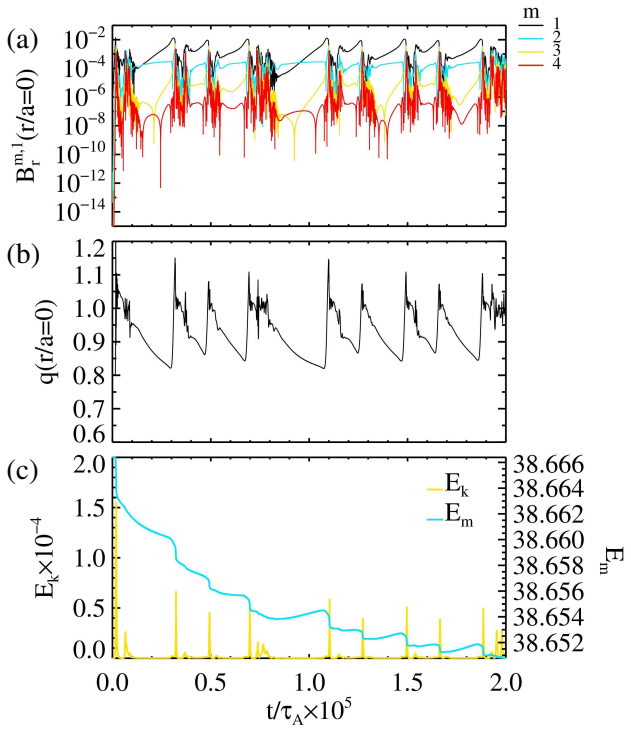

Figure 6.6: a) Temporal evolution of the radial magnetic field component in axis ($S = 10^6$, $M = 10^6$) associated with different harmonics of the internal kink mode (m,-n)=(1,1). b) The corresponding temporal evolution of q value profile in axis. c) The corresponding evolution of the total magnetic and kinetic energies.

As we will later discuss in Chapter 8, the previous configuration (with $S = 10^6$, $M = 10^3$) did not show any Alfvénic excitation during its MHD dynamics. So our first approach to produce a sawthooth dynamic able to excite Alfvén waves was to reduce the viscosity ν. The simulation in this section has same Fourier spectrum and plasma parameters as in the previous one except $\nu = 10^{-6}$, as same set up with $\nu = 10^{-4}$ and $\nu = 10^{-5}$ produced no results in terms of AEs excitation. In Figure 6.6 are plotted the time traces of radial magnetic field component in axis, together with the q value profile in time and

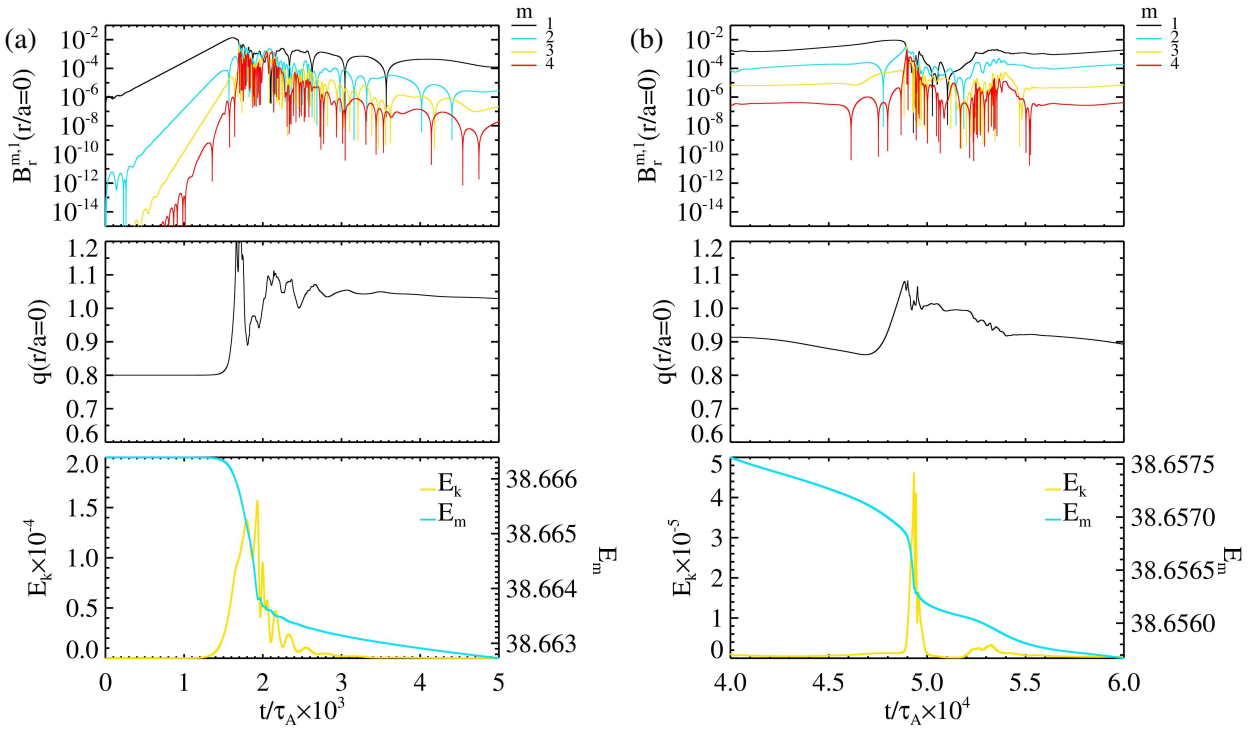

Figure 6.7: First (a) and third (b) sawtooth relaxation events in Fig. (6.6). **Top panels**: temporal evolution of the radial magnetic field component in axis ($S = 10^6$, $M = 10^6$) associated with different harmonics of the internal kink mode (m,-n)=(1,1). **Middle panels**: the corresponding temporal evolution of q value profile in axis. **Bottom panels**: the corresponding evolution of the total magnetic and kinetic energies.

the corresponding evolution of the total magnetic and kinetic energies. Again we observe the quasi periodic sawthooth crashes indicated by the oscilation of q_0 and corresponding spikes in the intensity of the kinetic energy. Sawthooth evolution now results less defined and irregular, with the crashes being more chaotic with respect to the previous simulation in Figure 6.3. Also now the kinetic energy spikes are more intense and more localized in time.

We focused our analysis on two sawthooth crashes: the first one, being the most intense with highest kinetic energy spike, and the third one, less intense and more spread out in time. In Figure 6.7 the two crashes in question are displayed with temporal evolution of the radial magnetic field for the considered Fourier modes (1/1, 2/2, 3/3, 4/4) with same helicity $h = 1$. The first crash in (a) is again clearly characterised by a ramp phase ($t = 0 - 1700\tau_A$) and a collapse phase($t = 1700 - 2200\tau_A$). Notice that, compared to the previous simulation in Figure 6.3, during the collapse phase the secondary harmonics more strongly nonlinearly interact with the previously dominant 1/1 kink/tearing mode, matching closely their amplitudes. The 1/1 mode becomes dominant again in between crashes until the next cycle. The sawthooth evolution now has much smaller time scales, with the first crash occuring much earlier in time ($\sim 1800t/\tau_A$ compared to previously analysed one at $\sim 9200t/\tau_A$), and the distinctive phases occuring in smaller time windows. The third cycle in (b) displays qualitatively similar features, although the phases

are less defined and less variation of the modes amplitudes is observed.

By looking at the helical flux function (for $h = 1$ helicity) in Figure 6.8 around the first sawtooth relaxation event (shown in Figure 6.7) we see a more pronounced elongation of the X-point but otherwise no change in overall dynamic of the reconnection process with respect to the previously considered case with higher viscosity displayed in Figure 6.4.

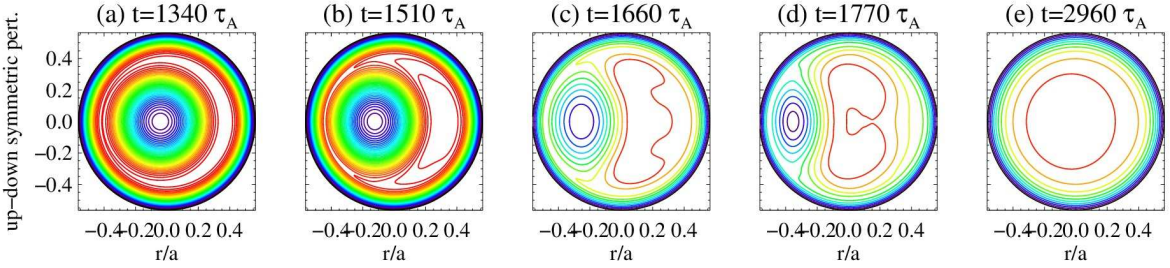

Figure 6.8: Time evolution of the internal kink mode in the cylindrical tokamak ($S = 10^6$, $M = 10^6$) around the first sawtooth relaxation event in Fig. (6.7). Magnetic reconnection event is observed at the current sheet on the $q = 1$ surface. Contour levels of the helical flux function with 1/1 helicity are shown for different time snapshots. Simulation with perfectly up–down symmetric initial perturbation.

32 harmonics of 1/1 mode

In order to check whether Fourier space resolution could influence Alfvén waves excitation following sawthooth relaxation event, for example due to the formation of smaller scale structures, a new simulation was performed with a wider spectrum of 32 harmonics with $h = 1$ helicity (instead of the previous 4). We focused on the first sawthooth relaxation event displayed in Figure 6.9. A similar dynamic is observed, characterised by the ramp and collapse phases, with the dominant mode 1/1 strongly interacting with secondary harmonics during the collapse phase. A quantitative difference in the dynamic is the crash time $\sim 2800t/\tau_A$ compared to previously analysed one at $\sim 1800t/\tau_A$ (with 4 harmonics in Figure 6.7). This shift is caused by the use of a smaller amplitude of the initial perturbation (10^{-9} compared to 10^{-6} in the previous section), done to mitigate as much as possible the intensity of the AEs excited by the initial perturbation (analogously to the mechanism used in Chapter 7), while keeping it high enough for the crash to occur in a reasonable amount of time.

Looking at helical flux function with 32 modes displayed in Figure 6.10, the temporal dynamic remains generally the same compared to 4 modes simulation. While the magnetic reconnection process displayed here still follows the previously described process in Section 6.2, new structures can be spotted in panel (d) around $r/a = -0.45$. In particular, we see the development of secondary tearing instabilities at the reconnecting $q = 1$ surface on the internal $1/1$ kink mode. Such instabilities, and the related topological structures called plasmoids, have been the subject of several studies related to high current/low q tokamak configurations and they are considered as a possible explanation for fast magnetic reconnection in tokamaks. For plasmoids to develop at the $q = 1$ surface in nonlinear MHD simulations of tokamak plasmas, the aspect ratio of the current sheet (i.e., the ratio between its longitudinal and transverse extent) must exceed a certain threshold. Since the aspect ratio of the current sheet increases

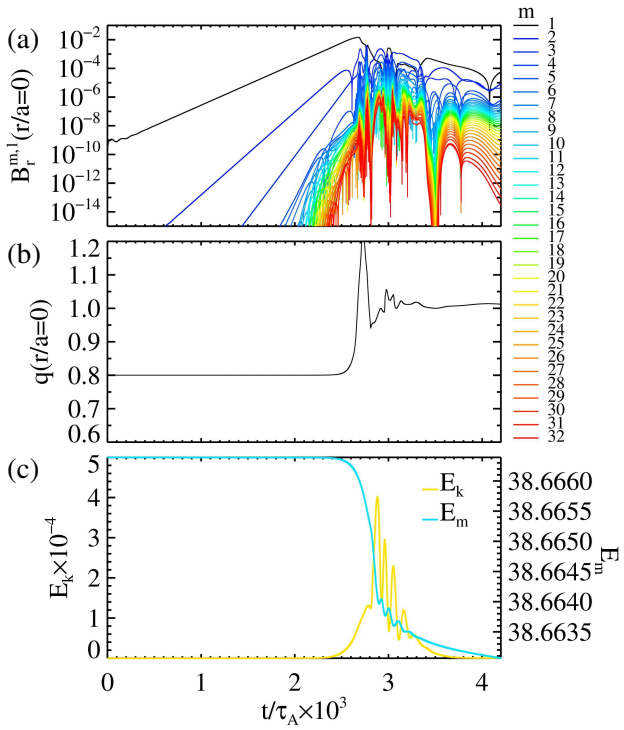

Figure 6.9: a) Temporal evolution of the radial magnetic field component in axis ($S = 10^6$, $M = 10^6$) associated with different harmonics of the internal kink mode (m,-n)=(1,1). b) The corresponding temporal evolution of q value profile in axis. c) The corresponding evolution of the total magnetic and kinetic energies.

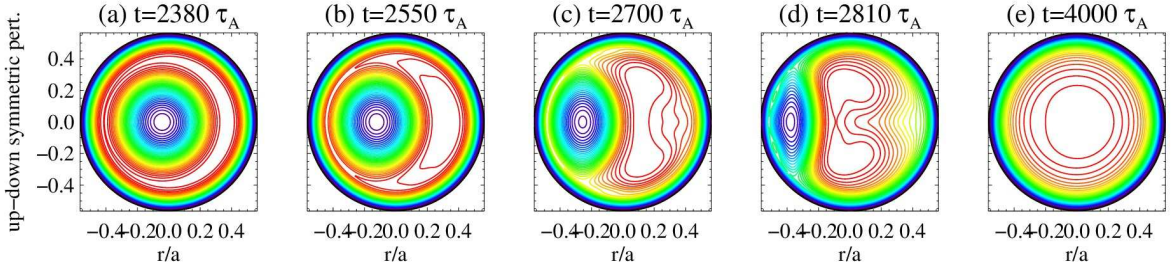

Figure 6.10: Time evolution of the internal kink mode in the cylindrical tokamak ($S = 10^6$, $M = 10^6$) around the sawtooth relaxation event in Fig.(6.9). Plasmoid formation is observed at the tearing unstable current sheet on the q = 1 surface. Contour levels of the helical flux function with 1/1 helicity are shown for same spacing of time snapshots as in Fig.(6.8) shifted by $t = 1040\tau_A$. Simulation with perfectly up–down symmetric initial perturbation.

with Lundquist number S, this translates into a threshold for the Lundquist number itself. For visco-resistive MHD calculations in cylindrical geometry, such a threshold was previously reported to be around

$S = 10^7$ [Yu et al., 2014; Ali et al., 2019]. In our simulation with $S = 10^6$ we encounter a borderline case. Indeed we observe plasmoid formation for lower S, but these structure do not alter the reconnection process in a meaningful way in this particular case. We will see in the following sections that indeed, in agreement with previously published papers, we obtain qualitatively similar dynamics and features for $S \geq 7$, with multiple plasmoid formation that coalesce into a single secondary island (dubbed "monster plasmoid" in [Ali et al., 2019]) that can significantly affect the primary island evolution. For this reason (to account for the full dynamics), in the following we will keep using 32 harmonics of 1/1 kink mode in the Tokamak modeling of sawthooth cycles. In addition, we will start using slightly asymmetric initial perturbation, as the formation of the "monster plasmoid" in the exact center of the X-point current sheet would prevent the complete reconnection of the 1/1 island, so due to the small asymmetry it will be slightly displaced allowing for a complete reconnection to occur.

6.2.1.3 High Lundquist case: plasmoids dynamics

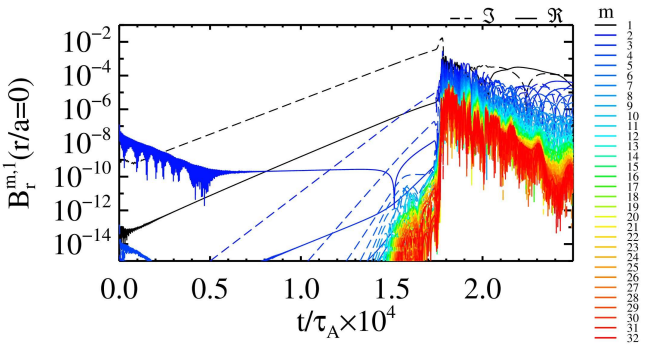

Figure 6.11: Pilot simulation. Temporal evolution of the radial magnetic field component in axis ($S = 10^8$, $M = 10^6$) associated with different harmonics in the Fourier spectrum. Up-down asymmetric initial perturbation. Dashed lines indicate immaginary part of $B_r^{m,1}$ for a fixed mode $(m, 1)$. Solid lines indicate the real part.

As anticipated the next step was to consider a tokamak simulation with same configuration and 32 harmonics as in previous case but a higher Lundquist $S = 10^8$. Additionally, now the initial perturbation that kick-starts the sawtooth dynamics will have a slight up-down asymmetry to allow the full reconnection to occur, as we will describe shortly. This was achieved by perturbing both real and immaginary parts of the magnetic field radial component for different helicities with different amplitudes, while the 1/1 mode initial amplitude was 10^{-9} as in the previous case, as shown in Figure 6.11. Compared to Figure 6.9 a similar dynamic is observed, characterised by the linear ramp phase and non linear collapse phase, where the dominant mode 1/1 strongly interact with secondary harmonics. One noticeable change is in the crash time, which takes much longer to occur for higher Lundquist ($\sim 18000 t/\tau_A$ compared to $\sim 2800 t/\tau_A$ in Figure 6.9). As such, to optimise and better handle these high-S simulations, we first produce a "pilot" simulation with much higher time step and then restart it with usual $10^{-4}\,\tau_A$ time step during its linear growth phase. The restarted simulation, showed in Figure 6.12, presents same linear growth and crash time of the pilot simulation, slightly diverging only in its non-linear phase. The kinetic

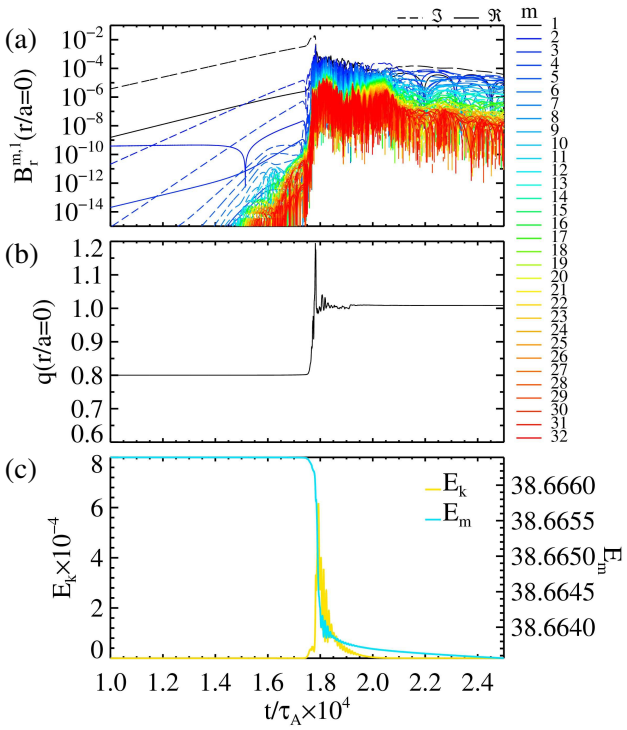

Figure 6.12: a) Temporal evolution of the radial magnetic field component in axis ($S = 10^8$, $M = 10^6$) associated with different harmonics in the Fourier spectrum, starting from $t = 1.0 \cdot 10^4 \tau_A$ in Fig.(6.11). b) The corresponding temporal evolution of q value profile in axis. c) The corresponding evolution of the total magnetic and kinetic energies.

energy spike is higher than before, while the decrease in magnetic one stayed the same.

The major effect of lowering the resistivity can be seen from analysing the temporal evolution of the helical flux function in Figure 6.13. The magnetic island associated with the 1/1 internal kink mode grows on the right-hand side of the plots, while a quite elongated current sheet develops on the left-hand side (panel a), as in the previous case. Now this elongated current sheet, being tearing unstable, breaks up to form a number of secondary islands (plasmoids in panel b). The number of plasmoids produced depends on the width of the current sheet and therefore, again, on the Lundquist number. Later in time, the plasmoids coalesce into a single larger secondary island ("monster plasmoid" in panels c and d), according to a typical competition between granulation and coalescence occurring in a current sheet, as shown in Ref. [Malara et al., 1992]. Due to the small asymmetry in the initial perturbation, this secondary island will be displaced toward the top, and its angular displacement will increase quite rapidly (panel d) until the island is absorbed into the main 1/1 island. During this displacement we can also observe formation of more plasmoids at the reconnecting $q = 1$ surface, between the current sheet and the original core region. As a result, complete magnetic reconnection occurs leading to a final state with nested circular magnetic surfaces and $q > 1$ everywhere in the plasma (panel e). As we will see in Chapter 8 this will be the first configuration with a clear and strong excitation of Alfvén waves. In Figure 6.14 the contour plot of the axial component of the plasma current density is plotted, showing a

correspondence between the structures observed in Figure 6.13: a thin current layer forms at the resonant surface on the X-point side, it becomes tearing unstable and breaks up into several current spikes (in a similar way to what is shown in Fig. 2 of Ref. [Yu et al., 2014]).

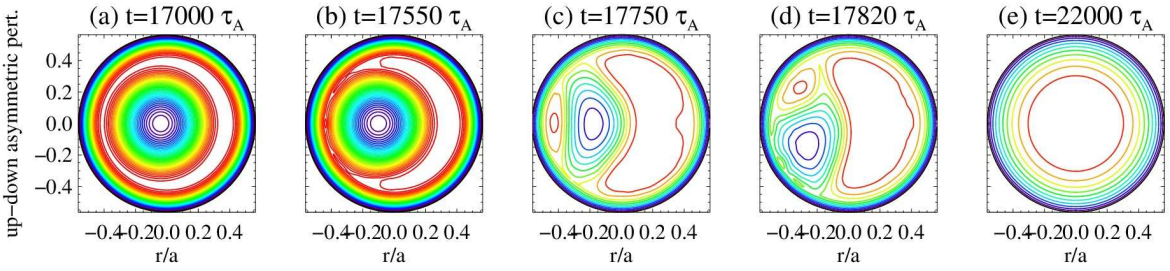

Figure 6.13: Time evolution of the internal kink mode in the cylindrical tokamak ($S = 10^8$, $M = 10^6$) around the sawtooth relaxation event in Fig.(6.12). Plasmoid formation is observed at the tearing unstable current sheet on the q = 1 surface. Contour levels of the helical flux function with 1/1 helicity are shown for different time snapshots. Simulation with up–down asymmetric initial perturbation.

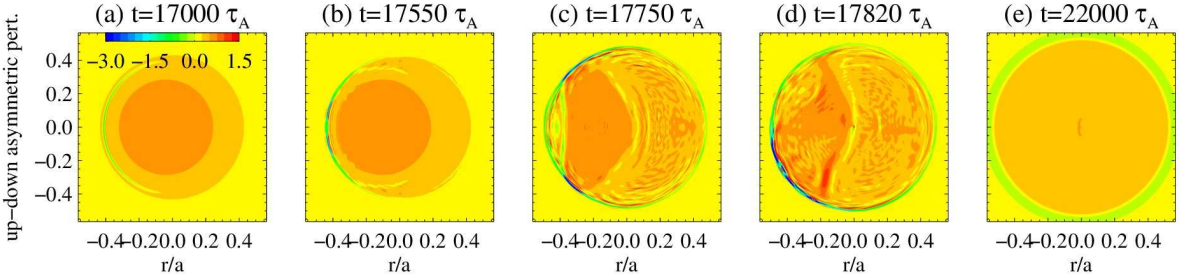

Figure 6.14: Time evolution of the axial component of the plasma current density ($S = 10^8$, $M = 10^6$), whose contour levels are shown for the same time snapshots of Fig. (6.13). Simulation with up-down asymmetric initial perturbation.

As already mentioned, plasmoids are mainly investigated in the literature as possible candidates to explain fast magnetic reconnection in high-temperature fusion plasmas. By exploiting a scan in the spectral resolution, we can observe in Figure 6.15 how plasmoid formation (facilitated at higher resolution) speeds up the process, and complete reconnection of the core $q < 1$ region occurs earlier (see Fig.6 in Ref.[Veranda et al., 2020], where the same analysis is performed). In Figure 6.15 three MHD simulations are reported, all with the same parameters except for the number of helical harmonics in the Fourier spectrum: 32 (corresponding to the same simulation described in the previous figures), 16 and 8. In the simulation with 32 harmonics, on top of the slowly growing 1/1 mode, fast growing high-m modes corresponding to secondary tearing instabilities of the current layer are observed. Soon, such modes reach the amplitude of the 1/1 mode and trigger a fast reconnection event. This fast reconnection is also observed in the simulation with 16 modes, although in a milder fashion. Indeed, the peak MHD activity corresponding to complete reconnection of the core region occurs later in time. On the other hand, in the

case with only 8 harmonics, high-m modes do not significantly contribute to the reconnection process. This is summarized in the last panel of the figure, showing the amplitude of the 1/1 radial perturbation on axis. This shows that high-m modes, corresponding to secondary tearing instabilities of the current layer causing plasmoid formation, do play a significant role for fast magnetic reconnection of the $q < 1$ core region in the visco-resistive MHD simulation reported here.

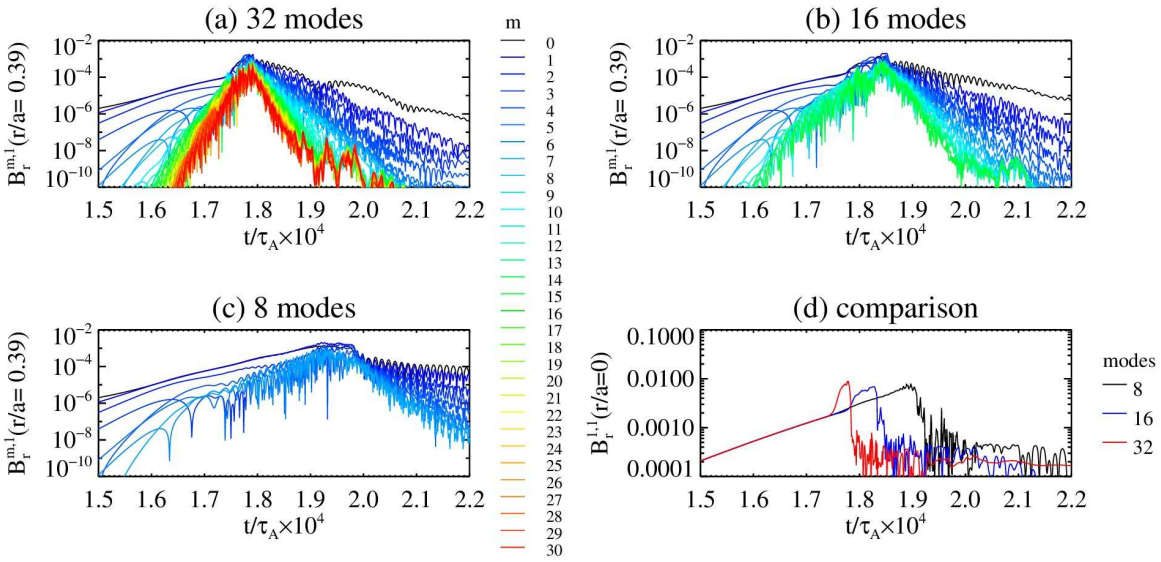

Figure 6.15: Comparison of simulations ($S = 10^8$, $M = 10^6$) with different number of harmonics in the Fourier spectrum. First three panels: temporal evolution of the radial magnetic field component at the $q = 1$ resonant surface ($r/a = 0.395$) associated with different harmonics for the simulations with 32 (a), 16 (b) and 8 (c) modes. In panel (d), the 1/1 radial magnetic field at $r/a = 0$ is compared for the three different simulations.

6.2.2 Fully 3D Tokamak configurations

In this section we will analyse non-linear MHD simulations in fully 3D Tokamak configuration. We will consider the 1/1 internal kink mode with 32 of its harmonics and visco-resistive parameters $S = 10^8$ and $M = 10^6$, as previously established. We are interested in studying the excitation of AEs with 1/0 periodicity, as esperimentaly the n=0 is found to be the dominant toroidal mode in Ohmic tokamak discharges. In order to excite the 1/0 mode spectrum by self-consistent velocity perturbation, triggered by the 1/1 internal kink mode, a three-wave coupling approach was adopted. The coupling of the 1/1 mode with other helicities would be naturally present in toroidal geometry, but in the cylindrical geometry approximation of our present simulations, the presence of at least an additional mode (like the 2/1 or the 3/2) was necessary to provide the coupling with the 1/0 mode. To this end a 3D configuration with a more complete spectrum of modes with multiple helicities was considered, including the previously analysed spectrum of 32 harmonics of 1/1 mode, the coupling mode 2/1 with its first harmonic 4/2 (or the 3/2 mode with its first harmonic 6/4) and a set of adjacent modes. The spectrum included in 3D

simulations with 2/1 coupling mode is shown in Fig. 6.20.

6.2.2.1 Coupling approach with marginally stable 2/1 mod

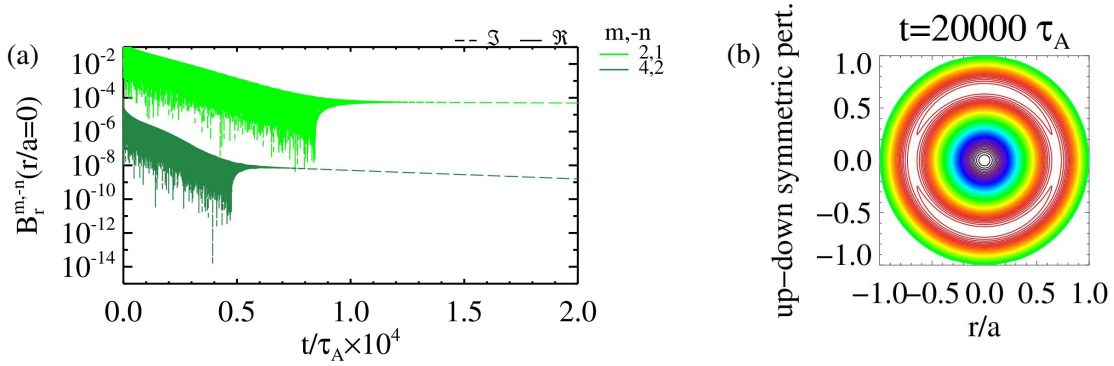

Figure 6.16: a) Temporal evolution of the radial magnetic field component in axis for the marginally stable $(m,-n) = (2,1)$ and its secondary harmonic $(m,-n) = (4,2)$. b) Snapshot of the saturated tearing mode $(m,-n) = (2,1)$ in the cylindrical tokamak ($S = 10^8$, $M = 10^6$). Two magnetic islands are observed on the $q = 2$ surface. Contour levels of the helical flux function with 2/1 helicity are shown. Simulation with perfectly up–down symmetric initial perturbation.

In order to excite the 1/0 mode spectrum by magnetic reconnection events, triggered by the 1/1 internal kink mode, a three-wave coupling approach with 2/1 mode was adopted. In the specific tokamak equilibrium considered by us displayed in Figure 6.1, the 2/1 mode turns out to be marginaly stable during the nonlinear evolution of sawtooth cycles, as shown in Figure 6.16. As a result, after its initial excitation, its amplitude stays almost constant in time, providing a way for the nonlinear coupling between 1/1 and 1/0 modes. In particular, the fast oscillations of the 2/1 mode related to alfvénic fluctuations take some time to stabilise, and to achieve a stable coupling during the first sawtooth crash (we focused on analysing so far), we resumed the usual "pilot" simulation from its linear growth phase by adding the already saturated (i.e. no fast oscillations) marginally stable 2/1 mode (and its first harmonic 4/2 mode). The resulting simulation is displayed in Figure 6.17, where the different harmonics with same poloidal number m are color coded with a greyscale (1/1 mode is indicated by the black dashed curve with highest amplitude right before the collapse), while the 1/0 and 2/1 modes are highlighted with violet and green colors respectively. In simpler terms, this is an analogous to the helically symmetric simulation discussed in Section 6.2.1.3, now with a wider spectrum that allows the three-wave coupling in a fully 3D configuration. By comparing the new 3D simulation with its analogous 2D one, Figure 6.17 and Figure 6.12 respectively, besides a more dense plot (due to a wider spectrum range), qualitatively the dynamics remain the same: the linear growth remains the same for the modes present in both simulations, with same time crash ($\sim 18000 t/\tau_A$) and similar variatrions in kinetic and magnetic energies. The same is true for the helical flux function evolution of the internal 1/1 island during the magnetic reconnection (not shown here): the dynamics remains qualitatively very similar, with the elongated X-point of the current sheet breaking into a chain of secondary islands that consequently coalesce into a single larger island, which is then completely absorbed into the main 1/1 island, as described in Section 6.2.1.3. This

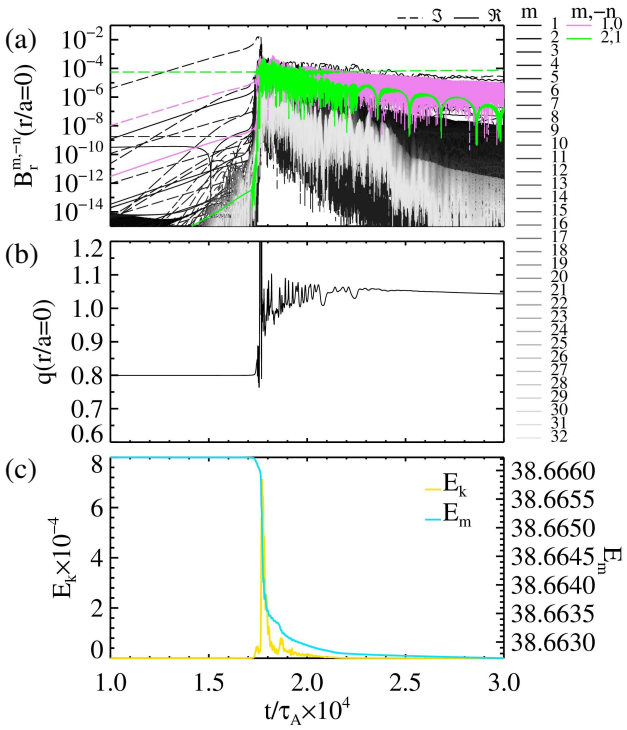

Figure 6.17: a) Temporal evolution of the radial magnetic field component in axis ($S = 10^8$, $M = 10^6$) associated with different harmonics in the Fourier spectrum, starting from $t = 1.0 \cdot 10^4 \tau_A$ in the linear growth phase of the corresponding pilot simulation. b) The corresponding temporal evolution of q value profile in axis. c) The corresponding evolution of the total magnetic and kinetic energies.

comparison shows that the inclusion of a wider spectrum with multiple helicities did not noticeably affect the overall sawtooth dynamics, while at the same time providing means to self-consistently excite the 1/0 mode.

In Figure 6.18 the evolution of the magnetic topology of the 2D helically symmetric simulation, discussed in Section 6.2.1.3, and the fully 3D simulation, analysed in this section, are showed. In particular four snapshots are displayed corresponding to the start of the simulation (a), during the magnetic reconnection event (b-c) and after it (d). The last three snapshots of the 2D simulation (I) correspond to the pannels (a), (c) and (e) of the helical flux function in Figure 6.13. At the start of the simulation (panel a) we can observe the nested magnetic surfaces in the whole plasma. The opening of the magnetic island 1/1 can be seen in panel (b) at $r/a = 0.39$ ($q = 1$ resonant surface), while the magnetic surfaces are still conserved. The magnetic topology during the sawtooth crash (panel c) breaks apart, with the region $q < 1$ stochastization of the magnetic field lines, while the original core region and the secondary island formed from the coalescence of the plasmoids (both visible in panel c around the 1/1 island) are reconnecting. Note also that the region around the 1/1 separatrix in panel (c) becomes stochastic, probably due to the 5/4 and 3/2 modes resonating near q=1 surface. After the complete magnetic reconnection, a final state with nested magnetic surfaces and $q > 1$ everywhere in the plasma (panel d) is established (the distorsion of the region close to the center is due to a small displacement

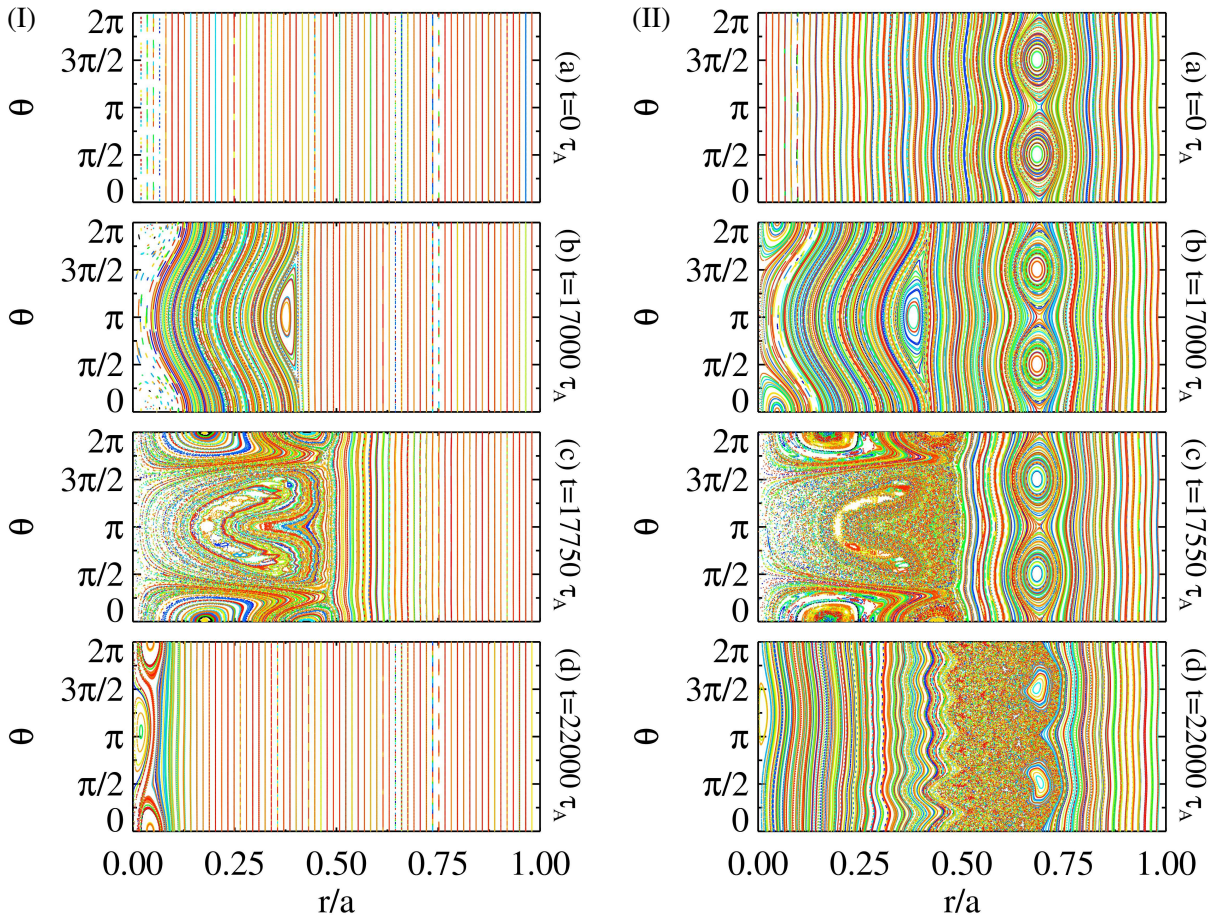

Figure 6.18: Poincaré plots in the z plane, for the simulation ($S = 10^8$, $M = 10^6$) with helically-symmetric configuration (I), and fully 3D configuration with marginaly stable $(m, -n) = (2, 1)$ mode (II). For each, four snapshots are displayed corresponding to the start of the simulation (a), during the magnetic reconnection event (b-c) and after it (d).

of the new magnetic axis). It can be proved mathematically that chaos cannot exist in 2D configuration (i.e. same helicity modes). The equivalent snapshots of the magnetic structures evolution for the fully 3D simulation are displayed in the right column (II). Most notably we see the marginaly stable 2/1 mode islands at $r/a = 0.69$ ($q = 2$ resonant surface). These islands do not seem to play a role in the reconnection dynamics, as we can see from panels (a), (b) and (c), but their effect can be seen in panel (d) where a chaotic region forms after the complete magnetic reconnection event. The relative dimension of the ergodic region depends on the interplay between the remaining MHD modes, in particular of the higher mode numbers as we will see in the following analysis. Furthermore with the chosen perturbation amplitude, the 2/1 island has a width of about 15% of the radius and thus quite large for a tokamak configuration. But as we will discuss in the following Section 6.2.2.1.2 the overall sawtooth dynamics

does not change qualitatively by decreasing the 2/1 island width.

6.2.2.1.1 Magnetic and kinetic energy cascades

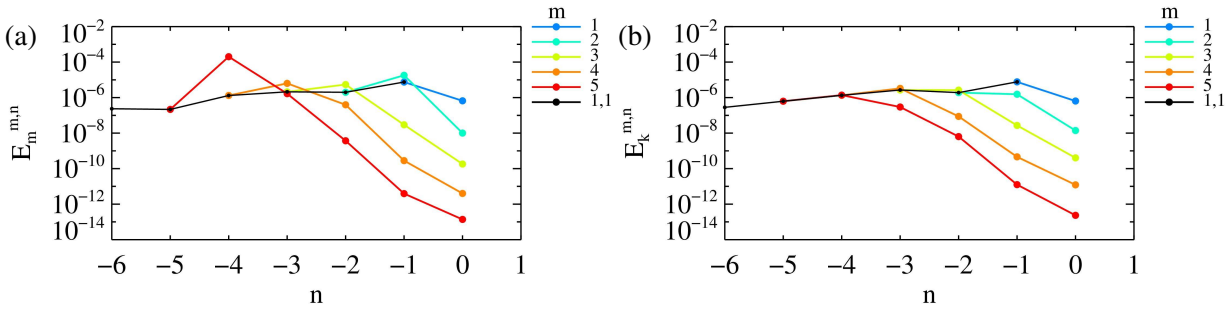

Figure 6.19: Magnetic (a) and kinetic (b) energy spectra for the Fourier modes considered in the simulation in Fig.(6.17) at $t = 1.9 \cdot 10^4 \tau_A$, color coded for different m modes and the harmonics of 1/1 (black line) up to 6/6.

We now investigate the energy cascades of the modes considered in the previous simulation, to determine if an adequate resolution was used. Figure 6.19 illustrates the magnetic and kinetic energy content for different (m,n) modes right after the magnetic reconnection event of the fully 3D simulation in Figure 6.17. Kinetic energy (panel b) behaves as expected, with the fluctuation dominated by the 1/1 mode, being the one that triggers the sawtooth crash. The energy spread over a large numbers of modes indicates an active exchange of energy among them, cascading from the dominant 1/1 mode. For the magnetic energy in panel (a) we notice that the modes with highest magnetic energy content are all above the harmonics of the 1/1 mode (indicated by the black solid line). This is also true for the kinetic energy, although to lesser extent. This is explained by the presence of the marginally stable 2/1 mode and its three-wave coupling with the resonant 1/1 mode exciting the 3/2 mode, which in turn will couple again and excite the 4/3 mode and so on. The 2/1 mode, being stable in time, is dominant after the magnetic reconnection until the 1/1 mode starts growing again, as can be seen from Figure 6.17. This means that the energy, after cascading from the resonant 1/1, will dissipate more slowly over time for modes coupled by the marginaly stable 2/1 mode, with respect to the harmonics of the 1/1 mode. Moreover, we observe an energy accumulation on the 5/4 mode, that is after the excitation by the reconnection event its magnetic energy dissipates much more slowly over time than any other mode. Notice that this is also the mode delimiting the chaotic region in Figure 6.18 (II)-(d), $m = 5$ mode at $r/a = 0.49$ ($q = 5/4$ resonant surface). In Figure 6.20 are displayed the countours of the E_m and the E_k for the same instant of time as in the Figure 6.19 to highlight the energy spread, over the whole simulation mode spectrum, right after the magnetic reconnetion event. To determine whether this accumulation is a result of the MHD dynamics or a lack of resolution, below we analysed the same configuration with a much wider spectrum.

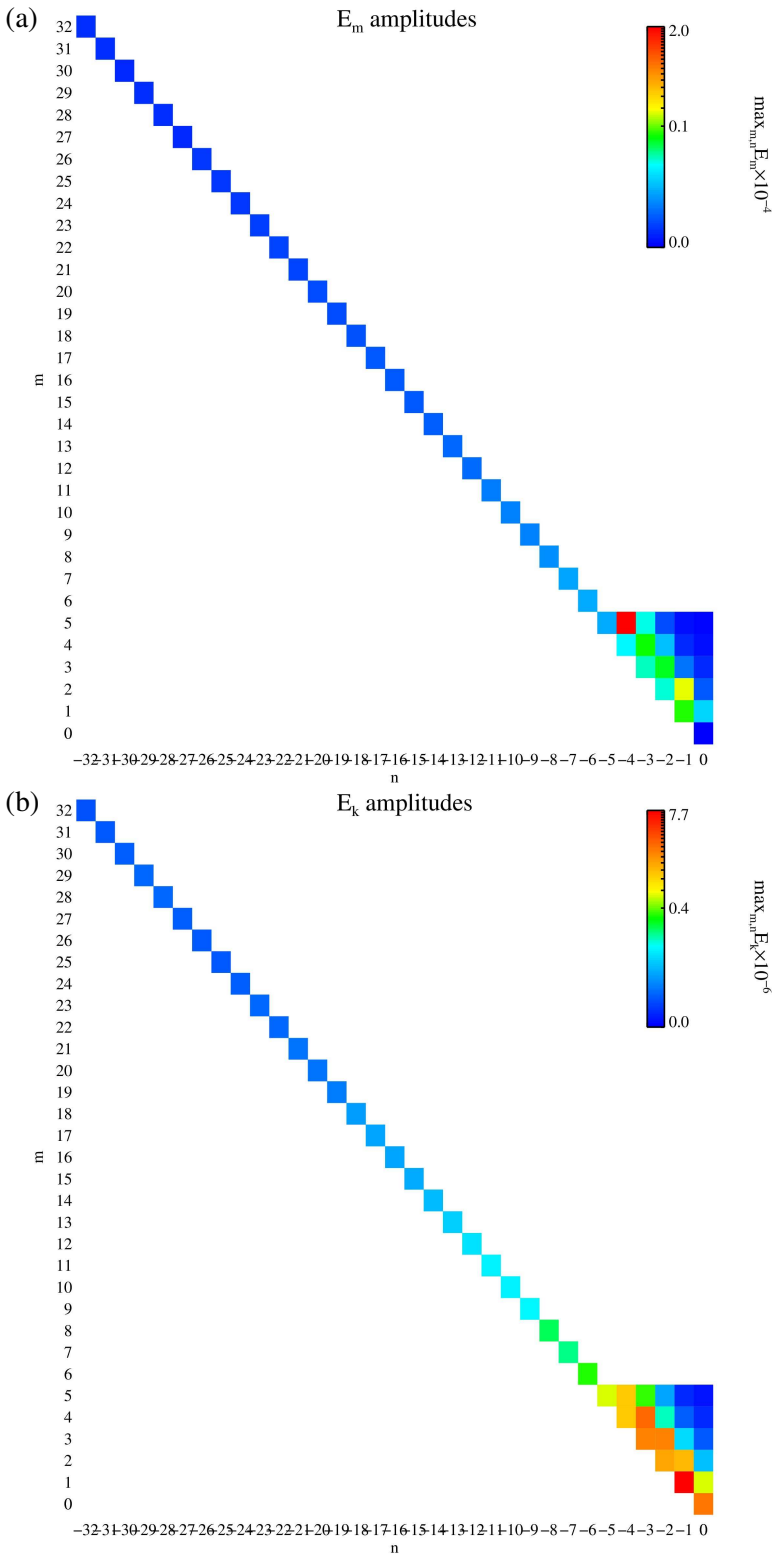

Figure 6.20: Contour of the magnetic (a) and kinetic (b) energies spectra for the Fourier modes considered in the simulation in Fig.(6.17) at $t = 1.9 \cdot 10^4 \tau_A$.

Wide Fourier mode spectrum

In Figure 6.22 are displayed the magnetic and the kinetic energy cascades of a simulation with same configuration and parameters as the previous but a wider spectrum ($0 \leq m \leq 8$ and $-8 \leq n \leq 8$). Again the energy fluctuation spectrum is dominated by the same modes (2/1,3/2,4/3,5/4...) as in the previous case, with an accumulation in energy this time on the 8/7 mode, which, analogously to the 5/4 in the previous case, is on the boundary of the Fourier spectrum of the simulation, as can be clearly seen in Figure 6.22a. The spectrum also drops sharply for $n > 0$ and in general modes far away from the $h = 1$ helicity (blue zones in Figure 6.22), corresponding to non resonant modes $q_{mn} < q_0$. This indicates that a large fraction of the modes included in this simulation are redundant, in the sense that the level of their excitation through the non linear cascading mechanism is several orders of magnitude lower than that of the dominant modes, and therefore is likely to give little contribution to the global dynamics.

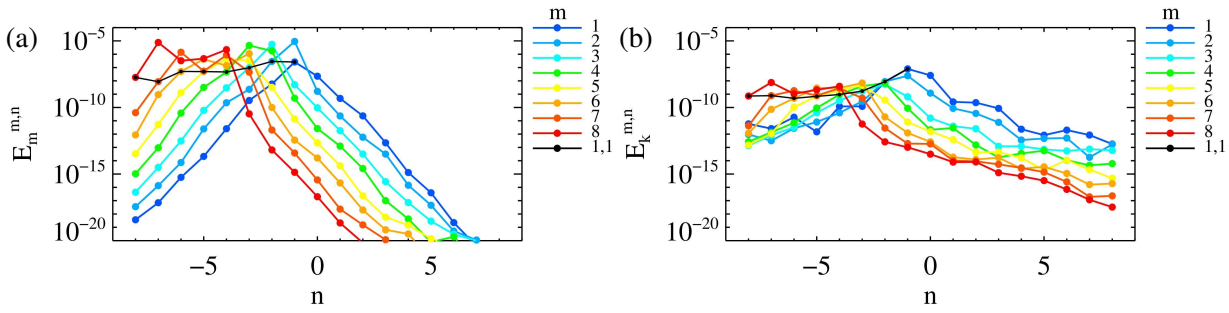

Figure 6.21: Magnetic (a) and kinetic (b) energy spectra for the Fourier modes right after the sawthooth relaxation event, color coded for different m modes and the harmonics of 1/1 (black line).

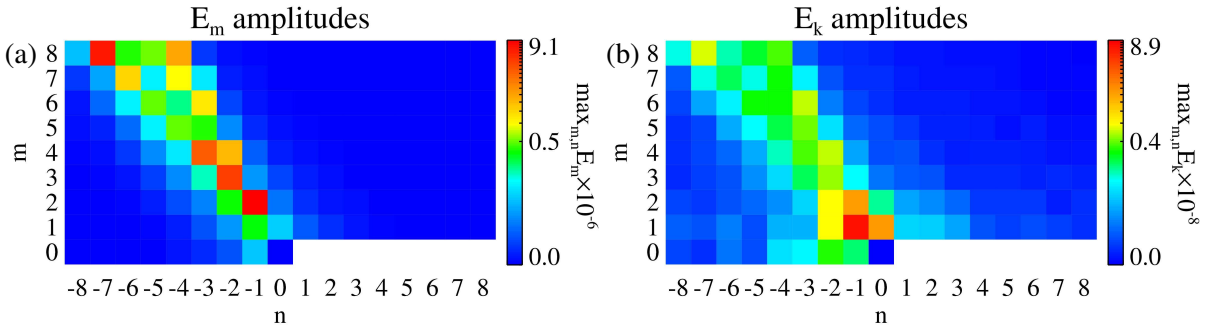

Figure 6.22: Contour of the magnetic (a) and kinetic (b) energies spectra for the Fourier modes right after the sawthooth relaxation event.

This analysis indicates that an increase in resolution (in particular modes $n + 1/n$) would be required to better define the dynamics after the magnetic reconnection event. Although as discussed above this does not influence the dynamics of the reconnection itself, and thus the resolution used in the previous simulations is satisfactory for our goal of describing AEs excitation by the magnetic reconnection events.

6.2.2.1.2 Effect of the amplitude of 2/1 mode

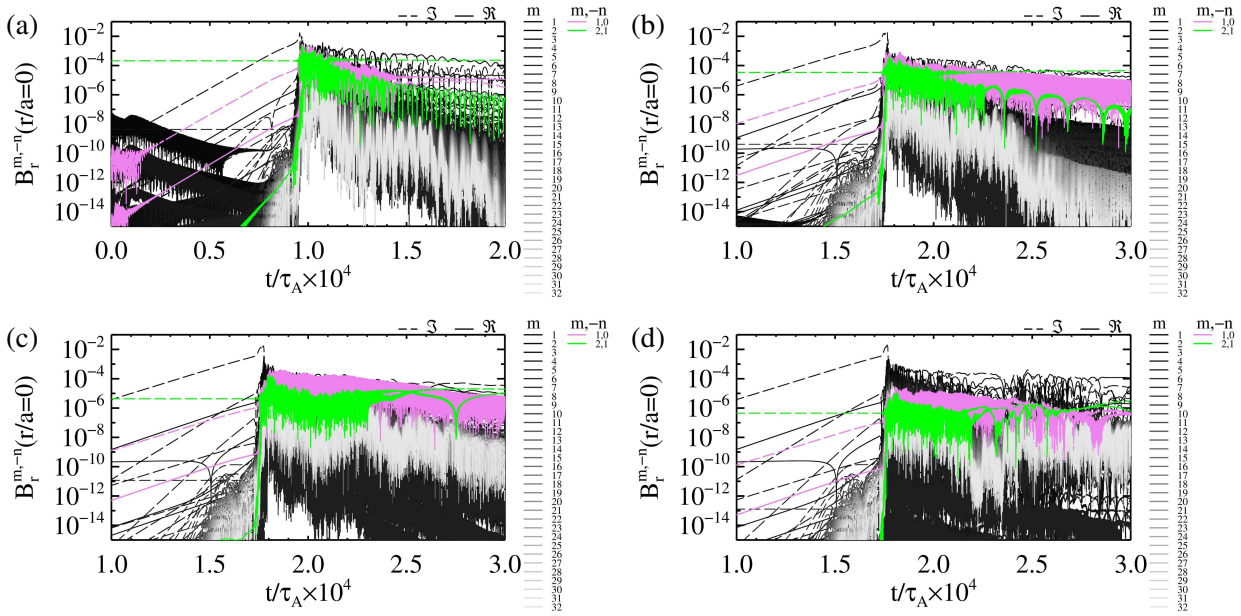

Figure 6.23: Simulations with decreasing amplitude of $(m,-n) = (2,1)$ mode, from highest (a) to lowest (d). Temporal evolution of the radial magnetic field component in axis ($S = 10^8$, $M = 10^6$) associated with different harmonics in the Fourier spectrum. Up-down asymmetric initial perturbation. Dashed lines indicate immaginary part of $B_r^{m,-n}$ for a fixed mode $(m,-n)$. Solid lines indicate the real part.

We were also interested in investigating the effect that the amplitude of the 2/1 mode can have on the dynamics of the sawtooth crash and the excitation of AEs by magnetic reconnection events, as its marginaly stable amplitude was set by the degree of the initial perturbation we chose to apply, and because of its disruptive nature in Tokamak discharges [Boozer, 2012; Zohm, 2014], we wanted to determine the lowest amplitude that could give enough coupling for the excitation of 1/0 mode AEs. In Figure 6.23 is displayed the temporal evolution of the radial magnetic field in axis for four different simulations, all with the same parameters as the previous fully 3D case (which is included in panel b) but different amplitude of the 2/1 mode, from the highest (panel a) to the lowest amplitude (panel d). The most notable effect on the dynamic is the crash time of the first magnetic reconnection, which for the highest amplitude of the 2/1 mode (panel a) occurs much sooner in time ($\sim 1.0\times10^4\, t/\tau_A$), compared to the previously analysed case ($\sim 1.8\times10^4\, t/\tau_A$ in panel b). Lower amplitudes (panels c and d) do not change the crash time. Notice that the degree of the excitation of the 1/0 mode is set by the amplitude of the 2/1 mode.

Moreover, the magnetic topology of each simulation after the magnetic reconnection event is shown in Figure 6.24. The highest amplitude case (panel a) displays the highest degree of ergodization around the 2/1 magnetic islands, as well as the excitation of more large instabilities ($m = 3$ instability around $r/a = 0.8$). Overall we see a trend of reducing size of the chaotic region as the 2/1 amplitude is lowered, with the last case (panel d) having the smallest chaotic region, with the 2/1 island barely visible. In Chapter 8 we will analyse the effects of different amplitudes of the 2/1 mode on the 1/0 AEs excitation.

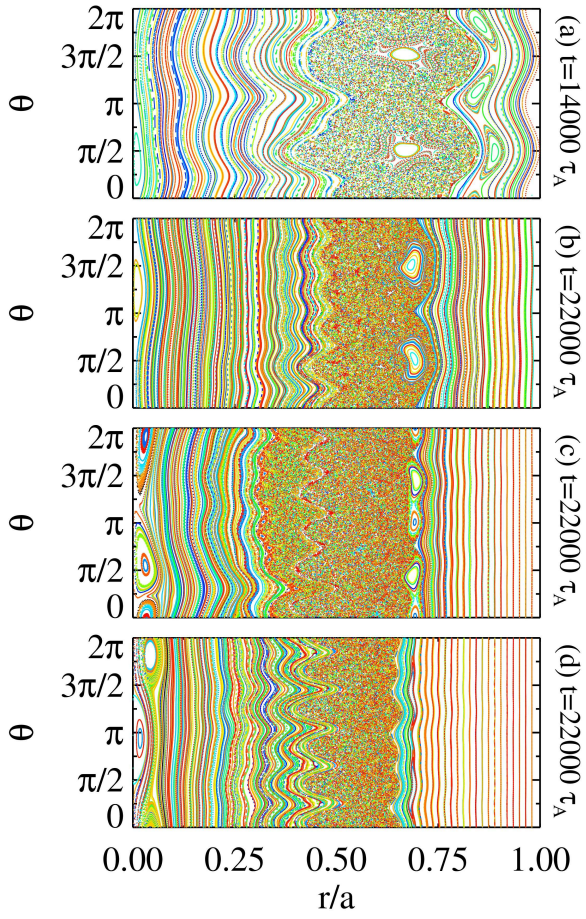

Figure 6.24: Poincaré plots in the z plane, for the four simulations in Figure 6.23 ($S = 10^8$, $M = 10^6$) after the magnetic reconnection event, with decreasing amplitude of $(m, -n) = (2, 1)$ mode, from highest (a) to lowest (d).

6.2.2.2 Coupling approach with marginally stable 3/2 mode

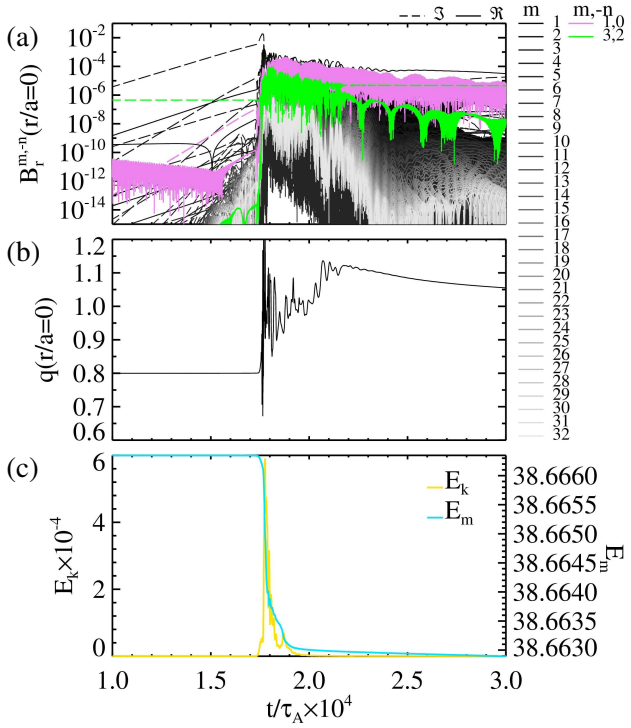

Figure 6.25: a) Temporal evolution of the radial magnetic field component in axis ($S = 10^8$, $M = 10^6$) associated with different harmonics in the Fourier spectrum. b) The corresponding temporal evolution of q value profile in axis. c) The corresponding evolution of the total magnetic and kinetic energies.

Lastly we consider an alternative coupling approach with the marginally stable 3/2 mode, both because this mode is less harmful for the magnetic confinement in Tokamak discharges and to show that the results of AEs excitation by self-consistent velocity perturbation we will discuss in Chapter 8 do not depend on the particular mode providing the coupling between the internal 1/1 kink instability and the 1/0 mode, recalling that the coupling between different helicities would be naturally present in toroidal geometry, with no need of employing a specific coupling mechanism as in the present cylindrical simulations.

Same parameters and configuration as in the fully 3D case discussed above are considered, except now we use the marginaly stable 3/2 mode analogously to what was done with the 2/1 mode, and a slightly extended Fourier space (up to $m = 6$ outside the $h = 1$ helicity to include the 6/4 mode, the 3/2 mode first harmonic). We compare this simulation dynamics (Figure 6.25) with the correspective simulation with 2/1 coupling approach (with the same 2/1 mode amplitude in Figure 6.23d). Overall the dynamics is qualitatively very similar, with the sawtooth crash occuring around the same time $\sim 1.8 \times 10^4 t/\tau_A$. In Figure 6.26 we also compare the topologies of the two simulations. Very similar topological structures and dynamics can be seen in both cases. We also notice that, with extended Fourier spectrum, the instability delimiting the chaotic region in panel (I)-(d) is charactherized by the dominant m=6 poloidal

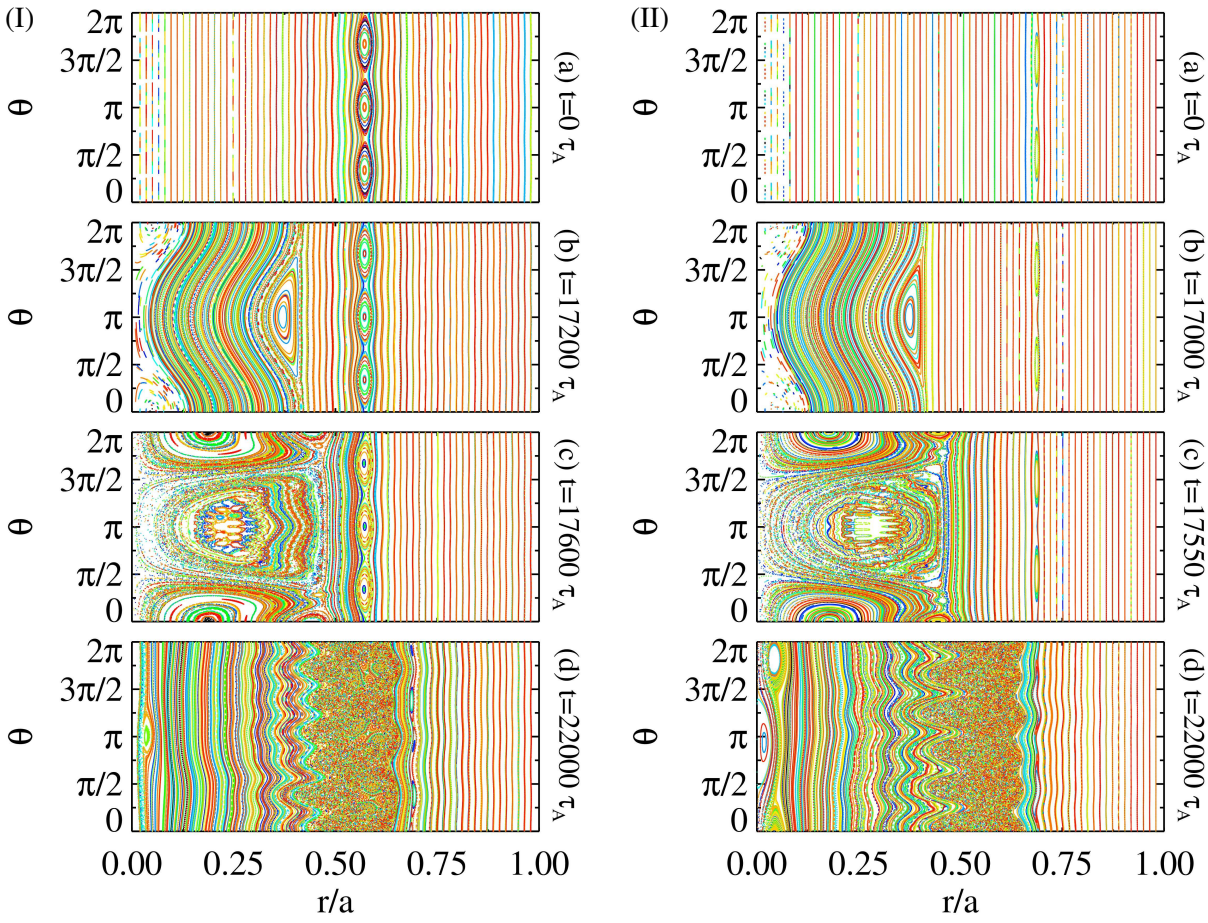

Figure 6.26: Poincaré plots in the z plane, for the simulation ($S = 10^8$, $M = 10^6$) with initially perturbed $(m,-n) = (3,2)$ marginaly stable mode (I), and $(m,-n) = (2,1)$ mode (II) with initial amplitudes of 10^{-6}. For each, four snapshots are displayed corresponding to the start of the simulation (a) and three snapshots around the magnetic reconnection event.

number, analogously to the delimiting m=5 instability in panel (II)-(d) discussed previously. All of this suggests that both coupling approches give equivalent results in terms of the dynamics and consequently 1/0 mode excitation.

6.3 Experimental-like helical self-organization in RFP modeling

In this Section we will give a brief review of the first nonlinear three-dimensional magnetohydrodynamic (MHD) numerical simulations , performed with the SpeCyl code, of the reversed-field pinch (RFP) that exhibit a systematic repetition of quasi-single helicity states with the same dominant mode in between reconnection events [Bonfiglio et al., 2013]. This was the first time that this distinctive experimental feature have been reproduced by a 3D MHD code. This analysis gave a satisfactory qualitative and quantitative agreement with respect to experimental observations that has been lacking so far (although previous modeling studies with the SpeCyl code played a fundamental role for the discovery of helical RFP states).

The same numerical simulation used in this publication will be later analyzed in this Thesis to see if the experimental observation of Alfvén Eigenmodes in RFP plasmas can be numerically reproduced in conditions of a fully-3D time-evolving RFP configuration (the most realistic RFP conditions achievable with the SpeCyl code, although with present limitations of the code, such as cylindrical approximation, zero-β etc.).

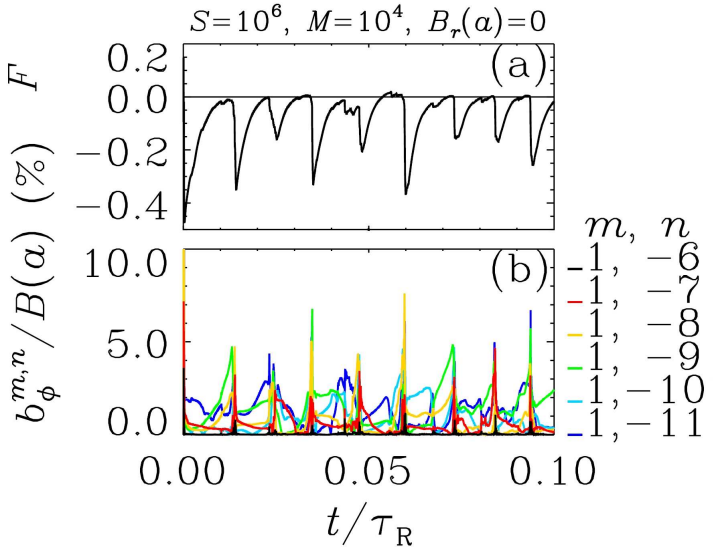

Figure 6.27: The temporal evolution of the simulation with ideal boundary condition, as discussed in the modeling study of the RFP [Bonfiglio et al., 2013].

The key ingredient to observe QSH states is the use of helical boundary conditions for the edge radial magnetic field B_r, consistent with a small helical modulation of the plasma magnetic boundary. Helical boundary conditions with $m = 1$ poloidal and $n = -7$ toroidal periodicity are used, corresponding to the standard dominant mode in RFX-mod.
In the simulation a wide spectrum of 225 modes with $0 \leq m \leq 4$ is used. This spectrum was employed and validated in previous simulation studies [Cappello, 2004; Cappello et al., 1996; Bonfiglio et al., 2010].

We first consider a simulation with ideal boundary conditions. The on-axis Lundquist and viscous Lundquist numbers are set to $S = 10^6$ and $M = 10^4$, respectively. This corresponds to Hartmann and

Prandtl numbers $H \equiv (SM)^{1/2} = 10^5$ and $P \equiv S/M = 100$, respectively. The initial condition is a nonreversed axis-symmetric Ohmic equilibrium with pinch parameter $\Theta = B_\theta(a)/< B_\theta > \simeq 1.6$ and reversal parameter $F = B_\phi(a)/< B_\phi > \simeq 0.15$, where $< \cdot >$ represents a volume average. The temporal evolution of the reversal parameter F and the normalized edge B_ϕ amplitudes of the most active $m = 1$ modes is shown in Figs. 6.27(a) and 6.27(b). The resulting sawtoothing dynamics closely reproduces what was already reported in past viscoresistive MHD studies with similar ideal boundary conditions. After a strong initial reconnection event leading to the reversal of the F parameter (i.e., to the formation of the RFP configuration), the system undergoes quasiperiodic cycles with reconnection events. This is followed by relatively longer phases with reduced MHD activity. In this simulation, the MH regime is typically observed in between reconnection events, while QSH phases occasionally occur, although without any specific dominant mode and with a rather small amplitude separation with respect to secondary modes.

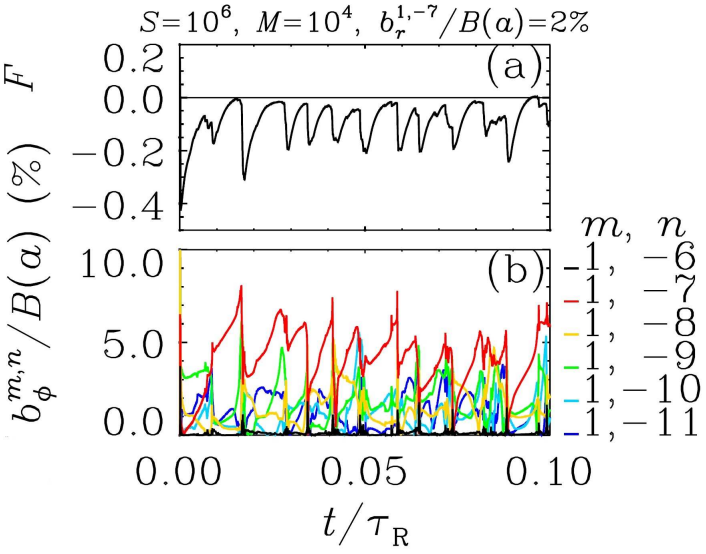

Figure 6.28: The temporal evolution of the simulation with helical boundary condition, as discussed in the modeling study of the RFP [Bonfiglio et al., 2013].

A qualitative change occurs with the inclusion of helical boundary conditions. We consider now a simulation with the addition of a helical perturbation of the edge radial magnetic field. This perturbation is chosen with $m = 1$, $n = -7$ periodicity and a constant in time amplitude around 2% of the mean edge field. Such boundary conditions provide a schematic representation of the plasma magnetic boundary during high current discharges in RFX-mod. The temporal evolution of the simulation with helical boundary conditions is shown in Figs. 6.28(a) and 6.28(b). It can be clearly seen that QSH phases with $1, -7$ dominant mode regularly occur in between reconnection events, while MH conditions seldom intervene. Thus, the observed numerical QSH dynamics presents the peculiar experimental features missing in previous modeling. The finite helical B_r perturbation also affects the periodic sawtoothing activity of the reversal parameter F, which on average becomes more frequent and less intense. This trend is confirmed for increasing helical perturbation amplitudes.

For comparison, a typical RFX-mod discharge with standard feedback control at high current is

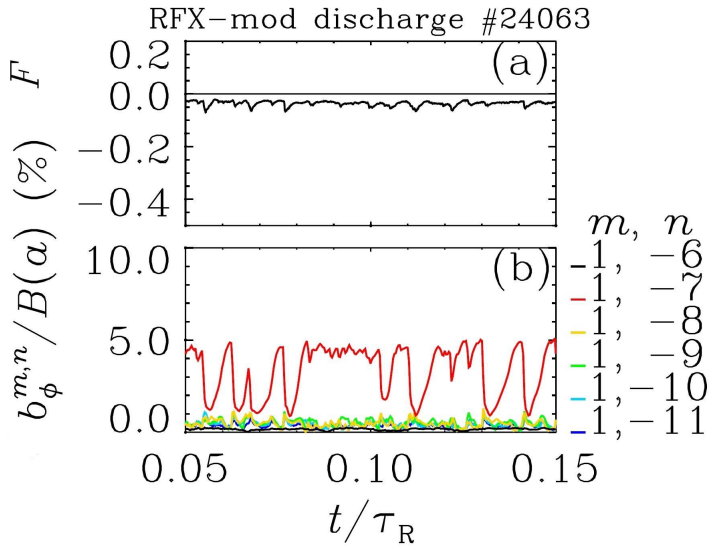

Figure 6.29: RFX-mod discharge, as discussed in the modeling study of the RFP [Bonfiglio et al., 2013].

shown in Figs. 6.29(a) and 6.29(b). The main quantitative differences with respect to experimental findings are the wider range of numerical F oscillations and the larger level of secondary modes. This difference is mainly due to the use of unrealistic dissipation parameters. Taking Lundquist numbers of the order of $S = 10^7$ a temporal evolution of the simulation is obtained, which is qualitatively similar to the previous one Fig. 6.28. However, the average total amplitude of secondary modes decreases. This makes the repetition of QSH phases in between reconnection events particularly clear and systematic. In fact, QSH phases turn out to occur always in between reconnection events,with a close to realistic amplitude separation with respect to secondary modes.

Part III

Alfvén waves excitation in nonlinear MHD simulations

Chapter 7

Alfvén waves excitation by initial perturbation

As a first approach to the study of Alfvén modes in nonlinear MHD codes, in this chapter we will analyse Alfvén waves excited starting from a stable 1D equilibrium configuration by applying a small initial perturbation to the velocity field. This can be intuitively understood with the analogy of plucking a string originally at rest, giving it an initial speed different from zero and letting it evolve in time. While in the subsequent chapters we will study the effects of self-consistent velocity perturbations, created by the dynamics itself, on Alfvén waves excitation.

We start to study Alfvén modes in nonlinear MHD simulations performed with the SpeCyl code, by considering three configurations: uniform axial magnetic field with uniform density, a non-uniform magnetic field in tokamak configuration with both uniform and bell-shaped density profiles and RFP-like configuration with both bell-shaped and RFX-mode like density profiles. For each simulation case, we will characterize Alfvén waves properties (such as frequency spectra and nonlinear dynamics) by computing the Fast Fourier Transform (FFT) and Continuous Wavelet Transform (CWT) of simulation data, depending on whether we want to analyse the frequency spectra as a function of space (normalised radius r/a) or time (normalized time t/τ_A), respectively. In particular, FFTs are performed over time windows spanning $500\tau_A$. This value is short enough for the fileld components not to change significantly and it allows to obtain FFTs with good frequency resolution. The computed FFTs spectra will be compared with the expected analitical ones derived from the theoretical models discussed in Chapter 5.

For the following simulations we used ideal boundary conditions, aspect ratio $R/a = 4$, a radial resolution of 256 points and a single Fourier harmonic in the angular directions, with periodicity $(m, -n)$ specified for each simulation case. The dissipation parameters are $S = 10^6$ and $M = 10^6$ respectively. The simulation time step is $10^{-4}\tau_A$, and fields were saved every $0.1\tau_A$.

7.1 Equilibrium configuration with uniform axial magnetic field

We start with the analysis of the simplest case, that is the equilibrium configuration with uniform axial magnetic field and uniform density ρ_0. In the case of a uniform magnetic field, the shear and compressional Alfvén waves are decoupled, as can be deduced from the theoretical model discussed in Chapter 5, and hence can be excited separately depending on the initially perturbed component (r, θ, z)

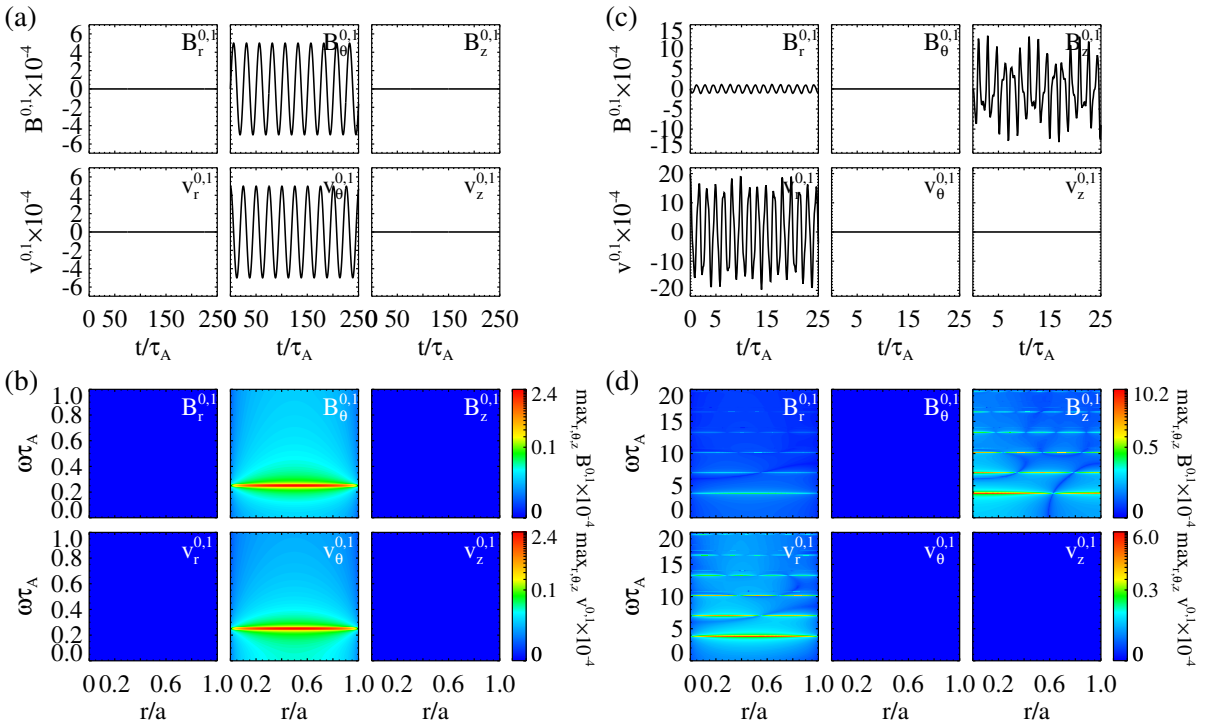

Figure 7.1: Results of numerical simulations with uniform axial magnetic field and density, and perturbation of the $(m,-n)=(0,1)$ mode, at the start of the simulation. In the first column, the simulazion with initial $v_\theta^{0,1}$ is reported. a)-c) Time traces of $\mathbf{v}^{0,1}$ and $\mathbf{B}^{1,0}$ normalized fields components are shown at a fixed radius $r/a=0.5$. b)-d) The corresponding frequency spectra of $\mathbf{v}^{0,1}$ and $\mathbf{B}^{0,1}$ normalized components are shown as a function of radius, computed for the time window $t\in[0,500\tau_A]$. The color scale, used for the contours in this paper, is not linear but follows a power law, which is necessary to detect higher order harmonics, and it refers to the absolute value of the spectral amplitude. In the second column, the same quantities are shown for the simulation with initial $v_r^{0,1}$ perturbation.

of the velocity field. We consider the mode $(m,-n)=(0,1)$, with initial $v_\theta^{0,1}$perturbation, or with initial $v_r^{0,1}$ perturbation. We choose this mode as this is the simplest case that presents both SAW and CAE solutions.

We start discussing the simulation with initial velocity perturbation on the azimuthal component $v_\theta^{0,1}$, with radial profile given by

$$v_\theta^{0,1}(r)=\varepsilon r(1-r), \tag{7.1}$$

where $\varepsilon=10^{-6}$. We can see from Figure 7.1a that in this case only the $B_\theta^{0,1}$ and the $v_\theta^{0,1}$ components are finite. Which component is excited by the initial perturbation depends on the MHD coupling between $\mathbf{B}^{0,1}$ and $\mathbf{v}^{0,1}$ components. The time traces of $B_\theta^{0,1}$ and $v_\theta^{0,1}$ at mid radius appear as sinusoids with a period ΔT such that about 10 cycles are observed in a range of $250\tau_A$. It is therefore expected that by doing the FFT of these time signals a single frequency $\omega\tau_A=2\pi\tau_A/\Delta T\simeq 2\pi/25\simeq 0.25$ would be

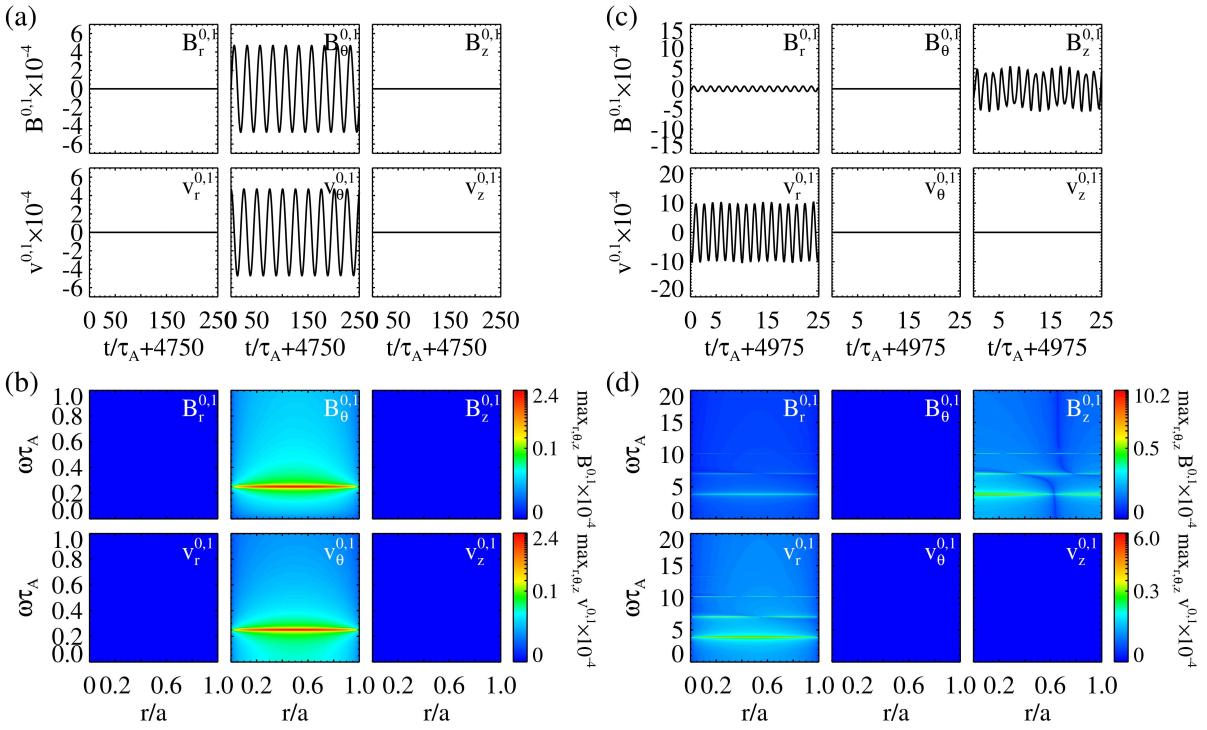

Figure 7.2: Results of numerical simulations with uniform axial magnetic field and density, and perturbation of the $(m,-n) = (0,1)$ mode, at the end of the simulation. In the first column, the simulazion with initial $v_\theta^{0,1}$ is reported. a)-c) Time traces of $\mathbf{v}^{0,1}$ and $\mathbf{B}^{1,0}$ normalized fields components are shown at a fixed radius $r/a = 0.5$. b)-d) The corresponding frequency spectra of $\mathbf{v}^{0,1}$ and $\mathbf{B}^{0,1}$ normalized components are shown as a function of radius, computed for the time window $t \in [4500, 5000\tau_A]$. In the second column, the same quantities are shown for the simulation with initial $v_r^{0,1}$ perturbation.

obtained. In fact, doing the FFT in the interval $t \in [0, 500\tau_A]$ as shown in Figure 7.1b, we obtain a spectrum with a well defined frequency centered on the expected value. This is the SAW expected from ideal MHD model in cylindrical geometry as discused in Chapter 5. In general the color scale can be different for velocity components and field components. It must also be noted that the color scale in not linear but follows a power law, which is necessary to detect higher order harmonics, and it refers to the absolute value of the spectral amplitude. As we can see in the verification benchmark reported in Figure 7.3a, we have an excellent agreement regarding both the frequency spectrum of the mode and its radial shape.

Let us see now what we obtain from a simulation in which the radial component of velocity is perturbed instead of the azimuthal one. As we can see from Figure 7.1c in this case we obtain three non-zero components, $B_r^{0,1}$, $B_z^{0,1}$ and $v_r^{0,1}$. We again recognize a wave pattern but this time it does not correspond to a simple sinusoidal wave. This is confirmed by Figure 7.1d, in which multiple harmonics are observed. The frequency spectrum shows the CAEs with their nodes, where the Alfvénic oscillations have zero amplitude. The expected spectrum of CAEs from ideal MHD model in cylindrical geometry was discused in Chapter 5. Note that in these simulations we are considering only the fast compressional

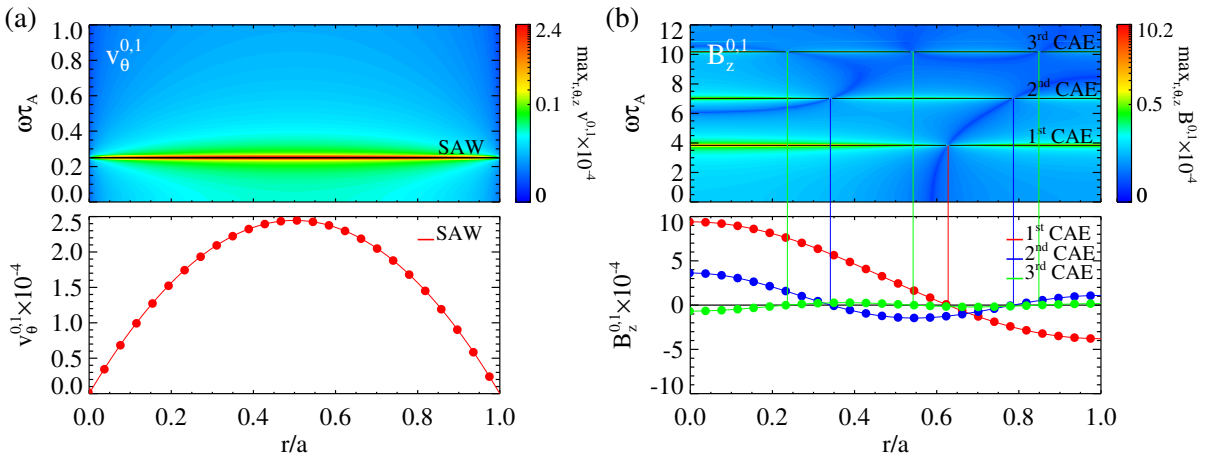

Figure 7.3: Verification benchmark between numerical simulations with uniform axial magnetic field and corresponding analytical spectra. a) Simulation with uniform axial magnetic field and uniform density. $(m,-n) = (0,1)$ mode with initial $v_\theta^{0,1}$ perturbation. On the top panel the agreement of simulation's frequency spectrum of the $v_\theta^{0,1}$ component and the expected theoretical one given by Eq.(5.8) (solid black line), are shown. On the bottom panel the analytical perturbation given by Eq.(7.1) (solid line) is displayed together with the corresponding values from the simulation spectrum (solid dots). b) Same equilibrium configuration and analised mode as in (a) but with initial $v_r^{0,1}$ perturbation. On the top panel, the simulation frequency spectrum of the $B_z^{0,1}$ component and the corresponding analytical spectrum given by Eq.(5.22) (solid black lines) are shown. On the bottom panel the analytical solution (Bessel function of order $m = 0$) for the frequencies of the first three CAEs (solid lines) are displayed together with the corresponding values from the simulation spectrum (solid dots). Note that on the top panel the oscillations are shown with their absolute values, while in the bottom panel they are not.

mode, as SpeCyl runs in zero-β approximation, that is no plasma pressure ($p = 0 \Rightarrow c_s^2 = \gamma p_0/\rho_0 = 0$). Indeed by assuming $c_s^2 = 0$ the slow compressional mode frequency is always zero. Again we have an excellent agreement between the simulation spectrum and the analytical solution as can be seen from Figure 7.3b. This is a further demonstration of the robustness of the SpeCyl code, after the nonlinear verification benchmark discussed in [Bonfiglio et al., 2010].

A slow decay of the waves amplitude, due to the finite resistivity and viscosity in the SpeCyl code given by Eqs. (6.2), is observed if we look at the analogous analysis at the end of the same simulation in Figure 7.2. However, resistivy and viscosity do not alter the frequencies of Alfvén waves with respect to the ideal MHD solutions, as discussed for instance in [Cross, 1988; Cramer, 2001]. In resistive theory the Alvén waves have a dispersion relation of the type $\omega = \omega_R - i\omega_I$. For our simulations the real part which gives the frequency value will not change perceptibly, as the term within it with dependence on visco-resistive coefficients will be tens of orders of magnitude lower than the ideal condition. While the immaginary part, responsible for damping, is only few orders of magnitude lower compared to the fields amplitude and thus a damping will occur proportional to the visco-resistive coefficients and m/n mode numbers. In particular for CAEs spectra, it will also be proportional to the derivative of the bessel function of order m (similarly to the discussion in Section 5.1.2), and thus the damping will increase for

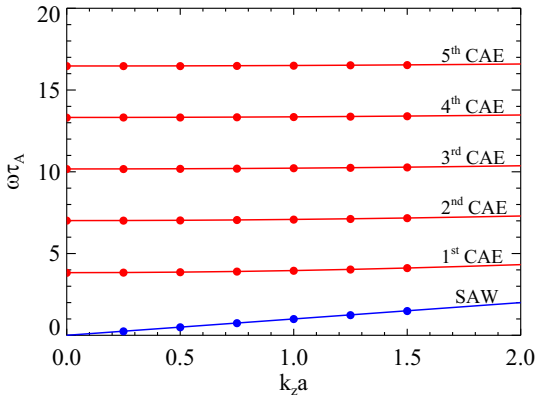

Figure 7.4: Verification benchmark between numerical results (solid dots) with uniform axial magnetic field and corresponding analytical spectra (solid lines). Same equilibrium configuration, and $m = 0$ analysed Fourier mode, as in Figures 7.1 and 7.3, but with different toroidal periodicities from $n = 0$ to $n = 6$. The frequency dependence on k_z wavevector component for the SAW and the first five CAEs from numerical simulations match very well the analytical solutions.

higher order CAEs (within the same mode m/n), as can be seen by comparing Figure 7.1d with Figure 7.2d where the degree of damping increases with the frequency of the CAEs.

The above analysis is applied to similar single-mode simulations with various mode numbers $m = 0$ and n chosen between $n = 0$ and $n = 6$ for both $v_r^{0,1}$ and $v_\theta^{0,1}$ initial perturbations in order to further verify the analytical dispersion relations for CAEs and SAW. As can be seen from Figure 7.4 the values of the CAEs and SAW frequencies (solid dots) from simulations are in complete agreement with the theoretical model (solid lines).

7.1.0.1 1/0 mode with initial v_r perturbation

Before proceeding to study non-uniform magnetic field configurations, we give a quick analisys of the (m,-n)=(1,0) Fourier mode. Going forward we will focus on this mode, so its useful to have a reference of its spectrum to compare how the CAEs frequencies change going from uniform to a tokamak configuration. Compared to the previous mode spectrum, now the CAEs are shifted downwards, shown in Fig.7.5 (notice different frequency range compared to Fig. 7.1d). We display here only the resulting spectrum from $v_r^{1,0}$ initial perturbation as for this mode, with uniform magnetic fiel, the SAW frequency is always zero (see Eq. 5.8).

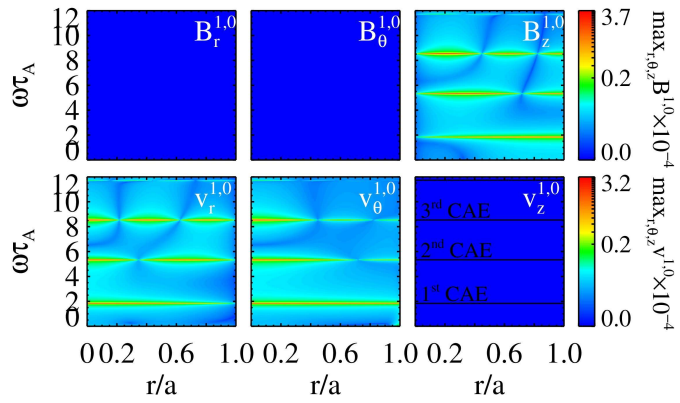

Figure 7.5: Results of numerical simulations with uniform magnetic field and uniform density profile. $(m,-n) = (1,0)$ mode with initial $v_r^{1,0}$ perturbation. The frequency spectra of $\mathbf{v}^{1,0}$ and $\mathbf{B}^{1,0}$ normalized fields components are shown as a function of radius, as computed for the time window $t \in [0, 500\tau_A]$. In the last panel the frequency spectrum is superimposed with the expected analytical solutions for CAEs.

7.2 Tokamak equilibrium configuration

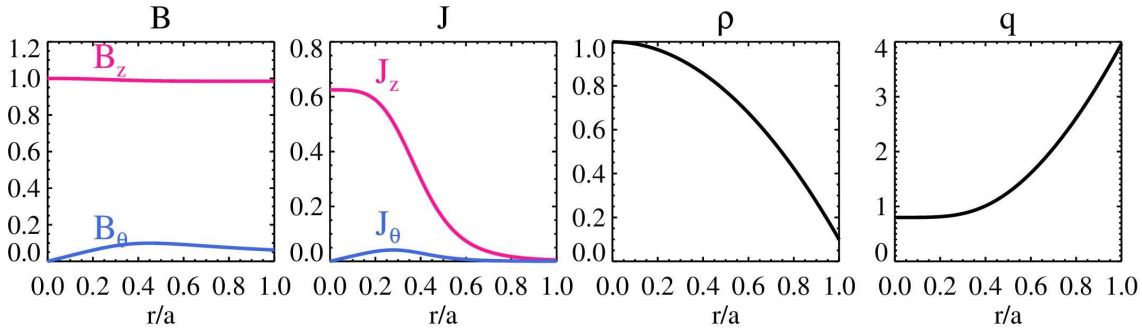

Figure 7.6: Equilibrium profiles for the tokamak configuration. From left to right: tokamak equilibrium radial profiles, the corresponding current density profiles, bell shaped density profile and q value profile. Magnetic field is normalized to its on-axis initial value.

Now we consider the first case with a non-uniform magnetic field. This configuration is a numerical solution of the 1D zero-β paramagnetic pinch equilibrium equations, discussed for instance in [Bonfiglio et al., 2010]. An azimuthal field (net plasma current) is added to the weakly non-uniform axial field, giving rise to a tokamak-like equilibrium configuration as shown in Figure 7.6. It corresponds to a paramagnetic pinch equilibrium with aspect ratio $R_0/a = 4$, uniform resistivity and an applied axial Electric field given by $\alpha_0 = 0.625$ (the parameter α_0 is defined in [Bonfiglio et al., 2010] and corresponds to the ratio between the applied electric field and the central resistivity).

For this tokamak configuration, with safety factor value in the center $q(0) = 0.8$ and at the edge $q(a) = 4.0$, we will consider both uniform and non-uniform bell-shaped density profile shown in Fig.

7.6. From now on we will also consider the $(m,-n) = (1,0)$ and $(m,-n) = (1,1)$ Fourier modes (instead of the $(0,1)$ mode considered in previous cases) for our analysis. As discussed in the next Chapter, this choice is dictated by both the necessity of studying and detecting Alfvén waves fluctuations during global MHD instabilities, where we will analyze mainly the $(m,-n) = (1,1)$ mode, and the need to investigate the mechanism of excitation of $(m,-n) = (1,0)$ Alfvénic modes, as toroidal mode number of the Alfvénic fluctuations detected during Ohmic discharges (simulated in the next Chapter) in a number of tokamak experiments was found to be $n = 0$.

7.2.1 Uniform density $\rho_0 = 1$

7.2.1.1 1/0 mode with initial v_r perturbation

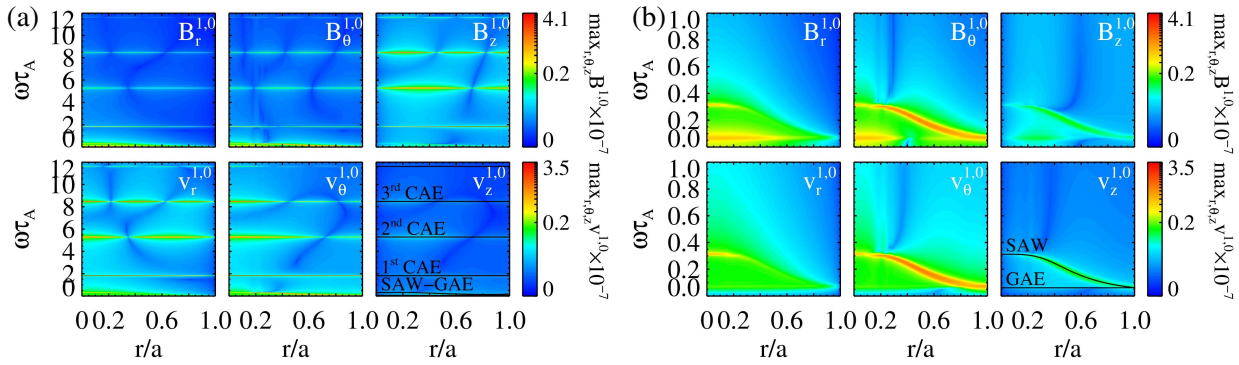

Figure 7.7: Results of numerical simulations with tokamak magnetic field and uniform density profile. $(m,-n) = (1,0)$ mode with initial $v_r^{1,0}$ perturbation. The frequency spectra of $\mathbf{v}^{1,0}$ and $\mathbf{B}^{1,0}$ normalized fields components are shown as a function of radius, as computed for the time window $t \in [0, 500\tau_A]$. In the last panel the frequency spectrum is superimposed with the expected analytical solutions for SAW, CAEs and GAE. b) Enlarged view in the frequency of the spectrum in (a) to emphasize the SAW and GAE spectra.

By perturbing $v_r^{1,0}$ we can see in Figure 7.7a that now the CAEs spectrum is present also in the $B_r^{1,0}$, $B_\theta^{1,0}$ and $v_z^{1,0}$ components, compared to the analogous Figure 7.5 of the uniform field case, in which these components are not excited at all. An additional basic phenomenon of Alfvén waves physics is observed. We can see from Figure 7.7b that the shear frequency spectrum is much different from the one with uniform density shown in Figure 7.1b. Now we have a SAW characterized by a continuous spectrum with a frequency that depends on the radius. This is the *continuous shear Alfvén wave spectrum* or the *Alfvén continuum* discussed in Chapter 5 [White, 2013; Biskamp, 1993]. Compared to the uniform case, now the continuous SAW is also present in all field components with similar amplitudes to the CAEs. In other words, we have a coupling of the shear and the compressional modes. This coupling is due to the fact that the wavevector $\mathbf{k}$ of the perturbation is now oblique to the magnetic field $\mathbf{B}^{0,0}$. Therefore only the perturbation in $v_r^{1,0}$ will be discussed in the following analysis. In addition, in this configuration it can be clearly seen in Figure 7.7b the occurrence of the global Alfvén eigenmode (GAE), which is a global mode right below the Alfvén continuum minimum (see Ref. [Villard et al., 1997]). The GAE will

be discussed in the next section.

In the last panel of Fig. 7.7 we overplot the numerical frequency spectrum with the expected theoretical one to identify the various frequencies. A good qualitative agreement between the numerical and theoretical spectra is observed. The small discrepancy is due to the fact that now the expected CAEs frequencies are obtained in the *local* or *Wentzel-Kramers-Brillouin (WKB) approximation* as the MHD equations are no longer analytically solvable for CAEs in case of non-uniform plasmas [Cramer, 2001]. The approximate analytical solution for CAEs and GAE in non-uniform plasmas was obtained in Chapter 5.

7.2.2 Bell shaped density profile

7.2.2.1 1/0 mode with initial v_r perturbation

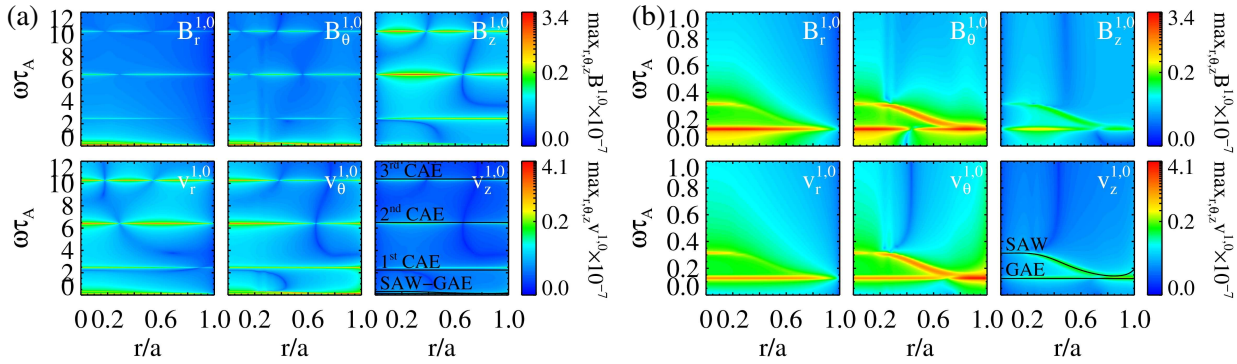

Figure 7.8: Results of numerical simulations with tokamak magnetic field and bell-shaped density profile. $(m,-n) = (1,0)$ mode with initial $v_r^{1,0}$ perturbation. The frequency spectra of $\mathbf{v}^{1,0}$ and $\mathbf{B}^{1,0}$ normalized fields components are shown as a function of radius, as computed for the time window $t \in [0, 500\tau_A]$. In the last panel the frequency spectrum is superimposed with the expected analytical solutions for SAW, CAEs and GAE. b) Enlarged view in the frequency of the spectrum in (a) to emphasize the SAW and GAE spectra.

We now consider the first case with a non-uniform bell-shaped density profile, depicted in the third panel of Figure 7.6. The Alfvén waves spectrum in this case, shown in Figure 7.8, is very similar to the uniform density case in Figure 7.7. Compared to the previous case, the CAEs frequencies are shifted upward, while the continuous SAW frequency becomes non monotonic near the edge, resulting in an upshift in the GAE frequency. The GAE is also more excited in this case, due to a wider minimum of the continuous shear.

In Figure 7.9, we look at the time evolution of $v_\theta^{1,0}$ component showing the SAW and GAE spectra during the nonlinear MHD simulation. To do this, we perform the FFT of simulation data on a moving time window, with same duration of $500\tau_A$ but increasing initial time. In the first panel we overplot the numerical frequency spectrum with the expected theoretical one to identify the various frequencies. By looking at the temporal evolution of the SAW spectrum, one can observe that the amplitude of the wave is damped very quickly at the radial positions with stronger radial gradient of the Alfvén frequency, while

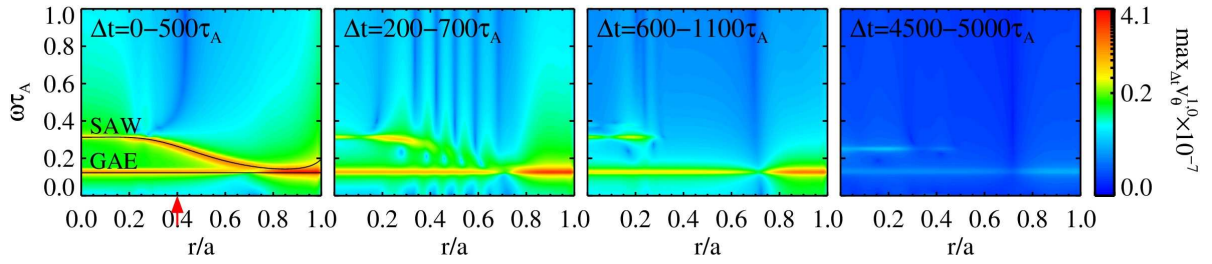

Figure 7.9: Temporal evolution of the spectrum of the numerical simulation with tokamak magnetic field and hollow density profile. $(m,-n)=(1,0)$ mode with initial $v_r^{1,0}$ perturbation. Time evolution of the frequency spectrum of the normalized velocity field component $v_\theta^{1,0}$ at the begining of the simulation (first three panels) and the end of the simulation (last panel), obtained with FFT. In the first panel the frequency spectrum is superimposed with the expected analytical solutions for SAW, CAEs and GAE.

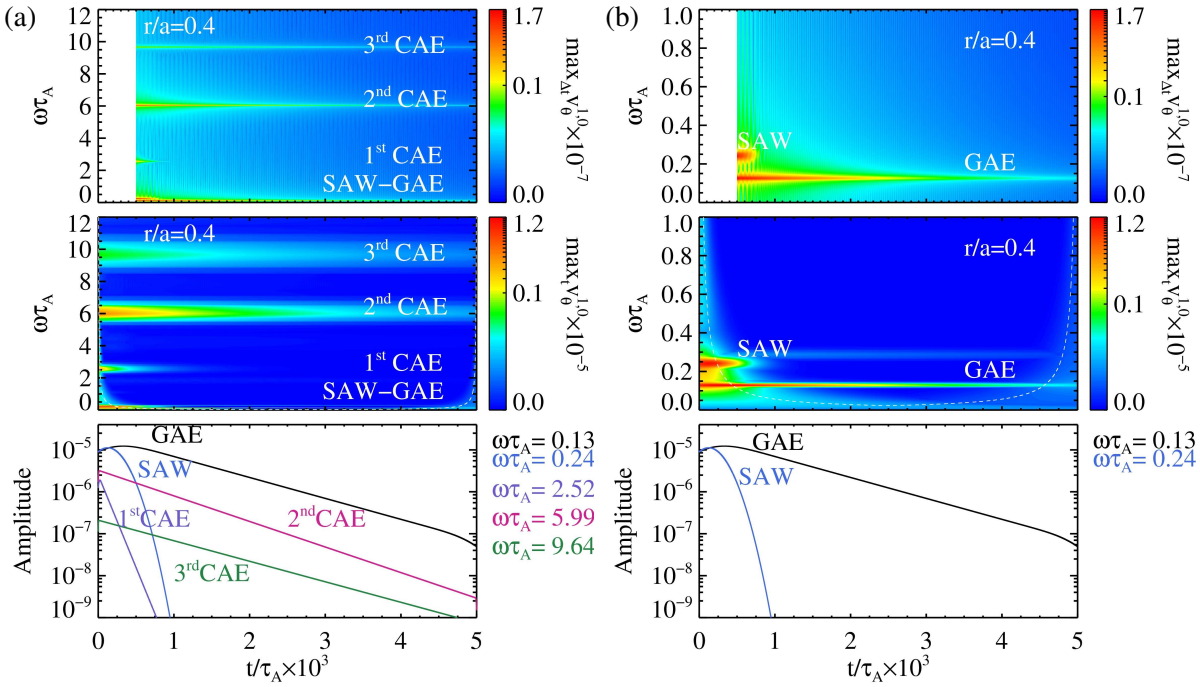

Figure 7.10: The time evolution of the frequency spectrum of the normalized velocity field component $v_\theta^{1,0}$ at a fixed radius of $r/a=0.4$ (marked in the first panel in Fig.(7.9)), obtained with STFT (top panel) and CWT (middle panel). COI in dashed white curve. Bottom panel: amplitude of $v_\theta^{1,0}$ at fixed frequencies $\omega\tau_A$ corresponding to different Alfvén modes. b) Enlarged view in the frequency of the spectrum in (a) to emphasize the SAW and GAE spectra.

it remains almost constant close to the extremes of the $\omega(r)$ profile, i.e. the regions around $r/a=0.1$ and 0.8. This is consistent with the phase mixing phenomenon, due to which the Alfvén wave tends to be

more rapidly damped in the regions with spatially variable Alfvén frequency [Cramer, 2001; Chen et al., 2016]. This damping mechanism acts on top of the damping due to the visco-resistive dissipation, which instead occurs uniformly throughout the plasma volume since the dissipation coefficients (resistivity and viscosity) are assigned to be uniform in these SpeCyl simulations, and their effect can be clearly seen on the GAE mode, which loses amplitude over time but survives throughout the duration of the simulation.

A very usefull tool for the analysis of frequency spectra variation in time is the Continuous Wavelet Transform (CWT), which allows for a pinpoint accurate analysis in time at a fixed radius in exchange for a wider dispersion of the Alfvén waves frequency, in particular it increases with frequency as can bee seen from Figure 7.10 (middle panels), in comparison with the Short-time Fourier Transform (STFT) (top panels) computed using the FFT for a sliding time window of $500t/\tau_A$ each alfvén time. The computed spectra for each window is than associated with the last time of the window, resulting in the frequency spectra in the top pannels of Fig.7.10. The CWT analysis will be more useful for signals that vary their frequency quickly in time, while for the monotonous ones like in this case the two transforms are approximately equivalent. In Figure 7.10 we can observe the evolution in time of the Alfvén modes. As expected the amplitude of the CAEs decreases in time due to visco-resistive dissipation. We notice that unlike 2^{st} and 3^{rd} CAEs, the 1^{st} one is damped much quicker, that is on top of the visco-resistive damping, there is in play another damping mechanism. As we could see from looking at the temporal evolution of the spectrum in Figure 7.7a and as we will see better in later simulations, this is caused by the non-uniformity of the density profile. Our hypothesis is that this is due to the resonance absorption mechanism and edge conditions in SpeCyl code, so that the continuous shear near the edge (where the shear changes its slope when non-uniform density is considered) diverges enough to meet the necessary condition for the 1^{st} CAE absorption (although we do not observe it clearly from the FFT analysis). The resonance absorption phenomenon occurs when a wave propagates in a smooth non-uniform plasma and couples with the continuous spectrum of the shear Alfvén wave, getting absorbed (and localy heating the plasma) [Cramer, 2001; Hasegawa et al., 1976]. In Figure 7.10b, on the other hand, we can see the disappearance of the SAW due to phase mixing in around $\sim 1000\tau_A$ (this value strongly depends on the frequency gradient at fixed radius, as discussed previously) and the visco-resistive damping of the GAE. By looking at the corresponding velocity field amplitude we can observe a distortion near the edges (start and end of the simulation). The region affected by edge-effect artifacts is defined by the Cone of Influence (COI) (outlined by a dashed white curve) and is typical effect related to CWT analysis.

7.2.2.2 1/1 mode with initial v_r perturbation

In this section we show the frequency spectra for (m,-n)=(1,1) Fourier mode in same tokamak configuration and bell-shaped density profile already considered before. This scrutiny will help us identify Alfvénic modes in the subsequent analysis, as this mode plays key role in the global MHD instability (sawthooth cycles) on which our study will focus. We can compare the frequency spectra of (m,-n)=(1,1) mode in Figure 7.11 with the previously analysed (m,-n)=(1,0) in Figure 7.8. The main difference is in the SAW frequency profile, which does not present the minimum, and consequently does not present a GAE. We also observe a high background noise in some fields components between $r/a = 0.0$ and $r/a = 0.4$. An important aspect to notice is the CAEs frequencies values. In this simulation 1^{st}, 2^{nd} and 3^{rd} CAE have the respective frequencies: $2.51\omega\tau_\mathrm{A}$, $6.42\omega\tau_\mathrm{A}$ and $10.29\omega\tau_\mathrm{A}$. While for the (m,-n)=(1,0) mode they are: $2.46\omega\tau_\mathrm{A}$, $6.42\omega\tau_\mathrm{A}$ and $10.28\omega\tau_\mathrm{A}$. There is very little difference in CAEs frequencies between the two modes because they have the same poloidal mode number m, which plays a bigger role

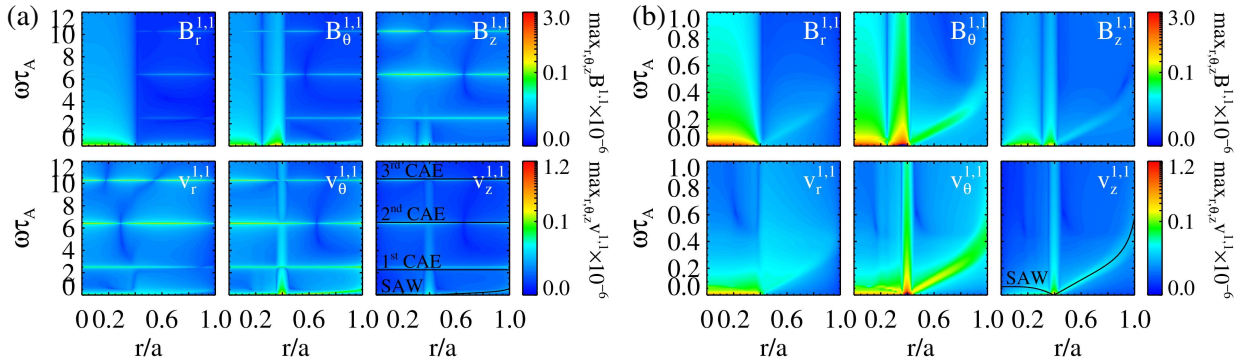

Figure 7.11: Results of numerical simulations with tokamak magnetic field and bell-shaped density profile. $(m,-n)=(1,1)$ mode with initial $v_r^{1,1}$ perturbation. The frequency spectra of $\mathbf{v}^{1,1}$ and $\mathbf{B}^{1,1}$ normalized fields components are shown as a function of radius, as computed for the time window $t\in[0,500\tau_A]$. In the last panel the frequency spectrum is superimposed with the expected analytical solutions for SAW, CAEs and GAE. b) Enlarged view in the frequency of the spectrum in (a) to emphasize the SAW and GAE spectra.

in the dispersion relation in equation (5.43) than the toroidal mode n.

7.2.2.3 0/0 mode with initial v_r perturbation

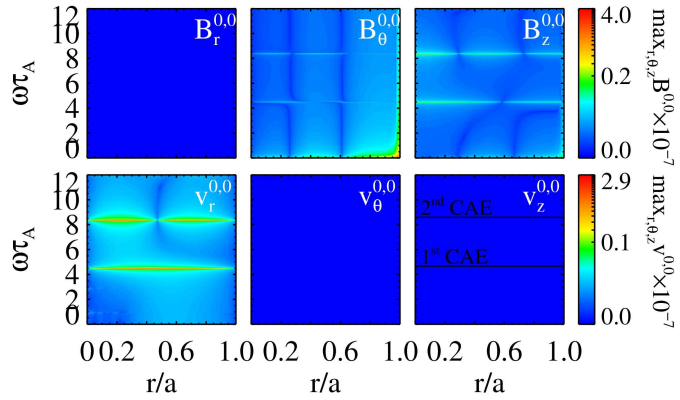

Figure 7.12: Results of numerical simulations with uniform magnetic field and uniform density profile. Equilibrium $(m,-n) = (0,0)$ mode with initial $v_r^{0,0}$ perturbation. The frequency spectra of $\mathbf{v}^{0,0}$ and $\mathbf{B}^{0,0}$ normalized fields components are shown as a function of radius, as computed for the time window $t \in [0, 500\tau_A]$. In the last panel the frequency spectrum is superimposed with the expected analytical solutions for CAEs.

The last single wave case we analyse is the equilibrium (m,-n)=(0,0) mode in tokamak configuration, which will be useful in next chapter simulations analysis. The two main features observed are the absence of the SAW/GAE, and the CAEs frequencies are much higher than in simulations with m=1. In particular from Figure 7.12 we can see that 1^{st} and 2^{nd} CAEs have frequencies: $4.5\omega\tau_\mathrm{A}$ and $8.4\omega\tau_\mathrm{A}$.

7.3 Paramagnetic pinch, RFP-like equilibrium configurations

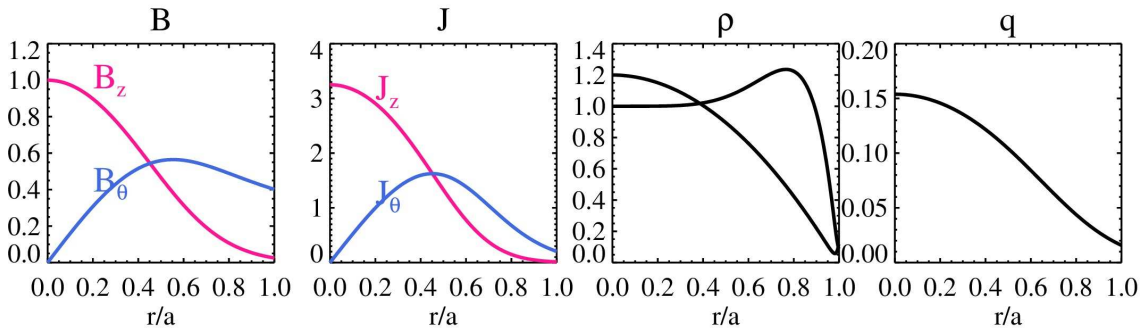

Figure 7.13: Equilibrium profiles for the RFP-like configuration. From left to right: RFP-like equilibrium radial profiles, the corresponding current density profiles, bell/hollow shaped density profiles and q value profile. Magnetic field is normalized to its on-axis initial value.

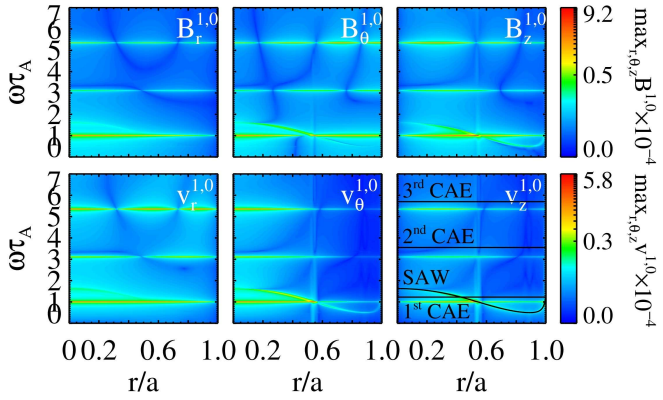

Figure 7.14: Results of numerical simulations with RFP-like magnetic field and hollow density profile. $(m,-n) = (1,0)$ mode with initial $v_r^{1,0}$ perturbation. The frequency spectra of $\mathbf{v}^{1,0}$ and $\mathbf{B}^{1,0}$ normalized fields components are shown as a function of radius, as computed for the time window $t \in [0, 500\tau_A]$. In the last panel the frequency spectrum is superimposed with the expected analytical solutions for SAW, CAEs and GAE.

We now consider the RFP-like configuration with RFX-mod-like hollow density profile. As in the previous tokamak case this configuration is a numerical solution of the 1D zero-β paramagnetic pinch equilibrium equations. The lack of the axial field reversal at the edge is just a mathematical consequence of the 1D equilibrium assumption, also known as Cowling's theorem (see also Escande et al., 2000b). The specific RFP-like equilibrium used in this paper is displayed in the first panel of Figure 7.13. It corresponds to a paramagnetic pinch equilibrium with aspect ratio $R_0/a = 4$, uniform resistivity and $\alpha_0 = 3.25$.

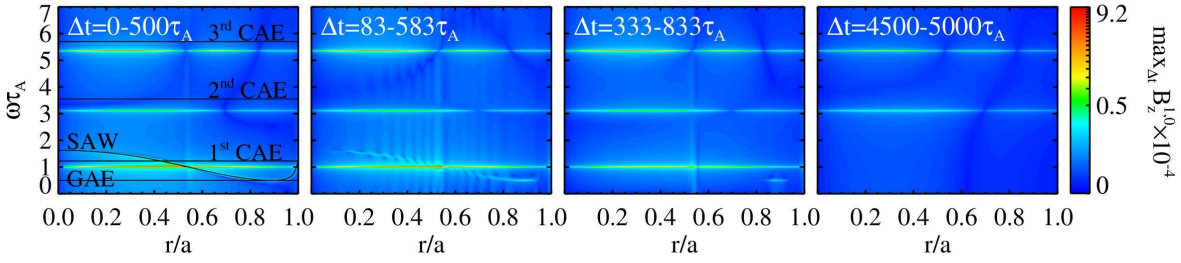

Figure 7.15: Temporal evolution of the spectrum of the numerical simulation with RFP-like magnetic field and hollow density profile. $(m,n) = (1,0)$ mode with initial $v_r^{1,0}$ perturbation. Time evolution of the frequency spectrum of the normalized magnetic field component $B_z^{1,0}$ at the begining of the simulation (first three panels) and the end of the simulation (last panel). In the first panel the frequency spectrum is superimposed with the expected analytical solutions for SAW, CAEs and GAE.

In Fig. 7.14 are displayed the frequency spectra $\mathbf{v}^{1,0}$ and $\mathbf{B}^{1,0}$ fields for this configuration. In the last panel we overplotted the numerical frequency spectrum with the expected theoretical one to identify the

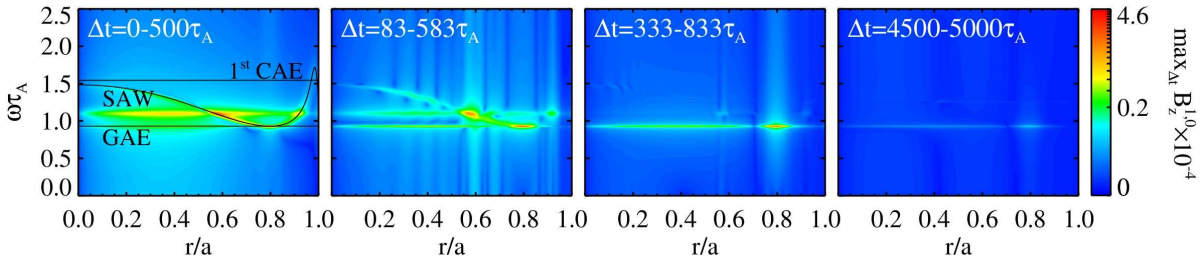

Figure 7.16: Temporal evolution of the spectrum of the simulation with RFP-like magnetic field and density profile peaked in the center. $(m,n) = (1,0)$ mode with initial $v_r^{1,0}$ perturbation. Time evolution of the frequency spectrum of the normalized magnetic field component $B_z^{1,0}$ at the begining of the simulation (first three panels) and the end of the simulation (last panel). In the first panel the frequency spectrum is superimposed with the expected analytical solutions for SAW, CAE and GAE.

various frequencies. Compared to the tokamak configuration now the SAW frequency range increases while the CAE frequencies are shifted down, so that a very peculiar condition occurs due to the RFP-like magnetic field profiles: the SAW and the 1^{st} CAE intersect each other. In Figure 7.15, we look at the time evolution of the $B_z^{1,0}$ component with an RFX-mod like hollow density profile (displayed in third panel in Fig. 7.13). From the spectrum temporal evolution we can observe again the phase mixing of the SAW, which disappears in the first $\sim 300\tau_A$ (although it survives longer at the radial location of the frequency minimum due to the negligible local gradient). We also observe the resonance absorption of the 1^{st} CAE, which completely vanishes by the end of the simulation.

In order to try to excite the GAE mode, which we expect to see as in the tokamak case, we investigated density profiles with different radial positions of their peak density, going from the wall to the plasma center. Here we only examine the profile that is most efficient to excite the GAE mode, namely the density profile peaked in the center (bell-shaped profile displayed in the third panel in Fig. 7.13). The temporal evolution of the frequency spectrum resulting from the SpeCyl simulation with perturbed $(m,n) = (1,0)$ mode and bell-shaped density profile is shown in Figure 7.16, where in the first panel we overplot the numerical spectrum with the expected theoretical one in order to identify the various frequencies. As we can see in the Figure, we observe the GAE just below the Alfvén continuum minimum, that is the GAE. We can also see, as in the previous case, the phase mixing of the SAW and the resonance absorption of the 1^{st} CAE. Both waves disappear as before, while the GAE mode survives along the whole simulation duration. This analysis points out that the GAE mode is more easily excited with density profiles peaked near the plasma center, which are typical in tokamak fusion plasmas.

Chapter 8

Alfvén waves excitation by magnetic reconnection events in Tokamak configuration

Our goal in this chapter will be to discuss the observation, in nonlinear MHD simulations of tokamak plasmas discussed in Chapter 6, of Alfvén waves following magnetic reconnection events. In other words, the excitation of AEs by a self-consistent MHD evolution of the tokamak sawtooth instability.

The analysis will center around the role of the MHD dynamics of the 1/1 internal kink mode in AEs excitation via magnetic reconnection events. We will revisit case by case, from helically-symmetric 2D to fully 3D with multiple helicities, Tokamak configurations described in Chapter 6 characterizing their frequency spectra and their excitation of AEs. Similarly to what described in the previous chapter, FFT and CWT analysis will be used to detect and study Alfvén waves, depending on whether we want to analyse the frequency spectra as a function of space or time, respectively. However now we will study Alfvén waves generated by velocity perturbations self-consistent with MHD dynamics, rather than from an externally imposed initial perturbation. Again, FFTs will be performed over time windows spanning $500\tau_A$. The computed spectra will be identified from theoretical models discussed in Chapter 5 and AEs spectra characterized in the previous chapter.

In the following we recall the setup of the simulations discussed in Chapter 6. We used ideal boundary conditions, aspect ratio $R/a = 4$ and a radial resolution of 256 points. We employed spatially uniform dissipation parameters with ranging values $S \in [10^6 - 10^8]$ and $M \in [10^3 - 10^6]$. The simulations time step is $10^{-3}/10^{-4}\tau_A$, and fields were saved every $0.1\tau_A$. Compared to the previous chapter, now the 1/1 mode (and its harmonics) will evolve non-linearly in time in a 2D/3D Fourier spectrum depending on whether we consider helically-symmetric 2D or fully 3D tokamak configurations with multiple helicities. Both helically-symmetric and fully 3D simulations start from an axisymmetric unstable Ohmic equilibrium with pinch parameter Θ (defined in Equation 2.12). The main features of this Ohmic axisymmetric equilibria for tokamak are presented in Figure 6.1. The safety factor q, plotted in the fourth panel, is computed from Equation 2.10 using the time-evolving axisymmetric part of the magnetic fields components. A uniform induction electric field $\mathbf{E} = E_0\hat{\mathbf{z}}$ is imposed to sustain the plasma current. Moreover, an initial perturbation of variable amplitude $\ll 1$ starts the MHD dynamics, typically driven by modes of resistive-kink/tearing nature.

8.1 Helically-symmetric Tokamak configurations

We start by analysing helically-symmetric Tokamak configurations, i.e. 2D simulations with Fourier spectrum composed of modes $(m, -n)$ with single helicity h (defined in Eq. 2.8), where the magnetic field variation can be described by two coordinates, the radial and a helical one. After analysing the sawthooth dynamics and the subsequent magnetic reconnection in Chapter 6, we probed whether this instability could excite Alfvén waves in Tokamak Ohmic configuration and under which constraints. Initial analysis in frequency spectra, of the typical well-defined sawtooth dynamics discussed in Section 6.2 ($S = 10^6$, $M = 10^3$), did not show any fluctuations of Alvénic modes, which spectra were characterised in Chapter 7. In the following sections our goal will be to investigate the mechanisms involved in AEs excitation and which parameters and quantities play key role in it. The progressive choice of parameters and configurations for different cases studied in Chapter 6 were guided by the following analysis.

8.1.1 First excitation of Alfvén waves by sawtooth instability

The first (weak) excitation of Alfvénic modes in helically-symmetric configuration is observed in the marginal case ($S = 10^6$, $M = 10^6$) for the formation of plasmoids (discussed in Section 6.2.1.2). The key parameter with respect to the first tokamak configuration we analyzed ($S = 10^6$, $M = 10^3$), where no AEs were detected, is the viscous Lundquist, i.e. the viscosity is three orders of magnitude lower. In particular $\nu = 10^{-6}$ was chosen, as same set up with $\nu = 10^{-4}$ and $\nu = 10^{-5}$ produced no results in terms of AEs excitation.

The simulation analyzed in this section has tokamak configuration, bell-shaped density profile and its dynamics is characterized by quasi periodic sawtooth relaxation events, displayed in Figure 6.6. A Fourier spectrum with 4 harmonics of the 1/1 mode is considered. We focused our analysis on the first and the third sawtooth relaxation events, as previously discussed. In Figure 8.1 are displayed the results of the CWT analysis on 1/1 Fourier component for the two cycles under examination. The CWT analysis was done at fixed radius $r/a = 0.8$ due to two considerations: we wanted to avoid the background noise in the 1/1 mode spectrum (see Figure 7.11) while being able to see the continuous SAW evolution ($\omega\tau_A = 0.21$ at $r/a = 0.8$) and for the future analysis and comparison with the 1/0 mode as the GAE has maximum amplitude for this choice of the radius (see Figure 7.8). In (b) we notice right away the spectrum excitation by the initial perturbation, analogously to what was done in the previous Chapter 7. This was foreshadowed in the previously discussed Figure 6.7, where oscilations of the radial magnetic field of 1/1 mode (black curve) can be observed at the very begining of the ramp phase. Thanks to the previous characterization of 1/1 mode (carried out in Section 7.2.2.2) we can identify the CAEs and the SAW spectra. At $\sim 1800t/\tau_A$ (during the collapse phase) we observe a sharp in time excitation of AEs: $1^{st} CAE$ excitation is observed. Other compressional modes or the shear mode are covered by either the initialy excited spectra or low frequency noise. Besides the expected spectra we also observe two more signals at $\sim 4.3\omega\tau_A$ and $\sim 8\omega\tau_A$. These values are consistent with 1^{st} and 2^{nd} CAEs of the 0/0 mode, discussed in Section 7.2.2.3. This shows that in our simulations different Fourier modes spectra can nonlinearly couple together, 1/1 and 0/0 in this case. Unlike the excitation of the 1/1 modes, this 0/0 spectrum is highly correlated to the kinetic energy oscillations (its intensity closely follows E_k profile), and as such its excitation coincides with the rise of kinetic energy ($\sim 1400t/\tau_A$) that leads to the crash ($\sim 1800t/\tau_A$).

To get an objective estimate of the contribution to the spectrum by various Alfvén modes, in Figure

8.1c is plotted the amplitude of the radial velocity field at various fixed frequencies, corresponding to different AEs in (b). For an easier reading of the graph, solid curves indicate AEs excitation by the magnetic reconnection event, dashed curves refer to modes excitation by initial perturbation and distortions due to edge effects. As discussed previously, the continuous shear is subject to the phase mixing damping, thus its amplitude will strictly rely on the low frequency noise that arises during the magnetic reconnection event, i.e. its amplitude gives a measure of the noise at low frequency. The 1^{st} CAE gets excited in $50t/\tau_A$ starting from $1700t/\tau_A$, while there is no confirmation of 2^{nd} and 3^{rd} CAEs as their frequencies are covered by the initial excitation of those modes. A cleaner picture can be seen by analysing the third cycle spectra in Figure 8.1e. It confirms a weak excitation of the 1^{st} and the 2^{nd} CAEs by the magnetic reconnection event, after which they decay quickly in time. In the following sections we will continue to explore which parameters and quantities play key role in AEs excitation and how to optimise them for this purpose.

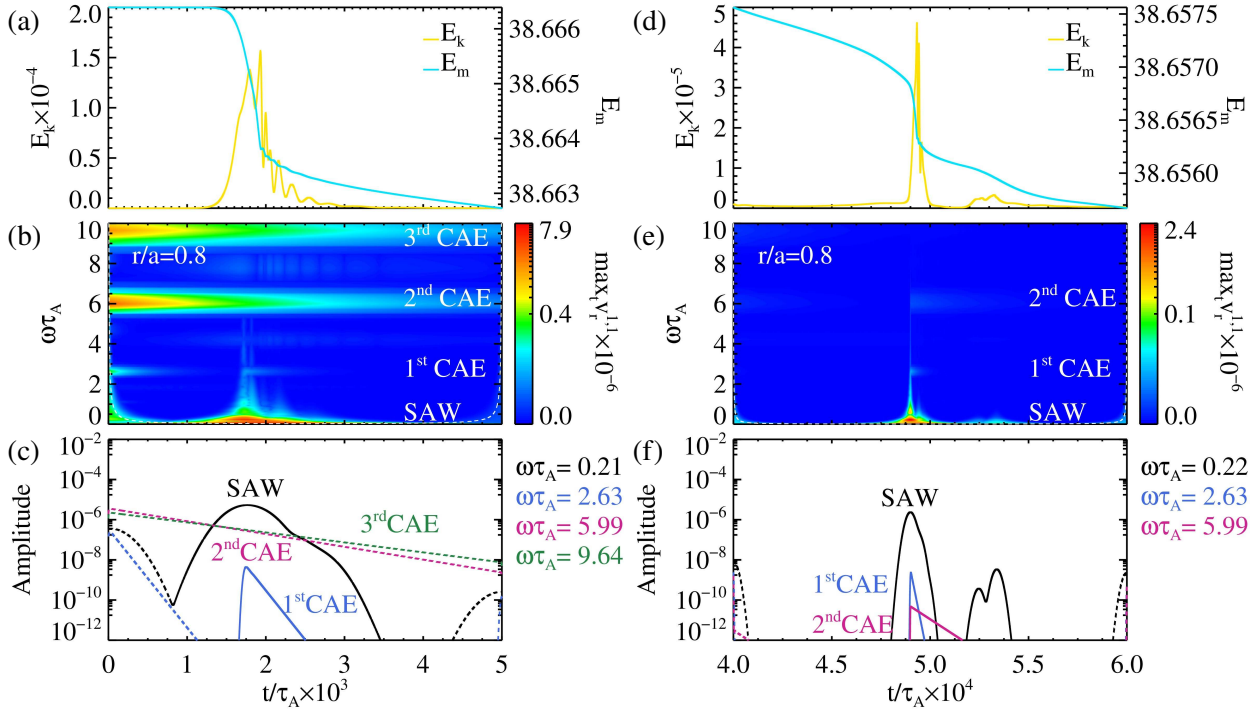

Figure 8.1: Time evolution of the total magnetic and kinetic energies ($S = 10^6$, $M = 10^6$) around the first sawtooth relaxation event (a) and the third one (b) in Fig.(6.6). b)-e) The corresponding evolution of the frequency spectrum of the normalized velocity field component $v_r^{1,1}$, obtained with CWT, at a fixed radius of $r/a = 0.8$. COI in dashed white curve. c)-f) Amplitude of $v_r^{1,1}$ at fixed frequencies $\omega\tau_A$ corresponding to different Alfvén modes. Solid curves indicate their excitation by the magnetic reconnection event, dashed curves refer to modes excitation by initial perturbation and distortions due to edge effects.

The next step in our analisys was to increase the Fourier space resolution from 4 to 32 harmonics with $h = 1$ helicity. As previously discussed this had the consequence of allowing the formation of smaller

scale structures, called plasmoids, along the reconnection current sheet, although in this treshold $S = 10^6$ case they did not affect the reconnection process in a meaningful way. Similarly their inclusion does not change the frequency spectrum or the degree of excitation of AEs by the reconnection event as can bee seen from Figure 8.2b, where the frequency spectra of the first sawtooth crash is shown (analogously to the spectrum with 4 harmonics in Fig. 8.1b). We can notice a shift of the sawtooth crash time, i.e. when the excitation of the Alfvén spectrum occurs. This shift is caused by the use of a smaller amplitude of the initial perturbation (10^{-9} compared to 10^{-6} in the previous case), done to mitigate as much as possible the intensity of the AEs excited by the initial perturbation, while keeping it high enough for the crash to occur in a reasonable amount of time. We observe, in panel (a), a slightly higher kinetic energy spike in correspondence to the sawthooth crash. This small increase does not noticeably change the AEs frequency spectra (panel (b)) and their amplitude (panel (c)) excited by the sawthooth crash. Furthermore now the initial excitation of AEs (dashed line at the begining) is comparable to the sawthooth excited spectrum (solid lines around $\sim 2900\, t/\tau_A$) as consequence of lower initial perturbation.

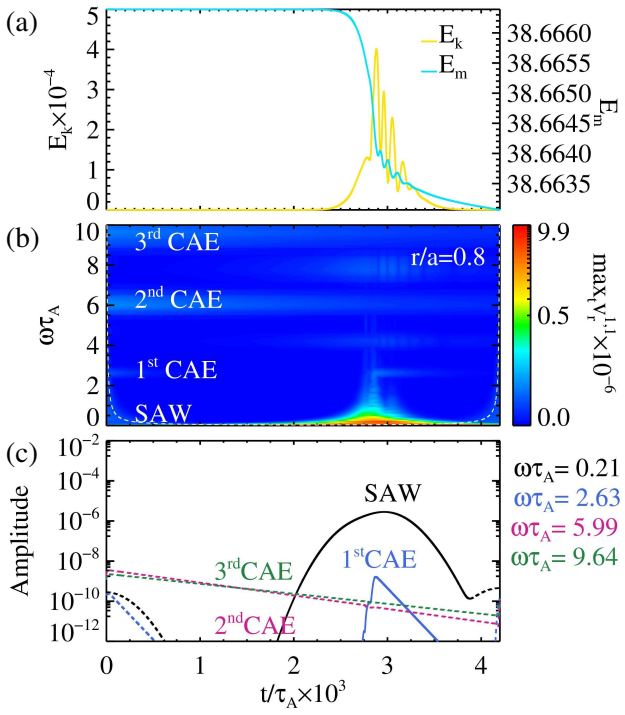

Figure 8.2: a) Time evolution of the total magnetic and kinetic energies ($S = 10^6$, $M = 10^6$) associated with different harmonics of the internal kink mode (m,-n)=(1,1). b) The corresponding evolution of the frequency spectrum of the normalized velocity field component $v_r^{1,1}$, obtained with CWT, at a fixed radius of $r/a = 0.8$. COI in dashed white curve. c) Amplitude of $v_r^{1,1}$ at fixed frequencies $\omega\tau_A$ corresponding to different Alfvén modes.

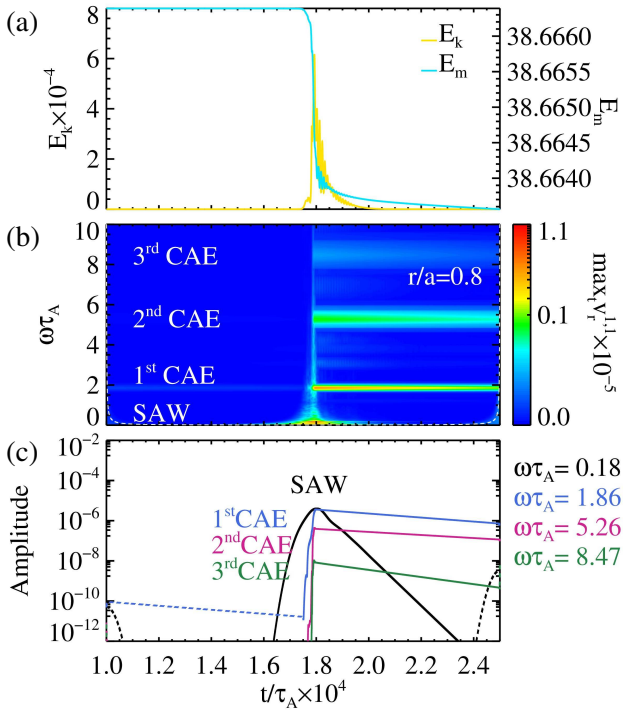

Figure 8.3: a) Time evolution of the total magnetic and kinetic energies ($S = 10^8$, $M = 10^6$) around the first sawthooth relaxation event in Fih. 6.17. b) The corresponding evolution of the frequency spectrum of the normalized velocity field component $v_r^{1,1}$, obtained with CWT, at a fixed radius of $r/a = 0.8$. COI in dashed white curve. c) Amplitude of $v_r^{1,1}$ at fixed frequencies $\omega\tau_A$ corresponding to different Alfvén modes.

8.1.2 High Lundquist case: role of plasmoids in Alfvén waves excitation

By lowering the resistivity (increasing Lundquist to $S = 10^8$) we get the full dynamics of the plasmoids (as described in Section 6.2.1.3): multiple plasmoids form and coalesce into a single secondary island that, due to the small asymmetry in the initial perturbation, displaces and fully reconnects with the main 1/1 island. This has the effect of speeding up the reconnection process, as was shown in Figure 6.15. Furthermore in this case we can observe in Figure 8.3a a higher kinetic energy spike, compared to before, and a wider delay of the crash, which is due to lower resisitivy itself. In panel (b) of the same figure is displayed the resulting frequency spectrum. A much stronger and defined excitation of Alfvén modes follows the magnetic reconnection event: the 1^{st}, the 2^{nd} and the 3^{rd} CAE can be clearly seen in the 1/1 mode spectrum. The excited spectrum is also much less damped over time and therefore persists for much longer after the sawtooth crash. In particular the 1^{st} CAE does not undergo the anomalous damping mechanism we discussed in Section 7.2.2, that is present when non-uniform density is considered. Indeed in this simulation a uniform density profile was used to better highligh the overall CAEs excitations, as CAEs intensity gets weaker the higher the frequency, and we wanted a clear and lasting 1^{st} CAE mode. This choice does not affect the MHD dynamics of the simulation, i.e. the

triggering mechanism of the AEs excitation, but only affects the anomalous damping in this case. This is not true in general, since the frequency of the SAW is a function of density, and consequently the GAE frequency is also affected. But as shown in Section 7.2.2.2 the 1/1 mode does not have a SAW minimum for the GAE to develop and moreover the SAW itself does not contribute much to the spectrum since it is damped quickly in time due to the phase mixing. This damping can be clearly seen in the panel (c), where the amplitudes of the various Alfvén modes are ploted, while the CAEs are damped slowly in time due to the visco-resistive dissipation.

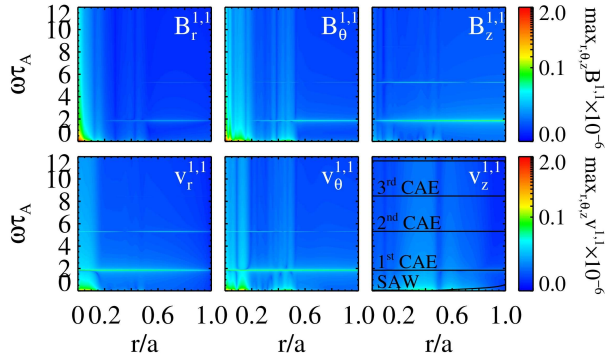

Figure 8.4: Analysis of $(m,-n) = (1,1)$ Fourier mode for the $t = (23000-23500)\,\tau_A$ snapshot from Fig.(8.3b). Results of numerical simulations with tokamak magnetic field and uniform density profile after the magnetic reconnection event characterized by the formation of plasmoids. The frequency spectra of $\mathbf{v}^{1,1}$ and $\mathbf{B}^{1,1}$ normalized fields components are shown as a function of radius, as computed for the time window $t \in [0, 500\tau_A]$. In the last panel the frequency spectrum is superimposed with the expected analytical solutions for SAW, CAEs and GAE.

We can look at a snapshot in time of the frequency spectrum as function of radius in Figure 8.4, obtained with the FFT analysis for the three components of the magnetic field and the velocity field. We consider the time window $t = (23000-23500)\,\tau_A$ after the reconnection event in order to avoid most of the intense low frequency fluctuations that is present around the sawtooth crash. We superimpose the frequency spectrum of the $v_z^{1,1}$ component with the theoreticaly expected one, as discussed in Section 7.2.2.2, in order to identify the various Alfvénic frequencies. This confirms the presence of the first three CAEs, the first one being the most excited while the third visible only with the CWT analysis in Figure 8.3b, while the SAW is several orders of amplitude lower than other modes (Figure 8.3c) and thus not visible in the spectrum.

8.2 Fully 3D Tokamak configurations

Finally we move to analyse fully 3D Tokamak configurations, charactherized by a Fourier spectrum composed of multiple helicities. Specifically, helicities $h = 1$ and $h = 2$ (or $h = 3/2$) to implement a three-wave coupling so that the 1/0 mode spectrum can be excited by self-consistent velocity perturbations produces by the sawtooth instability of the internal 1/1 kink mode. The coupling of the 1/1 mode with other helicities would be naturally present in toroidal geometry, but in the cylindrical geometry approximation of our present simulations, the presence of at least an additional mode (like the 2/1 or the 3/2) was necessary to provide the coupling with the 1/0 mode. We are interested in studying the AEs excitation with 1/0 periodicity as esperimentaly the n=0 is found to be the dominant toroidal number in Ohmic Tokamak discharges in a number of experiments, like Tokamak Fusion Test Reactor (TFTR) [Chang et al., 1995], ASDEX Upgrade [Maraschek et al., 1997] and Mega Ampere Spherical Tokamak (MAST) [Sykes, 2001]. Excitation and detection of Alfvén waves in Ohmic plasmas is not much studied and understood as currently the research on this subject is mostly centered around the excitation of AE by fast particles with velocities of the order of Alfvén speed, produced by neutral-beam injection (NBI), ion cyclotron resonance heating (ICRH), or even fusion born alpha particles, through the inverse Landau damping mechanism.

For the simulations in this section we employed the same Tokamak equilibrium with the spectrum of 32 harmonics of the 1/1 mode as in the last analyzed case, with now additionally the coupling mode 2/1 with its first harmonic 4/2 (or the 3/2 mode with its first harmonic 6/4) and a set of adjacent modes. Furthermore we continue to use the visco-resistive parameters set previously to $S = 10^8$ and $M = 10^6$.

8.2.1 Excitation of 1/0 mode spectrum by non-linear coupling with 2/1

In order to excite the 1/0 mode spectrum by magnetic reconnection events, triggered by the 1/1 internal kink mode, a three-wave coupling approach with 2/1 mode was adopted. As described in Section 6.2.2.1, in the specific tokamak equilibrium considered in this study (displayed in Figure 6.1), the 2/1 mode results marginaly stable during the nonlinear evolution of sawtooth cycles. As a result, after its initial excitation, its amplitude stays almost constant in time, providing a way for the nonlinear coupling between 1/1 and 1/0 modes. Therefore, in this section we will compute an analogous simulation to the helically symmetric one discussed in the previous section, now with a wider spectrum that allows the three-wave coupling in a fully 3D configuration, with tipical bell-shaped tokamak density profile that imitates experimental conditions.

In Figure 8.5 are plotted the frequency spectra of the 1/1 mode (left side), on which we focused our analysis in previous 2D simulations, and the 1/0 mode (right side) we are interested in analysing in 3D simulations. The first three CAEs are again clearly excited by the magnetic reconnection event in the 1/1 mode spectrum following the sawtooth crash (panel (b)). Comparing the 1/1 mode spectrum with the analogous one in 2D simulation in Figure 8.3b we notice right away the difference in the excitation of the 1^{st} CAE, due to the anomalous damping we described in Section 7.2.2 that is observed when considering non-uniform density profile. The 2^{nd} and 3^{rd} CAEs are closer in amplitude (panel (c)) than before, and as we will describe in the next section this is a consequence of the marginaly stable 2/1 mode amplitude. Moreover the CAEs frequencies are up-shifted in frequency, as expected from our analysis on single wave Tokamak cases in Chapter 7. The major difference in the new spectrum is the appearance of a new mode at low frequency $\omega\tau_A = 0.13$. This is a non linear coupling of the 1/0 GAE within the 1/1

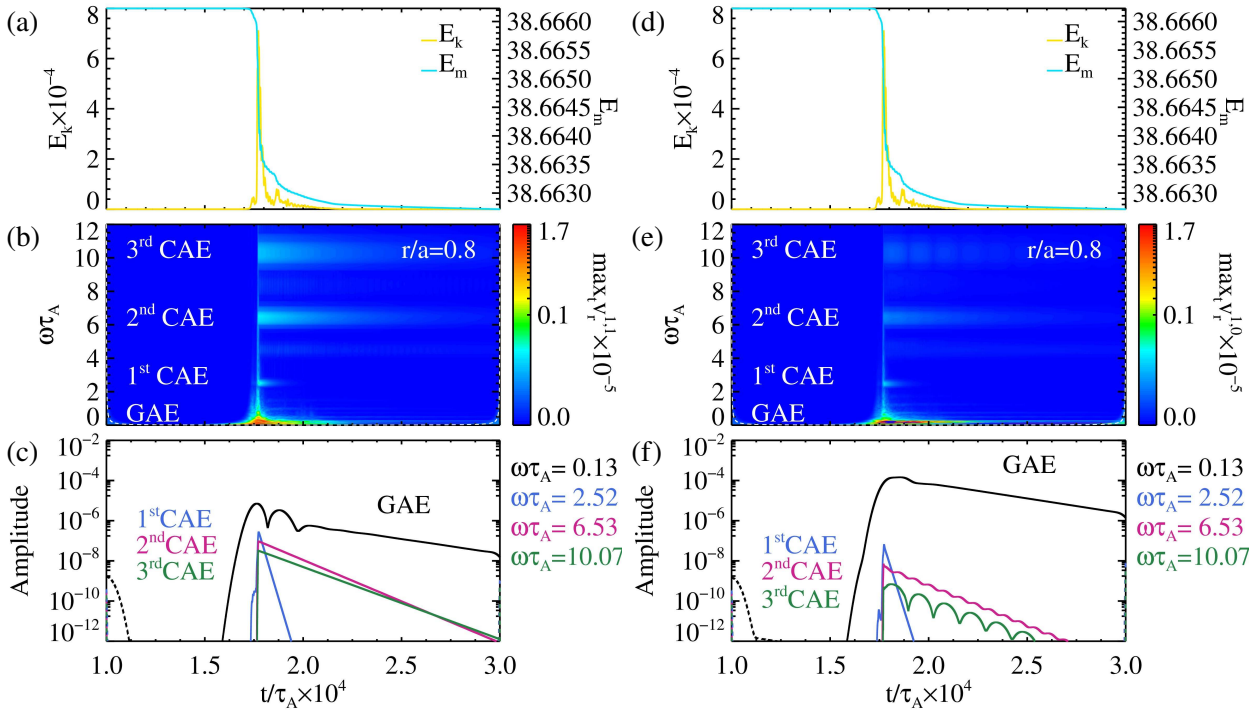

Figure 8.5: Left: analysis of $(m,-n) = (1,1)$ Fourier mode. Right: analysis of $(m,-n) = (1,0)$ Fourier mode. a)-d) Time evolution of the total magnetic and kinetic energies ($S = 10^8$, $M = 10^6$) around the first sawtooth relaxation event in Fig.(6.17). b)-e) The corresponding evolution of the frequency spectrum of the normalized velocity field component $v_r^{1,1}$, obtained with CWT, at a fixed radius of $r/a = 0.8$. COI in dashed white curve. c)-f) Amplitude of $v_r^{1,1}$ at fixed frequencies $\omega\tau_A$ corresponding to different Alfvén modes.

spectrum (the continuous shear with 1/1 periodicity does not have a local minimum for the GAE to be excited), similarly to the CAEs of the 0/0 mode we saw in the previous cases and that can be also seen here (very weak discrete signals around $\sim 4.3\omega\tau_A$ and $\sim 8\omega\tau_A$). This strong coupling is due to an even stronger excitation of the GAE in the 1/0 spectrum as can be seen in panel (f), while the CAEs are less excited compared to the 1/1 spectrum. The spontaneous arising of the 1/0 AEs by self-consistent MHD dynamic in Tokamak Ohmic plasmas was one of the goals of this Thesis.

This strong excitation of the 1/0 GAE is in agreement with an analogous study done by [McClements et al., 2002] where the GAE (with n=0 toroidal number) excitation by internal reconnection events (IREs) or edge localized modes (ELMs) was investigated. The numerical results we have obtained, showing that Alfvén waves can be excited by magnetic reconnection events in Ohmic Tokamak configuration charactherized by sawtooth dynamics, and in particular the 1/0 GAE strong excitation, provides a possible mechanism to explain the MHD mode activity in the Alfvén frequency that has been detected in the absence of energetic ions during discharges in several conventional tokamaks and spherical tokamaks, including the TokamakFusion Test Reactor (TFTR) [Chang et al., 1995] and the Mega-Amp Spherical Tokamak (MAST) [Sykes, 2001]. In TFTR the dominant toroidal mode number n was found to be

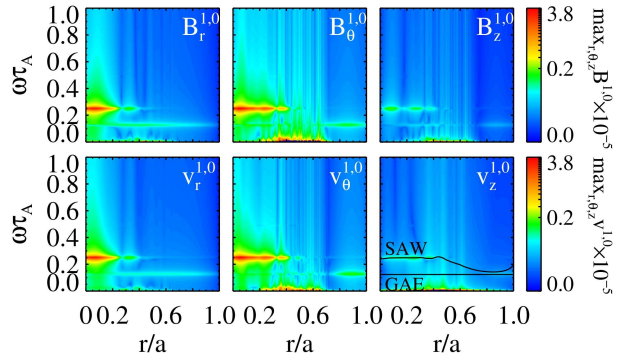

Figure 8.6: Analysis of $(m,-n) = (1,0)$ Fourier mode for the $t = (22500-23000)\,\tau_A$ snapshot from Fig.(8.5e). Results of numerical simulations with tokamak magnetic field and bell-shaped density profile, after the magnetic reconnection event characterized by the formation of plasmoids. The frequency spectra of $\mathbf{v}^{1,0}$ and $\mathbf{B}^{1,0}$ normalized fields components are shown as a function of radius, as computed for the time window $t \in [0, 500\tau_A]$. In the last panel the frequency spectrum is superimposed with the expected analytical solutions for SAW and GAE.

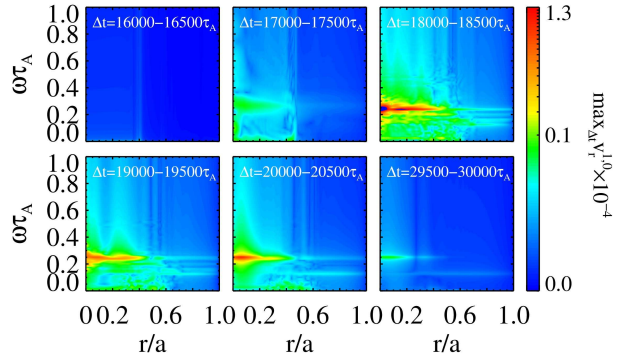

Figure 8.7: Numerical simulation with tokamak magnetic field and bell-shaped density profile. Time evolution of the frequency spectrum of the normalized velocity field component $v_r^{1,0}$ around the magnetic reconnection event (first 5 panels) and the end of the simulation (last panel), obtained with FFT.

zero; this is also the case in MAST discharges for which mode number information was available. The observed properties of these modes were shown to be consistent with global Alfven eigenmodes.

By comparing the analysis in frequency of the Tokamak simulation performed in this Chapter with the corresponding analysis of the sawtooth dynamics done in Chapter 6 we want to point out the strong correlation between the progressive appearance and influence (for $S \geq 10^7$) of plasmoids in the magnetic reconnection dynamics and the ease of excitation of AEs. As we will show in the next Chapter, plasmoids are not essential for the AEs excitation by reconnection events in the Ohmic RFP configuration (where $S = 10^6$ will be used) but they may play an important role in facilitating their excitation in Ohmic Tokamak configurations. Further investigation will be needed to establish the importance of this role.

To end this section we look at a snapshot in time of the frequency spectrum as function of radius in Figure 8.6, obtained with the FFT analysis for the time window $t = (22500 - 23000)\,\tau_A$ after the reconnection event in order to avoid most of the intense low frequency fluctuations that is present around the sawtooth crash. Here we look at low frequency which is more strongly excited and can be clearly analyzed with the FFT. We superimpose the frequency spectrum of the $v_z^{1,0}$ component with the theoreticaly expected one, as discussed in Section 7.2.2.1, in order to identify the Alfvénic frequencies. The GAE is excited right below the SAW minimum, while the latter underwent phase mixing and disapeared except the region near the center ($r/a \leq 0.4$) where its approximately constant. In Figure 8.7 are shown spanshots of the low frequency spectrum of the $v_r^{1,0}$ component from the start of the simulation (first panel), to the end (last panel), where the temporal evolution of the spectrum is displayed, showing the excitation of the SAW and GAE by the magnetic reconnection event.

8.2.1.1 Effect of 2/1 mode amplitude on excitation of Alfvén waves

We can further analyze the 2/1 coupling by investigating the effect that its amplitude can have on the excitation of AEs by magnetic reconnection events, as its marginaly stable amplitude was set by the degree of the initial perturbation we chose to apply as described in Section 6.2.2.1.2, and because of its disruptive nature in Tokamak discharges, we wanted to determine the lowest amplitude that could give enough coupling for the excitation of 1/0 mode AEs. In Figure 8.8 are displayed the temporal evolutions of the frequency spectra for four different simulations (including the previous case in panel (b)), all with the same parameters as the previous fully 3D case but different amplitude of the 2/1 mode, from the highest (panel a) to the lowest amplitude (panel d). The strongest effect on the overall dynamics can be seen for the highest 2/1 mode amplitude of 3×10^{-4} in panel (a): the sawtooth crash occurs much sooner in time compared to other cases, and it exhibits the highest kinetic energy spike, with the result of having the highest low frequency fluctuation around the sawtooth crash. For lower amplitudes of 5×10^{-5}, 7×10^{-6} and 7×10^{-7} the dynamics remain comparatively very similar, with overall similar levels of CAEs excitation. In particular, we can notice two consistent trends: the smaller the amplitude of the 2/1 mode, the larger the separation between the 2^{nd} and the 3^{rd} CAEs (1^{st} CAE trend is not clear due to its strong anomalous damping) and a lowering of the 1/0 GAE within the 1/1 spectrum, that is weaker non-linear coupling between different mode spectra, with the lowest amplitude case having the 1/0 GAE amplitude comparable to the 1/1 2^{nd} CAE (the bump in amplitude around 2.5×10^4 is due to an equally small bump in kinetic energy). This analysis indicates that the AEs excitaton via the three wave coupling does not heavily depend, at least qualitatively, on the specific amplitude of the 2/1 mode, excluding the extreme cases of high amplitude ($\geq 3 \times 10{-}4$) and low amplitude ($\leq 7 \times 10^{-7}$). In the next section we will also show that qualitatively similar results of AEs excitation can be obtained by using another helicity for the three wave coupling.

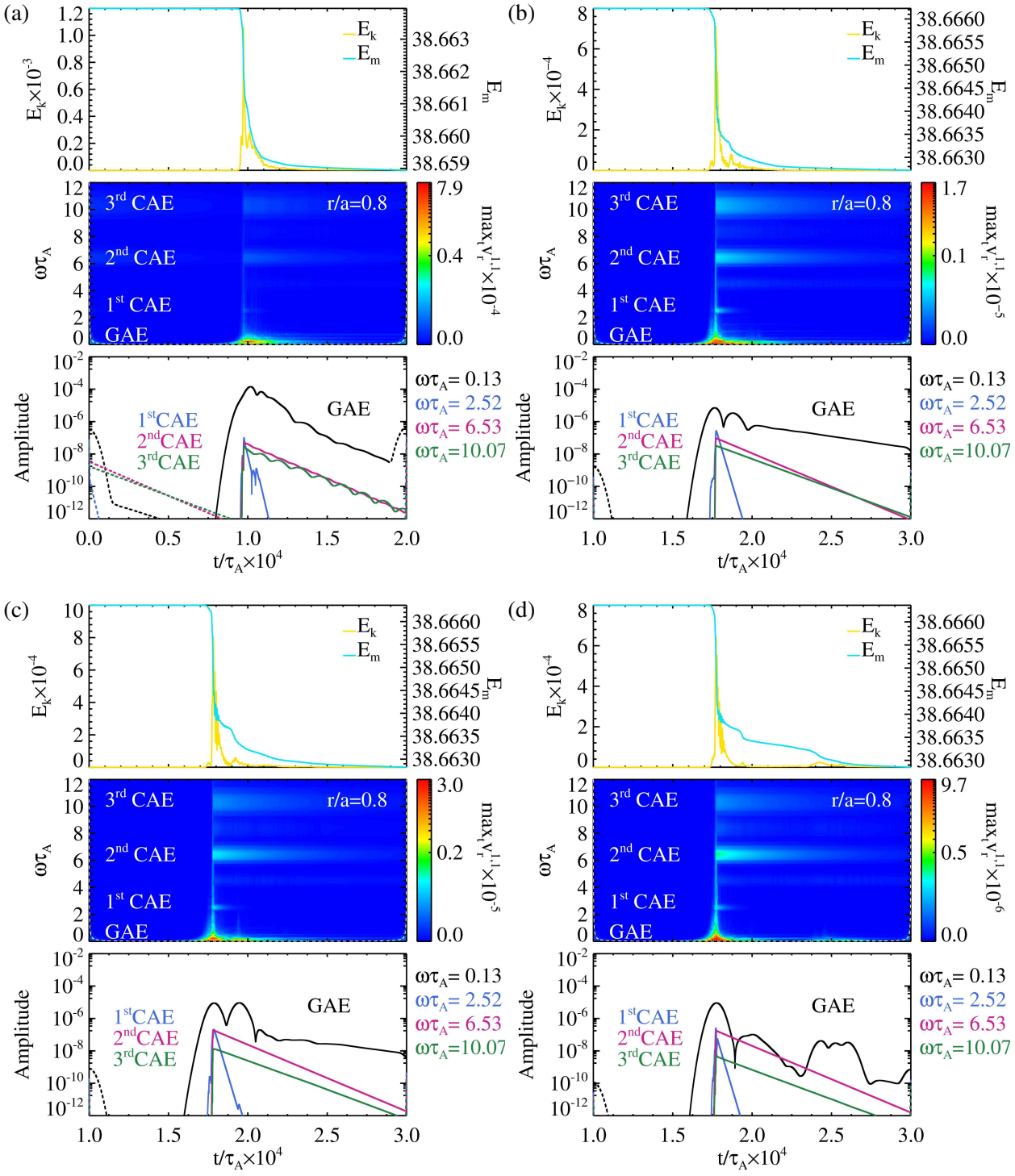

Figure 8.8: Analysis of $(m,-n) = (1,1)$ Fourier mode with decreasing amplitude of $(m,-n) = (2,1)$ mode, from highest (a) to lowest (d). **Top panels**: time evolution of the total magnetic and kinetic energies ($S = 10^8$, $M = 10^6$) around the first sawtooth relaxation events in Fig.(6.23). **Middle panels**: the corresponding evolution of the frequency spectrum of the normalized velocity field component $v_r^{1,1}$, obtained with CWT, at a fixed radius of $r/a = 0.8$. COI in dashed white curve. **Bottom panels**: amplitude of $v_r^{1,1}$ at fixed frequencies $\omega\tau_A$ corresponding to different Alfvén modes.

8.2.2 Comparison with 3/2 mode coupling approach

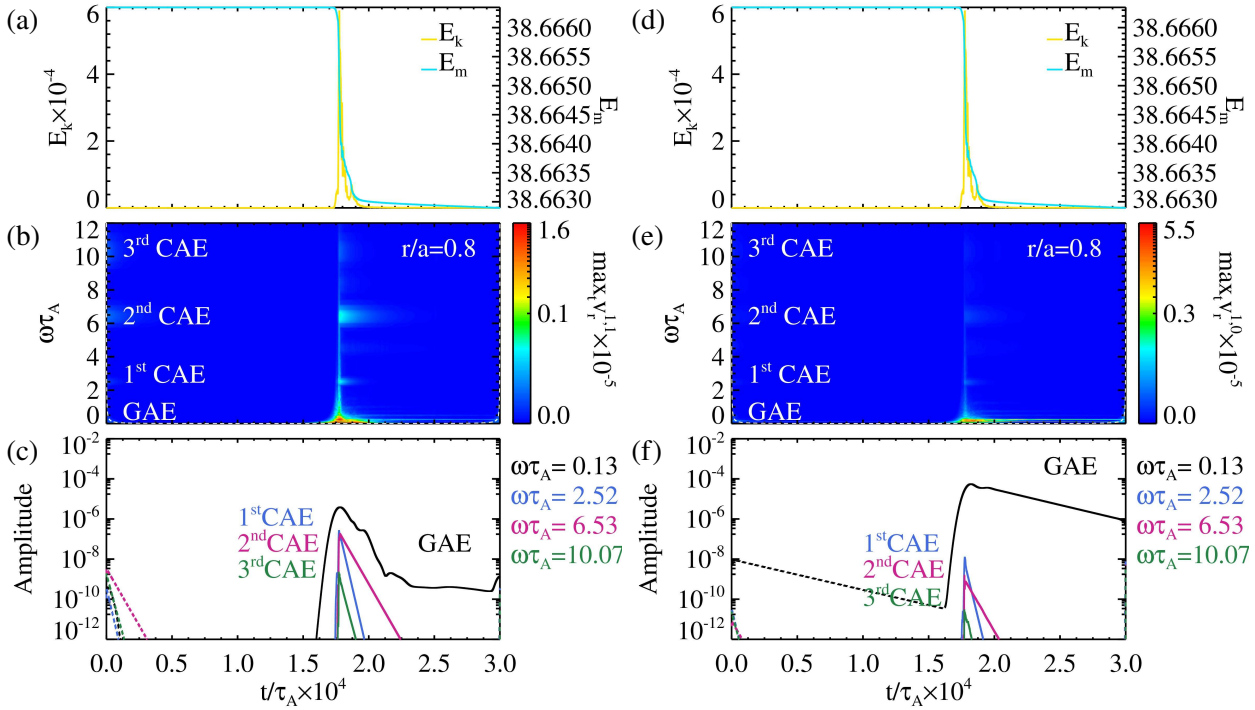

Figure 8.9: Left: analysis of $(m,-n) = (1,1)$ Fourier mode. Right: analysis of $(m,-n) = (1,0)$ Fourier mode. a)-d) Time evolution of the total magnetic and kinetic energies ($S = 10^8$, $M = 10^6$) around the first sawtooth relaxation event in Fig.(6.25). b)-e) The corresponding evolution of the frequency spectrum of the normalized velocity field component $v_r^{1,1}$, obtained with CWT, at a fixed radius of $r/a = 0.8$. COI in dashed white curve. c)-f) Amplitude of $v_r^{1,1}$ at fixed frequencies $\omega\tau_A$ corresponding to different Alfvén modes.

To end this Chapter we wanted to show that the results obtained above do not specificaly depends on the coupling helicity we chose but can also be qualitatively replicated with other helicities. Here an alternative coupling approach with the marginally stable 3/2 mode is used, as this mode is less harmfull for the magnetic confinement in Tokamak discharges. Same parameters and configuration as in the fully 3D case discussed above are considered, except now we use the marginaly stable 3/2 mode analogously to what was done with the 2/1 mode and a time step 10^{-3} was considered instead of 10^{-4}, to reduce the computational time. We can directly compare this simulation spectrum for the 1/1 mode (left-side of Figure 8.9) with the correspective simulation with 2/1 coupling approach (with the same 2/1 mode amplitude in Figure 8.8d). The 1/0 GAE mode shows a similar trend in time betwen the two simulations, with equal degree of excitation at the magnetic reconnection event around 1.8×10^4 and same amplitude at the end of both simulations. A significant difference instead is given by the damping rate of the CAEs, that are generally much more damped with the 3/2 coupling approach. This is most likely due to a numerical damping we encountered with SpeCyl code when same simulations

with different time steps were considered. In particular when increasing the time step a higher damping of the frequency spectrum was observed. However the spectrum itself remained consistent for time steps $\geq 10^3$, so the excited AEs can be reliably identified. In the right-side of the Figure 8.9 we can see the 1/0 mode spectrum and more importantly the strong excitation of the GAE mode, which closely match the corresponding GAE spectrum in Figure 8.5 for the 2/1 case. This analysis shows that both coupling approaches provide a consistent picture of the nonlinear excitation of 1/0 AEs, and most notably the 1/0 GAE for reasons described previously, by the sawtoothing 1/1 internal kink. Summarising, we find that CAEs and especially GAE modes are observed with 1/0 periodicity for all amplitudes of the 2/1 (or 3/2) tearing mode. Which would indicate that even in a normal Tokamak plasma, with typically very small tearing islands, the sawtooth should excite Alfvénic modes, which can explain the predominantly n=0 AEs observed in Ohmic Tokamak discharges.

Chapter 9

Alfvén waves excitation by magnetic reconnection events in RFP configuration

As the final step of this study, we consider the case of time-evolving fully-3D RFP simulation, with quasi-periodic magnetic reconnection events associated with the typical RFP sawthooting activity, as described in the modeling studies of Refs. [Bonfiglio et al., 2013; Veranda et al., 2017; Veranda et al., 2020]. This is close to the experimental conditions and this analysis will make possible a direct comparison with the experimental observations in the RFX-mod device.

The nonlinear MHD simulation that is analyzed here is a continuation of the original simulation reported in Ref. [Bonfiglio et al., 2013], with same MHD spectrum but with a non-uniform RFX-mod-like hollow density profile instead of the standard uniform density profile typically used in SpeCyl. As in the previous section, fields are saved each $0.1\,\tau_A$ (a high sampling frequency suitable for the analysis of Alfvén waves) instead of each $10\tau_A$ as done in the original simulation. The time step is also reduced from $t = 5\times10^{-2}\,\tau_A$ to $t = 10^{-3}\,\tau_A$ to obtain a more accurate characterization of Alfvén modes. These differences slightly change the dynamics with respect to the original simulation, but only quantitatively and not qualitatively. As in the original simulation, a spectrum of 225 Fourier harmonics with $0 \leq m \leq 4$ is used, the on-axis Lundquist and viscous Lundquist numbers are set to $S = 10^6$ and $M = 10^4$, respectively, and a seed helical perturbation with $m = 1$, $n = -7$ periodicity is applied to the edge B_r to stimulate quasi-helical states in between reconnection events as discussed in Ref. [Bonfiglio et al., 2013].

The temporal evolution of the edge safety factor $q(a)$ and the normalized edge B_z amplitudes of the most active $m = 1$ modes are shown in Figure 9.1, for the original simulation on the left column, and for the modified one on the right. The original simulation starts from a non-reversed 1D paramagnetic pinch equilibrium. The initially positive edge safety factor $q(a)$ suddenly reverses due to the nonlinear 3D MHD activity associated to resistive-kink tearing modes (see Ref. [Veranda et al., 2020]), providing the so-called dynamo mechanism (i.e. magnetic flux pumping provided by toroidal current density partially converted into poloidal one, due to kink effect). The system, then, undergoes sawtoothing oscillations exhibiting periodic magnetic reconnection events as highlighted by bursts in the MHD mode amplitudes. The new simulation starts from time $t = 3.0\times10^4\,\tau_A$ of the original simulation. We focus on two subsequent sawtoothing cycles.

We consider in particular the $(m,n) = (1,0)$ mode as in the previous single-wave RFP-like cases

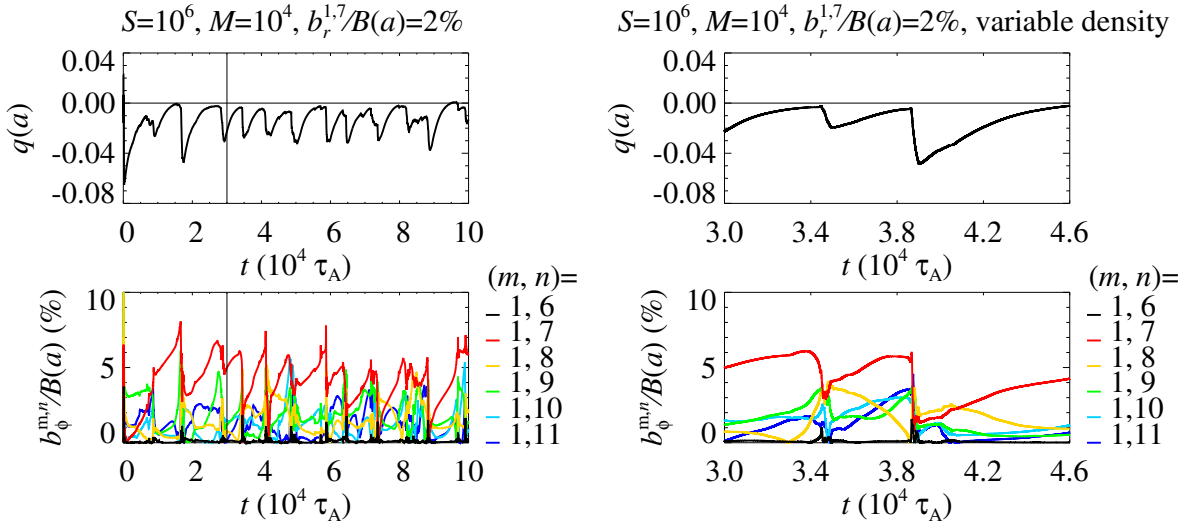

Figure 9.1: Time-evolving RFP configuration. In the top panels it is shown the temporal evolution of the edge $q(a)$, while in the bottom panels the edge amplitudes of the most active $m = 1$ modes (color coded) are shown as a function of time. The original simulation reported in Ref. [Bonfiglio et al., 2013] is shown in the left column, while on the right the new simulation with RFX-mod-like hollow density profile analysed in this paper is shown, starting from time $t = 3.0 \times 10^4 \tau_A$ of the original simulation and showing two subsequent magnetic reconnection events.

(discussed in Section 7.3), but a fundamental difference is that now the simulation includes many nonlinearly interacting MHD modes as shown in Fig. 9.1. Similarly to Tokamak simulations studied in the previous chapter, Alfvén modes in this simulation do not depend on specific details of the initial velocity perturbation. Now, each reconnection event self-consistently excites, through the associated velocity perturbation, Alfvén modes in a quasi-periodic fashion. Again, although in this new simulation the mean magnetic field is time evolving, such mean field is still changing much slower compared to the evolution of Alfvén waves, and therefore it can be used as before for theoretical predictions of the Alfvén modes frequency spectrum.

We now analyze for the new simulation the time evolution at fixed radius $r/a = 0.6$ of the $v_r^{1,0}$ spectrum using the CWT technique, as shown in Figure 9.2, where we also plot the time traces of the edge $B_z^{0,0}$ normalized magnetic field component and the corresponding trend of kinetic and magnetic energies. As expected, during the magnetic reconnection events, starting around $t = 3.45 \times 10^4 \tau_A$ and $t = 3.90 \times 10^4 \tau_A$, a rapid decrease of magnetic energy is observed while the kinetic energy has a peak. At the same time, we can observe an excitation of the frequency spectrum following the two magnetic reconnection events which lasts for some time. In particular, the frequency spectrum in time shows intense low-frequency fluctuations and also weaker discrete signals at higher frequencies (horizontal lines in the spectogram) which are particularly noticeable after the second reconnection event resulting in a much stronger velocity perturbation than the first one. The low-frequency fluctuations are due to tearing modes which dominates the dynamics of the system in this configuration. The discrete signals, on the other hand, can be identified as Alfvén modes as we will discuss shortly. We can also look at time

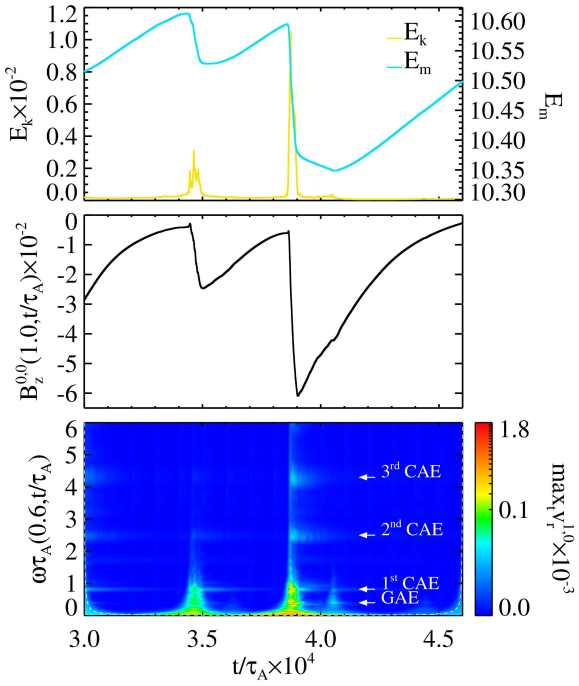

Figure 9.2: Results of the numerical simulation with time-evolving RFP magnetic field and RFX-mod-like hollow density profile ($S = 10^6$, $M = 10^4$). $(m,n) = (1,0)$ mode. a) The time trace of the normalized kinetic energy E_k and normalized magnetic energy E_m. b) The time trace of the normalized magnetic field component $B_z^{0,0}$ at a fixed radius $r/a = 1.0$. c) The CWT showing the time evolution of the frequency spectrum of the normalized velocity field component $v_r^{1,0}$ at a fixed radius $r/a = 0.6$.

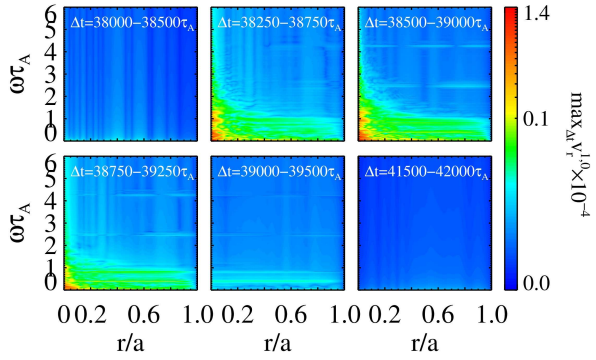

Figure 9.3: Numerical simulation with time-evolving RFP magnetic filed and RFX-mod-like hollow density profile. Time evolution of the frequency spectrum of the normalized velocity field component $v_r^{1,0}$ around the magnetic reconnection event (first 5 panels) and the end of the simulation (last panel), obtained with FFT.

snapshots as function of radius in Fig. 9.3, obtained with the FFT analysis around the second magnetic reconnection event in Figure 9.2. This confirms that the Alfvénic modes are excited by the magnetic reconnection event itself, in fact they are absent just before it (first panel) and after it (last panel). The Alfvénic modes disappear again after some thousand Alfvén times after the magnetic reconnection event (last panel), due to the various damping mechanisms already discussed in Chapter 7.

In Figure 9.4 we superimpose the frequency spectrum of the v_{1r} component, after the stronger magnetic reconnection event at $t = 3.90 \times 10^4\, \tau_A$, with the theoreticaly expected one in order to identify the various Alfvénic frequencies. We recognize the first three CAE frequencies, the first one being the most excited while the third being barely visible, and the GAE mode, which indirectly confirms the presence of the continuous SAW, being damped by phase mixing and hidden by noise from low-frequency MHD fluctuations. Note that in this case the GAE is seen with the RFX-mod-like hollow density profile, while in the RFP simulations with initial velocity perturbation (discussed in Section 7.3) it was seen only with the density profile peaked in the center. As mentioned previously, we have chosen to analyse the $(m,n) = (1,0)$ harmonic as in RFX-mod it is one of the modes with the strongest Alfvénic activity [Spagnolo et al., 2011]. This is also the case for the fully 3D simulation, as an analysis of the frequency spectra of a wide range of (m,n) modes ($0 \le m \le 2$ and $-9 \le n \le 9$) right after the magnetic reconnection events showed the strongest excitation of AEs in the $(m,n) = (1,0)$ mode (discussed below). The numerical result we have obtained, showing that Alfvén waves can be excited by magnetic reconnection events in RFP configuration, provides a theoretical confirmation of experimental observations in the RFX-mod device, where the same qualitative phenomenology (with Alfvénic fluctuations excited after reconnection events) is found.

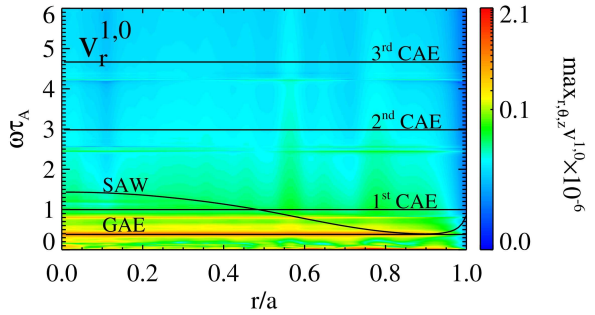

Figure 9.4: Time-evolving RFP magnetic field and RFX-mod-like hollow density profile. Verification of frequency spectrum right after the stronger magnetic reconnection event ($\Delta t = (3.90 - 3.95) \times 10^4 \tau_A$, fifth panel in Fig. (9.3)) with the theoretical model for the $v_r^{1,0}$ velocity field component. The color scale has been adjusted, compared to Fig. (9.3), to better highlight the presence of the GAE.

Excitation of Alfvénic modes for different Fourier harmonics (m,n)

As we mentioned before, we have chosen to analyse the $(m,n) = (1,0)$ harmonic because it is the one in which the Alfvénic modes are most excited. We can clearly see this from Figure 9.5 in which we plotted the 1^{st} CAE amplitude for a wide range of Fourier modes, in particular $-1 \le m \le 1$ and $-9 \le n \le 9$ (technically we analysed only half of those modes as the other half derives from the symmetry condition

(6.6)). This numerical observation is also in agreement with experimental observations [Spagnolo et al., 2011] in the RFX-mod experiment, where the poloidal and toroidal periodicities of the measured Alfvénic fluctuations can be reconstructed and appear to be consistent with a dominant $m = 1$, $n = 0$ component.

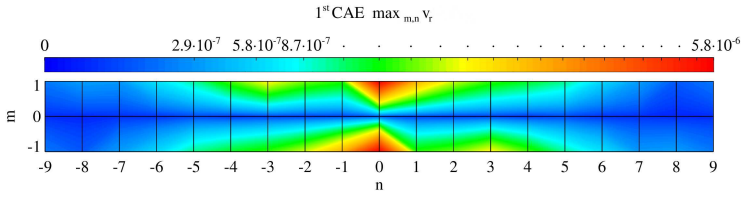

Figure 9.5: Simulations with time-evolving RFP magnetic field and RFX-mod-like hollow density profile. The variation in the amplitude of the 1^{st} CAE for different harmonics (m,n).

9.1 Comparison with experimental observations in RFX-mod

We now conclude this Chapter, on numerical results from nonlinear MHD modelling, with a qualitative comparison of numerical RFP results with experimental observations on the RFX-mod device. As discussed in Section 3.3, five distinct peaks have been observed in the power spectrum of the magnetic fluctuation measured at the plasma edge of RFX-mod device (Figure 3.5). These peaks have been named a, b, c, d and e following the increase of their frequency, from ~ 130 kHz to ~ 1 MHz. While the first three peaks (a,b,c) are present only during the SHAx state, in which the plasma is in an almost stationary equilibrium with helical symmetry with a single magnetic axis, as discussed in Section 3.2, the two highest frequency peaks, d and e, do not seem to be associated to any particular behavior of the dominant mode, being present during almost the full discharge duration. All of these peaks are interpreted as Alfvén waves because their frequencies scale linearly with the Alfvén velocity of the plasma, as shown in Figure 3.7.

We will give now an interpretation of those experimental observations, based on the results of the analysis carried out in this Chapter. In particular we want to compare the experimental findings with the analysis results of the most sophisticated and the closest to the experimental conditions simulation, that is the one with the time-evolving fully-3D RFP magnetic configuration with hollow-like density profile, discussed in the previous section.

We start by comparing the frequencies of the experimentally observed Alfvén waves (the five peaks) with the frequency spectrum of the fully-3D RFP simulation from Figure 9.4. In order to do so we first need to plot the numerical frequency spectrum in physical units, as until now we have always considered dimensionless units. By tacking the RFX-mod minor radius $a = 0.459$ m and a reference Alfvén speed of $v_A = 2500$ km/s, we obtain the following Alfvén time $\tau_A = a/v_A \simeq 0.2\ \mu$s. The resulting frequency spectrum in physical units is shown in Figure 9.6, where we indicated the Alfvénic nature of the discrete signals, identified in the previous Sections. On the other hand, in Figure 9.7 we mark the frequencies of d and e peaks corresponding to the reference Alfvén speed.

Comparing the two previous plots, we immediately notice that the GAE and the 1^{st} CAE frequencies values appear in the same frequency range of d and e peaks, with comparable separation between them. This brings us to formulate the following hypothesis on the Alfvénic nature of those peaks, namely that d corresponds to a GAE mode, while e corresponds to the 1^{st} CAE. Moreover this tells us the physical

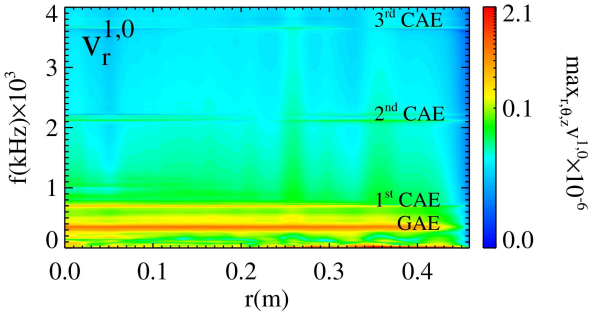

Figure 9.6: Same frequency spectrum as in Fig.(9.4), but in physical units by taking $v_A = 2500$ km/s and a minor radius of RFX-mod $a = 0.459$ m.

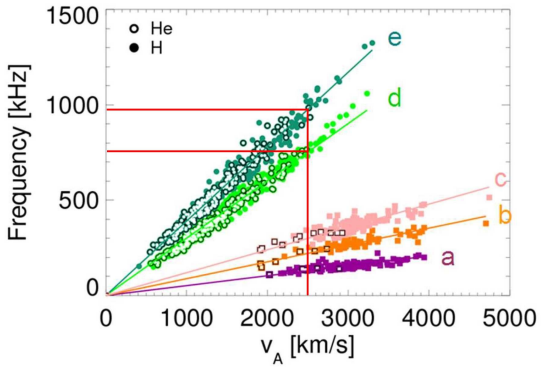

Figure 9.7: Relation between modes frequency and Alfvén velocity for a large database of H and He plasmas (as also discussed in Ref. [Spagnolo et al., 2011]). The frequencies for peaks *d* and *e* corresponding to the Alfvén velocity $v_A = 2500$ km/s are marked in red.

mechanism from which these Alfvén waves (*d* and *e* peaks) arise. Indeed from analysing fully-3D RFP simulations, we have found out that the Alfvén modes, such as CAE and GAE, are excited by the reconnection magnetic events. The phenomenon of periodic magnetic reconnection events is also found in the RFX-mod discharges from which the data in Figure 9.7 were taken. We can see the signature of those events in the power spectrum of the magnetic fluctuation in Figure 3.4. Thus we can conclude that the Alfvén waves corresponding to the *d* and *e* peaks are physically excited by the magnetic reconnection events taking place in the plasma. We also point out the resemblance of the experimental frequency spectrum in time during a magnetic reconnection event of Figure 3.4 and the numerical one in Figure 9.2. In particular similarly to the experimental spectrum, in the numerical one during a reconnection event we can also see the vertical bright lines, which are a global (i.e. at all frequencies) enhancement of the fluctuation level. As mentioned before, the experimental Alfvén waves that are present during the full discharge duration (*d* and *e* peaks) do not show a significant damping in time, while the numerical one are excited only during the reconnection events, after which they decay more or less quickly in time, especially in case of the hollow-like density profile because of resonance absorption. It is worth

noting that we used higher resistivity and viscosity values compared to those estimated experimentally [Piovesan et al., 2009b] and this contributes to a stronger damping of the Alfvénic modes in between the magnetic reconnection events in our simulation than in the experiment.

At last, to further validate the numerical findings with respect to the experimental ones, we show below in Figure 9.8 the experimental frequency spectrum in time, of the derivative of the poloidal magnetic field ($\dot{b}_\theta$) fluctuation at $r/a = 1$, in particular plasma conditions for which the d and e peaks are shifted in frequency from ~ 1 MHz to around 600 kHz, as can bee seen from the power spectrum in Figure 9.9. This shift allows us to see higher frequencies in the power spectrum, and as we can see a new faint signal (f peak) appears around $1,2$ MHz. By qualitatively comparing this spectrum with the numerical one in Figure 9.6, the natural conclusion is to identify this new peak with the 2^{nd} CAE, both for its frequency value in relation to the d and e peaks and its lower amplitude, being much less excited that the e peak, similarly to the excitation of the 2^{nd} CAE compared to the 1^{st} one in Figure 9.6.

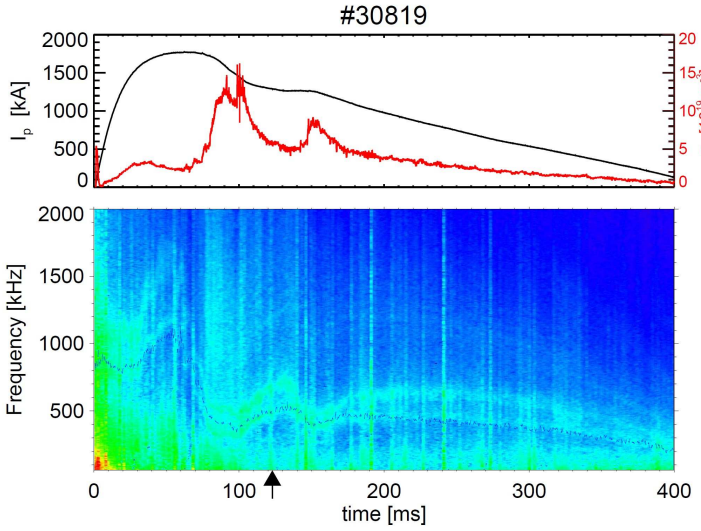

Figure 9.8: Top: plasma current I_p time trace; bottom: spectrogram of a $\dot{b}_\theta$ signal. The black arrows refer to the time instant for the analysis in Figure 9.9. [M. Zuin, private communication]

In our study we could not reproduce the three lower frequency experimental peaks (a, b and c) observed only during the improved confinement quasi-helical states. This can be due to approximations of the employed numerical model, which neglects toroidal, finite beta and kinetic effects. A toroidal geometry and finite beta would allow for the TAE and the BAE gaps to be excited, with frequencies below the GAE one [Villard et al., 1997; Liu et al., 2019], by either energetic particle tails (observed in past studies in RFX-mod plasmas, for which a wave-particle interaction model was proposed [Costa et al., 1999]) or other mechanisms. Maraschek *et al* [Maraschek et al., 1997] proposed the role of the inverse energy cascades on the coupled drift Alfvén small-scalle turbulence to explain the observation of TAEs in ohmically heated tokamak plasmas. Such a coupling has also been identified in the edge region of the RFX-mod plasmas in the form of drift Alfvén vortex structures [Vianello et al., 2010], so that the role of TAEs excitation played by the inverse cascade also for RFX-mod plasmas cannot be excluded. Similarly BAEs destabilization by resonant magnetic perturbations in Ohmic discharges in J-TEXT tokamak have also been observed [Liu et al., 2019]. Furthermore it was shown [Breizman et al., 2005; Fu et al., 2006]

that the coupling of pressure gradient and the averaged magnetic curvature is important and favorable to the existence of the RSAE, more so in RFP configuration due to the low q value [Cai et al., 2014] and the possible identification of experimental peaks a, b and c as RSAEs has been speculated [Spagnolo et al., 2010].

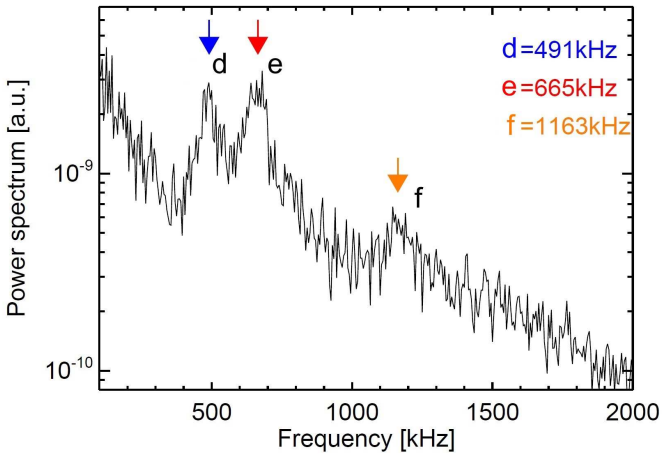

Figure 9.9: Power spectrum of a $\dot{b}_\theta$ signal evaluated during the time instant indicated by the arrow of Figure 9.8. [M. Zuin, private communication]

To conclude we have a qualitative agreement between the numerical simulations and the experimental observations of Alfvén waves in the RFX-mod device, and therefore we propose the following physical interpretation: in RFX-mod some Alfvén waves are excited directly by the magnetic reconnection events occurring during the plasma discharge in which high energy particles are also generated, and afterwards they are sustained by these energetic particles in between the reconnection events. In particular, we have identified the experimental peaks d, e and (when observed) f as a GAE, the 1^{st} CAE, and the 2^{nd} CAE, respectively.

Part IV

Summary and conclusions

Summary and conclusions

The work presented in this Thesis focuses on a systematic investigation of the physics of Alfvén waves in magnetically confined plasmas, by means of analytical theory and numerical simulations based on the nonlinear 3D MHD model. *The main goal* of this research was the characterization and interpretation of Alfvén waves spectra and their excitation mechanism based on periodic magnetic reconnection events in Tokamak and RFP configurations. To achieve this, the modelling of quasi-periodic sawtooth cycles, triggered by an internal kink instability, was considered for the Tokamak configuration. Similarly a systematic repetition dynamics of quasi-single helicity (QSH) states in between relaxation events was considered for the RFP configuration. The results thus obtained are consistent with the experimental detection of Alfvénic modes in the absence of energetic particles during Ohmic Tokamak discharges in several conventional and spherical tokamaks, including TFTR [Chang et al., 1995], ASDEX [Maraschek et al., 1997] and MAST [Sykes, 2001]. Similarly, the results of AEs excitation in RFP modelling are in agreement with the detection of coherent modes of Alfvénic nature observed in the power spectrum of magnetic fluctuations at the RFX-mod plasma edge [Spagnolo et al., 2011], and their identification is proposed based on simulation results.

This characterization of Alfvén waves was achieved following four approches of study that can be synthetized in four main categories: preparatory *nonlinear MHD modelling*, *AEs excitation in single wave simulations with fixed equilibrium fields*, *AEs excitation in sawtoothing Ohmic Tokamak* and *AEs excitation in sawtoothing Ohmic RFP*. The results obtained during my PhD following the different approaches, described in the next four paragraphs, are deeply inter-connected and provide a further step in the path toward a qualitative and quantitative predictive capability of the numerical tools.

The first challenge of the *nonlinear MHD modelling* (Part II, Chapter 6) study was the setup of plasma parameters and Fourier space resolution aimed at achieving a self-consistent dynamics of magnetic reconnection events, in both RFP and Tokamak, that were consistent with the typical dynamics of each magnetic configuration as well as able to excite Alfvénic modes by self-generated perturbations of velocity fieds. In particular for Tokamak configuration this was achieved by conditions in which the magnetic reconnection of the sawtooth cycle developed secondary tearing instabilities, called plasmoids, along the current sheet developing along the elongated X point of the internal 1/1 kink mode. The second challenge was to nonlinearly couple the 1/1 to the 1/0 mode, in order to self consistently excite the latter, as esperimentaly the n=0 is found to be the dominant toroidal mode in Ohmic tokamak discharges. The coupling of the 1/1 mode with other helicities would be naturally present in toroidal geometry, but in the cylindrical geometry approximation of our present simulations, the presence of at least an additional mode (like the 2/1 or the 3/2) was necessary to provide the coupling with the 1/0 mode. It's important to note that the numerical simulations were obtained from a non-linear code, SpeCyl, which can give the

plasma temporal evolution, unlike the linear stability codes widely used in literature that can just provide the linear growth rates for a given magnetic configuration (notable exceptions being several fully kinetic and gyrokinetic codes, together with hybrid kinetic-MHD codes such as HYMAGIC and MEGA [Vlad et al., 2021]).
More in detail, the dynamics of quasi-periodic sawtooth cycles, in Tokamak configuration with bell-shaped density profile, were analized starting from a helically-symmetric 2D classical case with relatively high resistivity characterized by an internal m/n=1/1 kink instability. Magnetic reconnection events, consistent with the Kadomtsev nonlinear complete reconnection model, is described. Then a marginal case with threshold resistivity was considered, for different number of harmonics of the 1/1 internal kink mode. First appearance of plasmoids was observed for 32 harmonics case. This number of helical harmonics of the 1/1 was kept for the following analysis. By further lowering the resistivity a complete evolution of plasmoids is observed: formation, coalescence into a single larger secondary island and subsequent complete reconnection with the primary island of the internal kink instability. A comparison of same simulation with 4, 16 and 32 harmonics was then carried out, showing that high-m modes, corresponding to secondary tearing instabilities of the current layer causing plasmoid formation, do play a significant role for fast magnetic reconnection of the $q < 1$ core region in the visco-resistive MHD simulations. Subsequently, the previous simulation with 32 modes was reiterated in fully 3D configuration and compared with its 2D case, observing analogous dynamics of plasmoids evolution. In order to excite the 1/0 mode spectrum by magnetic reconnection events, triggered by the 1/1 internal kink mode, a three-wave coupling approach with 2/1 mode was adopted. In the specific tokamak equilibrium considered by us, the 2/1 mode results marginaly stable during the nonlinear evolution of sawtooth cycles. As a result, after its initial excitation its amplitude stays almost constant in time, providing a way for the nonlinear coupling between 1/1 and 1/0 modes. In order to check whether Fourier space resolution of MHD modes considered was sufficient, kinetic and magnetic energies cascades were analyzed. An accumulation in energy was detected at the edge of the Fourier space. A wider Fourier space resolution analysis showed no noticeable effects on the dynamics aspects of interest to our study. Lastly a magnetic topology analysis was carried out, considering different degree of excitation of the 2/1 mode and an alternative coupling approach with marginally stable 3/2 mode. The results confirmed the soundness of the coupling approach used in our simulations.
In the end of the corresponding chapter, a summary of a published study of fully 3D RFP simulations characterized by a systematic repetition of QSH states in between magnetic reconnection events was reported, as analogous simulations with slightly different parameters were used in later chapter for the study of AEs excitations by self-consistent dynamics of RFP plasmas.

The main goal of the *AEs excitation in single wave simulations with fixed equilibrium fields*, and by initial perturbations, (Part III, Chapter 7) study was to provide a classification of Alfvén waves spectra and related phenomena for different configurations of magnetic field and density profiles considered in this Thesis, to be used in subsequent analyses for the identification of Alfvén modes excited by self-generated perturbations of velocity fieds. In particular, simulations with single Fourier mode were considered. A small initial perturbation was applied to the velocity fields in order to excite the Alfvén frequency spectrum.
More in detail, the first analyzed configuration (the simplest one) was an equilibrium configuration with uniform axial magnetic field with a uniform density profile. This case was used as a verification testbed, since it is the only one for which an exact analytical solution for different Alfvénic modes (namely

the shear Alfvén wave, SAW, and compressional Alfvén eigenmodes, CAEs) can be obtained from the theoretical models. The verification of the numerical frequency spectra with the theoretical ones showed excellent agreement, thus demonstrating the applicability of the SpeCyl code as a well suited simulation tool for the study of Alfvén waves. Next the analysis of a tokamak configuration considered first with a uniform density profile, then with a variable one, was performed. Identification of Alfvén waves in the frequency spectrum was achieved by employing techniques such as the Wentzel–Kramers–Brillouin (WKB) approximation. Compared to the previous case a new mode emerged, the global Alfvén eigenmode (GAE), and phenomena like phase mixing, a damping mechanism for the continuous Alfvén waves, and a coupling between different Alfvén modes, were observed as theoretically predicted. A brief comparison between two different techniques of computing frequency spectra, namely the FFT and the CWT, was presented. For the tokamak configuration the relevant Fourier modes (that play an important role in later analysis) characterized were the 1/1, 1/0 and the equilibrium mode 0/0. The last configuration considered was an RFP-like equilibrium configuration with two different density profiles. The first employed density profile was an RFX-mod like hollow density profile, which mimics the experimentally measured density in RFX-mod device. The second was a bell-shaped density profile (analogous to the one considered in the tokamak configuration) which more strongly excites the GAE mode with respect to the hollow one. Compared with the previous case, the frequencies of CAEs are lower and in particular the frequency of the first CAE crosses the SAW continuum. As a consequence the resonance absorption of the 1^{st} CAE was observed. In this case only the relevant 1/0 mode was analyzed.

In the study of *AEs excitation in sawtoothing Ohmic Tokamak* plasmas (Part III, Chapter 8) we examine the numerical spectra of the simulations previously discussed in Chapter 6, in order to detect whenever the sawtooth dynamic could excite Alvénic modes and characterize under which condition this occurs. The first (weak) excitation of Alfvénic modes in helically-symmetric configuration is observed in the marginal case for the formation of plasmoids: the 1^{st} and 2^{nd} CAEs can be detected and are damped rapidly over time. A much stronger excitation is observed in simulations with lower resistivity: the SAW and the first three CAEs are clearly excited by the magnetic reconnection event in the 1/1 mode spectrum. In the corresponding fully 3D configuration excitation of Alfvén waves with 1/0 periodicity, due to the three-wave coupling of 2/1 mode with 1/1 mode, are investigated. A strong excitation of the GAE mode is observed, with the compressional modes being excited although to a lower degree. On the contrary, the CAEs are more excited in the 1/1 mode spectrum and a non linear coupling of the 1/0 GAE mode is observed within the 1/1 spectrum (the continuous shear with 1/1 periodicity does not have a local minimum for the GAE to be excited). This analysis provides a possible explanation for the experimental observations of modes with Alfvénic frequency during Ohmic discharges in a number of present tokamak experiments, for which the dominant toroidal mode number was found to be n=0 [McClements et al., 2002]. Furthermore the effect of the marginally stable 2/1 mode amplitude on the excitation of 1/0 periodicity Alfvén waves and comparison with the 3/2 mode coupling approach is examined. Both analyses provide a consistent picture of the nonlinear excitation of 1/0 AEs by the sawtoothing 1/1 internal kink.

The final study of *AEs excitation in sawtoothing Ohmic RFP* plasmas (Part III, Chapter 9) focuses on the analysis of the frequency spectra of the fully 3D RFP case with hollow density profile, discussed at the end of Chapter 5, to detect the Alfvénic activity following the relaxation events in between QSH states, a characteristic dynamic of RFP configuration. Investigation of a wide range of Fourier modes determined

the 1/0 mode to be the most excited one by the magnetic reconnection events, which is consistent with experimental observations in RFP devices in Ohmic regime, thus confirming the similarity of the 3D numerical simulations compared to the RFX-mod discharges. Finally a comparison between the numerical results and experimental observations [Spagnolo et al., 2011] was carried out, allowing us to propose the identification of the experimental coherent Alfvén modes, named d, e and f in Section 9.1 as GAE, the 1^{st} CAE, and the 2^{nd} CAE, respectively.
Part of the results of this Thesis, particularly the contents of Chapter 7 and Chapter 9, are discussed in a paper recently published in Nuclear Fusion [Kryzhanovskyy et al., 2022]. While the contents of Chapter 8 will soon to be submitted for publication.

In conclusion, the results achieved in this Thesis and the employed theoretical methods contribute to the understanding of the physics of Alfvén waves in fusion plasmas, in particular a further confirmation of the common physics basis between Tokamak and RFP confinement techniques is presented. As a matter of fact, we have demostrated within the nonlinear MHD model in cylindrical geometry that magnetic reconnection events can stimulate Alfvénic Eigenmodes in both the RFP and Tokamak configurations. As next step, to include more advanced configurations in the modelling and a wider range of plasma phenomena, several aspects not taken into account in this Thesis will need to be addressed: two-fluids physics, finite beta with (anisotropic) heat transport, toroidal geometry and the coupling with fast particles. This will enable us to take into account a wider variety of Alfvénic modes and instabilities, in particular Toroidal Alfvén Eigenmodes (TAEs) [Breizman et al., 1995] and Energetic Particle Modes (EPMs) [Sharapov et al., 2013]. Notably in Tokamak discharges, TAEs often experience frequency modulation known as chirping [White et al., 2020; Wang et al., 2018]. These events modify the local high energy particle distribution and are expected to also occur in future fusion devices [Duarte et al., 2018], which include energetic beams or fusion products. The study carried out in this Thesis forms a solid basis for further investigation into advanced modelling studies of Alfvén waves excitation by fast magnetic reconnection events in toroidal plasmas, with the final goal of contributing in making magnetic confinement fusion a viable and practical solution for thermonuclear power production.

Appendices

Appendix A

Induction equation and Alfvén theorem

In this appendix we derive the induction equation. The Ampère's law (4.1c) states

$$\nabla \times \mathbf{B} = \mu_0 \mathbf{J}. \tag{A.1}$$

We can write the Ohm's law (4.1d) as

$$\mathbf{J} = \frac{1}{\eta}(\mathbf{E} + \mathbf{v} \times \mathbf{B}). \tag{A.2}$$

Combining (A.1) and (A.2) we can write the electric field as

$$\mathbf{E} = \frac{\eta}{\mu_0} \nabla \times \mathbf{B} - \mathbf{v} \times \mathbf{B}. \tag{A.3}$$

Finally substituting from (A.3) into the Faraday's law (4.1b), and using the following identity

$$\nabla \times (\nabla \times \mathbf{B}) = \nabla(\nabla \cdot \mathbf{B}) - \nabla^2 \mathbf{B}, \tag{A.4}$$

where $\nabla \cdot \mathbf{B} = 0$, we obtain the *induction equation*

$$\frac{\partial \mathbf{B}}{\partial t} = \nabla \times (\mathbf{v} \times \mathbf{B}) + \frac{\eta}{\mu_0} \nabla^2 \mathbf{B}. \tag{A.5}$$

Now we will prove the Alfvén's theorem of flux freezing. In ideal MHD limit ($\eta = 0$), we can write

$$\frac{\partial \mathbf{B}}{\partial t} = \nabla \times (\mathbf{v} \times \mathbf{B}). \tag{A.6}$$

To continue we state a more general version of *Kelvin's vorticity theorem*: if any vector field $\mathbf{Q}$ in a fluid satisfies the equation

$$\frac{\partial \mathbf{Q}}{\partial t} = \nabla \times (\mathbf{v} \times \mathbf{Q}), \tag{A.7}$$

then

$$\frac{\mathrm{d}}{\mathrm{d}t} \int_S \mathbf{Q} \cdot \mathrm{d}\mathbf{S} = 0. \tag{A.8}$$

where **S** is a surface inside the fluid. The proof of this theorem can be found in [Choudhuri, 1998, p. 67]. Since (A.6) is of (A.7) form, we can directly apply this theorem and conclude that

$$\frac{\mathrm{d}}{\mathrm{d}t}\int_S \mathbf{B}\cdot\mathrm{d}\mathbf{S} = 0, \tag{A.9}$$

where the surface integral can be thought to be over a surface made up of definite fluid elements and the Lagrangian time derivative implies that we are considering the variation in time while following the surface as the fluid elements making it are moving. Physically we can say that the magnetic fields move with the fluid, i.e. the magnetic fields are completely "frozen" in the fluid. This result is called *Alfvén's theorem of flux-freezing*. A direct consequence of this theorem is that if two fluid elements are connected by a field line, they will always remain connected by a field line in the limit of ideal MHD. The preservation of such connectivities introduce some constrains on the dynamics of the system. In particular the magnetic topologies are exactly preserved in a magnetofluid with zero electrical resistivity.

Appendix B

Fourier Transforms

Both the fluid and kinetic descriptiopns of a plasma employ the theory of Fourier transforms, which we summarize here. If the equilibrium state of the plasma is assumed uniform, and the fluid equations are linearized, the coefficients in the resulting wave equatios are constants. A Fourier transform in space and time will then yield an algebraic equation in the Fourier amplitude of, for example, the perturbation velocity $\mathbf{v}_1$, which is a function of time t and space x. The Fourier transform of $\mathbf{v}_1$ is defined as

$$\mathbf{v}(\omega, \mathbf{k}) = \int \mathrm{d}t \, \mathrm{d}^3\mathbf{x} \;\; \exp\left(i\left(\omega t - \mathbf{k}\cdot\mathbf{x}\right)\right) \mathbf{v}_1(t, \mathbf{x}) \tag{B.1}$$

with the inverse transform

$$\mathbf{v}_1(t, \mathbf{x}) = \int \frac{\mathrm{d}\omega \, \mathrm{d}^3\mathbf{k}}{(2\pi)^4} \;\; \exp(-i(\omega t - \mathbf{k}\cdot\mathbf{x}))\mathbf{v}(\omega, \mathbf{k}). \tag{B.2}$$

Taking the Fourier transform in the uniform plasma case is simply equivalent to seeking plane wave solutions, that is, to assuming the form

$$\exp[i(k_x x + k_y y + k_z z - \omega t)] \tag{B.3}$$

for the wave fields, with k_x, k_y and k_z the constant wavenumbers in a Cartesian coordinate system.

Appendix C

Visco-resistive MHD equations in dimensionless units

The equations of the visco-resistive MHD model in dimensionless form can be obtained from those in SI units:

$$\rho\left[\frac{\partial \mathbf{v}}{\partial t}+(\mathbf{v}\cdot\nabla)\mathbf{v}\right]=\mathbf{J}\times\mathbf{B}+\rho\nu\nabla^2\mathbf{v} \tag{C.1a}$$

$$\frac{\partial \mathbf{B}}{\partial t}=-\nabla\times\mathbf{E} \tag{C.1b}$$

$$\nabla\times\mathbf{B}=\mu_0\mathbf{J} \tag{C.1c}$$

$$\mathbf{E}+\mathbf{v}\times\mathbf{B}=\eta\mathbf{J} \tag{C.1d}$$

$$\nabla\cdot\mathbf{B}=0. \tag{C.1e}$$

The physical variables will be normalized to the characteristic values of the system under examination and the density will be considered constant equal to ρ_0, in particular we have:

$$r=\tilde{r}a \tag{C.2a}$$

$$t=\tilde{t}\tau_A \tag{C.2b}$$

$$\rho=\rho_0 \tag{C.2c}$$

$$\mathbf{B}=\tilde{\mathbf{B}}B_0 \tag{C.2d}$$

$$\mathbf{J}=\tilde{\mathbf{J}}J_0 \tag{C.2e}$$

$$\mathbf{v}=\tilde{\mathbf{v}}v_A, \tag{C.2f}$$

with a plasma radius in cylindrical geometry, B_0 value of the axial component of the magnetic field at the axis of the cylinder at the initial instant, $v_A=\frac{B_0}{(\mu_0\rho_0)^{1/2}}$ Alfvén's speed and $\tau_A=\frac{a}{v_A}$ Alfven's time.

From the equation (C.1c) we obtain the normalization factor for the current:

$$\tilde{\mathbf{J}}J_0\frac{\mu_0 a}{B_0}=\tilde{\nabla}\times\tilde{\mathbf{B}}\Rightarrow J_0=\frac{B_0}{\mu_0 a}. \tag{C.3}$$

From the equation (C.1a) we obtain the normalization factor for the resistivity:

$$\frac{\mathrm{d}\tilde{\mathbf{v}}}{\mathrm{d}\tilde{t}} = \frac{\tau_A}{v_A}\left(\frac{J_0 B_0}{\rho_0}\tilde{\mathbf{J}}\times\tilde{\mathbf{B}} + \frac{\nu v_A}{a^2}\tilde{\nabla}^2\tilde{\mathbf{v}}\right) = \tilde{\mathbf{J}}\times\tilde{\mathbf{B}} + \frac{\nu}{v_A a}\tilde{\nabla}^2\tilde{\mathbf{v}} \Rightarrow \tilde{\nu} = \frac{\nu}{v_A a} = \frac{1}{M}, \tag{C.4}$$

where M is the viscous Lundquist number, which represents the inverse of viscosity in dimensionless units. The analysis of the equation (C.1c) makes it possible to find the normalization factor for the electric field $\mathbf{E}$:

$$\frac{\partial\tilde{\mathbf{B}}}{\partial\tilde{t}} = \frac{E_0}{v_A B_0}\tilde{\nabla}\times\tilde{\mathbf{E}} \Rightarrow E_0 = v_A B_0. \tag{C.5}$$

Considering the Ohm equation (C.1d) instead we obtain:

$$\tilde{\mathbf{E}} + \tilde{\mathbf{v}}\times\tilde{\mathbf{B}} = \frac{\eta}{\mu_0 v_A a}\tilde{\mathbf{J}} = \tilde{\eta}\tilde{\mathbf{J}}. \tag{C.6}$$

One notices in particular the identity:

$$\tilde{\eta} = \frac{\eta}{\mu_0 v_A a} = \frac{\eta a}{\mu_0 v_A a^2} = \frac{\tau_A}{\tau_R} = S^{-1}, \tag{C.7}$$

wherein $\tau_R = \frac{\mu_0 a^2}{\eta}$ represents the resistive diffusion time and S the Lundquist number.

With these normalizations, the visco-resistive MHD equations in dimensionless units are obtained (tildas have been omitted):

$$\frac{\partial\mathbf{v}}{\partial t} + (\mathbf{v}\cdot\nabla)\mathbf{v} = \mathbf{J}\times\mathbf{B} + \nu\nabla^2\mathbf{v} \tag{C.8a}$$

$$\frac{\partial\mathbf{B}}{\partial t} = -\nabla\times(\eta\mathbf{J} - \mathbf{v}\times\mathbf{B}) \tag{C.8b}$$

$$\mathbf{J} = \nabla\times\mathbf{B} \tag{C.8c}$$

$$\nabla\cdot\mathbf{B} = 0 \tag{C.8d}$$

Note that our model equations highlights only two dimensionless parameters η and ν that matter for the dynamics of the system. In other words, once the dimensionless values of η and ν have been chosen, SpeCyl provides a solution of the visco-resistive MHD equations in dimensionless units, which can be rescaled for different choices of the normalization factors.

Appendix D

Helical flux function χ

In this appendix we derive the helical flux function $\chi(\mathbf{r})$. Let us consider a magnetic field $\mathbf{B}(\mathbf{r})$ in a three-dimensional space with a curvilinear coordinate system whose coordinates are labeled as $u^i = (u^1, u^2, u^3)$. Let us suppose that the system has a symmetry, i.e., $\partial/\partial u^3 = 0$. The magnetic field can be written using the vector potential $\mathbf{A}(\mathbf{r})$ as:

$$\mathbf{B} = \nabla \times \mathbf{A} = \frac{\varepsilon^{ijk}}{J} \frac{\partial A_j}{\partial u^i} \mathbf{e}_k, \tag{D.1}$$

where ε^{ijk} represents the Levi-Civita tensor, J the jacobian of the coordinate transformation, A_j the covariant component of the vector potential and $\mathbf{e}_k$ is the covariant basis vector. Imposing the relation $\mathbf{B} \cdot \nabla \chi = 0$ choosing a gauge $A_1 = 0$ and remembering that $\partial/\partial u^3 = 0$ it is found that

$$\frac{\partial A_3}{\partial u^2} \frac{\partial \chi}{\partial u^1} - \frac{\partial A_3}{\partial u^1} \frac{\partial \chi}{\partial u^2} = 0, \tag{D.2}$$

meaning that the equaility is satisfied if

$$\chi = A_3 = \mathbf{A} \cdot \mathbf{e}_3. \tag{D.3}$$

In helical geometry the helical flux function is given by the third covariant component of the vector potential, that will be indicated as A_{3h} . The next step is the determination of the helical flux function in cylindrical geometry, using the transformation law of vector between different geometries. Indicating with A_{ih} the covariant components of the vector potential in helical geometry and with A_{ic} the covariant components of the vector potential in cylindrical geometry the transformation law can be written as [D'haeseleer, 1991] $A_{ic} = A_{ih} \frac{\partial u^{ih}}{\partial u^{ic}}$. The helical geometry is defined by the three coordinates $u^{ih} = (\rho, u, l)$, while the cylindrical one is defined by $u^{ic} = (r, \theta, z) = m\theta + \frac{n}{R_0} z$. The quantity ρ represents a radial coordinate, u represents a helical angle and the third coordinate l is ignorable in the case of helical symmetry under analysis. The coordinates of the helical geometry can be written in terms of the cylindrical coordinates as $\rho = r$, $u = m\theta + \frac{n}{R_0} z$ and $l = z$. Other choices are possible, in particular for the ignorable coordinate.

This identification allows transforming the helical flux function in helical geometry to cylindrical geometry.

Simple calculations show that $\chi = A_{3h} = A_{3c} - \frac{n}{mR_0} A_{2c}$, that, in terms of the physical cylindrical components of the vector potential $(\tilde{A}_r, \tilde{A}_\theta, \tilde{A}_z)$ the helical flux function (multiplied by m), is given by:

$$\chi = m\tilde{A}_z - \frac{n}{R_0} r\tilde{A}_\theta. \tag{D.4}$$

Bibliography

Ali, A. and P. Zhu (2019). "Effects of plasmoid formation on sawtooth process in a tokamak". In: *Physics of Plasmas* **26**.5, p. 052518.

Bessel function roots (n.d.). URL: http://wwwal.kuicr.kyoto-u.ac.jp/www/accelerator/a4/besselroot.htmlx.

Biskamp, Dieter (1993). "Magnetic reconnection". In: *Nonlinear Magnetohydrodynamics*. Cambridge Monographs on Plasma Physics. Cambridge University Press, 127–174.

Bonfiglio, D., L. Chacón, and S. Cappello (2010). "Nonlinear three-dimensional verification of the SPECYL and PIXIE3D magnetohydrodynamics codes for fusion plasmas". In: *Physics of Plasmas* **17**.8, p. 082501.

Bonfiglio, D. et al. (2013). "Experimental-like Helical Self-Organization in Reversed-Field Pinch Modeling". In: *Phys. Rev. Lett.* **111** (8), p. 085002.

Bonofiglo, P. J. et al. (2019). "Fast ion transport in the quasi-single helical reversed-field pinch". In: *Physics of Plasmas* **26**.2, p. 022502.

Boozer, Allen H. (2012). "Theory of tokamak disruptions". In: *Physics of Plasmas* **19**.5, p. 058101.

Breizman, B. N., M. S. Pekker, and S. E. Sharapov (2005). "Plasma pressure effect on Alfvén cascade eigenmodes". In: *Physics of Plasmas* **12**.11, p. 112506.

Breizman, B.N. and S.E. Sharapov (1995). "Energetic particle drive for toroidicity-induced Alfven eigenmodes and kinetic toroidicity-induced Alfven eigenmodes in a low-shear tokamak". In: *Plasma Physics and Controlled Fusion* **37**.10, pp. 1057–1074.

Cai, H. et al. (2014). "Effects of pressure gradient on global Alfvén eigenmodes in reversed field pinch". In: *Physics of Plasmas* **21**.2, p. 022513.

Cappello, S. (2004). "Bifurcation in the MHD behaviour of a self-organizing system: the reversed field pinch (RFP)". In: *Plasma Physics and Controlled Fusion* **46**.12B, B313.

Cappello, S. and D. Biskamp (1996). "Reconnection processes and scaling laws in reversed field pinch magnetohydrodynamics". In: *Nuclear Fusion* **36**.5, p. 571.

Cappello, S. and R. Paccagnella (1992). "Nonlinear plasma evolution and sustainment in the reversed field pinch". In: *Physics of Fluids B: Plasma Physics* **4**.3, pp. 611–618.

Chang, Z. et al. (1995). "Alfven frequency modes at the edge of TFTR plasmas". In: *Nuclear Fusion* **35**.12, pp. 1469–1479.

Chapman, I. T. (Jan. 2011). "Controlling sawtooth oscillations in tokamak plasmas". In: *Plasma Physics and Controlled Fusion* **53**.1, 013001, p. 013001.

Chen, F.F. (1984). *Introduction to Plasma Physics and Controlled Fusion*. Introduction to Plasma Physics and Controlled Fusion v. 1. Springer.

Chen, Liu and Akira Hasegawa (1974). "Plasma heating by spatial resonance of Alfvén wave". In: *The Physics of Fluids* **17**.7, pp. 1399–1403.

Chen, Liu and Fulvio Zonca (2016). "Physics of Alfvén waves and energetic particles in burning plasmas". In: *Rev. Mod. Phys.* **88** (1), p. 015008.

Choudhuri, A.R. (1998). *The Physics of Fluids and Plasmas: An Introduction for Astrophysicists*. Cambridge University Press.

Costa, S. et al. (1999). "A wave-particle interaction model for tail ion acceleration in reversed field pinch plasmas". In: *Plasma Physics and Controlled Fusion* **41**.12, pp. 1485–1496.

Cramer, N.F. (2001). *The physics of Alfvén waves*. Wiley-VCH.

Cross, R. (1988). *An Introduction to Alfven Waves,* Taylor & Francis.

D'haeseleer, W.D. (1991). *Flux Coordinates and Magnetic Field Structure: A Guide to a Fundamental Tool of Plasma Structure*. Computational Physics Series. Springer-Verlag.

Dippolito, D. A. and J. P. Goedbloed (Dec. 1980). "Mode coupling in a toroidal sharp-boundary plasma. I. Weak-coupling limit". In: *Plasma Physics* **22**.12, pp. 1091–1107.

Donne, A. and Y. Liang (July 2012). "MHD control in burning plasmas". In: *Nuclear Fusion* **52**.

Duarte, V.N. et al. (2018). "Study of the likelihood of Alfvénic mode bifurcation in NSTX and predictions for ITER baseline scenarios". In: *Nuclear Fusion* **58**.8, p. 082013.

Energy Drive, ITER Physics Expert Group on and ITER Physics Basis Editors (1999). "Chapter 5: Physics of energetic ions". In: *Nuclear Fusion* **39**.12, pp. 2471–2495.

Escande, D. F. et al. (2000a). "Chaos Healing by Separatrix Disappearance and Quasisingle Helicity States of the Reversed Field Pinch". In: *Phys. Rev. Lett.* **85** (15), pp. 3169–3172.

Escande, D. F. et al. (2000b). "Single helicity: a new paradigm for the reversed field pinch". In: *Plasma Physics and Controlled Fusion* **42**.12B, B243.

Escande, D.F., V. Gondret, and F. Sattin (Oct. 2019). "Relevant heating of the quiet solar corona by Alfvén waves: a result of adiabaticity breakdown". In: *Scientific Reports* **9**, p. 14274.

Freidberg, Jeffrey P. (2014). *Ideal MHD*. Cambridge University Press.

Fu, G. Y. and H. L. Berk (2006). "Effects of pressure gradient on existence of Alfvén cascade modes in reversed shear tokamak plasmas". In: *Physics of Plasmas* **13**.5, p. 052502.

Garcia-Munoz, M. et al. (2019). "Active control of Alfvén eigenmodes in magnetically confined toroidal plasmas". In: *Plasma Physics and Controlled Fusion* **61**.5, p. 054007.

Goeler, S. von, W. Stodiek, and N. Sauthoff (1974). "Studies of Internal Disruptions and $m = 1$ Oscillations in Tokamak Discharges with Soft—X-Ray Tecniques". In: *Phys. Rev. Lett.* **33** (20), pp. 1201–1203.

Goldston, R.J. and P.H. Rutherford (1995). *Introduction to Plasma Physics*. Institute of Physics Pub.

Grad, H. and H. Rubin (1958). "Hydromagnetic equilibria and force-free fields". In: *Page 190 of: Proceedings of the Second United Nations International Conference on the Peaceful Uses of Atomic Energy, United Nations, Geneva* **31**.

Hasegawa, A. and L. Chen (1976). "Kinetic processes in plasma heating by resonant mode conversion of Alfvén wave". In: *The Physics of Fluids* **19**.12, pp. 1924–1934.

Hastie, R. J. et al. (1987). "Stability of ideal and resistive internal kink modes in toroidal geometry". In: *The Physics of Fluids* **30**.6, pp. 1756–1766.

Holst, B. van der, A. J. C. Beliën, and J. P. Goedbloed (2000). "New Alfvén Continuum Gaps and Global Modes Induced by Toroidal Flow". In: *Phys. Rev. Lett.* **84** (13), pp. 2865–2868.

Holties, H. A. et al. (1997). "Determination of local tokamak parameters by magnetohydrodynamic spectroscopy". In: *Physics of Plasmas* **4**.3, pp. 709–719.

Kadomtsev, Boris B (1975). "Disruptive instability in tokamaks". In: *Sov. Tech. Phys. Lett.(Engl. Transl.);(United States)* **1**.5.

Koliner, J. J. et al. (2012). "Fast-Particle-Driven Alfvénic Modes in a Reversed Field Pinch". In: *Phys. Rev. Lett.* **109** (11), p. 115003.

Kryzhanovskyy, Artur et al. (2022). "Alfvén waves in reversed-field pinch and tokamak Ohmic plasmas: nonlinear 3D MHD modelling and comparison with RFX-mod". In: *Nuclear Fusion*.

Li, M. et al. (2014). "Alfvén modes in the Madison Symmetric Torus". In: *Physics of Plasmas* **21**.8, p. 082505.

Lin, L. et al. (2014). "Energetic-particle-driven instabilities and induced fast-ion transport in a reversed field pinch". In: *Physics of Plasmas* **21**.5, p. 056104.

Liu, Linzi et al. (2019). "Beta-induced Alfvén eigenmodes destabilized by resonant magnetic perturbations in the J-TEXT tokamak". In: *Nuclear Fusion* **59**.12, p. 126022.

Lorenzini, R. et al. (2009a). "Improvement of the magnetic configuration in the reversed field pinch through successive bifurcations". In: *Physics of Plasmas* **16**.5, p. 056109.

Lorenzini, R. et al. (Aug. 2009b). "Self-organized helical equilibria as a new paradigm for ohmically heated fusion plasmas". In: *Nature Physics* **5**, pp. 570–574.

Malara, Francesco, Pierluigi Veltri, and Vincenzo Carbone (1992). "Competition among nonlinear effects in tearing instability saturation". In: *Physics of Fluids B: Plasma Physics* **4**.10, pp. 3070–3086.

Maraschek, M. et al. (1997). "Observation of Toroidicity-Induced Alfvén Eigenmodes in Ohmically Heated Plasmas by Drift Wave Excitation". In: *Phys. Rev. Lett.* **79** (21), pp. 4186–4189.

Martin, P. et al. (2003). "Overview of quasi-single helicity experiments in reversed field pinches". In: *Nuclear Fusion* **43**.12, p. 1855.

McClements, K.G. et al. (2002). "Excitation of axisymmetric Alfvénic modes in Ohmic tokamak discharges". In: *Nuclear Fusion* **42**.9, pp. 1155–1161.

Musielak, Z. E. and S. T. Suess (1989). "MHD surface waves in high- and low-beta plasmas. Part 1. Normal-mode solutions". In: *Journal of Plasma Physics* **42**.1, 75–89.

Ortolani, S. and D.D. Schnack (1993). *Magnetohydrodynamics of Plasma Relaxation*. World Scientific.

Parnell, C.E. and I. De Moortel (2012). "A contemporary view of coronal heating". In: *Philosophical Transactions of the Royal Society A: Mathematical, Physical and Engineering Sciences* **370**.1970, 3217–3240.

Perkins, F., P. Barabaschi, and D. Boucher (1995). *ITER physics basis*. International Atomic Energy Agency (IAEA): IAEA.

Piovesan, P. et al. (2009a). "Magnetic order and confinement improvement in high-current regimes of RFX-mod with MHD feedback control". In: *Nuclear Fusion* **49**.8, p. 085036.

Piovesan, P. et al. (July 2009b). "Magnetic order and confinement improvement in high-current regimes of RFX-mod with MHD feedback control". In: *Nuclear Fusion* **49**, p. 085036.

Poedts, S et al. (1992). "Damping of global Alfven waves in tokamaks due to resonant absorption". In: *Plasma Physics and Controlled Fusion* **34**.8, pp. 1397–1422.

Regnoli, Giorgio et al. (Apr. 2005). "Observations of toroidicity-induced Alfvén eigenmodes in a reversed field pinch plasma". In: *Physics of Plasmas* **12**.

Sharapov, S.E. et al. (2013). "Energetic particle instabilities in fusion plasmas". In: *Nuclear Fusion* **53**.10, p. 104022.

Sonato, P. et al. (2003). "Machine modification for active MHD control in RFX". In: *Fusion Engineering and Design* **66-68**. 22nd Symposium on Fusion Technology, pp. 161 –168.

Spagnolo, S. et al. (2010). "Alfvén Eigenmodes in the RFX-mod reversed-field pinch plasma". In: *37th EPS Conference on Plasma Physics* **34A**, P4.162.

Spagnolo, S. et al. (2011). "Alfvén eigenmodes in the RFX-mod reversed-field pinch plasma". In: *Nuclear Fusion* **51**.8, p. 083038.

Stefani, F. et al. (2021). "Mode Conversion and Period Doubling in a Liquid Rubidium Alfvén-Wave Experiment with Coinciding Sound and Alfvén Speeds". In: *Phys. Rev. Lett.* **127** (27), p. 275001.

Sykes, A. (2001). "Overview of recent spherical tokamak results". In: *Plasma Physics and Controlled Fusion* **43**.12A, A127–A139.

Vaclavik, J. and K. Appert (1991). "Theory of plasma heating by low frequency waves: Magnetic pumping and Alfvén resonance heating". In: *Nuclear Fusion* **31**.10, pp. 1945–1997.

Veranda, M. et al. (2017). "Magnetohydrodynamics modelling successfully predicts new helical states in reversed-field pinch fusion plasmas". In: *Nuclear Fusion* **57**.11, p. 116029.

Veranda, M. et al. (Aug. 2020). "Magnetic reconnection in three-dimensional quasi-helical pinches". In: *Rendiconti Lincei. Scienze Fisiche e Naturali* **31**.

Vianello, N. et al. (2010). "Drift-Alfvén vortex structures in the edge region of a fusion relevant plasma". In: *Nuclear Fusion* **50**.4, p. 042002.

Villard, L. and J. Vaclavik (1997). "Alfven frequency modes and global Alfven eigenmodes". In: *Nuclear Fusion* **37**.3, p. 351.

Villard, L et al. (1995). "Alfvén wave heating and stability". In: *Physica Scripta* **T60**, pp. 44–56.

Vlad, G., F. Zonca, and S. Briguglio (2008). "Dynamics of Alfvén waves in tokamaks". In: *La Rivista del Nuovo Cimento (1978-1999)* **22**.7, p. 1.

Vlad, G. et al. (2021). "A linear benchmark between HYMAGYC, MEGA and ORB5 codes using the NLED-AUG test case to study Alfvénic modes driven by energetic particles". In: *Nuclear Fusion* **61**.11, p. 116026.

Wang, G. et al. (2018). "Frequency chirping in the Alfvén continuum". In: *Nuclear Fusion* **58**.8, p. 082014.

Wesson, J. (2004). *Tokamaks*. International series of monographs on physics. Clarendon Press.

White, R. B. et al. (2020). "Phase-space dynamics of Alfvén mode chirping". In: *Physics of Plasmas* **27**.5, p. 052108.

White, Roscoe (Jan. 2013). *The theory of toroidally confined plasmas: Third edition*, pp. 1–494.

Yu, Q., S. Günter, and K. Lackner (2014). "Formation of plasmoids during sawtooth crashes". In: *Nuclear Fusion* **54**.7, p. 072005.

Zohm, Hartmut (2014). In: *Magnetohydrodynamic Stability of Tokamaks*. John Wiley & Sons, Ltd, pp. 1–244.